

**Numerical Investigation of the Pollutant Dispersion in the  
Heterogeneous Urban Settings from Rooftop Sources**

by

Mohammad Reza Kavian Nezhad

A thesis submitted in partial fulfillment of the requirements for the degree of

Doctor of Philosophy

Department of Department of Mechanical Engineering  
University of Alberta

© Mohammad Reza Kavian Nezhad, 2024

# Abstract

Exhaust gases emitted from roof-based sources are recognized as one of the primary sources of urban air pollution that could considerably deteriorate both outdoor and indoor air quality. Urban planners frequently use analytical and semi-empirical dispersion models to assess the pollutant distribution field, leading to extremely conservative and less sustainable guidelines in the design process. In this regard, contributing to the effective and efficient passive approaches to control these contaminants, with the aid of urban morphology modifications, has been set as the ultimate goal of this research.

Given the limitations and complexities of the experimental investigations and the known weaknesses of the semi-empirical correlations, Computational Fluid Dynamics (CFD) has been selected as the method used in this study. The Mock Urban Setting Tests experiment (or MUST, performed in Utah in 2001) was simulated in this work to test and evaluate various modeling settings and to introduce a well-tested infrastructure to contribute to the "Best-Practice" in reliable modeling of dispersion flow within complex urban geometries. The performance of three widely suggested closure models of standard  $k - \varepsilon$ , RNG  $k - \varepsilon$ , and SST  $k - \omega$  were assessed with a specific emphasis on the effects of the source locations. This work demonstrates that the relative over-prediction of the turbulence kinetic energy by the standard  $k - \varepsilon$  model counteracts the general under-predictions by time-averaged methods in geometries with building complexes, leading to the least discrepancies with the measurements. A sensitivity study was also conducted to find the optimum turbulence Schmidt number ( $Sc_t$ ), using both the constant and locally variable values.

To further improve the accuracy of the numerical predictions, a re-calibration study is conducted to optimize the standard  $k - \varepsilon$  model by incorporating the recommended modeling settings from the previous step. A modified optimization framework based on a genetic algorithm was adapted to alleviate the computational expenses and to further identify ranges for each empirical coefficient, to achieve the most reliable and accurate predictions. A robust objective function was defined, incorporating both the flow parameters and pollutant concentration through several linear and logarithmic measures. The coefficients were trained using the MUST data set, leading to proposed ranges of  $0.14 \leq C_\mu \leq 0.15$ ,  $1.30 \leq C_{\varepsilon_1} \leq 1.46$ ,  $1.68 \leq C_{\varepsilon_2} \leq 1.80$ ,  $1.12 \leq \sigma_\varepsilon \leq 1.20$ , and  $0.87 \leq \sigma_k \leq 1.00$ . Using the modified turbulence closure, the fraction of predictions within the acceptable ranges from measurements increased by 8% for pollutant concentration and 27% for turbulence kinetic energy.

Employing the assembled infrastructure designed for CFD simulations of atmospheric pollutant dispersion lays the foundation for the primary objective. In the final step, a series of systematic studies aimed to explore the synergistic effects of unique urban morphologies or heterogeneous geometries on turbulent mixing and pollutant diffusion. This research contributes to ongoing efforts to advance urban planning practices, offering a passive approach to control pollutant dispersion from rooftop sources. Additionally, it advances the understanding of pollutant dispersion patterns in the presence of urban non-uniformities.

# Preface

This thesis is an original work by Mohammad Reza Kavian Nezhad.

## **Journal papers from Ph.D. thesis:**

- **M. R. Kavian Nezhad**, C. F. Lange, and B. A. Fleck, “Performance evaluation of RANS models in predicting the pollutant concentration field within a compact urban setting: Effects of the source location and turbulence Schmidt number”, *Atmosphere*, vol. 13, no. 7, p. 1013, 2022.
- **M. R. Kavian Nezhad**, K. RahnamayBahambary, C. F. Lange, and B. A. Fleck, “Modified accuracy of RANS modeling of urban pollutant flow within generic building clusters using a high-quality full-scale dispersion data set”, *Sustainability*, vol. 15, no. 19, p. 14317, 2023.
- **M. R. Kavian Nezhad**, C. F. Lange, and B. A. Fleck, “Unravelling the synergistic effects of urban morphological characteristics on dilution of air pollution emitting from roof-based sources in the proximity of the fresh air intakes”, Ready for submission to the journal of Science of the Total Environment.

## **Conference presentations:**

- **M. R. Kavian Nezhad**, C. F. Lange, and B. A. Fleck, “Evaluating the validity of CFD model of dispersion in a complex urban geometry using two sets of experimental measurements”, 16th International Conference on Computational Fluid Dynamics (ICCFD), Tokyo, January 7-8, 2022.

- **M. R. Kavian Nezhad**, C. F. Lange, and B. A. Fleck, “CFD modeling of near-field pollutant dispersion in urban settings: Combined effects of the source location and planar heterogeneities”, Proceedings of the Canadian Society for Mechanical Engineering International Congress (CSME Congress), Edmonton, June 5-8, 2022.
- **M. R. Kavian Nezhad**, C. F. Lange, and B. A. Fleck, “Energy efficient exhaust gas emission and dispersion from rooftop stacks in an actual urban setting: A case study in North campus of the University of Alberta”, Proceedings of the Canadian Society for Mechanical Engineering International Congress (CSME Congress), Edmonton, June 5-8, 2022.
- **M. R. Kavian Nezhad**, C. F. Lange, and B. A. Fleck, “Analysis of the urban non-uniformities influence on pollutant dispersion patterns emitting from roof-based sources using a tuned RANS closure”, 16th International Conference on Wind Engineering (ICWE16), Florence, August 27-31, 2023.

**Other journal papers:**

- S. J. Mattar, **M. R. Kavian Nezhad**, C. F. Lange, and B. A. Fleck, “Validation process for rooftop wind regime CFD model in complex urban environment using an experimental measurement campaign”, *Energies*, vol. 14, no. 9, p. 2497, 2021.

# Acknowledgements

I am profoundly grateful to my exam committee and supervisors, Dr. Brian Fleck, Dr. Carlos Lange, and Dr. Lexuan Zhong for their exceptional guidance and unwavering support throughout my doctoral studies. Their scholarly insights and continuous encouragement have been pivotal in shaping my research journey.

Dr. Fleck's mentorship extended beyond academic boundaries, offering invaluable advice and support during both professional and personal challenges. His role as both a supervisor and a mentor has profoundly impacted my growth. I consider myself lucky that our paths have crossed each other in life. My interactions with Dr. Lange have also been immensely enriching, enlightening me with sophisticated techniques in numerical simulations and introducing me to essential tools for conducting effective and efficient research. I am sincerely grateful for all those informative and interesting discussions we had.

The completion of this work was made possible by the financial support from the Natural Sciences and Engineering Research Council of Canada (NSERC) and the Canada First Research Excellence Fund (CFREF), for which I am deeply grateful.

My gratitude goes to my parents for their boundless love and constant encouragement. I also extend my sincere thanks to my friends and colleagues, for the great friendship and happy times we shared during my studies.

Finally, to my beloved wife, my best friend, and the one who is my past, present, and future, Sahar. Your steadfast support and countless sacrifices were the foundation of my success. Without you, this journey would not have been even possible. Your love and strength have brightened every step of this challenging and rewarding path.

# Table of Contents

<b>1</b>	<b>Introduction</b>	<b>1</b>
1.1	Thesis Objectives . . . . .	3
1.2	Thesis Outline . . . . .	6
<b>2</b>	<b>Background</b>	<b>8</b>
2.1	Atmospheric boundary layer . . . . .	9
2.1.1	Scales of the atmospheric dispersion studies . . . . .	10
2.1.2	Atmospheric stability classification . . . . .	11
2.2	Modeling methods in ABL studies . . . . .	13
2.2.1	Full-scale field experiment . . . . .	13
2.2.2	Reduced-scale laboratory experiment . . . . .	14
2.2.3	Semi-empirical models . . . . .	15
2.2.4	Numerical models . . . . .	17
2.3	CFD in urban dispersion modeling . . . . .	18
2.3.1	Turbulence modeling resolution . . . . .	19
2.3.2	Modeling considerations . . . . .	20
2.3.3	Dispersion around buildings . . . . .	23
<b>3</b>	<b>Performance evaluation of the RANS models in predicting the pollutant concentration field within a compact urban setting: Effects of the source location and turbulence Schmidt number</b>	<b>26</b>
3.1	Introduction . . . . .	26
3.2	Fundamentals and governing equations . . . . .	30
3.3	Description of case studies . . . . .	34
3.4	CFD model description . . . . .	38
3.4.1	General settings . . . . .	38
3.4.2	Grid sensitivity study . . . . .	40
3.5	Statistical analysis method . . . . .	41
3.6	Results and discussion . . . . .	43

3.6.1	Performance evaluation of closure models: Source location effects	43
3.6.2	Turbulent Schmidt number . . . . .	57
3.7	Conclusions . . . . .	60
<b>4</b>	<b>Modified accuracy of RANS modeling of urban pollutant flow within generic building clusters using a high-quality full-scale dispersion data set</b>	<b>63</b>
4.1	Introduction . . . . .	63
4.1.1	Objectives . . . . .	68
4.2	Mathematical model . . . . .	69
4.3	Closure model calibration . . . . .	74
4.4	Description of case studies . . . . .	80
4.5	CFD simulation . . . . .	83
4.5.1	General settings . . . . .	83
4.5.2	Grid convergence study . . . . .	85
4.5.3	Horizontal homogeneity . . . . .	86
4.6	Results and discussions . . . . .	89
4.6.1	Closure re-calibration . . . . .	89
4.6.2	Performance and generality evaluation . . . . .	97
4.7	Conclusion . . . . .	107
<b>5</b>	<b>Unravelling the synergistic effects of urban morphological characteristics on dilution of air pollution emitting from roof-based sources in proximity of the fresh air intakes</b>	<b>110</b>
5.1	Introduction . . . . .	110
5.1.1	Objectives . . . . .	114
5.2	Fundamental and mathematical model . . . . .	115
5.3	Methodology . . . . .	117
5.3.1	Description of case studies . . . . .	117
5.3.2	Outdoor ventilation and dispersion indices . . . . .	120
5.3.3	Numerical scheme . . . . .	124
5.4	Results and discussions . . . . .	129
5.4.1	Outdoor ventilation and pollutant dispersion . . . . .	129
5.4.2	Dynamics of dispersion patterns . . . . .	138
5.4.3	Regression analysis . . . . .	151
5.5	Conclusion . . . . .	154

<b>6</b>	<b>Conclusions and Future Work</b>	<b>158</b>
6.1	Conclusions . . . . .	158
6.2	Future Work . . . . .	163
	<b>Bibliography</b>	<b>166</b>

# List of Tables

3.1	Four selected trials of MUST field experiment. . . . .	37
3.2	Results of the grid independence analysis. . . . .	41
3.3	Statistical evaluation of the concentration predictions for the selected trials. . . . .	45
3.4	Statistical evaluation of the concentration predictions at horizontal and vertical sampling lines. . . . .	55
3.5	Statistical evaluation of the $C^*$ predictions of Trial 3 for different $Sc_t$ . . . . .	60
4.1	The ideal value and the recommended ranges for validation metrics [54]. . . . .	77
4.2	Standard and revised values of $k - \varepsilon$ empirical constants with their predetermined variation ranges. . . . .	80
4.3	Specifications of all MUST sampling points considered in the calibration study. . . . .	82
4.4	Summary of selected trials of MUST experiment for RANS calibration study. . . . .	83
4.5	Performance evaluation of the modified closure model in predicting the pollutant concentration field. . . . .	99
4.6	Performance evaluation of the modified closure model in predicting the velocity and TKE fields for the training case study. . . . .	103
4.7	Validation metrics for three selected test cases during the generalizability study. . . . .	106
5.1	Summary of geometric specifications for the investigated and reference case studies. . . . .	120
5.2	Coefficients of the bi-variate polynomials (Equation 5.10) fitted over the $C_{vol,n}^*$ data. . . . .	152
5.3	Performance evaluation of fitted regressions given in Table 5.2, using coefficient of determination ( $R^2$ ), average relative error ( $e_{avg}$ ), and maximum relative error ( $e_{max}$ ). . . . .	152

# List of Figures

3.1	(a) Planar schematic view of MUST container array; (b) Schematic view of all six types of re-leasing locations. . . . .	36
3.2	Comparison of concentration profiles at the first horizontal sampling line in Trial 1 for (a) cases with SST $k - \omega$ and for (b) cases with $k - \varepsilon$ based closure models. . . . .	42
3.3	Contours of the predicted concentration field obtained by different closure models on a horizontal plane at $z/H=0.64$ (The height at which all horizontal PIDs are installed). . . . .	44
3.4	The turbulence kinetic energy, TKE ( $\text{m}^2 \text{s}^{-2}$ ), distribution in the vicinity of the source location (red circle) in Trial 1. . . . .	46
3.5	Comparison of vertical profiles of (a) TKE and (b) velocity at the 32m central tower with the field measurements of Trial 1. . . . .	47
3.6	The turbulence kinetic energy, TKE ( $\text{m}^2 \text{s}^{-2}$ ), distribution in the vicinity of the source location (red circle) in Trial 2. . . . .	48
3.7	Comparison of vertical profiles of (a) TKE and (b) velocity at the 32m central tower with the field measurements of Trial 2. . . . .	49
3.8	The turbulence kinetic energy, TKE ( $\text{m}^2 \text{s}^{-2}$ ), distribution in the vicinity of the source location (red circle) in Trial 3. . . . .	51
3.9	Comparison of vertical profiles of (a) TKE and (b) velocity at the 32m central tower with the field measurements of Trial 3. . . . .	52
3.10	The turbulence kinetic energy, TKE ( $\text{m}^2 \text{s}^{-2}$ ), distribution in the vicinity of the source location (red circle) in Trial 4. . . . .	53
3.11	Comparison of vertical profiles of (a) TKE and (b) velocity at the 32m central tower with the field measurements of Trial 4. . . . .	54
3.12	Scatter diagrams between the predicted and observed concentrations in (a) horizontal and (b) vertical sampling lines. . . . .	56
3.13	Comparison of the $C^*$ profiles at the first horizontal sampling line in Trial 2 for different (a) inflow wind directions and (b) inflow turbulence profiles. . . . .	57

3.14	$C^*$ for different $Sc_t$ , and (b) the corresponding variable $Sc_t$ for the second sampling line of Trial 3. . . . .	59
4.1	MUST experiment schematic; (a) Dimensions and source locations, (b) Top planar view with samplers locations. . . . .	81
4.2	Computational domain . . . . .	84
4.3	Mesh sensitivity of (a) normalized velocity at 32 m central tower and (b) normalized concentration at the second horizontal sampling line. . . . .	87
4.4	The velocity, TKE and turbulence dissipation rate profiles in an empty domain. . . . .	88
4.5	Elementary effects of closure coefficients on (a) linear and (b) logarithmic validation metrics. . . . .	92
4.6	Comparing (a) $\overline{E}$ and (b) $\sigma_E$ of the elementary effects of closure coefficients on the validation metrics . . . . .	93
4.7	Variation of validation metrics during the re-calibration (a) FAC2 for pollutant concentration and (b) HR for TKE. . . . .	94
4.8	Surface plots of FAC2 variation for pollutant concentration field during the calibration process. . . . .	95
4.9	Variation of FB, VG, and MG for pollutant concentration field during the calibration process. . . . .	96
4.10	Sensitivity of the (a) linear and (b) logarithmic validation metrics to the variations of $\sigma_k$ . . . . .	98
4.11	Normalized concentration iso-surfaces ( $C^* = 10^{-2}$ ) flooded with TKE, predicted by (a) standard, and (b) optimized revision of $k - \varepsilon$ turbulence model. . . . .	99
4.12	Comparison of the predicted concentration fields at horizontal sampling lines. . . . .	100
4.13	Comparison of the predicted concentration fields at vertical sampling lines. . . . .	101
4.14	Scatter plot between the observed and predicted concentrations at all sampling points for standard and optimized closure sets. . . . .	102
4.15	Vertical profiles of the predicted TKE (a) at 32 m central tower and (b) at the tower $T_C$ . . . . .	104
4.16	Point-to-point evaluation and comparison of the predicted flow field across the test domain: (a) Velocity, (b) TKE. The error bars represent a 25% deviation from the experimental measurements. . . . .	105
5.1	Schematic and model descriptions of the defined case studies. . . . .	118

5.2	Evaluation regions to assess outdoor ventilation capacity in the proximity of the target building. . . . .	121
5.3	Pollutant concentration profile in case [S-25-25-45] along a horizontal line midway between the target building and its immediate upwind row at $Z/H = 0.75$ . . . . .	126
5.4	Schematic of the wind tunnel experiment “Case C” by Architectural Institute of Japan (AIJ). The model’s reference length scale is $B_C=0.2$ m. Small black circles depict 120 measurement points. . . . .	127
5.5	Predicted $V^*$ profiles at shown sampling lines for inflow wind direction of (a) $\theta = 0^\circ$ , and (b) $\theta = 45^\circ$ at $Z/B_C = 0.1$ . The error bars represent a 25% deviation from the experimental measurements. . . . .	128
5.6	Variations in (a) $V_{vol}^*$ and (b) $\tau$ , normalized to their respective reference values with identical $\lambda_p$ (but no disposition), within the control volume enclosing the target building under a $\theta = 0^\circ$ wind incidence. . . . .	130
5.7	Contours of non-dimensionalized concentration ( $C^*$ ) and velocity ratio ( $V^*$ ) distribution at the midplane of the upper half of the cluster height ( $Z/H = 0.75$ ) for three different disposition levels in three cases: (a) $\lambda_p = 6\%$ , (b) $\lambda_p = 11\%$ , and (c) $\lambda_p = 20\%$ for $\theta = 0^\circ$ wind direction. . . . .	132
5.7	(Continued). . . . .	133
5.8	Variations in (a) $V_{vol}^*$ and (b) $\tau$ , normalized to their respective reference values with identical $\lambda_p$ (but no disposition), within the control volume enclosing the target building under a $\theta = 45^\circ$ wind incidence. . . . .	135
5.9	Contours of non-dimensionalized concentration ( $C^*$ ) and velocity ratio ( $V^*$ ) distribution at the midplane of the upper half of the cluster height ( $Z/H = 0.75$ ) for three different disposition levels in three cases: (a) $\lambda_p = 6\%$ , (b) $\lambda_p = 11\%$ , and (c) $\lambda_p = 20\%$ for $\theta = 45^\circ$ wind direction. . . . .	136
5.9	(Continued). . . . .	137
5.10	Normalized pollutant transport rate due to turbulence diffusion, $F_{t,n}$ , and due to mean flow, $F_{m,n}$ , under $\theta = 0^\circ$ inflow wind through faces of the defined control volume around the target building. . . . .	140
5.10	(Continued). . . . .	141
5.11	Normalized pollutant transport rate due to turbulence diffusion, $F_{t,n}$ , and due to mean flow, $F_{m,n}$ , under $\theta = 45^\circ$ inflow wind through faces of the defined control volume around the target building. . . . .	144
5.11	(Continued). . . . .	145
5.12	Heat maps of the area averaged $C_n^*$ on the faces of the target building under $\theta = 0^\circ$ wind direction: (a) T <sub>b</sub> , (b) F <sub>b</sub> , (c) B <sub>b</sub> , (d) L <sub>b</sub> , (e) R <sub>b</sub> . . . . .	148

5.13	Heat maps of the area averaged $C_n^*$ on the faces of the target building under $\theta = 45^\circ$ wind direction: (a) T <sub>b</sub> , (b) F <sub>b</sub> , (c) B <sub>b</sub> , (d) L <sub>b</sub> , (e) R <sub>b</sub> . . . . .	150
5.14	$C_{vol,n}^*$ distribution in terms of the $\lambda_p$ and $\zeta$ under $\theta = 0^\circ$ wind direction using (a) linear, (b) quadratic, and (c) cubic polynomials. . . . .	153
5.15	$C_{vol,n}^*$ distribution in terms of the $\lambda_p$ and $\zeta$ under $\theta = 45^\circ$ wind direction using (a) linear, (b) quadratic, and (c) cubic polynomials. . . . .	153

# List of Symbols

## Latin

$B$	Building width
$C$	Scalar concentration
$C^*$	Non-dimensionlized scalar concentration
$C_\mu$	Constant in the $k - \varepsilon$ model
$C_o$	Observed concentration
$C_p$	Predicted concentration
$c_p$	Specific heat capacity at constant pressure
$C_s$	Source concentration
$C_{\varepsilon 1}$	Constant in the $k - \varepsilon$ model
$C_{\varepsilon 2}$	Constant in the $k - \varepsilon$ model
$D$	Molecular diffusivity
$D_t$	Eddy diffusivity
$E_i$	Elementary effect of model coefficients
$F_m$	Pollutant transport rate due to mean flow
$F_t$	Pollutant transport rate due to turbulent flow
$g$	Gravitational acceleration
$H_{ref}$	Reference height
$k$	Turbulence kinetic energy (TKE)
$k_s^+$	Dimensionless sand grain roughness
$k_s$	Sand grain roughness
$M_i$	Measured value
$O_{fi}$	Objective function ith

$P_k$	TKE production rate
$P_i$	Predicted value
$q_s$	Scalar volumetric flowrate
$R_o$	Rossby number
$Re_t$	Turbulence Reynolds number
$S$	Strain rate invariant
$S_b$	Building row disposition in the urban array
$S_{ij}$	Strain rate tensor
$Sc$	Schmidt number
$Sc_t$	Turbulence Schmidt Number
$T$	Air temperature
$u'_i$	Component of fluctuating velocity
$u_i$	Component of wind velocity
$U_P$	Velocity at the center of the first cell next to the wall
$u_\tau$	Friction velocity
$U_{ref}$	Reference velocity
$V^*$	Velocity ratio
$W$	Spacing between buildings in urban array
$x_i$	component of space coordinate
$z_0$	Aerodynamic roughness

### **Greek**

$\delta_{ij}$	Kronecker delta
$\kappa$	Von Karman constant
$\lambda_p$	Urban planar density
$\mu$	Dynamic molecular viscosity
$\mu_t$	Dynamic eddy viscosity
$\nu$	Kinematic molecular viscosity
$\nu_t$	Kinematic eddy viscosity
$\Omega$	Vorticity rate invariant

$\omega$	Specific dissipation rate
$\rho$	Density
$\sigma_\varepsilon$	Constants in the $k - \varepsilon$ model
$\sigma_{Ei}$	Standard deviation of the elementary effect
$\sigma_k$	Constants in the $k - \varepsilon$ model
$\tau$	Pollutant retention time
$\theta$	Inflow wind incident
$\Theta_l$	Adiabatic lapse rate
$\varepsilon$	Turbulence dissipation rate
$\zeta$	Planar heterogeneity level

# Abbreviations

**ABL** Atmospheric boundary layer.

**ADMS** Atmospheric dispersion modeling system.

**AIJ** Architectural institute of Japan.

**AR** Building aspect ratio.

**CERC** Cambridge environmental research consultant.

**CFD** Computational fluid dynamics.

**FAC2** Fraction of the predictions within a factor of 2 of the observations.

**FB** Fractional bias.

**GA** Genetic algorithm.

**GCI** Grid convergence index.

**HR** Hit-Rate.

**LES** Large eddy simulations.

**MG** Mean geometric bias.

**MUST** Mock urban setting tests.

**NMSE** Normalized mean square error.

**PDF** Probability density function.

**RANS** Reynolds-averaged Navier–Stokes.

**RNG** Renormalization group.

**RTS** Roof-top structures.

**SST** Shear stress transport.

**VG** Geometric variance.

# Chapter 1

## Introduction

The adverse consequences of rapid urbanization in response to worldwide population growth, particularly in developing countries, have clarified the importance of the field of environmental health. The negative implications of expanding our urban area footprint, combined with continuing industrialization, manifest in various challenges regarding water quality, waste management, noise pollution, food security, mental health, climate change, and of course, air quality. As documented by the World Health Organization (WHO), deterioration of air quality is directly linked to severe health issues, by causing respiratory and cardiovascular diseases [1]. Recent statistical data indicate that one out of every six premature deaths across the world in 2019 was potentially associated with ambient air pollution [2]. These alarming statistics highlight the need for immediate and appropriate actions to address this critical issue.

The effective management of urban air quality is quite challenging and necessitates devising pollution mitigation strategies that can only be achieved by thoroughly understanding dispersion dynamics in a wide range of situations. In urban settings, the unique behavior of pollutant streams is governed by factors such as dense building clusters with varying configurations, building heights, urban density, and meteorological conditions [3]. These variables collectively contribute to complex airflow behavior, making it difficult to predict pollutant movement and concentration [4]. Moreover, the diverse types of pollutant sources (e.g., industrial emissions, vehicular exhausts, con-

struction dust, commercial and residential ventilation, etc.), each with their specific characteristics, can result in distinct dispersion patterns [5–7]. One particular type of urban pollution source often less emphasized in the literature than traffic-related pollutants is roof-based sources. While these sources may not receive as much attention, they can potentially have an important impact on the health of urban occupants. That is because the turbulence generated by available buildings and other obstacles can increase the chance of these pollutants being reintroduced into the ventilation system via fresh air intakes, due to the localized re-circulation zones, compromising indoor and outdoor air quality [8].

A range of methods and techniques have been developed over the years to address these challenges and better understand the dispersion dynamics mentioned above [9, 10]. Among these methods, including full-scale experiments, reduced-scale physical modeling, semi-empirical correlations, as well as numerical methods, each with its known limitations and challenges, Computational Fluid Dynamics (CFD) stands out for its flexibility in terms of applicability, convenience, and cost [11]. The potential of CFD for providing guidance in enhancing urban air quality lies in its capability of modeling a wide range of fluid flows and in producing detailed representations of the complex interactions between air flows and urban structures [12]. Using CFD models, researchers and urban planners can explore pollutant behavior in urban settings, and manipulate urban design effectively to promote sustainable configurations and enhance pollutant dispersion. Being aligned with the ultimate objective of this study, this is crucial for developing strategies for air quality management, which is not only a matter of environmental concern but also a public health imperative.

The application of CFD in urban environments has its own set of challenges. Urban landscapes are characterized by complex geometries, varying surface roughness, and a range of atmospheric conditions, all of which need to be accurately represented in the models. Due to the necessity of simplifying assumptions, the reliability of the results becomes highly dependent on modeling choices, and therefore, their validity must

be verified [13]. Dispersion data sets generated by tracer gas experiments have been shown to serve this purpose [14–16]. Nevertheless, it is not feasible to obtain high-quality data for every geometry with its unique features, due to logistic difficulties. A comprehensive review study by Toparlar et al. claimed that a high portion of CFD investigations in urban micro-climate studies lack validating evidence [17]. Such a scarcity has encouraged the research community of the field to progressively advance the atmospheric dispersion modeling framework [18–20]. Despite the previous efforts, achieving a fully comprehensive framework remains an ongoing pursuit [21].

To address these challenges, this research focuses on modifying CFD methodologies and developing more accurate predictive models for urban pollutant dispersion, particularly emphasizing emissions from rooftop sources. This part of the study targets an available shortcoming within the current body of the literature that is characterized as a gap in methodological advancements. By refining these models to more effectively capture the realistic scenarios of urban environments, the research aims to further bridge the gap between theoretical modeling and the broader narrative of practical urban development and environmental sustainability. An exhaustive review of the previous attempts has identified gaps in the area of formulating urban planning guidelines for future developments. In this regard, this work tries to address a recognized knowledge gap in understanding the interplay of some of the most influencing morphological indices on the bulk quantities representing urban ventilation and pollutant diffusion paths. Such insights can significantly help designers in passively promoting urban air quality.

## **1.1 Thesis Objectives**

Despite the endeavors made by previous researchers, precise prediction of the pollutant concentration field and dispersion in high-density urban settings has shown to remain quite challenging. Recognizing the gap in the literature and considering the primary purpose of this research to contribute to the development of sustainable

urban planning practices, the following objectives have been set:

- **Assemble a well-tested framework for reliable and efficient numerical modeling of the pollutant dispersion in compact urban regions.**

Considering the randomized, chaotic, and intermittent characteristics of the turbulent dispersion flow within the Atmospheric Boundary Layer (ABL), there is a wide range of influencing parameters and simplifying assumptions that severely impact the outcomes of the CFD models. The RANS method was used in this study to treat the governing equations, along with assuming the Boussinesq hypothesis to model the resulting shear fluxes. Steady-state modeling of the fundamentally transient flow features and fluctuating turbulent fluxes definitely results in imperfect solutions, which could be because of RANS's inability to reproduce the largest eddies in a turbulent flow. In this regard, performing a systematic validation study to guarantee acceptable model accuracy and estimating the uncertainty levels is of great importance. To achieve this goal, full-scale experiments in complex geometries with available high-quality and comprehensive data sets, such as the Mock Urban Setting Tests (MUST) experiment, were numerically modeled to analyze the chosen methods of simplification for flow and pollutant transport modeling. This was done to propose a framework for reliable and efficient modeling of the dispersion flow in complex urban geometries where the field measurements were not available for validation. Several of the most influencing turbulence modeling parameters and scenarios were carefully investigated. The necessary modifications and recommendations were proposed to accurately model the scalar dispersion or concentration field. The effectiveness and uncertainties of the proposed modeling settings were further evaluated through both quantitative and qualitative comparisons with high-quality experimental data.

- **Optimize Turbulence Closure Models for Enhanced Urban Atmo-**

**spheric Dispersion Prediction.** For this objective, the emphasis was on refining atmospheric dispersion modeling in urban clusters by enhancing the performance of turbulence closure models. Leveraging the framework established earlier, the goal was to re-calibrate the model’s empirical coefficients, focusing on both the turbulence and scalar dispersion. This was achieved through a strategic optimization process, employing a modified genetic algorithm, and utilizing the high-quality data set from the MUST experiment. The re-calibration aimed to improve the model’s fidelity in representing pollutant concentration and turbulence kinetic energy (TKE) within urban settings. By attaining greater accuracy and reliability in the CFD model, this objective directly contributed to addressing urban environmental challenges, particularly in air quality management. The refined model provided pivotal insights for urban planning and public health, offering enhanced tools for assessing and mitigating air pollution in densely populated urban areas. This endeavor not only advanced the field of environmental modeling but also supported the development of sustainable and health-conscious urban environments.

- **Define and conduct parametric studies to identify and study the unique effects of urban morphologies on scalar dispersion and street ventilation efficiency in heterogeneous geometries.** While implementing the proposed guidelines of the previous step for modeling the dispersion flow, idealized but systematically irregular arrays were created to investigate the physics of the scalar transport emitted from roof-based sources in the presence of urban heterogeneities. This approach was an intermediary between the studies in actual geometries with case-specific outcomes and studies in idealized and regular arrangements with missing impacts of the non-uniformities available in urban areas. For this objective, we parametrically studied the combined effects of the pollutant source location, array orientation, planar density, and

planar heterogeneity on the urban ventilation capacity and, consequently, on the pollutant concentration fields in the proximity of the building exterior faces, where the fresh air intakes are typically positioned. This study contributed to sustainable urban and building planning practices by further informing designers on how the interplay of urban morphological parameters could impact the dispersion dynamics and the resulting bulk concentration levels.

## 1.2 Thesis Outline

Chapter 2 of this thesis provides essential background information to facilitate a better understanding of the subsequent main chapters. It encompasses discussions on pollutant dispersion within the atmospheric boundary layer, investigation methods, turbulence modeling fundamentals, CFD modeling, and a survey of relevant literature on the topic.

This thesis document was structured using the "paper-based thesis" [22], with Chapters 3, 4 and 5 nearly exact copies of three successive peer-reviewed publications (the first two in print and Chapter 5 under review at the time of completion of this document). The versions in this thesis have had minor graphical editing and I have removed the three separate abstracts, preferring a single overall abstract for the entire thesis included above. These next three chapters show the step-wise logical progress of my research as I worked toward meeting my final goals following these three important steps.

In Chapter 3, I conducted a comprehensive validation study, including a thorough statistical assessment, to establish the most effective framework for atmospheric dispersion modeling in the context of building clusters. In Chapter 4, I explored the avenues for improving the accuracy and reliability of numerical predictions by modifying turbulence modeling, specifically addressing the dispersion of rooftop-emitted pollutants within compact urban arrays. My Chapter 5 addressed the final objective of conducting an in-depth investigation of the synergistic effects of urban morpholo-

gies on dispersion pattern dynamics. The findings have implications for informed urban planning practices, particularly concerning rooftop emissions and the placement of fresh air intakes. Finally, Chapter 6 concludes the thesis by summarizing key findings and discussing their significance for urban planning, air quality management, and the promotion of sustainable urban environments.

# Chapter 2

## Background

Dispersion, in general, refers to the spread or distribution of a substance, such as pollutants, throughout an environment. Depending on the specific characteristics of the background environment, dispersion can manifest itself in various forms. Of particular interest in this study is atmospheric dispersion, a phenomenon in which pollutants spread more rapidly and cover wider areas than in other environments, such as liquids, solids, or porous media [23]. In urban environments, the emission of pollutants is common due to factors like high population density, heavy vehicular traffic, and industrial activities, resulting in the dispersion of these pollutants [24]. This complex process is influenced by a multitude of factors, including meteorological conditions, terrain, and pollution sources. Understanding and effectively managing atmospheric dispersion in urban areas is crucial for mitigating the health and environmental impacts of air pollution and improving the overall quality of life for urban residents. This essential task can not be achieved unless one acquires the necessary basic understanding of the underlying principles and science behind it. Therefore, this section will offer a concise overview of the basics and key fundamentals, providing readers with the necessary background information on the topic, while a more detailed review of the relevant literature, directly tied to the specific objectives of this study, will be presented at the beginning of the upcoming chapters.

## 2.1 Atmospheric boundary layer

The phrase Atmospheric Boundary Layer (ABL) typically refers to the lowermost layer of the troposphere, which is directly affected by the earth's surface through vertical fluxes of momentum, heat, and moisture (i.e., mass) [25]. The profound significance of investigating and researching this layer arises from the fact that all human daily activities, down to breathing, take place within its confines. Variation in surface fluxes due to differing surface characteristics, along with the influence of geostrophic wind aloft, results in diurnal fluctuations in the thickness of the ABL [26]. The typical thermal mixing that happens during the day due to solar radiation extends the depth of ABL. Conversely, the surface cooling that happens during the night triggers the downward flux of heat that reduces the layer thickness considerably [27].

Similar to any boundary layer, the ABL is further subdivided into three main sublayers. The lowest layer within the ABL is generally referred to as the roughness sublayer with a thickness in the order of the aerodynamic roughness height,  $z_0$ . Given the overall height of the ABL, neglecting the roughness sublayer in certain applications is often justifiable. Alternatively, its impact on the layers above can be effectively accounted for through the use of wall-functions [28]. Moving upwards, the next layer is called the surface layer, constituting approximately 10% of the ABL. This sublayer is entirely turbulent, characterized by strong vertical gradients in wind speed, temperature, and humidity. Coriolis forces are typically negligible here, with the vertical wind velocity profile primarily determined by a balance between pressure and friction forces. Considering the typical horizontal length scales in atmospheric studies, it is reasonable to regard this layer as shallow. Consequently, the substantial fluxes of physical quantities experience minimal vertical variation and are generally assumed to remain constant. Such an assumption facilitates the conceptualization of an ideal surface layer [29]. The outermost sublayer of the ABL is the Ekman layer, where the Coriolis force becomes significant and notably affects both wind direction

and speed. Beyond the Ekman layer lies the free atmosphere, where surface effects on wind gradually diminish, and a balance between pressure and Coriolis forces derives the geostrophic winds [30].

Given the broad spectrum of situations within the ABL, it is necessary to place additional emphasis on specifying the study’s underlying physics. This emphasis aids in refining governing equations and selecting appropriate methodologies prior to initiating a study. As a result, the subsequent sections will offer an overview of various classifications in atmospheric dispersion flow studies, with a particular focus on scale and atmospheric stability states.

### **2.1.1 Scales of the atmospheric dispersion studies**

Considering the objectives outlined in this work, which center around the investigation of flow and pollutant dispersion dynamics, the layer of focus will be the surface layer. The dispersion phenomena within the surface exhibit a multi-scale nature, highlighting the great importance of appropriately defining the spatial scale of study. According to Oke’s classification, atmospheric flow can generally be divided into four main meteorological categories based on horizontal length scales: micro-scale (up to an order of  $10^3$  m), local scale ( $10^2$  to  $10^4$  m), meso-scale ( $10^4$  to  $10^5$  m), and macro-scale ( $10^5$  to  $10^8$  m) [31]. The meteorological scales beyond the macro-scale are typically classified as global-scale with dispersion time-scales that could take up to years [32].

The study of urban pollutant dispersion over and around clusters of buildings falls within the micro-scale category. This necessitates explicit modeling of geometry, including all available structures, as they exert a significant influence on local flow characteristics [33]. Micro-scale dispersion studies can be further divided into various categories [34]. These include building-scale studies, which focus on the investigation of isolated buildings [35–37], street-scale studies that encompass the spaces between two or more buildings [38–40], neighborhood-scale studies conducted over a cluster of

buildings [41–43], and city-scale studies that consider groups of urban settings, often treated as urban blocks with bulk morphological characteristics [15, 44].

Considering the variations in turbulent diffusion of pollutants relative to their distance from the source, an alternative classification has been introduced. This categorization divides dispersion studies into three main groups based on the interaction between pollutant plumes and atmospheric flow influenced by nearby obstacles [45]. The first is near-field dispersion, where the plume retains a width smaller than the length scale of available structures [46]. In this scenario, the plume is highly influenced by localized flow structures, resulting in significant spatial variations. As the plume progresses downstream, it enters an intermediate scale of dispersion, reaching a width comparable to the size of buildings. While turbulence induced by buildings and flow modifications still contribute to plume growth, the overall dispersion pattern experiences milder changes compared to the near-field scenario. At a considerable distance from the source, the size of the plume width surpasses that of the buildings. Consequently, it follows a Gaussian distribution, with all available geometric structures treated as surface roughness [47]. Given that the source locations in this thesis are embedded within the cluster of buildings, the investigations are therefore classified as near-field dispersion studies at the neighborhood scale.

### **2.1.2 Atmospheric stability classification**

Atmospheric stability refers to a particular state of equilibrium that defines the capacity of the atmosphere to either enhance or resist vertical mixing. Understanding different states of atmospheric stability is pivotal due to its undeniable influence on weather conditions, air quality, and the dispersion of pollutants. To this aim, the definition of the adiabatic lapse rate,  $\Theta_l$ , is typically employed to assess the stability state of the atmosphere [48].  $\Theta_l$  is defined as the rate at which the temperature of an air parcel decreases adiabatically, solely due to cooling and expansion resulting from

its rise within the atmosphere:

$$\Theta_l = -\frac{dT}{dz} = \frac{g}{c_p} = 9.76^\circ\text{C/km} \quad (2.1)$$

where  $T$  is the air parcel temperature,  $g$  is the gravitational acceleration, and  $c_p$  is the specific heat capacity at constant pressure.

In general, three main categories of atmospheric stability can be identified. A stable atmosphere is formed when the environmental lapse rate falls below  $\Theta_l$ . In such circumstances, if an air parcel is vertically lifted, it becomes surrounded by a warmer ambient air, causing it to have a higher density. As a result, the air parcel shows the tendency to return to its initial position, indicating a suppression of vertical mixing. Conversely, when the environmental lapse rate surpasses the  $\Theta_l$ , it gives rise to an unstable atmosphere. In such circumstances, an air parcel displaced upward encounters an ambient with a lower temperature than itself, causing it to continue ascending in the direction of its initial displacement. This results in enhanced vertical mixing and momentum transfer. Lastly, a neutral atmosphere is present when the environmental lapse rate equals  $\Theta_l$ . In this scenario, a displaced air parcel encounters surrounding air with the same temperature, leading to neither enhanced nor suppressed vertical mixing [26].

While  $\Theta_l$  provides valuable information for assessing atmospheric stability, it lacks accounting for turbulence induced by wind shear over the earth's surface. To this aim, the Monin-Obukhov similarity theory offers a measure that relates the stability state to the available momentum and heat fluxes. The Obukhov length,  $L_O$  has shown to be a practical scale in determining the level of atmospheric stability as it reflects the height where the turbulence flow generated by buoyancy effects is comparable to the one caused by wind shear [49]. Equation 2.2 provides the Monin-Obukhov length ( $L_O$ ), where  $u_\tau$  represents the friction velocity,  $\kappa = 0.4$  denotes the Von Karman constant, and  $Q_H/\rho_0 c_p$  stands for the kinematic heat flux [50]. Here,  $\rho_0$  and  $T_0$  are defined as the reference density and temperature, respectively. Using this definition,

$L_O \rightarrow \infty$  corresponds to a neutral surface layer, while  $L_O < 0$  and  $L_O > 0$  indicate an unstable and stable atmosphere, respectively. To focus solely on the impact of urban layouts on turbulence and dispersion patterns, without accounting for the influence of stability effects on vertical fluxes, a neutral atmosphere is assumed in this thesis.

$$L_O = \frac{-u_\tau^3 T_0 \rho_0 c_p}{\kappa g Q_H} \quad (2.2)$$

## 2.2 Modeling methods in ABL studies

The selection of an appropriate modeling approach holds significant importance in the scope of ABL studies. Each method provides the opportunity to simulate a realistic physical process set by a series of necessary assumptions and limitations. The accuracy level and uncertainty inherent in these models are key factors that influence their suitability for a given problem. Due to these facts, the decision is far from straightforward, often complicated by the challenge of assessing model uncertainty. Additionally, factors like cost, resource limitations, time constraints, and data availability further complicate the process. In this section, an overview of various methodologies will be presented, accompanied by a discussion of their advantages and limitations.

### 2.2.1 Full-scale field experiment

Conducting full-scale field tests, such as tracer gas experiments, can provide invaluable data sets that serve as essential resources for developing and validating dispersion models. These tests capture real-world atmospheric conditions, encompassing factors like urban wind flow, buoyancy forces, atmospheric stratification, and the dynamic effects of surrounding structures on plume dispersion [34]. However, the inherently uncontrolled meteorological conditions make it nearly impossible to independently study influencing parameters and to collect data that can be used to define a general guideline to predict the dispersion patterns within a particular geometry. Further-

more, in a full-scale experiment, measurements can be taken at only a limited number of accessible points and locations [51].

The typical approach in these experiments is to continuously release a tracer gas with negligible background concentration in the atmosphere and collect samples at multiple locations of interest to effectively show the dispersion pattern in the flow field. For the tracer gas to be considered a passive scalar throughout the experiment and to avoid possible environmentally destructive effects, it is necessary to limit the emission rate. On the other hand, limiting the emission rates results in considerably low tracer concentrations detected at sampling points, which demands high accuracy and specialty gas analyzers. The concentration data must also be supplemented with comprehensive meteorological measurements, including but not limited to wind speeds and directions at multiple locations and temperatures at different heights. Tests should be repeated on several occasions to cover an acceptable range of meteorological conditions. Measurements at high frequency and for adequately long periods are also essential during each trial so quasi-steady periods can be extracted from the data set for steady-state purposes [49]. Consequently, conducting tracer gas experiments in densely populated urban areas presents significant challenges, demanding substantial financial resources and logistical considerations. The aforementioned challenges have resulted in a noticeable scarcity of full-scale dispersion measurements, with only a limited number of reliable data sets currently available [52–55].

### **2.2.2 Reduced-scale laboratory experiment**

Wind tunnel and water channel experiments provide effective means to investigate plume dispersion in complex geometries, while supplying dependable data sets to develop and validate dispersion models [56]. These experiments are founded on the theoretical assumption that the flow and dispersion patterns around scaled-down obstacles exhibit dynamic similarity with those encountered in full-scale tests. In contrast to full-scale field experiments, wind tunnel, and water channel measurements can

be conducted within a controlled setting, ensuring consistent test conditions (inflow wind velocity, direction, temperature, background concentration, etc.) throughout the experiments [57]. This controlled environment facilitates the examination of how specific parameters affect dispersion patterns. Nevertheless, despite these advantages, there are certain drawbacks to this approach, including the absence of realistic atmospheric effects, the associated high costs, and intricate scaling and similarity issues [10]. The number of conducted reduced-scale experiments within the current body of literature is considerably higher than that of the full-scale tests [58–60].

### 2.2.3 Semi-empirical models

The limitations associated with both full-scale and reduced-scale tests have motivated many researchers to develop and adapt various parametric dispersion models over the years. These models incorporate mathematical functions that integrate analytical solutions with experimental observations, providing a straightforward approach that finds widespread application in urban planning exercises [9]. Notably, these widely adopted dispersion models are mainly defined based on the Gaussian distribution of plumes. The Gaussian distribution represents an analytical solution to the scalar transport equation, derived under highly optimistic assumptions about meteorological conditions and simplified geometric topographies. Some of these assumptions include steady distribution, neglecting wind shear, assuming a flow field with parallel and linear streamlines, and presuming that all meteorological factors and turbulence characteristics remain uniform throughout the domain [13, 61, 62]. These necessary simplifications, however, adversely affect the model’s accuracy and applicability.

Equation 2.3 shows an example of the Gaussian plume distribution equation derived for a scenario involving an elevated source. The spatial concentration distribution is denoted by  $C$ , while  $q$  represents the emission rate, and  $H$  corresponds to the physical height of the source. Additionally,  $U$  represents the freestream wind velocity at height  $H$ , and  $\sigma_y$  and  $\sigma_z$  stand for the standard deviations of the concentration

spread in the cross-wind ( $y$ ) and vertical ( $z$ ) directions, respectively. In theory, both  $\sigma_y$  and  $\sigma_z$  are considered functions of turbulence diffusion. Nevertheless, their actual values are determined via empirical equations that take into account the atmospheric stability state and the distance from the source, denoted as  $x$ . Further empirical modification to the definitions of  $\sigma_y$  and  $\sigma_z$  could expand this model’s applicability for case-specific scenarios [6]. As Equation 2.3 suggests, an undefined value of  $\infty$  is computed when the wind velocity equals zero, suggesting a limitation in the reliability of model predictions under extremely calm wind conditions.

$$C(x, y, z) = \frac{q}{\pi U \sigma_y \sigma_z} \exp\left(-\frac{y^2}{2\sigma_y^2}\right) \left[ \exp\left(-\frac{(z-H)^2}{2\sigma_z^2}\right) + \exp\left(-\frac{(z+H)^2}{2\sigma_z^2}\right) \right] \quad (2.3)$$

Wilson introduced a semi-empirical model aimed at estimating dilution levels along the plume centerline downstream of the source. However, this model significantly underpredicted the observed concentrations, with discrepancies observed in approximately 98% of the measurements [63]. Notably, the underprediction was more severe at greater distances from the source, being approximately 10,000 times lower far from the source compared to 200 times lower in near-field regions. In an attempt to account for additional dilution caused by stack height, ASHRAE proposed a minimum dilution model based on the Gaussian plume distribution. This model assumed a virtual source point upwind of the stack by adding the stack height to the distance between the source and intake [62]. However, experimental results indicated that this model was overly conservative, with observed concentrations ranging from approximately 40 to 450 times higher than the predictions. Moreover, these models failed to consider the impact of rooftop structures (RTS) and the resulting downstream recirculation zones [64]. The Atmospheric Dispersion Modeling System (ADMS), developed by Cambridge Environmental Research Consultants (CERC) [65], is another widely recognized computer model rooted in the Gaussian plume model. ADMS has undergone extensive validation in the literature and is among the few models that relatively closely align with wind tunnel and full-scale experimental data [9, 66]. Nevertheless,

while available dilution models like ADMS generally perform well in cases involving isolated buildings, they often provide inaccurate estimates in the vicinity of the source and in complex terrains where turbulent fluctuations and three-dimensional strain fields significantly influence pollutant dispersion. The uncertainty surrounding these dispersion models has led urban planners and building designers to adopt overly conservative approaches, resulting in substantial energy losses [67].

#### **2.2.4 Numerical models**

The need for a more accurate and comprehensive estimate of the plume behavior around complex urban geometries has made numerical modeling an appealing solution. Computational Fluid Dynamics (CFD) is defined as the computer-based simulation and analysis of systems that involve fluid flow, heat transfer, and any other related phenomena [68]. CFD stands out for its ability to deal with complex environmental scenarios, primarily due to its use of fine-scale and adaptable grids. This capability distinguishes CFD from larger-scale models that use simpler grids, making CFD particularly effective for detailed studies of pollutant dispersion and airflow in urban areas at a micro-scale level [69]. CFD offers numerous compelling advantages, making it a more favorable alternative method to be used in sustainable building designs [70]. These benefits include a marked reduction in lead times and costs for designing new scenarios, precise estimation of concentration and flow characteristics at each grid point within the computational domain, enhanced flexibility in modeling complex systems that are difficult or impossible to replicate with physical modeling, capability to analyze scenarios involving hazardous conditions safely, and the facilitation of rigorous and comprehensive parametric studies in atmospheric dispersion research.

Conversely, CFD comes with several inherent limitations and disadvantages. It relies on idealizations of reality, incorporating geometric simplifications and assumptions regarding flow and boundary conditions that can affect the accuracy of its

simulations. CFD solutions are approximations, typically obtained through iterative processes that may accumulate errors at each time step. Turbulence, a crucial aspect of fluid dynamics, poses a particularly challenging problem for accurate modeling in CFD and is often addressed with a significant degree of approximation. Although CFD offers detailed insights, its limitations become evident when considering factors like computational intensity and the expertise required for result interpretation. This underscores its disadvantages when compared to more direct experimental methods and simpler semi-empirical models [12]. Considering these inherent complexities and uncertainties associated with CFD, it becomes evident that the validation and verification of modeling choices and numerical results are crucial. It is essential to compare all CFD models with high-quality experimental measurements to ascertain their validity.

## **2.3 CFD in urban dispersion modeling**

Upon conducting a thorough comparison of various methodologies, CFD has been for its unparalleled flexibility in modeling complex urban dispersion flows. This flexibility is particularly valuable for performing studies to explore the intricate effects of heterogeneous urban configurations on dispersion dynamics and local ventilation capacities. However, it's important to address the inherent uncertainties in these methods to ensure the reliability of the results. This is specifically crucial for novel cases where high-quality data sets matching the physical geometry are not available. In this section, the focus will be on the most influential modeling settings and decisions in the context of atmospheric dispersion within complex urban settings. This overview aims to identify areas for improvement in the current state of urban dispersion modeling and its implications for urban planning. A more specific and detailed review of the previous literature directly related to the thesis objectives will be presented at the beginning of the respective chapters.

### 2.3.1 Turbulence modeling resolution

The turbulent nature of the ABL and its three-dimensional interactions with available structures (e.g., buildings) have made reliable modeling of the urban dispersion flows a challenge. The presence of turbulence in fluid flow leads to the formation of eddies characterized by various length and time scales, creating a dynamically intricate phenomenon. The smaller eddies are universal and typically governed by the inherent properties of the fluid dynamics, while larger ones are typically influenced by the physical structure available in the geometry [71]. Numerous pioneering efforts in the field of fluid dynamics have revolved around the development of numerical methods aimed at accurately capturing and resolving these eddies. Direct Numerical Simulation (DNS) is a highly detailed approach employed in solving the governing equations for fluid flow without any approximation or modeling. To accomplish this, DNS requires an exceptionally fine spatial grid to capture even the smallest eddies and a correspondingly small time step to capture the fastest fluctuations in the flow [72]. Due to its prohibitively high computational demands, DNS is primarily used for fundamental research and small-scale problems, making it impractical for use in urban flow simulations.

Two widely used methods for simulating turbulence in fluid flow are Large Eddy Simulation (LES) and Reynolds-Averaged Navier-Stokes (RANS). LES offers an intermediate approach to turbulence calculations by resolving the larger eddies in the field and filtering the unsteady Navier-Stokes equations to eliminate smaller eddies (usually smaller than the size of the computational mesh) [73]. RANS, however, focuses on the mean flow quantities in the turbulent field by solving the time-averaged equations to exclude the fluctuation effects while accounting for turbulent transport with modeled turbulence viscosity [74]. Consequently, RANS directly resolves the mean flow and uses closures to model turbulence across all scales. The debate among researchers regarding the relative merits of RANS versus LES dates back many years

and continues to be a topic of discussion [75–78]. Although LES tends to yield more accurate results compared to RANS by accounting for the effects of large eddies, it comes with substantially higher computational requirements and poses greater post-processing challenges. This is the main rationale for observing a gradually increasing focus on implementing this method in the research within the recent decade. However, such a transition has not been noted yet in the design and consultancy discipline [79]. The fundamental challenge in engineering is still to identify methods that yield adequately accurate results at minimal cost [80].

On the topic of near-field atmospheric dispersion modeling, RANS has remained quite popular among researchers with respect to urban geometries of great sizes and high planar densities. On the other hand, LES is also shown to be the most suitable choice for modeling the sudden accidental or deliberate release of hazardous airborne scalars in geometry where instantaneous local concentrations are of great importance [81]. In this research, the dispersion of the pollutant scalar in the complex urban geometry is investigated which is being continuously released from the source points. Therefore, considering the large size of the computational domain and the interest in the mean quantities of flow characteristics, the RANS method has been chosen to solve the governing equations.

### **2.3.2 Modeling considerations**

The accuracy and reliability of the results obtained from a CFD code heavily depend not only on the underlying physical and chemical models but also on the expertise of the user within the respective field. Several critical considerations come into play when performing ABL CFD modeling. To establish a well-defined urban flow CFD model, one must make well-informed decisions on the required level of geometric detail, the size of the computational domain, how much to refine the grid, which turbulence model to use, whether to use a logarithmic or power law profile for the wind in the atmospheric surface layer, what near-wall treatment methods to use, which dis-

cretization schemes to pick, and what criteria to use for convergence. [82]. Examples of sensitivity investigations can be found in the literature that have addressed the uncertainties associated with influencing factors such as computational domain size [83], grid resolution [84, 85], boundary conditions [86, 87], near-wall treatment [88, 89], and horizontal homogeneity [90, 91].

The importance of establishing well-defined procedures for quality modeling has initiated several efforts for developing "Best-Practice" guidelines that date back decades [18, 92–94]. However, in the context of complex urban environments, the intricate interplay of turbulence parameters and available structures further complicates the task. Despite the effort of previous researchers to perfect the CFD modeling of dispersion flows around a cluster of buildings, the science is still inexact, highlighting the necessity of continuous development [95, 96].

Focusing on the complexities of CFD modeling in urban settings, a key aspect that demands further attention is the selection of a suitable turbulence closure model. The balanced compromise between accuracy and computational complexity offered by RANS, as discussed in Section 2.3.1, has made this method quite popular in numerical urban studies. As a result of implementing this approach, additional terms, known as Reynolds stress components are introduced in momentum equations. The influence of turbulence on the mean flow is represented by these stresses, and further modeling and supplementary equations are required to resolve them [68]. A wide range of turbulence closure models, commonly known as eddy viscosity models, have been developed to effectively recapture the pivotal turbulence-induced features (e.g., recirculation zones, vortices, etc.) within the flow. Among all, a few of the most widely used first-order closures in urban flow simulation are the standard  $k - \varepsilon$  [97], renormalization group (RNG)  $k - \varepsilon$  [98], realizable  $k - \varepsilon$  [99], standard  $k - \omega$  [100], shear stress transport (SST)  $k - \omega$  [101], and Spalart-Allmaras [102].

Due to the empirical nature of the turbulence models, as they are derived through extensive flow measurements in the context of classical generic flows (e.g., free shear

flow, fully developed turbulent channel flow, etc.), none can be considered universal [103]. Therefore, a turbulence closure that proves effective in one scenario may exhibit poor performance in another [79]. Several studies regarding ABL flows can be cited that assessed the closure models' performance in specific scenarios such as mean and turbulent flow over a rural flat surface [104], hilly terrain [105, 106], generic case of an isolated cube [107], high-rise isolated building [108], two uniform low-rise buildings [109], or dispersion flow between two buildings of different heights [38], behind a single-block building [40, 110], within an isolated street canyon [78], and around an isolated high-rise building with elevated pollutant source [111]. The variations in results obtained from different turbulence models for each distinct geometry emphasize the importance of conducting such sensitivity studies tailored to the specific case of interest.

Considering that these empirically developed closure models are not inherently defined for ABL flows, they can be further modified to more accurately capture the characteristics of ABL dynamics [112]. Achieving this involves obtaining high-quality measurements specific to the intended generic case, which allows for the definition of an appropriate training case. Furthermore, an objective function must be carefully formulated, incorporating the desired parameters of focus. However, the process of re-calibrating turbulence closure models is computationally demanding, mainly due to the numerous coefficients requiring simultaneous adjustment. Therefore, an optimization framework is also required to reduce the computational cost as much as possible, while preserving the quality of the results. Several efforts have been made over the years to fine-tune turbulence models to some extent in the context of ABL. For example, certain studies have focused on the adjustment of a single empirical coefficient, particularly in scenarios involving flow over flat or irregular terrain [113, 114]. Others have specifically addressed flow characteristics over a cross-shaped building [115]. In addition, certain investigations have employed data-driven methodologies, such as Bayesian approaches [116], whereas others have conducted linear sensitivity analy-

ses by systematically varying individual coefficients [117]. Notably, there are also instances where researchers have trained the turbulence model using the generic geometry of an isolated building [20, 118].

To the best of the author’s knowledge, none of the previous studies have specifically addressed a generic case of a building cluster. They all focused primarily on flow-related parameters when defining their objective functions, and none of them utilized full-scale data sets that incorporated realistic atmospheric conditions. Therefore, there is a clear gap for an optimized turbulence closure model that is carefully calibrated for a generic building cluster scenario. This model should also incorporate both turbulence-related and dispersion-related parameters in its formulation, which is currently lacking.

### **2.3.3 Dispersion around buildings**

Understanding how pollutants are advected and diffused, influenced by the interactions between ABL flow and the available structures in urban settings is of great importance for urban health and safety. Accurately predicting dispersion patterns in the presence of buildings is crucial for sustainable urban planning and environmental management practices. Given the gravity of the topic, an overwhelming amount of research has been done, employing all forms of modeling as described in Section 2.2, to continuously advance the knowledge in this field. Historically, research in this area has primarily focused on more simplified, generic cases to build foundational understanding. Examples include studies on an isolated cube [35–37, 107, 119, 120], an isolated high-rise building [108, 121, 122], or an isolated street canyon [39, 76, 78].

Urban flows exhibit intricate flow features, examples being large wake regions, three-dimensional strain rates, and strong pressure gradients [10]. For such reasons, the problem of air quality becomes even more critical when it should be addressed in a bigger picture, for example, in a region with a high building density. A pioneering work by Oke [123] suggested that depending on the spacing between buildings

in an array, three different flow regimes could occur. When buildings are sparsely arranged, an isolated roughness flow occurs with minimal to no wake interactions. As the arrangement becomes more packed, a wake interference flow takes place, in which the available spacing still allows for the entertainment of flow from above the canopy. However, the spacing is not that wide, and the wake behind the upstream building interferes with the recirculation zone in front of the downstream building. As buildings become adequately packed, the flow treats the canopy as a rough surface and does not penetrate it. This condition, known as skimming flow, results in a steady recirculation zone with relatively low-velocity regions. With the exception of the isolated roughness regime, the wind and dispersion flow in urban areas exhibit fundamentally different patterns compared to those around isolated buildings [124]. Therefore, while the insights of the initial studies are valuable, they lack the generality required for compact urban planning practices.

Additionally, it is crucial to highlight that semi-empirical models fall far short of even remotely providing very conservative estimates for dispersion patterns in cases of near-field emissions within building clusters. This limitation arises because the near-field plume within an array experiences significant distortion and expansion due to the presence of individual buildings, resulting in a distribution that deviates significantly from the expected Gaussian shape [125]. The enhanced turbulence levels resulting from interactions between multiple buildings are highly dependent on the geometric arrangements of the buildings [126]. Semi-empirical models, by some case-specific modifications to their spread parameter ( $\sigma_y$  and  $\sigma_z$ ), can only provide rough estimates of pollutant distribution in the far-field by superimposing the flow around individual buildings in very sparse configurations, or, treating the entire array as a single block in highly dense packed clusters [69]. Given all these details, CFD is strongly recommended as the only practical tool for urban planners to investigate the complex dispersion patterns within urban settings through well-defined parametric studies.

A clear shift is evident in the literature toward applied cases within urban settings. However, it is important to note that this area is relatively young and not as extensively explored as the well-studied generic case of an isolated building [3]. Strategically modifying urban forms can greatly enhance the built environment’s ability to disperse outdoor air pollution [15]. A pioneering study on building arrays specified the most influential bulk geometric characteristics of building clusters that have a significant effect on near-field dispersion patterns. These include planar density, the standard deviation of building heights, the mean pattern of the layout, and the mean shape of the buildings [127].

A detailed review of the recent literature suggests that while some studies have examined the impact of urban morphologies on wind flow and pollutant dispersion in idealized, regularly aligned building arrays, providing key insights, there is still a notable gap in understanding the effects of more complex, heterogeneous urban forms. These studies often show a positive correlation between array permeability and pedestrian-level air quality [110, 128, 129], but they also highlight that air quality is significantly influenced by the array’s specific layout and geometric characteristics [44, 130]. The complexity of investigations increases for actual urban environments, where non-uniform building arrays create more intricate flow and turbulence structures [131]. Recent studies have started to explore the generic non-uniform arrays and unique urban terrains, but there is a scarcity of studies focusing on pollutant transport in such settings [132]. This lack of comprehensive research on this topic, especially regarding the interplay of non-uniformities and planar densities in urban clusters, underscores the need for more in-depth and novel studies. This need is especially notable in scenarios involving elevated pollutant sources and non-perpendicular wind directions, which deviate from the typical airflow patterns [111, 133–135]. These studies are crucial for understanding how geometric variations in urban arrangements can affect pollutant dispersion, emphasizing the urgent need for further investigation in this area.

## Chapter 3

# Performance evaluation of the RANS models in predicting the pollutant concentration field within a compact urban setting: Effects of the source location and turbulence Schmidt number

### 3.1 Introduction

Statistical studies show a significant soar in the urban population in recent years, with a prediction that around 70% of the earth's population to be living in urban regions by the next few decades [136]. This sudden surge in urbanization has come with detrimental impacts on urban air quality caused by airborne pollutants emitted from various sources. In this regard, acquiring a thorough understanding of how these pollutants are dispersed in the presence of structural obstacles with varying shapes and dimensions is essential to effectively maintain air quality at acceptable levels. For this purpose, urban planners have used analytical and semi-empirical dispersion models to assess the pollutant distribution field [62, 63]. However, using these dispersion models, which were mostly developed based on very idealized generalizations of the meteorological conditions and simplified geometrical topographies, leads to extremely conservative and less energy-efficient guidelines in the design [9, 66, 67, 137].

Computational Fluid Dynamics (CFD) can be introduced as a reliable alternative method to predict the dispersion pattern in complex turbulent flow fields [3]. It is generally less costly than experiments, provides flow estimates at every point in the computational domain, and can predict the concentration field more accurately than the analytical and semi-empirical models [138]. However, the highly complex nature of the turbulent flow in the Atmospheric Boundary Layer (ABL) demands simplifications and assumptions in every step of modeling. Special considerations are required to implement a suitable numerical algorithm and carefully define grid resolution, boundary conditions, wall functions, and other modeling settings [139–141]. Additionally, CFD models must be validated by comparison with high-quality experimental measurements to assess the severity of the introduced errors and uncertainties [142]. Tracer gas experiments can produce valuable data to validate the open-field dispersion CFD models [16, 52, 143]. Nevertheless, there are high costs and challenges associated with conducting such tracer experiments in urban regions, which make it impractical to acquire a reliable data set in every geometry with each unique domain topography and diverse structural arrangement [10, 14, 144]. In this regard, introducing a well-tested and improved infrastructure is considerably beneficial in setting the guidelines for a reliable and efficient practice in numerical prediction of pollutant dispersion in analogous cases.

Attempts have been made in recent years to perfect the numerical modeling of atmospheric dispersion flows in simplified geometries (e.g., isolated buildings, the street canyon between two buildings, flat terrain, etc.) [5, 121, 122, 145, 146]. However, many studies have pointed out the unique and considerable impacts of the neighboring buildings and urban morphologies on the wind and dispersion fields and emphasized the importance of these types of investigations [14, 147, 148]. Despite the endeavors made by previous researchers, precise prediction of the pollutant concentration field and dispersion in high-density urban settings remains very challenging. This is due to the behavior of the turbulent flows with large-scale recirculation struc-

tures and three-dimensional strain fields that challenge turbulence models. In this regard, contributing to the “Best-Practice” in simulating the ABL dispersion flow within compact urban settings is set as the primary goal of this research paper.

One of the most critical decisions that need to be made by the modeler is selecting a suitable physical model to recreate the flow field in the regions of interest. Considering the well-established balance of the Reynolds-Averaged Navier-Stokes (RANS) model between the computational cost and the prediction accuracy, this approach has been extensively suggested for atmospheric dispersion, where the mean quantities of the flow characteristics are studied [76, 78]. A wide variety of turbulence models are proposed in the literature to estimate the turbulence viscosity resulting from the Boussinesq hypothesis and to close the RANS equations [68]. Properly selecting the closure model can immensely impact the quality and efficiency of the predictions. Therefore, it is considered an essential step in contributing to the “Best-Practice” in CFD modeling of the near-field pollutant dispersion.

Narjisse et al. evaluated the capability of the standard  $k - \varepsilon$  and Shear Stress Transport (SST)  $k - \omega$ , in accurately resolving the wind flow in the presence of a hilly terrain [105]. They concluded that even though standard  $k - \varepsilon$  overpredicted the wind velocity near the wall, it was still a more reasonable choice for modeling the flow for these geometries than SST  $k - \omega$  which offered slightly better predictions at a much higher computational cost. Tominaga et al. also tested the performance of several RANS closures in modeling the atmospheric wind flow with results of the unsteady simulations and showed that RNG  $k - \varepsilon$  provided a comparatively accurate representation of the flow around the building [108]. However, the results were only validated for a case of an isolated high-rise building, and a general conclusion could not be drawn for more complicated situations of complex urban geometries. Hosseinzadeh et al. performed a series of validation studies on CFD models of wind flow between two buildings and examined standard  $k - \varepsilon$ , realizable  $k - \varepsilon$ , standard  $k - \omega$ , SST  $k - \omega$  closure models [109]. They found that  $k - \varepsilon$  based models predicted more accurate

results for this configuration compared with of  $k - \omega$  based models, with standard  $k - \varepsilon$  performing slightly better overall.

The selection of a proper closure model to represent the wind and turbulence fields becomes even more crucial in cases of accurately modeling the pollutant dispersion flows. Lateb et al. carried out a comparison study by simulating the dispersion flow between two buildings of different heights using three types of  $k - \varepsilon$  turbulence models to find the proper selection for the geometry configuration of his study [38]. They observed that the realizable model produced more accurate results in cases with lower stacks' momentum ratios and heights, while RNG performed better for other cases. An et al. numerically modeled the dispersion of a pollutant emitting from a ground-level source around a single-block building to build a validation case. The SST  $k - \omega$  was used, and a comparison with wind tunnel data demonstrated the satisfactory performance of this closure model [110]. However, a systematic comparison with other closure models was missing to indicate whether SST  $k - \omega$  was the best possible choice for this case or not. Keshavarzian et al. studied the effects of the pollutant source location (different heights on the building sidewall) on the dispersion pattern by numerically simulating flow around an isolated high-rise building [111]. They only validated the standard  $k - \varepsilon$  closure model in this paper, and therefore, it is not clear how the location of the source might affect the performance of the closure models and the overall prediction of the concentration field.

Several other studies also evaluated the performance of various turbulence models in modeling the atmospheric dispersion flow in different geometries [41, 149–151]. The fact that each turbulence model provides relatively different predictions in each geometry justifies carrying out this sensitivity study as an essential step of this research to understand each model's limitations and further contribute to the “Best-Practice” in urban dispersion modeling. Additionally, the type of pollutant source location (ground-level sources upstream or downstream of an obstacle, sources in urban canopies, rooftop sources, etc.) is another factor that might impact the accuracy

of the results generated by each turbulence model [79]. In this regard, to address the gap in the literature, three of the most commonly used models in computational wind engineering ([88]), including standard  $k - \varepsilon$ , RNG  $k - \varepsilon$ , and SST  $k - \omega$ , have been chosen to be comparatively analyzed in the context of the compact urban-like geometries. Four different case studies from the detailed and thorough Mock Urban Setting Tests (MUST) dispersion data set have been selected that provide four distinct types of source locations.

The turbulence Schmidt number ( $Sc_t$ ) is another influencing parameter in atmospheric dispersion modeling that needs to be tested and modified for benchmarking the “Best-Practice”. Despite the proven profound effects of  $Sc_t$ , there is no clear definition of this parameter, and most previous studies used a constant value in the broad range of 0.2-1.3, depending on the specific flow properties and geometry of the problem [152]. The common approach for determining the optimum  $Sc_t$  suggests conducting a series of validation studies beforehand to test different values [66, 153, 154]. In this paper, in addition to the conventional method of finding the optimum and constant value of  $Sc_t$ , the method of using a variable  $Sc_t$  will also be tested in the context of dispersion modeling in complex urban geometries.

## 3.2 Fundamentals and governing equations

The pattern in which an emitted pollutant plume will be dispersed in the atmosphere is dependent on the wind regime and turbulence. Wind flow in a compact urban setting is disturbed by the presence of structural features such as buildings of various heights and shapes and by natural landscapes, which form a wind profile that is quite distinct from the ones in the open rural area. As this work aims to model the dispersion of the emitting plume from sources within an urban setting, a quick overview of the governing equations and methodology is beneficial to justify the applicable assumptions.

The mass, momentum, and energy conservation laws can be applied in the form of

Navier-Stokes equations to govern the dynamics of ABL flow. Assuming an isothermal fluid flow in a neutral atmosphere, the energy equation will not be used in the context of this study. The remaining governing equations are simplified by considering the applicable assumptions, such as steady-state, incompressible airflow, and constant isotropic viscosity. Since the region of interest in this study is limited to the inner sublayer of the ABL, the terrestrial Coriolis effects can also be neglected [28]. To further evaluate the validity of this assumption, the non-dimensionalized Rossby number ( $R_o$ ) was estimated.  $R_o$  is defined as the ratio of the inertial forces to the Coriolis forces and can be expressed as [155]:

$$R_o = \frac{U}{Lf} \quad (3.1)$$

where  $U$  is the characteristic horizontal velocity,  $L$  is the characteristic horizontal length scale, and  $f$  is the Coriolis frequency. Considering that the order of magnitudes of these parameters in this research are  $U \sim 1$ ,  $L \sim 10^2$ , and  $f \sim 10^{-5}$ , the resulting  $R_o$  is of the order of  $10^3$  which justifies the assumption of negligible Coriolis effects.

Large length scales caused by the available structures, as well as the typical wind speeds of interest in these types of studies, will result in the Reynolds number being the order of  $10^6 - 10^8$ . Therefore, the airflow and pollutant dispersion in the ABL will have an inherently turbulent nature. In this work, the dispersion of the pollutant scalar in the complex urban geometry is investigated which is continuously released from the source points. Therefore, considering the large size of the computational domain and the interest in the mean quantities of flow characteristics, the RANS method has been chosen to solve the governing equations. Using the Reynolds decomposition, the continuity and momentum equations can be presented in their time-averaged forms as follows:

$$\frac{\partial \bar{u}_i}{\partial x_i} = 0 \quad (3.2)$$

$$\bar{u}_j \frac{\partial \bar{u}_i}{\partial x_j} = -\frac{1}{\rho} \frac{\partial \bar{p}}{\partial x_i} + \nu \frac{\partial^2 \bar{u}_i}{\partial x_j^2} - \frac{\partial \overline{u'_i u'_j}}{\partial x_j} \quad (3.3)$$

where  $\bar{u}_i$  and  $u'_i$  are the time-averaged and the fluctuating fluid velocity in the three  $(i, j, k)$  Cartesian directions, and  $x_i$  denotes these directions,  $\rho$  is the density, and  $p$  is the pressure. On the right-hand side of Equation 3.3, the introduced turbulence term is the time-averaged Reynold stress tensor ( $\overline{u'_i u'_j}$ ) which contributes to the convective momentum transfer due to the turbulent eddies. With the use of the Boussinesq approximation, the Reynolds stress term in Equation 3.3 is modeled as:

$$-\rho \overline{u'_i u'_j} = 2\mu_t(S_{ij} - \frac{1}{3} \frac{\partial \bar{u}_k}{\partial x_k} \delta_{ij}) - \frac{2}{3} \rho k \delta_{ij} \quad (3.4)$$

here  $\mu_t$  is the turbulence viscosity,  $k = 0.5 \overline{u'_i u'_i}$  is the turbulence kinetic energy per unit mass,  $S_{ij} = \frac{1}{2} (\frac{\partial \bar{u}_i}{\partial x_j} + \frac{\partial \bar{u}_j}{\partial x_i})$  is the shear strain rate, and  $\delta_{ij}$  is the Kronecker delta. It should be noted that although the molecular viscosity,  $\mu$ , is a property of the fluid, the turbulence viscosity is considered to be a property of the flow [79]. Considering the number of unknowns in Equations 3.2-3.4 for solving the flow field, supplementary equations are required to close the problem, which are provided through the available closure models.

The Menter SST  $k - \omega$  has been considered as one of the possible choices in this research paper, following the success of implementing this model in similar research work [156]. SST  $k - \omega$  is introduced as a hybrid turbulence model by providing a transformation from the  $k - \varepsilon$  into a  $k - \omega$  model in the near-wall regions and using the standard  $k - \varepsilon$  model in the fully turbulent regions of the geometry far from the wall [101]. The Standard  $k - \varepsilon$  and RNG  $k - \varepsilon$  closure models have been selected along with the SST  $k - \omega$  for further evaluation of their performance in predicting the mean concentration field in a compact urban-like geometry. Detailed descriptions of the mentioned closure models can be found in the ANSYS CFX user guide [157].

The different turbulence models also require case-specific modifications in the meshing procedure since the appropriate wall treatment heavily depends on it. One of the advantages of the SST  $k - \omega$  model is that it directly resolves the viscous sublayer. Even though the accurate reproduction of the separation and recirculation zones can

be achieved using this model, extra refinement is necessary adjacent to the wall, which could considerably increase the computational expenses. The  $k - \varepsilon$  based models, on the other hand, utilize the wall functions to resolve flow near the surfaces, which by comparison, reduces the computational cost and the modeling complexities [88]. However, this could lead to a poor prediction of viscous effects near the walls, leading to the inaccurate prediction of the pollutant dispersion in cases where the source is located near the ground or on the roofs. In this regard, a careful investigation of the overall performance of the selected turbulence models is necessary to benchmark the recommended practice for modeling the dispersion of pollutants emitting from different types of source locations. In this paper, the widely used scalable wall function will be tested to resolve the flow adjacent to the wall when considering the  $k - \varepsilon$  based models [157].

Furthermore, the governing equations are supplemented with the Eulerian diffusion-advection equation. With the flow field and the turbulent characteristics solved, the mass fraction of the scalar (pollutant) needs to be decomposed into mean,  $\bar{c}$ , and the fluctuating,  $c'$ , components. The turbulent scalar fluxes,  $-\overline{c'u'_j}$ , can be estimated as  $D_t(\frac{\partial \bar{c}}{\partial x_j})$  assuming the standard gradient diffusion hypothesis (SGDH).  $D_t$  is the turbulence mass diffusivity and is defined as the ratio of eddy viscosity ( $\nu_t$ ) to the turbulence Schmidt number ( $Sc_t$ ). Numerous studies have demonstrated the profound influence of  $Sc_t$  on turbulence diffusion, which drastically affects the predicted concentration field by RANS equations. Employing the SGDH, the transport equation can be expressed as:

$$\bar{u}_j \frac{\partial \bar{c}}{\partial x_j} = (D + D_t) \frac{\partial^2 \bar{c}}{\partial x_i \partial x_j} + S' \quad (3.5)$$

where  $D$  is the molecular diffusion coefficient for the pollutant in the airflow field, and  $S'$  represents the scalar source term. The pollutant is assumed to be a passive scalar, meaning that due to its low mass fraction in the field and its non-reactive nature, its concentration does not affect the conservation of momentum or bulk continuity. Therefore, the scalar transport equation can be solved after the flow field is estimated.

To effectively make a comparison between the numerical and experimental results, the non-dimensionalized concentration parameter ( $C^*$ ) defined by Equation 3.6 is used hereafter, where  $C$  is the mean concentration in ppm at a given location in the domain,  $U_{ref}$  is the mean upstream wind velocity,  $H_{ref}$  is an arbitrary characteristic length, and  $q_s$  is the source’s volumetric flowrate. Using the  $C^*$ , the plume concentration field and its lateral and vertical spreads in various case studies can be compared quantitatively to draw appropriate conclusions at any wind speed and discharge flow rates.

$$C^* = \frac{10^{-6}U_{ref}CH_{ref}^2}{q_s} \quad (3.6)$$

### 3.3 Description of case studies

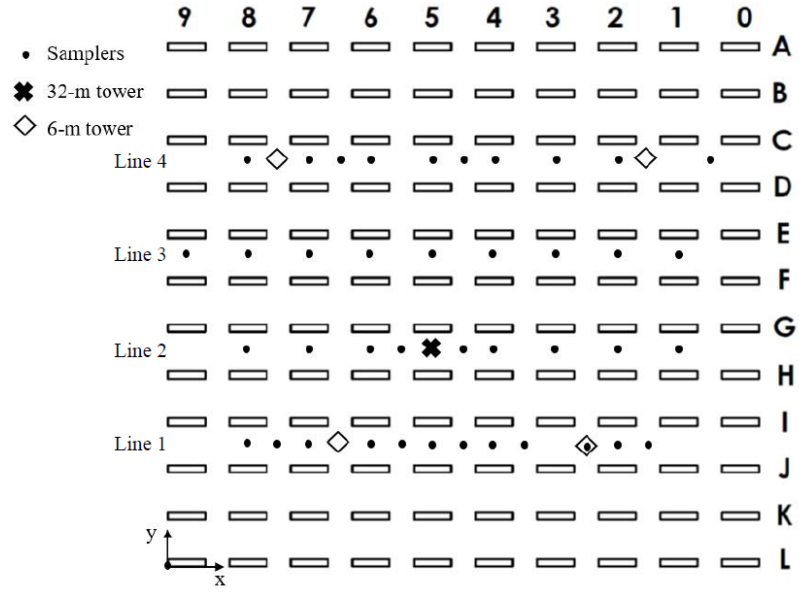
The comprehensive dispersion data set of the MUST experiments has been selected to evaluate the modeling method and test several modeling settings that have the most profound effects on the accuracy of the predictions. The MUST tracer study refers to a series of tests conducted in an urban-like setting with the primary purpose of providing a valuable resource that includes the meteorological and dispersion data, suitable for validating the accuracy of the dispersion models and CFD simulations [158–162]. In this experimental setup, a 10 by 12 array of shipping containers was placed outdoors in the center of the test domain over relatively flat ground. The containers were 12.2 m long, 2.4 m wide, and 2.5 m high, forming an approximately 200 m by 200 m square array (Figure 3.1a). Propylene was used as the tracer gas in this experiment, and six different release configurations (with assigned letters A to F) were considered to cover a wide variety of cases (Figure 3.1b). In total, 68 trials were performed: 63 with continuous releases and 5 with puff releases. The source locations varied from positions within or upwind of the test array (37 locations).

The horizontal concentration field was measured using 40 Digital Photoionization Detectors (dPID) located in four parallel lines downstream of the source at the height

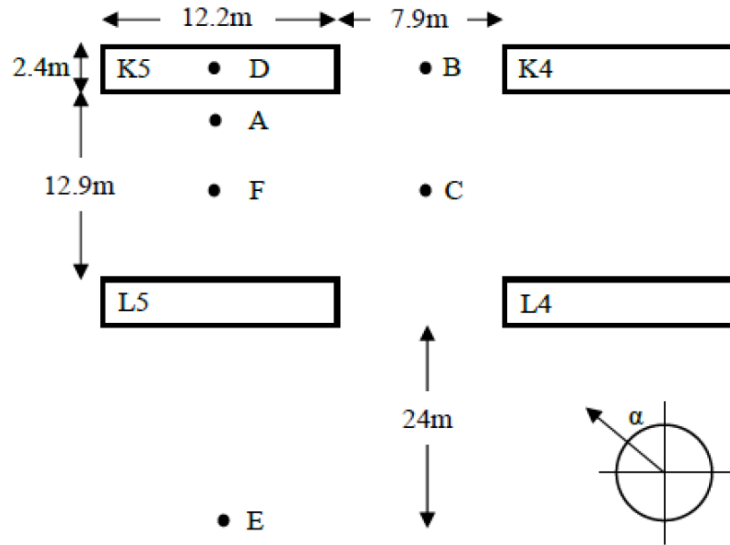
of 1.6 m. The horizontal sampling lines are named as Lines 1-4 (Figure 3.1a). The vertical concentration field was mapped using 8 dPIDs installed on the central tower at various heights, and 6 Ultra Violet Ion Collectors (UVIC) installed on each of the four 6m towers. Since the climatological analysis suggested that the test region frequently experiences wind flow coming from the two directions of Southeast and Northwest, two 16m masts were also installed, approximately 30 m Southeast and Northwest of the array, to capture flow characteristics upstream and downstream.

In an attempt to collect data in neutral and stable atmospheric conditions, 15-minute trials were done mainly in the early mornings or nights when surface cooling takes place in the absence of sun [55]. During these periods, the ground generally cools more quickly than its surrounding air due to radiation, resulting in a temperature gradient less negative than the adiabatic lapse rate that suppresses vertical mixing. However, in the presence of a strong wind, nocturnal stability can be diminished by turbulent mixing, which results in a temperature gradient closer to neutral conditions. The uncontrolled nature of the boundary conditions in field experiments results in the instantaneous variation of the measurements, making it quite challenging to use the generated data to validate quasi steady-state numerical models based on Reynolds averaging. In this regard, Yee ([49]) further processed the data set and extracted 200 seconds in each trial with the least recorded variation in the upstream flow that could be considered quasi-steady periods.

Considering the number of available test cases in the MUST data set, a careful assessment of all 68 trials was necessary to define the appropriate case studies. The selected cases should contain high-quality measurements, be consistent with the assumptions, and represent diverse scenarios to enrich the outcomes of this paper. In this regard, only trials with continuous tracer gas release were considered, and cases with puff releases were disregarded. The state of atmospheric stability during the remaining trials is another important factor that should be considered for selecting the target case studies. The Obukhov length ( $L_{MO}$ ) has been shown to be a practical



(a)



(b)

Figure 3.1: (a) Planar schematic view of MUST container array; (b) Schematic view of all six types of re-leasing locations.

scale in determining the level of atmospheric stability [122, 163]. Considering the assumption of the neutral atmospheric conditions in this work, the ideal choice was to use the measurements from the trials conducted in similar stability states. In this

regard, the number of possible case studies is further limited to tests with positive and large  $L_{MO}$  to account for neutral and near-stable conditions.

The height and the location type of the source point are considered to be the final criterion needed to select trials that assure diverse situations for comparatively assessing the turbulence closure models. For the purpose of this study, four distinct source location types were selected (Figure 3.1b):

- Type A: located 1m upstream of container J3 within the array ( $z/H = 0.72$ ).
- Type D: located on the rooftop of container J9 within the array ( $z/H = 1.04$ ).
- Type E: located 24m upstream of container L1 outside the array ( $z/H = 0.52$ ).
- Type F: located on the road, centered between containers K8 and L8 long sides ( $z/H = 0.72$ ).

The final four case studies are shown in Table 1 with all the necessary quantities (mean calculated values during the 200 seconds of quasi-steady period) required for accurately modeling the dispersion flow. The quantities presented in Table 1 are the tracer release rate ( $q_s$ ), the source location type, the source height ( $Z_s$ ), the upstream wind speed at 4 m height ( $S_{04}$ ), the upstream wind direction at 4 m height with a positive angle measured counter-clockwise from the  $y$ -axis ( $\alpha_{04}$ ). The Obukhov length ( $L_{MO}$ ) is also calculated at 4 m height on the central tower.

Table 3.1: Four selected trials of MUST field experiment.

<b>Trial No.</b>	<b>Trial I.D.</b>	$q_s$ ( $\frac{1}{\text{min}}$ )	<b>Source type</b>	$Z_s$ (m)	$S_{04}$ ( $\frac{\text{m}}{\text{s}}$ )	$\alpha_{04}$ (deg)	$L_{MO}$ (m)
1	2681829	225	F	1.8	7.93	-41	28000
2	2672213	200	A	1.8	2.68	30	150
3	2682320	225	D	2.6	4.55	-39	170
4	2692250	225	E	1.3	3.38	36	130

## 3.4 CFD model description

### 3.4.1 General settings

The ANSYS CFX software was used to model the passive scalar dispersion of the MUST experiments by discretizing the RANS equations described previously. Deciding on the size and shape of the computational domain was the first step toward setting up a reliable framework for modeling the dispersion flow. Rectangular computational domains were selected for our simulations, having the inlet and outlet planes perpendicular to the free stream. Following guidelines recommended by Franke et al. [18], the distance from the inlet, lateral, and top boundary to the building cluster should be at least  $5H$ , while a minimum distance of  $10H$  should be considered to the outlet ( $H$  represents the height of the tallest obstacle within the geometry). Having these criteria in mind and testing different arrangements, the size of the computational domain in this research was extended ( $14H$  from the inlet,  $10H$  from the lateral,  $12H$  from top boundaries, and  $20H$  from the outlet) to ensure that no backflow at the boundaries hampered the convergence of the iterative solver. Considering the size of the MUST array and the maximum height of the obstacles within ( $H=2.5$  m), a nested computational domain with an inner domain of  $200\text{ m}\times 200\text{ m}\times 10\text{ m}$  and an outer domain of  $285\text{ m}\times 250\text{ m}\times 32.5\text{ m}$  was defined.

Properly setting up the boundary conditions and applicable constraints significantly affects the accuracy of the predictions made by the CFD model [18]. Zero relative pressure was selected as the boundary condition at the outlet plane of the computational domain, top and side planes were set to symmetry, and all the solid surfaces in the geometry (building walls, roofs, and grounds) were defined as no-slip walls. To accurately model the dispersion process in a complex urban area, setting appropriate inflow wind and turbulence profiles is critical to account for the effects of the upstream terrain roughness (not included in the domain) and the available vertical wind gradient in the boundary layer. The two widely considered approaches for

defining the boundary conditions at the inlet are the power-law and the logarithmic profiles [164]. Depending on the availability of the information, either method could be the appropriate choice. The logarithmic profile provides acceptable estimates in cases with known upstream surface roughness, atmospheric stability conditions, and approaching velocity at a given height. On the other hand, the power-law profile could be the choice when upstream velocity at different heights is known, and an appropriate power can be estimated. Therefore, assuming constant vertical shear stress in the surface layer, the logarithmic inflow profiles derived by Richard and Hoaxy were used in this work [165]. In the case of using SST  $k - \omega$  closure model, it is also required to convert the profile of the dissipation rate,  $\varepsilon$ , to the specific dissipation rate,  $\omega$ , using Equation 3.10:

$$U(z) = \frac{u_\tau}{\kappa} \ln \left( \frac{z + z_0}{z_0} \right) \quad (3.7)$$

$$k(z) = \frac{u_\tau^2}{\sqrt{C_\mu}} \quad (3.8)$$

$$\varepsilon(z) = \frac{u_\tau^3}{\kappa(z + z_0)} \quad (3.9)$$

$$\omega(z) = \frac{\varepsilon}{C_\mu k} \quad (3.10)$$

where  $k$  is the turbulence kinetic energy,  $u_\tau$  is the friction velocity associated with the logarithmic wind speed profile,  $z$  is the vertical displacement, and  $z_0$  is the aerodynamic roughness length,  $\kappa$  is the von Karman constant  $\kappa = 0.4$  ([165]), and  $C_\mu$  is a model constant,  $C_\mu = 0.09$ . The reference wind speeds measured at the reference height of  $4m$  upstream of the MUST array were used along with the aerodynamic ground roughness of  $0.045m$  to estimate the inflow wind speed and turbulence profiles [49].

### 3.4.2 Grid sensitivity study

The parts in the computational domain with no structures were meshed using hexahedral elements, and unstructured tetrahedral elements were considered to mesh the inner domain. As explained before, the mesh refinement process near the solid surfaces strongly depends on the selected closure models. In this regard, extra grid refinement was considered near the wall for cases with the SST  $k - \omega$  model to keep the average  $y^+$  of less than 5 ( $y^+ = (\rho u_\tau y)/\mu$ ). To investigate the dependence of results on the grid size, three different grid resolutions were analyzed for two cases: one with SST  $k - \omega$  and the other with the  $\varepsilon$  based turbulence models. Following the recommended procedure by Celik [166], the uncertainties resulting from discretization are estimated for three grids in each case with different levels of refinement. Three main parameters of grid refinement factor ( $r$ ), average relative error ( $e_{avg}$ ), and Grid Convergence Index (GCI) were calculated to measure the grid refinement error.

The grid refinement factor is defined as the ratio of the representative cell size ( $h$ ) of two successive grids ( $r = h_{coarse}/h_{fine}$ ). Equation 3.11 can be used to calculate the representative cell size of a three-dimensional grid:

$$h = \left( \frac{1}{n} \sum_{j=1}^n \Delta V_j \right)^{\frac{1}{3}} \quad (3.11)$$

in which  $n$  represents the total number of cells, and  $\Delta V_j$  is the volume of the  $j$ th cell. Furthermore,  $e_{avg}$  in the predicted normalized concentration field (four trials with 72 sampling points each) was calculated as follows:

$$e_{avg} = \frac{1}{m} \sum_{j=1}^m \left| \frac{C_{j,coarse}^* - C_{j,fine}^*}{C_{j,fine}^*} \right| \quad (3.12)$$

where  $m$  is the total number of sampling points. Having the  $e_{avg}$  value from the last step, Equation 3.13 was used to calculate GCI for two successive grids.  $F_s$  is the safety factor and has a value of 1.25, as recommended for cases when at least three levels of grid refinement are studied [38, 167]. Considering the second-order discretization

scheme used in this work, an order of accuracy  $p = 2$  was taken.

$$\text{GCI} = \frac{F_s e_{avg}}{r^p - 1} \quad (3.13)$$

The calculated GCI and  $e_{avg}$  are presented in Table 3.2. The predicted concentration profiles at the first horizontal sampling line of Trial 1 are also presented in Figure 3.2 for qualitative comparison. The refinement factors,  $r$ , in both cases with SST  $k - \omega$  and  $k - \varepsilon$  based closure models are 1.20. As shown in Table 3.2, the lowest values of GCI and  $e_{avg}$  for both cases belong to the two finer grids. Furthermore, the presented results indicate a much stronger grid independency for cases with SST  $k - \omega$  models, with  $e_{avg}$  and GCI of 1.97% and 5.60%, respectively. These values show lower deviations between the predicted concentration field obtained by SST  $k - \omega$  model as the grid is refined. However, one should note that this slightly better grid independency comes at much greater computational costs. Finally, it can be shown in Figure 3.2 that there are minimal apparent deviations between the predicted concentration fields by the medium and fine grids, justifying the use of the medium grids throughout this research.

Table 3.2: Results of the grid independence analysis.

Model	# Nodes( $10^6$ )			Coarse-Medium		Medium-Fine	
	Coarse	Medium	Fine	$e_{avg}\%$	GCI%	$e_{avg}\%$	GCI%
SST $k - \omega$	7.65	11.59	17.50	14.00	39.77	1.97	5.60
$k - \varepsilon$ based	6.39	9.68	14.62	5.61	15.94	2.33	6.62

### 3.5 Statistical analysis method

The performance of the modeling methods and settings in accurately predicting the plume concentration field was evaluated using the statistical measures introduced by Chang et al. [168]. The performance measures calculated in this research are the fractional bias (FB), the mean geometric bias (MG), the normalized mean square errors (NMSE), the geometric variance (VG), and the fraction of numerical data

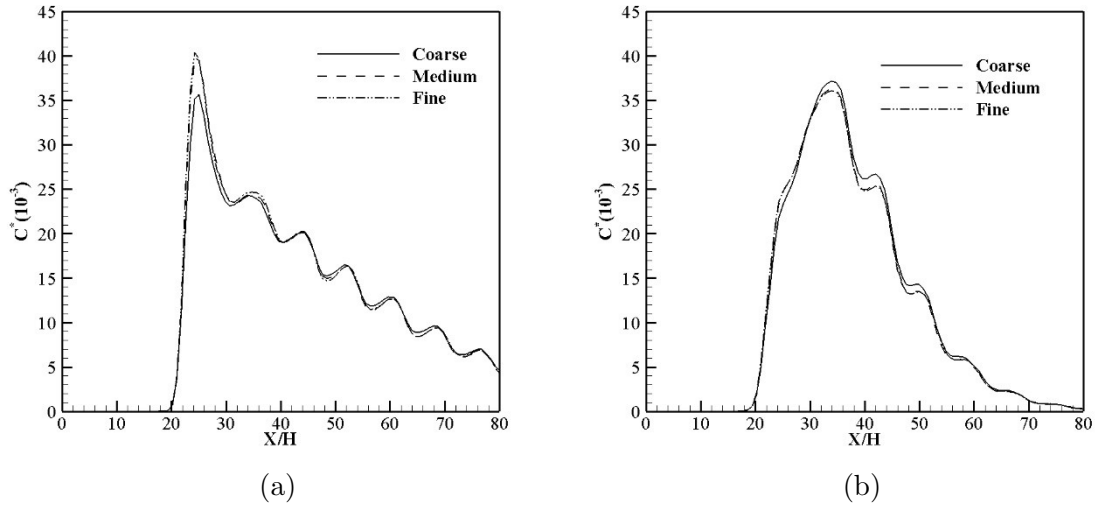


Figure 3.2: Comparison of concentration profiles at the first horizontal sampling line in Trial 1 for (a) cases with SST  $k - \omega$  and for (b) cases with  $k - \varepsilon$  based closure models.

that fall within a factor of two of the field measurements ( $0.5 < C_p/C_o < 2$ ). It should be noted that in cases of dispersion modeling where the concentration varies significantly from point to point, calculating all the mentioned statistical parameters is recommended to capture both the linear systematic bias (FB and NMSE) and the random scatter of the data changing on different orders of magnitude (MG and VG). These performance measures for dispersion modeling are defined as follows, where  $C_o$  is the observed concentration,  $C_p$  is the predicted concentration by the CFD model, and  $\overline{C}$  is the average value over the entire data set:

$$\text{FB} = \frac{(\overline{C_o} - \overline{C_p})}{0.5(\overline{C_o} + \overline{C_p})} \quad (3.14)$$

$$\text{MG} = \exp(\overline{\ln C_o} - \overline{\ln C_p}) \quad (3.15)$$

$$\text{NMSE} = \frac{\overline{(C_o - C_p)^2}}{\overline{C_o} \overline{C_p}} \quad (3.16)$$

$$\text{VG} = \exp[\overline{(\ln C_o - \ln C_p)^2}] \quad (3.17)$$

The ideally accurate CFD model would generate results that give FB and NMSE of 0, and MG, VG, and FAC2 of 1. However, Chang et al. [168], suggested acceptable ranges for these performance measures by investigating several dispersion data

sets that are  $-0.3 < FB < 0.3$ ,  $NMSE < 4$ ,  $VG < 1.6$ ,  $0.7 < MG < 1.3$ , and  $FAC2 > 0.5$ . However, extra considerations are required when calculating the logarithmic measures as they are sensitive to the small values and return undefined values for zero concentrations. Therefore, as suggested by Chang et al. [168], a lower threshold equal to the sampler’s detection precision (0.04 ppm) is defined for the averaged concentrations when MG and VG are calculated.

## 3.6 Results and discussion

### 3.6.1 Performance evaluation of closure models: Source location effects

The predicted turbulence field, especially the turbulence viscosity ( $\mu_t$ ), has an undeniable impact on the accuracy of the predicted concentration field [169]. In addition to the expected differences due to the various definitions of  $\mu_t$  offered by each closure model, the produced turbulence by the available row of containers upstream of the source point also affects the predictions [11]. Using the appropriate computational grids, the performance of the selected turbulence models in predicting the concentration field was evaluated and compared in four cases with different types of the source location. Figure 3.3 illustrates the predicted concentration fields in all four trials represented by all three selected models, demonstrating clear distinctions in the vicinity of the source. However, as the pollutant plume progresses downstream, the differences in the predicted concentration fields at the plume centerline seem to be gradually reduced. Furthermore, it is evident from Figure 3.3 that the modeled concentration field by SST  $k - \omega$  promotes greater lateral spread of the plume compared to other models, with standard  $k - \varepsilon$  showing the least.

Table 3.3 presents the calculated statistical measures for the point-to-point comparison in all the four selected trials. As it can be seen, the statistical measures (except for VG) show values within the acceptable ranges, indicating the validity and reliability of the CFD results despite the selected closure models. The VG represents

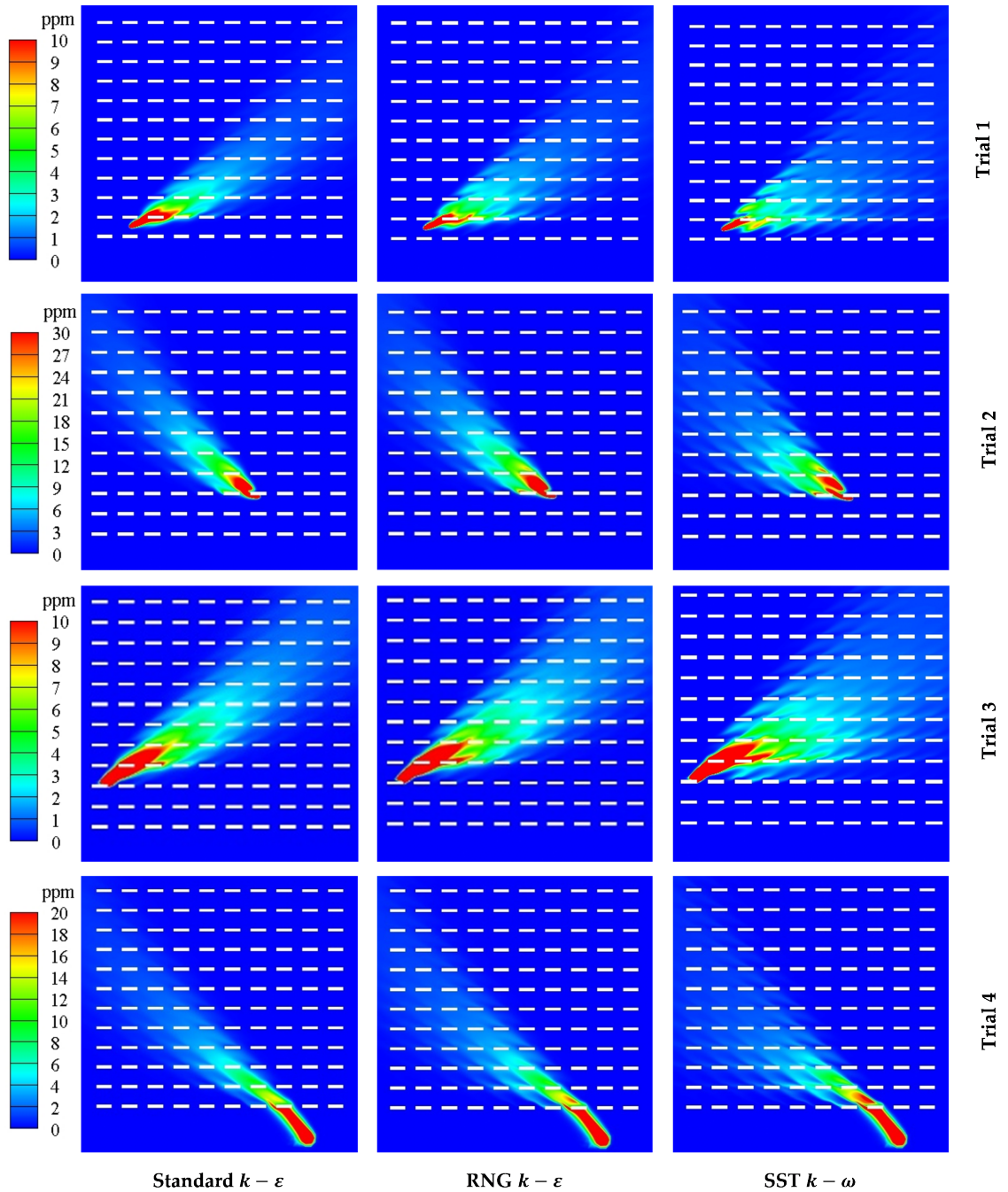


Figure 3.3: Contours of the predicted concentration field obtained by different closure models on a horizontal plane at  $z/H=0.64$  (The height at which all horizontal PIDs are installed).

the unsystematic scatter of the predictions and is calculated to be larger than the acceptable limit for all cases. That refers to a relatively larger scatter that is primarily

due to the available deviations at the edge of the plume, where the concentrations are relatively low, and even minor differences between observed and predicted values could lead to considerably large VG values.

The simulation results for Trial 1, where the scalar source is positioned midway between containers K8 and L8, show an overestimation of the concentration field in all cases (negative values of the FB). The net overprediction of the simulation results is further emphasized by the calculated MG values of less than 1, using all the three turbulence models. However, the overall superiority standard  $k - \varepsilon$  closure is evident, with 62% of predicted concentrations within the FAC2 of the observed values. Further analysis of the parameters presented in Table 3.3 also suggests a relatively higher quality of the simulation results produced by standard  $k - \varepsilon$ , showing less scatter (both linear, NMSE, and logarithmic, VG) compared with the field measurements.

Table 3.3: Statistical evaluation of the concentration predictions for the selected trials.

Case	Model	FB	NMSE	VG	MG	FAC2
Trial 1	Standard $k - \varepsilon$	-0.01	0.79	2.65	0.98	0.62
	RNG $k - \varepsilon$	-0.17	1.45	3.11	0.84	0.59
	SST $k - \omega$	-0.23	2.06	3.81	0.80	0.59
Trial 2	Standard $k - \varepsilon$	-0.11	1.04	2.35	1.24	0.70
	RNG $k - \varepsilon$	-0.25	2.21	3.76	1.13	0.65
	SST $k - \omega$	-0.20	2.23	5.65	1.06	0.64
Trial 3	Standard $k - \varepsilon$	-0.02	0.59	3.13	0.85	0.68
	RNG $k - \varepsilon$	-0.22	0.76	3.25	0.94	0.58
	SST $k - \omega$	-0.29	0.66	5.36	0.97	0.53
Trial 4	Standard $k - \varepsilon$	0.07	0.46	1.98	1.01	0.65
	RNG $k - \varepsilon$	0.00	0.62	2.54	0.86	0.65
	SST $k - \omega$	0.01	1.01	3.51	0.78	0.61

As suggested by previous studies, the inaccurate representation of the turbulence field by two-equation viscosity models can be one of the primary sources of discrepancies found between the predictions and measurements [38, 105, 108]. In this regard, making a comparison between the predicted wind and turbulence flow field by all the

studied closure models in this work is beneficial. Figure 3.4 maps the distribution of the turbulence kinetic energy (TKE) in the vicinity of the source location for Trial 1. Relatively higher TKE productions by standard  $k - \varepsilon$  are observed near the source location, with the least values obtained by SST  $k - \omega$  model. The higher TKE values produced by standard  $k - \varepsilon$  model further compliments the generated TKE by available containers in the geometry, which contradicts the well-established limitation of the RANS methods in underestimating the TKE fields [11]. Consequently, higher values of turbulence viscosity will be estimated by the standard  $k - \varepsilon$  model that promotes higher particle diffusivity (assuming a constant  $Sc_t$ ), which justifies the relatively milder overprediction of the concentration field.

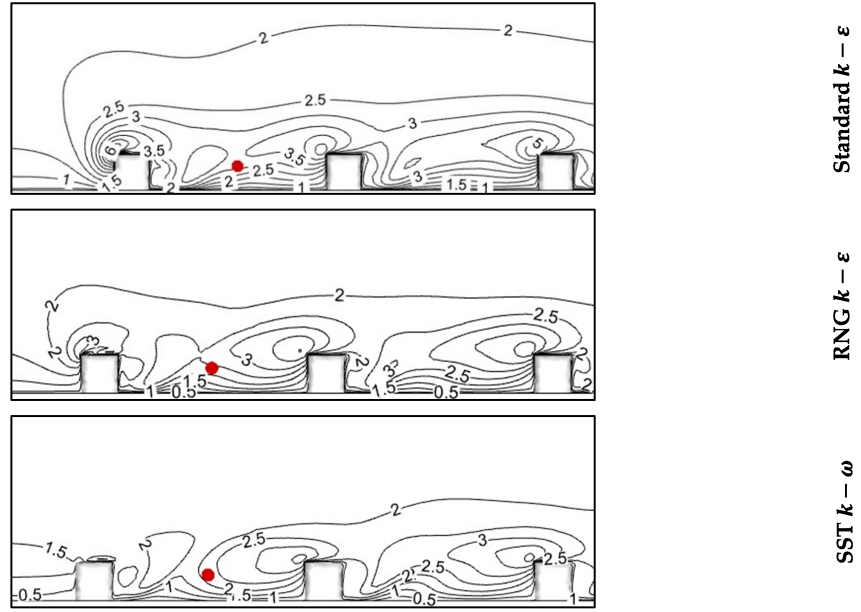


Figure 3.4: The turbulence kinetic energy, TKE ( $\text{m}^2 \text{s}^{-2}$ ), distribution in the vicinity of the source location (red circle) in Trial 1.

The estimated vertical profiles of the TKE and wind velocity obtained by the selected closure models at the central measuring tower are shown in Figure 3.5, along with the corresponding field measurements. As Figure 3.5a suggests, the standard  $k - \varepsilon$  offers a more accurate representation of the TKE vertical variation compared to the two other closure models, with SST  $k - \omega$  predictions showing the largest deviations

with the field data. Furthermore, the standard  $k - \varepsilon$  model slightly overpredicts the TKE at the lower region of the ABL (where the available structures heavily affect the flow field), while the opposite is true in cases with the RNG  $k - \varepsilon$  and SST  $k - \omega$  models. In addition, Figure 3.5b illustrates an overprediction of the velocity profile in all cases, with standard  $k - \varepsilon$  outperforming the other closures. It should also be noted that the predicted velocity profiles are not considerably affected by the selection of the turbulence model, with a maximum relative difference of less than 7.2%.

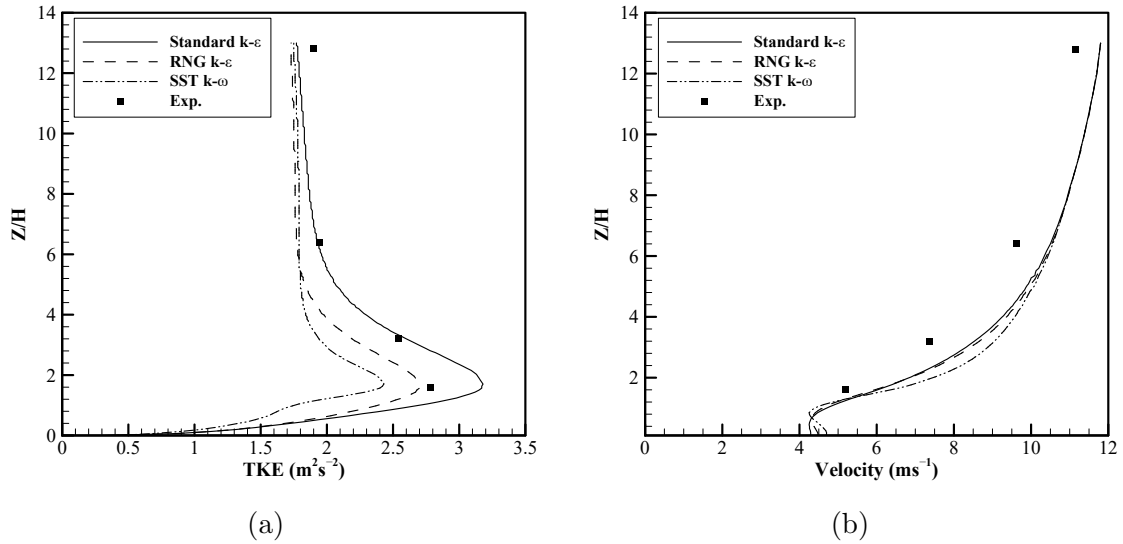


Figure 3.5: Comparison of vertical profiles of (a) TKE and (b) velocity at the 32m central tower with the field measurements of Trial 1.

The tracer gas in Trial 2 is released from a type A location, positioned immediately (1 m) upstream of the container J3. As shown in Table 3.3, 70% of the estimated concentrations using standard  $k - \varepsilon$  are within a FAC2 of the observations, while this number is 65% and 64% for RNG  $k - \varepsilon$  and SST  $k - \omega$ , respectively. Similar to Trial 1, negative values of the calculated linear fractional bias suggest that overpredicted concentration fields (near the plume centerline where the concentrations are high) were obtained by all the selected closure models. However, MG values larger than one indicate net underprediction in all cases, which is a consequence of underestimation of the concentrations near the edge of the plume. Considering the logarithmic nature of

the MG, even minor discrepancies between the numerical results and measurements at the plume edge contribute to the determination of the net over/underprediction. Nonetheless, considering all the calculated statistical measures, the superiority of the results produced by the standard  $k - \varepsilon$  model is evident.

The correct reproduction of the wind and turbulence field in the vicinity of the container J3 windward face is vital in capturing the initial spread of the scalar plume, which has a profound impact on the accuracy of the predicted concentration field. In this regard, the distributions of the TKE isolines in the vicinity of the scalar source are given in Figure 3.6. As it can be seen, larger values of TKE have been predicted using the standard  $k - \varepsilon$  model near the source that is more than  $0.3 \text{ m}^2\text{s}^{-2}$ , compared to less than  $0.3 \text{ m}^2\text{s}^{-2}$  and  $0.2 \text{ m}^2\text{s}^{-2}$  predicted by RNG  $k - \varepsilon$  and SST  $k - \omega$ , respectively. The larger values of TKE, regardless of their accuracy concerning the field data, promote a greater particle diffusivity that results in predicting lower concentrations downstream. This explains the larger values of FB and MG for predictions made using the standard  $k - \varepsilon$  (3.3).

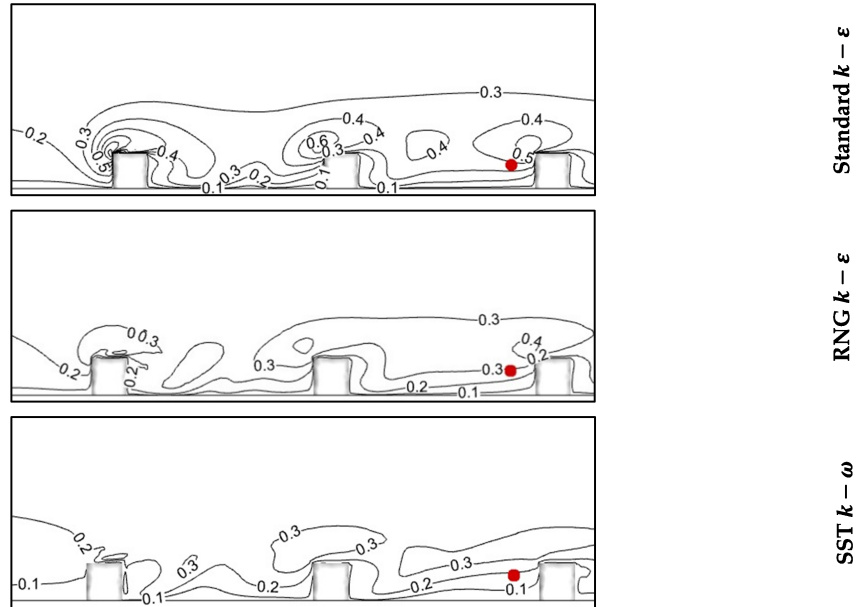


Figure 3.6: The turbulence kinetic energy, TKE ( $\text{m}^2 \text{ s}^{-2}$ ), distribution in the vicinity of the source location (red circle) in Trial 2.

The estimated vertical profiles of TKE and wind velocity at the central tower inside the array are presented in Figure 3.7. As expected, both the  $k - \varepsilon$  based models predicted larger values of TKE within the lower heights of the ABL, where the flow field is heavily affected by the presence of containers. However, by further progress in the  $z$  direction and moving away from the solid surfaces (ground and containers), the SST  $k - \omega$  gradually switches from the standard  $k - \omega$  to the standard  $k - \varepsilon$  closure. As a result, larger values of TKE are estimated by SST  $k - \omega$  compared to RNG  $k - \varepsilon$  from around an elevation of  $z/H = 5$  aloft. All the turbulence models underpredict the TKE at the central tower, with the standard  $k - \varepsilon$  showing a better agreement, which agrees with the presented statistical measures in Table 3.3. The estimated velocity profiles obtained by all three simulations of Trial 2 show minor differences with respect to each other and generally agree well with the field measurement at lower elevations. However, considerable deviations are observed from field data at the upper levels of the ABL, which could originate from the logarithmic profiles estimated at the inlet boundary [165]. Considering the height of the containers,  $z/H = 1$ , these recorded discrepancies with actual wind velocities at higher elevations do not impact the accuracy of the predicted concentration fields.

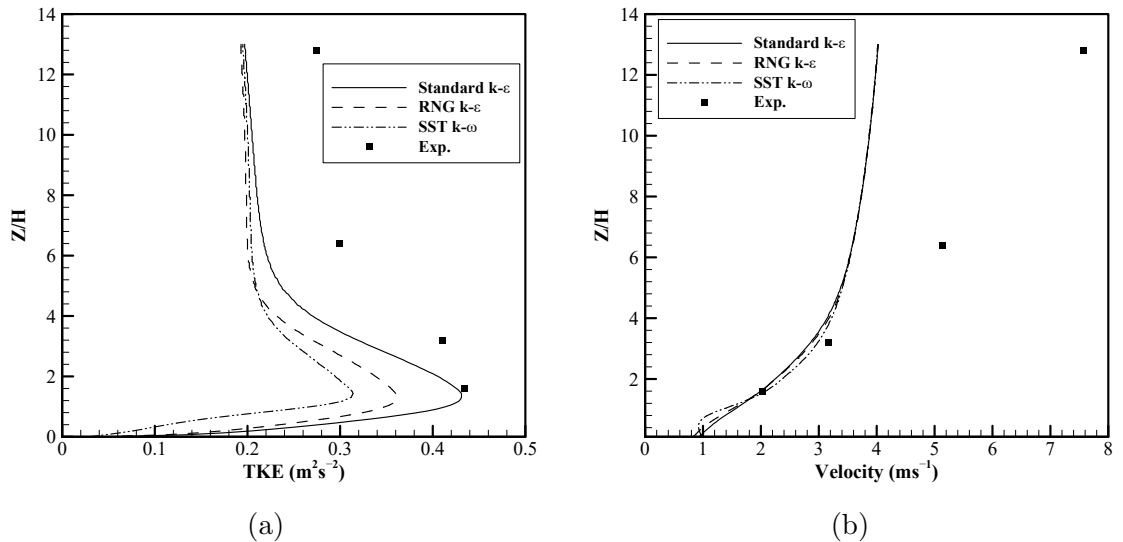


Figure 3.7: Comparison of vertical profiles of (a) TKE and (b) velocity at the 32m central tower with the field measurements of Trial 2.

Rooftop-based sources of air pollution (e.g., rooftop exhausts) are known as one of the main causes of air quality deterioration in compact urban regions. In this regard, Trial 3 has been purposely selected in this work for further evaluation of the modeling settings and methods. The scalar source in Trial 3 is of type D, positioned 10 cm above the container J9 roof. The standard  $k - \varepsilon$  model significantly outperforms the other selected models by predicting 68% of the concentration field within the FAC2 of the field measurements. On the contrary, the SST  $k - \omega$  barely passes the validation assessment by only estimating 53% of the concentration field within the FAC2 of the field data. An overall overprediction of the scalar concentration field is observed, with calculated MG values of less than one and negative FB in all cases. Regarding the quality of results, the presented statistical measures in Table 3.3 strongly suggest the superiority of the standard  $k - \varepsilon$  model, showing milder overall overpredictions (FB=-0.02) and relatively fewer scatter with the experiment (NMSE=0.59 and VG=3.13).

Figure 3.8 illustrates the estimated distributions of the TKE by all three turbulence models in the vicinity of the roof-based source. Consistent with previous studies [11, 119], an overprediction of the TKE by the standard  $k - \varepsilon$  is evident near the upwind corner of containers, leading to poor estimation of the separation flow. The TKE obtained by the standard  $k - \varepsilon$  near the source is approximately  $1.75 \text{ m}^2\text{s}^{-2}$ , compared to less than  $1.0 \text{ m}^2\text{s}^{-2}$  and  $0.75 \text{ m}^2\text{s}^{-2}$  predicted by RNG  $k - \varepsilon$  and SST  $k - \omega$ , respectively. However, as previously mentioned, this overprediction of TKE makes up for the general underprediction of TKE by the RANS method [36], resulting in a more accurate representation of the concentration field downstream.

The vertical profiles of wind velocity and TKE at the central tower within the MUST array are presented in Figure 3.9. As shown in Figure 3.9a, all three closure models overpredict the TKE up to an elevation of  $z/H = 2$ , with SST  $k - \omega$  performing relatively better. Furthermore, the deviation between numerical results and field measurements reduces with the elevation increase in ABL, where the effects of the

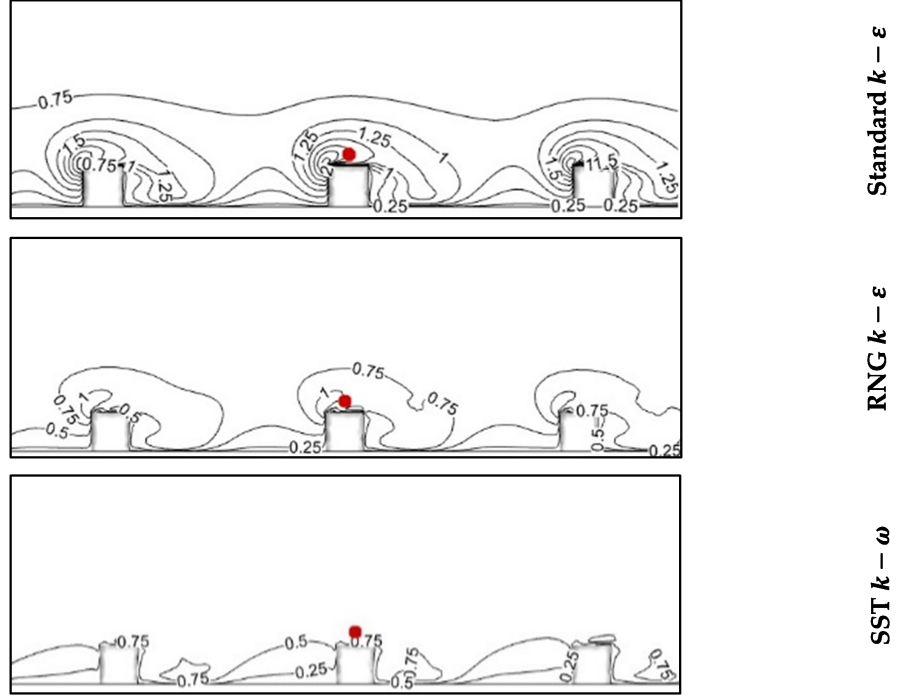


Figure 3.8: The turbulence kinetic energy, TKE ( $\text{m}^2 \text{s}^{-2}$ ), distribution in the vicinity of the source location (red circle) in Trial 3.

available structures are negligible. Similar to what was discussed in two previous cases (Trials 1 and 2), the standard  $k - \varepsilon$  model produces higher levels of TKE, and as expected, its solution asymptotically approaches ones of SST  $k - \omega$  at higher elevations. Additionally, the wind velocity profiles estimated by all the three closures, Figure 3.9b, show a good agreement with the MUST measurements at lower heights, with  $k - \varepsilon$  based closures performing slightly better.

The numerical modeling of Trial 4 provides the opportunity to evaluate the turbulence models if the source is located upstream outside of the array. As the statistical metrics in Table 3 indicate, all three closures performed relatively similarly when the scalar source and its initial spread were not impacted by the presence of obstacles (containers). This observation further justifies investigating the effects of the source location on the accuracy of predictions made by two-equation viscosity models. Both  $k - \varepsilon$  based models predicted 65% of the resulted concentration field within a FAC2

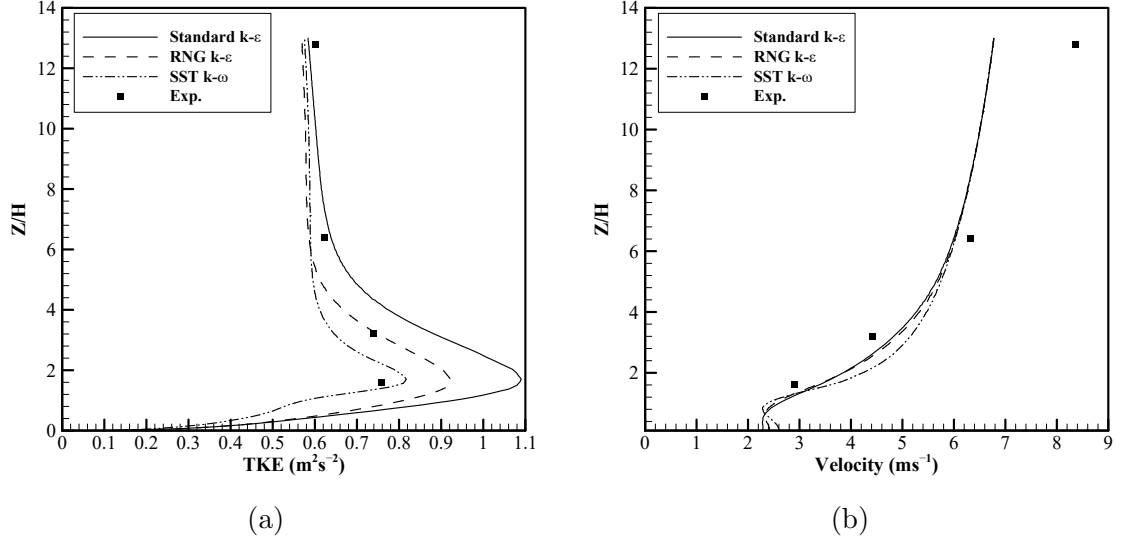


Figure 3.9: Comparison of vertical profiles of (a) TKE and (b) velocity at the 32m central tower with the field measurements of Trial 3.

of the MUST data, while the number is 61% for SST  $k - \omega$ . Furthermore, an overall minor tendency to underpredict the concentrations was observed using the standard  $k - \epsilon$  (with a FB of 0.07 and a MG of 1.01). RNG  $k - \epsilon$  and SST  $k - \omega$ , however, produced an overpredicted solution of the concentration field with an MG of 0.86 and 0.78, respectively. Assessing all five-performance metrics together, the overall superiority of the standard  $k - \epsilon$  is clear over the other two models, as all the calculated measures are within a closer range to the ideal values.

The distributions of the TKE isolines near the source, shown in Figure 3.10, further enforce the arguments made based on the statistical measures. As it can be seen, the predicted TKE fields by the three closure models are very similar in the vicinity of the scalar source. Taking a closer look at Figure 3.3, it can be clearly observed that all three representations of the concentration contours have similar shapes upstream of the array, and differences emerge as the generated plume passes the first row of containers. Therefore, having the source in regions where the simulated turbulence field is minimally affected by the type of the turbulence model (e.g., flow over an empty flat terrain) [88] seems to be an influencing factor in observing less distinction

among the statistical measures presented for selected models.

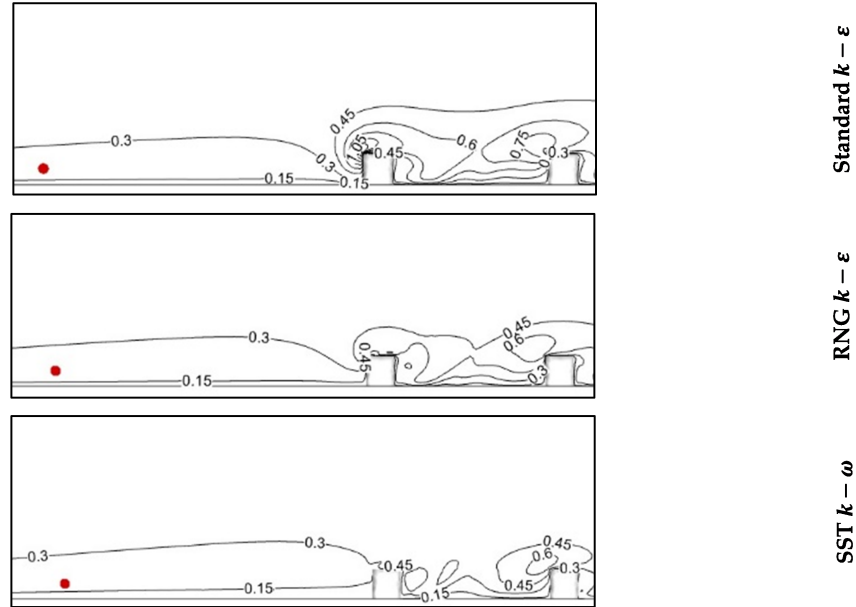


Figure 3.10: The turbulence kinetic energy, TKE ( $\text{m}^2 \text{s}^{-2}$ ), distribution in the vicinity of the source location (red circle) in Trial 4.

Figure 3.11 plots the vertical velocity and TKE profiles at the central measuring tower of MUST geometry in Trial 4. Considerable underestimations of TKE at lower elevations are observed when SST  $k - \omega$  is used, which explains its less accurate representation of the concentration field (FAC2 of 61%). Using the standard  $k - \epsilon$  model, an overprediction of the TKE field is observed at lower heights, where the produced turbulence by available containers is available and compliments the TKE overprediction of this model. As the building-generated turbulence disappears after further progress aloft in the ABL, the reported TKE underprediction of RANS prevails, which consequently results in a general underestimation in all cases.

To further assess the accuracy of the CFD models, the predicted results in horizontal and vertical directions were also evaluated, and the calculated statistical measures are presented in Table 3.4. As the given performance metrics suggest, all three closure models offer a more accurate representation of the vertical concentration field than the horizontal field, with the standard  $k - \epsilon$  model outperforming the other two

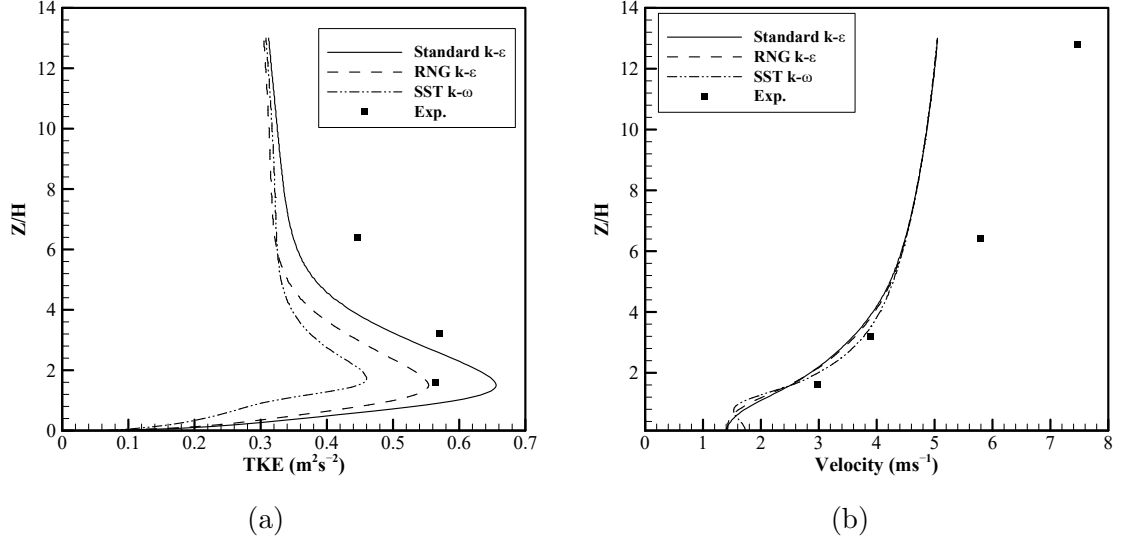


Figure 3.11: Comparison of vertical profiles of (a) TKE and (b) velocity at the 32m central tower with the field measurements of Trial 4.

closure models in every case. Additionally, less scatter is observed in vertical lines (lower VG values) than in all the horizontal sampling lines. The negative values of FB for vertical and the two immediate horizontal lines (sampling lines 1 and 2) indicate an overall over-prediction. In contrast, the opposite is valid for the two farther horizontal sampling lines where all three models generally under-predict the scalar concentration field.

The under-prediction of the scalar concentration on sampling Line 4 is much higher than the other lines, with FB values outside the acceptable range. It is suggested by Hanna et al. [54] that linear performance measures (FB and NMSE) could be excessively affected by randomly available large observed or modeled concentrations, which necessitates assessing the logarithmic metrics (MG and VG) to process them in a more balanced manner. A further look at the logarithmic measures also indicates excessive under-predictions (MG values larger than 1.3) and considerable scatter (VG values larger than 4.5) at the horizontal receptors of Line 4. Overall assessment of the statistical measures in Table 3.4 suggests that even though the accuracy and reliability of the predictions using standard  $k - \epsilon$  degrade as the distance from the

source increases, this model performs considerably better than the other two on every level.

Table 3.4: Statistical evaluation of the concentration predictions at horizontal and vertical sampling lines.

Sampling line	Model	FB	NMSE	VG	MG	FAC2
Line 1	Standard $k - \varepsilon$	-0.18	1.36	1.86	0.91	0.67
	RNG $k - \varepsilon$	-0.39	2.92	2.42	0.79	0.50
	SST $k - \omega$	-0.48	3.21	5.67	0.84	0.38
Line 2	Standard $k - \varepsilon$	-0.04	0.56	2.88	0.83	0.58
	RNG $k - \varepsilon$	-0.18	0.95	5.69	0.71	0.50
	SST $k - \omega$	-0.11	0.90	5.85	0.53	0.53
Line 3	Standard $k - \varepsilon$	0.25	0.88	3.86	0.86	0.64
	RNG $k - \varepsilon$	0.17	1.15	4.12	0.93	0.58
	SST $k - \omega$	0.38	1.66	6.81	1.16	0.53
Line 4	Standard $k - \varepsilon$	0.59	1.56	4.55	1.39	0.56
	RNG $k - \varepsilon$	0.67	1.99	4.64	1.56	0.56
	SST $k - \omega$	0.81	2.56	6.66	1.81	0.53
Vertical	Standard $k - \varepsilon$	-0.08	1.49	1.74	0.99	0.68
	RNG $k - \varepsilon$	-0.18	1.16	2.37	0.84	0.61
	SST $k - \omega$	-0.12	1.66	3.22	0.85	0.61

Scatter diagrams are presented for the horizontal and vertical sampling lines to better visualize the results of the conducted statistical analysis and the overall performance of the closure models in predicting the concentration field (Figure 3.12). The superiority of the standard  $k - \varepsilon$  over the other two closure models is evident, predicting around 62% and 68% of the horizontal and vertical concentration fields within a FAC2 of the measurements, respectively. Aligned with the presented statistics in Table 3.4, the least scatter is observed for predictions made using the standard  $k - \varepsilon$ , while the results obtained by SST  $k - \omega$  show the most. The predicted concentrations with relatively high values, which belong to the samplers near the source (e.g., sampling line 1) and along the plume centerline, are shown to be closer to the 1:1 line. In contrast, the predicted lower concentrations, mostly far from the source and

the plume centerline, show considerably more scatter (this statement is supported by the performance measures provided in Table 3.4). Constantly varying meteorological conditions during field measurements, and inaccurate estimation of the inflow velocity and turbulence profiles could be two possible reasons for this scatter.

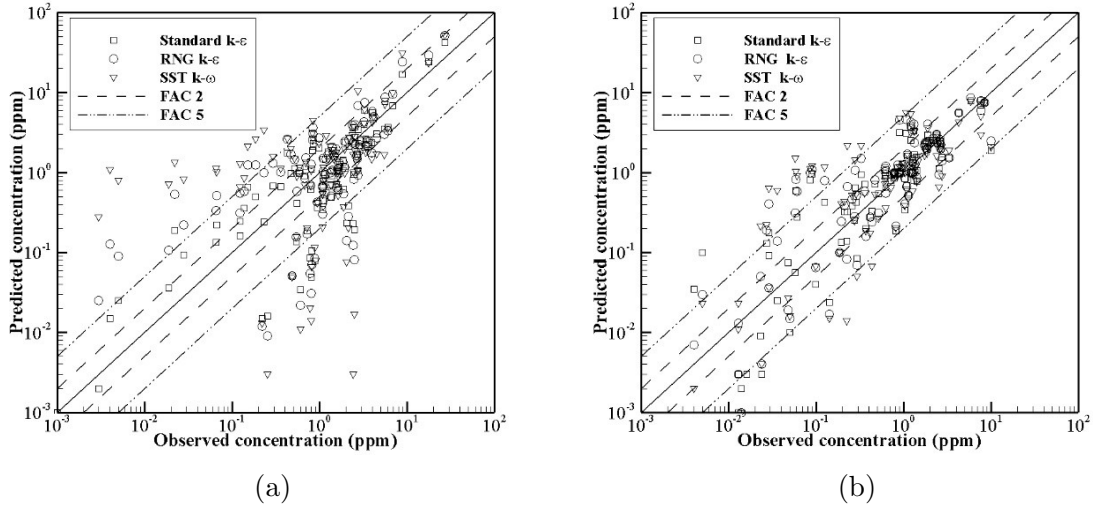


Figure 3.12: Scatter diagrams between the predicted and observed concentrations in (a) horizontal and (b) vertical sampling lines.

In this regard, the effects of the inlet boundary conditions on the accuracy of the predicted results were first investigated by examining the wind direction in Trial 2. As mentioned before, the provided quantities in Table 3.1 are, in fact, the calculated mean values over the 200-second quasi-steady period. Regardless of how minor the variations in meteorological conditions are during the quasi-steady period, that could give rise to the well-known shortcomings of the RANS method. Knowing the standard deviation of  $7.9^\circ$  in the instantaneous inflow wind direction in Trial 2 [49], two more cases were simulated with different inflow wind directions of  $22.1^\circ$  and  $37.9^\circ$ . Considering the superiority of the standard  $k - \varepsilon$ , this model was used as the closure to the RANS equations. Figure 3.13a shows the substantial deviation in the predicted concentration field caused by minor variations in the inflow wind direction during the field measurements, which further emphasizes the presence of discrepancies that could

not be avoided.

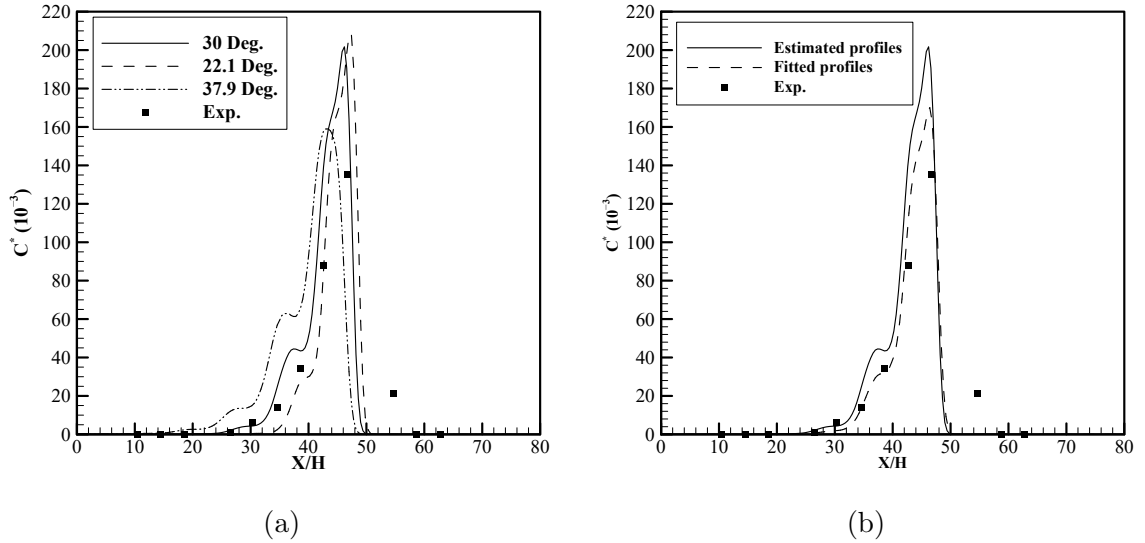


Figure 3.13: Comparison of the  $C^*$  profiles at the first horizontal sampling line in Trial 2 for different (a) inflow wind directions and (b) inflow turbulence profiles.

The estimated inflow turbulence profiles are another known source of error in urban wind modeling. Figure 3.13b compares the predictions resulting from the estimated turbulence profiles, Equations 3.8-3.9, and the fitted inflow profiles using the available upstream measurements. As can be seen, a better agreement between predictions and observations is achieved by using the fitted turbulence profile at the inlet boundary instead of using the equilibrium equations. Noting that the detailed upstream measurements for every meteorological condition are scarce in actual applications, the estimated inflow profiles used in this study are shown to provide acceptable predictions.

### 3.6.2 Turbulent Schmidt number

The turbulent Schmidt number ( $Sc_t$ ) is the next modeling parameter shown to considerably affect the predicted concentration field. Noting that there is no clear instruction on specifying the optimum  $Sc_t$ , different values are usually tested beforehand based on the physical characteristics of the geometry (e.g., natural landscapes, an isolated building, cluster of buildings, etc.) and the modeling scheme (e.g., turbu-

lence closure model). Many studies have used different values of  $Sc_t$  specific to their cases, as a remedy to make up for the under/over-prediction of the turbulent diffusion [66, 152–154]. The findings of a wind tunnel investigation by Koeltzsch, however, demonstrated the variation of the observed  $Sc_t$  with respect to the position in the boundary layer [170]. Additionally, several other studies strongly advised on the local variability of  $Sc_t$  [152, 171]. Therefore, conducting prestudies in generic cases is crucial to define  $Sc_t$  properly, as well as to evaluate the level of uncertainties associated with predictions.

Here, in addition to the conventional method of finding the optimum and constant value of  $Sc_t$ , the method of using a variable  $Sc_t$  will also be tested in the context of the dispersion modeling within complex urban geometries. For this purpose, Equation 3.18 will be incorporated into Equation 3.5 to account for the local variability of the  $Sc_t$ . Equation 3.18 was recently proposed by Longo et al. [172] with the purpose of estimating the optimum  $Sc_t$  based on the local turbulence state, that has shown promising results compared to very few other available  $Sc_t$  formulations [171].  $Sc$  in Equation 3.18 is the molecular Schmidt number,  $Re_t$  is the turbulent Reynolds number,  $S$  is the strain-rate invariant, and  $\Omega$  is the vorticity invariant.

$$Sc_t = \exp [0.6617 Sc - 0.8188 Re_t^{0.01} - 0.00311 S - 0.0329 \Omega] \quad (3.18)$$

$$Re_t = \frac{\rho k}{\omega \mu} \quad (3.19)$$

$$S = \frac{k}{\varepsilon} \sqrt{2\overline{S_{ij}}\overline{S_{ij}}} \quad S_{ij} = \frac{1}{2} \left( \frac{\partial \overline{u}_i}{\partial x_j} + \frac{\partial \overline{u}_j}{\partial x_i} \right) \quad (3.20)$$

$$\Omega = \frac{k}{\varepsilon} \sqrt{2\overline{\Omega_{ij}}\overline{\Omega_{ij}}} \quad \Omega_{ij} = \frac{1}{2} \left( \frac{\partial \overline{u}_i}{\partial x_j} - \frac{\partial \overline{u}_j}{\partial x_i} \right) \quad (3.21)$$

As an example, the results of further investigations done on Trial 3 (with a roof-based scalar source) to specify the optimum  $Sc_t$  are presented in this paper. Keeping

in mind the superiority of the standard  $k - \varepsilon$  in predicting the concentration fields, this closure model will be considered for the remaining studies of this research. Figure 3.14a shows the concentration profiles resulting from different  $Sc_t$  values at the second sampling line. The corresponding variable  $Sc_t$  calculated using Equation 3.18 is also represented by Figure 3.14b. As Figure 3.14a shows, increasing the  $Sc_t$  will generally result in larger values of  $C^*$  to be predicted by the numerical model. This clearly shows the inverse relation of the turbulent diffusivity with  $Sc_t$ , which provides the modeler with the opportunity to control over/underpredictions of scalar diffusion. An initial analysis of Figure 3.14a also indicates that  $Sc_t = 0.5$  provides relatively better predictions of the concentration field, except at the plume centerline, where it considerably underpredicts the peak values. Accurate prediction of relatively higher pollutant concentrations near the plume centerline is of great importance due to exposure-related complications that might arise. Therefore, to better evaluate the results of this sensitivity study, a detailed statistical analysis was conducted on the predicted concentration field for a wide range of  $Sc_t$ .

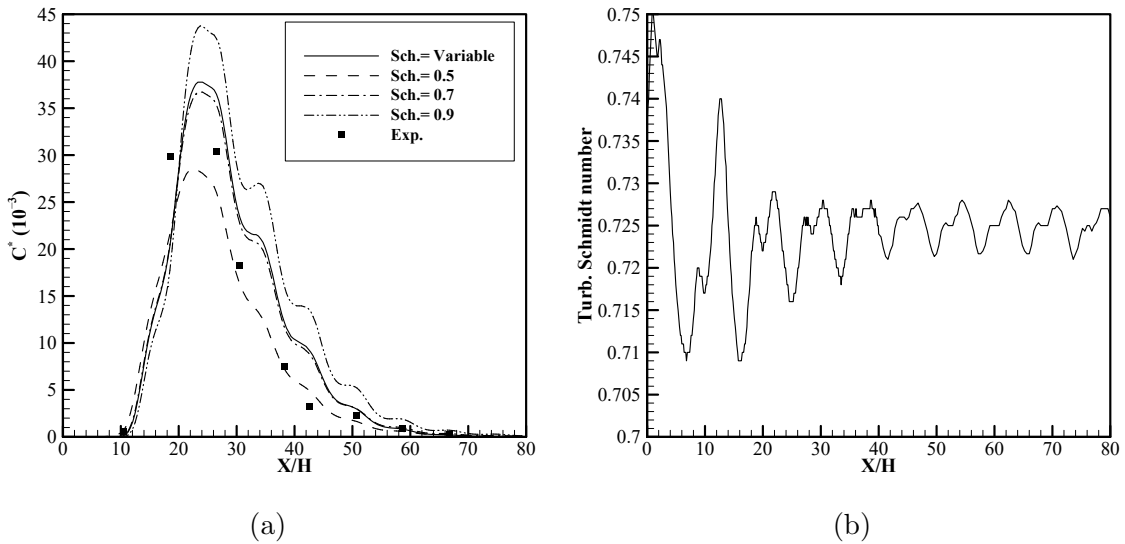


Figure 3.14:  $C^*$  for different  $Sc_t$ , and (b) the corresponding variable  $Sc_t$  for the second sampling line of Trial 3.

The numerical results obtained using  $Sc_t$  of 0.3, 1.1, and 1.3 are shown to have in-

adequate qualities to be considered for further investigations in this work. It also can be concluded from Table 3.5 that even though  $Sc_t = 0.5$  results in FAC2 of 0.8, it generally provides predictions with an unacceptable level of underprediction (FB=0.42). The relatively large value of the MG (1.22) further indicates the net underprediction of the concentration field obtained using  $Sc_t$  of 0.5. Considering all the performance metrics provided in Table 3.5, a constant  $Sc_t$  of 0.7 appears to be the optimum value in this case study while showing relatively milder underpredictions (FB of 0.16 and MG of 0.97) and fewer linear and logarithmic scatters (NMSE of 0.40 and VG of 1.74). It is noteworthy that implementing the variable  $Sc_t$ , Equation 3.18, instead of using the conventional “constant value” approach, also resulted in performance metrics quite similar to the optimum  $Sc_t$  (0.7). Figure 3.14b maps the variation of the predicted  $Sc_t$  by Equation 3.18 in the selected case study, which shows its fluctuations between 0.7 and 0.75. This justifies the implementation of this method in future applications and studies that lack field measurements for carrying out a validation study to determine the optimum  $Sc_t$ .

Table 3.5: Statistical evaluation of the  $C^*$  predictions of Trial 3 for different  $Sc_t$ .

<b>Turb. Schmidt Number</b>	<b>FB</b>	<b>NMSE</b>	<b>VG</b>	<b>MG</b>	<b>FAC2</b>
0.3	0.86	1.48	4.57	2.40	0.50
0.5	0.42	0.44	1.97	1.22	0.76
0.7	0.16	0.40	1.74	0.97	0.71
0.9	-0.02	0.59	3.13	0.85	0.68
1.1	-0.15	0.85	7.79	0.79	0.62
1.3	-0.23	1.12	22.27	0.78	0.55
Variable	0.13	0.41	1.82	0.98	0.71

### 3.7 Conclusions

A sensitivity study was carried out to evaluate the performance of the most widely used two-equation turbulence models in representing the pollutant dispersion flow

within a compact urban geometry. Four distinct case studies of the MUST comprehensive dispersion data set were chosen to further investigate the impacts of the source location on the accuracy of the concentration fields predicted by the closure models. The sources in Trials 1-3 are located within the MUST array, where the structure-generated turbulence substantially influences the plume’s immediate spread. The source in Trial 4, however, is positioned upstream and outside of the array, where all three closure models estimate similar representations of the turbulence fields (flow over an open flat terrain). Somewhat similar performance measures (FAC2 of 65% for  $k - \varepsilon$  based models and 61% for SST  $k - \omega$  model) were calculated for predictions obtained by all closure models in Trial 4 compared to other case studies, which further justified the importance of conducting this sensitivity study.

Overall, Standard  $k - \varepsilon$  showed superiority in predicting the concentration fields for all the selected trials with higher calculated FAC2 than the other two models. Except for Trial 4, the negative value of the calculated linear fractional biases (FB) indicated overprediction by the CFD models, in which the standard  $k - \varepsilon$  showed better performance compared to the two other closure models. In comparison to Trials 1-3, the predictions in Trial 4 obtained by the Standard  $k - \varepsilon$  showed minimal underprediction (positive values of FB). RANS methods are known for underestimating the TKE field due to their inability to reproduce the large-scale eddies, which generally results in underestimating the turbulent diffusivity and, consequently, overpredicting the concentration field. However, the turbulence produced by the available obstacles (here, containers) in compact urban geometries will make up for the underestimation of the TKE by RANS models. The buildings’ effects on turbulence, combined with the reported overestimation of the TKE by Standard  $k - \varepsilon$ , leads to milder overprediction of the concentration field by this closure model in Trials 1-3. Similar reasoning also justifies the relatively higher positive FB value (0.07) calculated by the standard  $k - \varepsilon$  model in Trial 4.

To further improve the accuracy of the simulations, another sensitivity study was

also carried out to determine the proper value of the  $Sc_t$ . Following the conventional procedure in finding the optimum  $Sc_t$ , several values in the range of 0.3 – 1.3 were tested, and the resultant concentration fields were compared with the field measurements. An optimum  $Sc_t$  of around 0.7 was found to produce the most accurate and reliable results. However, acquiring a high-quality dispersion data set for most applications in actual geometries is quite challenging and impractical to do similar sensitivity studies. In this regard, another approach was tested in the context of a compact urban geometry, in which the  $Sc_t$  was defined as a locally variable parameter. The calculated  $Sc_t$  varied in the range of 0.7 – 0.75, and considerable improvements were observed in the accuracy of the predictions.

# Chapter 4

## Modified accuracy of RANS modeling of urban pollutant flow within generic building clusters using a high-quality full-scale dispersion data set

### 4.1 Introduction

The continuous growth in the world's population in recent decades and the need for higher living standards have led to rapid urbanization worldwide [15, 136]. However, despite the countless benefits of the ongoing developments, several detrimental impacts on the environment and public health are also inevitable. The emergence of industrial facilities, along with the growth in the popularity of motor vehicles, have aggravated poor urban air quality [39, 173, 174]. Additionally, the intensive construction of crucial infrastructures in response to rapid urbanization has resulted in a compact and diverse arrangement of buildings [175]. With these growing pressures, anticipating and controlling the possible health hazards of living in compact regions has become a topic that requires attention. The constantly changing layout of urban areas affects the wind flow patterns, which, if not properly planned, can aggravate poor air quality by progressively worsening urban ventilation performances [24]. Therefore, to mitigate the possibility of pollutant accumulation, assessing the wind

flow field and the dispersion patterns around the buildings prior to construction is strongly advised [34, 43].

Full-scale field measurements and reduced-scale laboratory experiments (i.e., wind tunnels and water channels) have been used in the past to investigate wind flow and dispersion patterns around the buildings and to further identify design shortcomings [142, 176–179]. Even though field measurements can account for the realistic atmospheric state, the uncontrolled meteorological conditions make it costly to independently study influencing parameters and collect data that can be used to predict dispersion patterns [10].

Reduced-scale experiments can be performed in a controlled arrangement, facilitating parametric studies. However, in addition to missing actual environmental effects, this method has some disadvantages, such as complicated scaling and similarity issues [56]. The apparent complexities, limitations, and high costs associated with the experimental methods have limited their applications to general cases mainly used for model validation studies. Therefore, the need for a more effective and practical approach has made computational fluid dynamics (CFD) very popular among environmental researchers and urban planners [12, 149].

CFD can estimate the pollutant concentration and other flow characteristics on every grid point in a computational domain and is generally less costly than experiments. However, the numerical modeling of the urban dispersion flow within the atmospheric boundary layer (ABL) is quite challenging due to its turbulent nature with large-scale recirculation zones and three-dimensional strain fields [142]. Therefore, considering appropriate assumptions and modeling settings at every step of the process is essential to having a reliable and efficient CFD model. That includes efforts to evaluate the applicable approaches to treat the governing equations, examples being Reynolds-averaged Navier–Stokes (RANS) and large eddy simulations (LES) [79]. LES was found to produce relatively richer results than RANS by resolving the large and most prominent eddies; however, that comes with prohibitively greater computa-

tional demands. Given the large size of the computational domain in urban dispersion studies and the focus in the mean quantities of flow characteristics (assuming a continuous release of the pollutant from the source), RANS has remained quite popular in resolving the Navier–Stokes equations [40, 180–182].

The time-averaged treatment of this completely chaotic and randomized phenomenon (i.e., turbulent atmospheric dispersion flow) can be achieved by applying the Boussinesq hypothesis to model the intermittent shear fluxes [68]. However, neglecting the available fluctuations during the momentum transport (using modeled turbulence viscosity) undermines the reliability of the CFD model predictions. Under-prediction of the turbulence kinetic energy (TKE) or inaccurate representation of the separation points and the reattachment lengths in flows around bluff bodies are among the few well-established flaws of RANS [108]. Several closure models, along with their modifications, have been introduced over the years to remediate these deficiencies. Notably, these models were developed in the context of conventional classical flows (e.g., fully developed turbulent channel flow, simplified wall-bounded, or free shear flow, etc.), but their applications can be extended to a wide range of engineering problems [103]. Despite the apparent disparity between the nature of the mentioned classical flows and the ABL flow, common two-equation closures, such as standard  $k - \varepsilon$  [97], realizable  $k - \varepsilon$  [99], renormalization group (RNG)  $k - \varepsilon$  [98], and the shear stress transport (SST)  $k - \omega$  [101] have been widely used in urban studies [10, 21]. To ensure the reliability of an urban dispersion model, conducting a sensitivity study to select the most suitable closure for the specific case of interest is advised [38, 105, 109, 183]. Moreover, the accuracy of the selected model in the context of ABL can be further improved by re-calibrating the empirical coefficients to better fit the critical features of this particular flow.

The majority of CFD codes employ the revised values offered by Launder and Spalding ([97]) as the default closure coefficients for the standard  $k - \varepsilon$  model ( $C_\mu = 0.09$ ,  $C_{\varepsilon 1} = 1.44$ ,  $C_{\varepsilon 2} = 1.92$ ,  $\sigma_k = 1$ , and  $\sigma_\varepsilon = 1.3$ ). Previous researchers have made efforts

to modify the closure coefficients with the purpose of improving the representation of the urban flow in various cases. As one of the initial attempts, Detering [113] modified the original definition of coefficients for modeling the neutrally stratified, one-dimensional atmospheric flow over flat and irregular terrain (e.g., hills, valleys, etc.). In this work,  $C_\mu$  was assumed to be inversely proportional to the depth of the atmospheric boundary layer, which consequently led to a new set of constants ( $C_\mu = 0.03$ ,  $C_{\varepsilon 1} = 1.13$ ,  $C_{\varepsilon 2} = 1.9$ ,  $\sigma_k = 0.77$ , and  $\sigma_\varepsilon = 1.29$ ). Later, Bechmann proposed a hybrid RANS/LES method based on the standard  $k - \varepsilon$  model and adopted a  $C_\mu = 0.03$ , as suggested for atmospheric flows over irregular terrain, instead of the original value of 0.09 for industrial flows [114]. The number of unknowns was reduced in this proposed adjustment by keeping  $C_{\varepsilon 2}$ ,  $\sigma_k$ , and  $\sigma_\varepsilon$  the same as the standard values but calculated  $C_{\varepsilon 1} = 1.30$  using an empirical correlation between the model constants in the ABL. The mentioned correlation was developed by Richards and Hoaxy [165], assuming constant shear stress in the atmospheric surface layer, resulting in an equilibrium between shear production and viscous dissipation. The results of Bechmann’s model of flow over Askervein hill showed an improved accuracy compared to the ones offered by Detering. However, it could not be confidently distinguished whether this progress was mainly due to the re-calibration of coefficients or the proposed hybrid model.

The modification of the standard  $k - \varepsilon$  model was further extended to a more complicated scenario by Guilass et al. [116], in which the airflow within a regular street canyon was considered. The authors performed a Bayesian calibration to tune four out of the five constants by excluding  $\sigma_\varepsilon$  and calculating it directly via the correlation between the model constants within the ABL [165]. The vertical profile of the TKE at the center of the street canyon was considered as the optimization objective, and the results of the 135 CFD runs were processed to determine a set of constants that produced the preferable match with the wind tunnel measurements ( $C_\mu = 0.12$ ,  $C_{\varepsilon 1} = 1$ ,  $C_{\varepsilon 2} = 2.1$ ,  $\sigma_k = 0.46$ , and  $\sigma_\varepsilon = 0.42$ ). In another work by Zahid

Iqbal and Chan [115], an investigation of the wind flow field around a cross-shaped building at the pedestrian level was conducted. The modification of the  $k - \varepsilon$  closure model in this attempt was based on the proposed coefficients by Guilass et al. [116]. The number of unknowns was reduced to simplify the process by just varying  $C_\mu$  at four equal intervals within the range of 0.09–0.12 while keeping the values of  $\sigma_k = 0.53$  and  $\sigma_\varepsilon = 0.5$  constant, as suggested by Edeling et al. [184]. Setting the normalized velocity field as the modification objective in their study,  $C_\mu = 0.12$  was shown to provide the least discrepancies with wind tunnel measurements, though the superiority of the tuned model over the one proposed by Guilass et al. [116] was insignificant. This conclusion heightens the importance of calibrating the whole set of coefficients simultaneously to accomplish a worthwhile improvement, in contrast to alleviating the computational complexity by just doing a linear sensitivity study on a selected coefficient.

The demonstrated uncertainty inherent in these coefficients implies the necessity of their objective modification within the reference frame of generic case studies. Because of the non-linear relationship between coefficients, a complete closure optimization for ABL flow in large models (e.g., compact urban settings) becomes substantially more challenging. Implementing data assimilation methods, such as the Bayesian calibration, demands a large number of CFD runs, creating the need for more robust optimization approaches to obtain the best coefficient set. In this regard, Shirzadi et al. [118] used stochastic optimization combined with the Monte Carlo sampling scheme and adopted the streamwise velocity around an isolated building as the optimization objective. They used available wind tunnel measurements to introduce a set that better represents the flow characteristics compared with the standard model ( $C_\mu = 0.146$ ,  $C_{\varepsilon 1} = 1.489$ ,  $C_{\varepsilon 2} = 2.801$ ,  $\sigma_k = 1$ , and  $\sigma_\varepsilon = 0.373$ ). Shirzadi et al. later performed a parametric sensitivity study to evaluate the possibility of improving the numerical simulation of cross-ventilation in compact urban regions [117]. They did not use an optimization framework in this study but mitigated the associated com-

putational costs by considering 10 uniformly distributed values for each coefficient within the recommended ranges. The resultant set only offered modifications to  $C_{\varepsilon 2}$  and  $\sigma_\varepsilon$  (3.2 and 0.35, respectively), while keeping the rest of the coefficients the same as their original values. The aptness of the suggested coefficients was examined using wind tunnel measurements of the wind pressure difference over the faces of the central building (i.e., the objective function in this study). Even though an improved agreement with measurements was observed, the accuracy of the calibrated model was found to be inadequate and in need of further efforts [185].

### 4.1.1 Objectives

Following the previous endeavors, this study aims to enhance the reliability and generality of the closures in ABL dispersion studies. Based on the presented review, a well-tested set of coefficients that accurately represents the pollutant concentration field within an urban array has yet to be developed. The current research is part of a project to improve the existing practices in dispersion modeling. In our previous paper, the effects of several critical modeling decisions (e.g., closure model, inflow boundary conditions, computational domain size, and turbulent Schmidt number) were investigated, and a relatively efficient framework was introduced [183]. Considering different venting scenarios (i.e., various source locations), the standard  $k - \varepsilon$  model coupled with the locally variable turbulent Schmidt number ( $Sc_t$ ) was found to be the most efficient setup with the least calculated deviations from field measurements. Therefore, the present study conducts a thorough optimization of the standard  $k - \varepsilon$  closure by incorporating the recommended modeling settings.

The importance of selecting a high-quality data set for the robust calibration of the turbulence model constants is undeniable. Among all of the previous attempts reviewed, none included the pollutant concentration field in their defined focus parameters. Additionally, to the best of our knowledge, all earlier ABL calibration studies used reduced-scale wind tunnel data produced in controlled and steady test

arrangements. Full-scale field measurements, however, have the effects of constantly varying the meteorological features and realistic atmospheric conditions inherent in them, making them very valuable for improving the time-averaged representation of an intrinsically unsteady phenomenon. To this aim, the unique data set of the mock urban setting tests (MUST) is employed, as it provides comprehensive measurements of both the concentration and airflow fields throughout a compact building array (74 measuring points for the concentration field and 22 measuring points for the airflow field) [55]. Using full-scale field measurements of this kind creates an unprecedented opportunity to account for realistic atmospheric features that could potentially lead to a more accurate representation of the dispersion flow by RANS simulations. Given the variation in the concentrations in a broad range inside the domain (0.001–100 ppm), an exhaustive statistical analysis is carried out that includes both the linear and logarithmic validation metrics. In addition to the optimization objective, the predicted turbulence characteristics are also assessed to evaluate uncertainties of the coefficients more extensively. Ultimately, three other test cases representing different meteorological conditions (e.g., inflow wind speed and turbulent kinetic energy, wind direction, etc.) and source locations are modeled to further examine the generality of the proposed set of constants for an idealized array simulating urban regions.

## 4.2 Mathematical model

The pattern in which an emitted pollutant stream is dispersed in the ABL heavily depends on the wind regime and flow features. In this regard, acquiring a solid understanding of urban flows is essential prior to characterizing the physics of this phenomenon. The ABL generally refers to the lowest portion of the atmosphere, which can be divided into two main sublayers. The outer region (i.e., the Ekman layer) makes up approximately 90% of this layer and shows a balance among pressure gradient, friction, and Coriolis forces. The inner region (i.e., the surface layer) exhibits strong vertical fluxes of physical quantities with negligible variation within

its depth [28]. As our work aims to model pollutant dispersion within a compact urban setting, the surface layer is the area of interest in investigating the flow characteristics. Therefore, disregarding the Coriolis effects on the direction of the urban wind flow is deemed an acceptable assumption. This claim can be further argued by assessing the non-dimensional Rossby number ( $R_o$ ), which quantifies the ratio of inertial to Coriolis forces [155]. Given the typical velocity and length scales in urban studies,  $R_o$  is estimated to be in the order of  $10^3$ , which indicates a strong dominance of inertial forces [183].

The atmospheric flows in urban areas with a horizontal length scale of less than 10 km are typically treated at the micro-scale range [186]. The CFD simulation of pollutant dispersion within this spatial scope demands explicit modeling of the available structures. These roughness elements, such as buildings of varying shapes and dimensions, intensify the turbulent nature of the ABL flows. This generates three-dimensional flow features, such as flow separation, recirculation, and substantial directional change of the wind around the bluff bodies. As a result, eddies with varying lengths and time scales are formed, and modeling them requires special considerations. The RANS equations would be an appropriate method to employ in cases dealing with time scales that are considerably greater than turbulent fluctuations. On pollutant dispersion modeling in full-scale urban geometries, the RANS equations provide an acceptable compromise between accuracy and computational cost and are, therefore, adopted in this study.

The physics of a steady-state, incompressible, and iso-thermal flow within a neutrally stratified atmosphere with no body forces can be described by time-averaged continuity and momentum equations:

$$\frac{\partial \bar{u}_i}{\partial x_i} = 0 \tag{4.1}$$

$$\bar{u}_j \frac{\partial \bar{u}_i}{\partial x_j} = -\frac{1}{\rho} \frac{\partial \bar{p}}{\partial x_i} + \nu \frac{\partial^2 \bar{u}_i}{\partial x_j^2} - \frac{\partial \overline{u'_i u'_j}}{\partial x_j} \tag{4.2}$$

where  $\bar{u}_i$  and  $u'_j$  are the mean and fluctuating velocity components in the Cartesian directions of  $x_i$  and  $x_j$ , respectively ( $i, j = 1, 2, 3$ ).  $\rho$  is the air density,  $\bar{p}$  is the time-averaged pressure, and  $\nu$  is the kinematic viscosity defined as  $\nu = \mu/\rho$  with  $\mu$  being the dynamic viscosity.

The Reynolds stress tensor ( $\overline{u'_i u'_j}$ ) further promotes an enhanced diffusive transport of momentum due to the fluctuating velocity components. However, this term introduces additional unknowns, leading to more variables than the available equations. Assuming an isotropic turbulent flow, the Boussinesq hypothesis can be applied to model these Reynolds stresses in terms of mean velocity gradients:

$$-\overline{u'_i u'_j} = 2 \left( \nu_t \bar{S}_{ij} - \frac{1}{3} k \delta_{ij} \right) \quad (4.3)$$

$$\bar{S}_{ij} = \frac{1}{2} \left( \frac{\partial \bar{u}_i}{\partial x_j} + \frac{\partial \bar{u}_j}{\partial x_i} \right) \quad (4.4)$$

$$k = \frac{1}{2} \overline{u'_i u'_i} \quad (4.5)$$

in which  $\bar{S}_{ij}$  represents the mean strain rate tensor,  $k$  is the turbulence kinetic energy (i.e., TKE),  $\delta$  is the Kronecker delta, and  $\nu_t$  denotes the eddy viscosity.

$\nu_t$  is a parameter defined as a property of the flow to reflect and control turbulence through a form of viscosity, analogous to the role of molecular viscosity in laminar flow [100]. In order to mathematically close the governing equations, several eddy-viscosity closure models have been developed over the years to approximate  $\nu_t$  and provide supplementary equations. These closures aim to model the eddy viscosity as a product of turbulent velocity and length scales. Based on the argument made in the introduction, the standard  $k - \varepsilon$  model is adopted in the current study to model  $\nu_t$  and estimate all the other turbulence quantities [100]. The TKE represents the turbulent velocity scale in this closure and can be calculated using a transport equation as follows:

$$\bar{u}_j \frac{\partial k}{\partial x_j} = \frac{\partial}{\partial x_j} \left[ \left( \nu + \frac{\nu_t}{\sigma_k} \right) \frac{\partial k}{\partial x_j} \right] - \overline{u'_i u'_j} \frac{\partial \bar{u}_i}{\partial x_j} - \varepsilon \quad (4.6)$$

where  $\sigma_k$  is a model constant referred to as turbulence Prandtl number, and  $\varepsilon$  represents the dissipation rate of the TKE into internal energy (heat). The second term on the right-hand side of the Equation 4.6 serves as a source of TKE production ( $P_k$ ), which can alternatively be expressed in terms of the mean velocity shear stresses using the Boussinesq hypothesis:

$$P_k = -\overline{u'_i u'_j} \frac{\partial \bar{u}_i}{\partial x_j} \approx \nu_t \left( \frac{\partial \bar{u}_i}{\partial x_j} + \frac{\partial \bar{u}_j}{\partial x_i} \right) \frac{\partial \bar{u}_i}{\partial x_j} \quad (4.7)$$

In addition to the TKE, another turbulence quantity is required to estimate the associated length scales of eddies within the flow field. The appearance of dissipation rate in the form of a sink term in Equation 4.6 suggests that solving a transport equation for  $\varepsilon$  is a logical choice to close the equation set. It is worth noting that the TKE equation remains the same among all variants of  $k - \varepsilon$  closure, whereas the proposed equation for  $\varepsilon$  is what distinguishes these models. Using the standard version of  $k - \varepsilon$  model, the transport of  $\varepsilon$  can be resolved by:

$$\bar{u}_j \frac{\partial \varepsilon}{\partial x_j} = \frac{\partial}{\partial x_j} \left[ \left( \nu + \frac{\nu_t}{\sigma_\varepsilon} \right) \frac{\partial \varepsilon}{\partial x_j} \right] + \frac{\varepsilon}{k} (C_{\varepsilon 1} P_k - C_{\varepsilon 2} \varepsilon) \quad (4.8)$$

$\sigma_\varepsilon$ ,  $C_{\varepsilon 1}$ , and  $C_{\varepsilon 2}$  are the model's empirical constants that were derived through intensive data fitting with a number of classical flows [97]. The TKE and dissipation rates resulting from supplementary equations can be further used in Equation 4.9 to estimate the eddy viscosity. The factor of proportionality in this equation,  $C_\mu$ , is another empirical model constant.

$$\nu_t = C_\mu \frac{k^2}{\varepsilon} \quad (4.9)$$

The dispersion of the pollutant within the resolved wind and turbulence fields can be modelled by solving the Eulerian advection-diffusion transport equation. Considering a neutrally buoyant and inert gas emitting from a source point without initial momentum, the Reynolds averaging method is once again employed to decompose the instantaneous quantities (i.e., velocity components and scalar concentration) into

their mean and fluctuating elements:

$$\bar{u}_j \frac{\partial \bar{c}}{\partial x_j} = \frac{\partial}{\partial x_j} \left( D \frac{\partial \bar{c}}{\partial x_j} \right) - \overline{\partial u'_j c'} + S' \quad (4.10)$$

where  $\bar{c}$  and  $c'$  are the mean and fluctuating scalar concentrations, respectively.  $S'$  denotes the scalar source term, and  $D$  represents the molecular diffusivity defined as the ratio of molecular viscosity to molecular Schmidt number ( $D = \frac{\nu}{Sc}$ ). Equation 4.10 is coupled with the RANS equation system in one-way under the assumption of a passive scalar, which considerably reduces the computational cost and modeling complexity [187].

The convective transport of the scalar concentration due to the fluctuating velocities (i.e., unresolved flow field) is expressed by  $\overline{u'_j c'}$ . With an analogy similar to the Boussinesq hypothesis (i.e., the random isotropic motion), the Standard Gradient Diffusion Hypothesis (SGDH) assumes that turbulent convective transport of a scalar occurs in the direction of the time-averaged concentration gradient [188]. From this, the turbulent scalar transport can be approximated as follows:

$$-\overline{u'_j c'} = D_t \frac{\partial \bar{c}}{\partial x_j} \quad (4.11)$$

Similar to eddy viscosity, eddy diffusivity ( $D_t = \nu_t/Sc_t$ ) is also a property of the turbulence and not of the fluid. On another note, a normalized definition of pollutant concentration ( $C^*$ ) will be used in this work for making comparisons between predictions and measurements. In this equation,  $U_{ref}$  is the upstream reference velocity,  $C$  is the predicted or measured concentration at a given location,  $H_{ref}$  is a reference length scale,  $C_s$  is the source concentration, and  $q_s$  is the volumetric flowrate at which pollutant is being released from the source.

$$C^* = \frac{U_{ref} C H_{ref}^2}{C_s q_s} \quad (4.12)$$

The turbulent Schmidt number,  $Sc_t$ , is a variable in the scalar transport equation that substantially affects the accuracy of the predicted concentration field. Having

in mind that the turbulent mass flux is approximated through a closure assumption (i.e., SGDH), a universal value of  $Sc_t$  cannot be determined [152]. To this end, similar to the coefficients of the eddy-viscosity turbulence models, obtaining case-dependent  $Sc_t$  might be a practical approach. However, in addition to time demanding sensitivity studies required by this approach, several experimental and validated numerical studies have demonstrated the strong local variability of  $Sc_t$  [170, 171]. As part of our ongoing efforts to improve the reliability of the urban dispersion modeling, the proposed framework in [183] is adopted in this study. Following these recommendations, a well-tested locally variable  $Sc_t$  is incorporated into the advection-diffusion equation. The aforementioned  $Sc_t$  formulation accounts for the local state of turbulence and estimates the optimum value in every computational node [172]. Implementation of the locally variable  $Sc_t$  further strengthens the dependency of the transport equation on the flow-related parameters. Using Equation 4.13,  $Sc_t$  is defined as:

$$\log(Sc_t) = 0.6617 Sc - 0.8188 Re_t^{0.01} - 0.00311 S - 0.0329 \Omega \quad (4.13)$$

$$Re_t = \frac{k^2}{\nu \varepsilon} \quad (4.14)$$

$$S = \frac{k}{\varepsilon} \sqrt{\frac{1}{2} \left( \frac{\partial \bar{u}_i}{\partial x_j} + \frac{\partial \bar{u}_j}{\partial x_i} \right)^2} \quad (4.15)$$

$$\Omega = \frac{k}{\varepsilon} \sqrt{\frac{1}{2} \left( \frac{\partial \bar{u}_i}{\partial x_j} - \frac{\partial \bar{u}_j}{\partial x_i} \right)^2} \quad (4.16)$$

where  $Re_t$  is the turbulent Reynolds number,  $S$  is the strain rate invariant, and  $\Omega$  is the vorticity rate invariant.

### 4.3 Closure model calibration

The empirical coefficients of RANS closures were primarily tuned to provide a satisfactory compromise between accuracy and applicability to a broad range of flows. However, a review of the previous studies shows that these coefficients are not universal, implying they can be further adjusted for turbulent flow in case studies that were

not originally considered [189]. This paper addresses the identified research gaps by developing an adjusted set of coefficients suitable for ABL dispersion flows within a generic form of urban settings.

A vital step in this process is deciding on the appropriate output constraints upon which to base the modification of the model coefficients. To improve the reliability of the air quality assessments in urban regions, a closure re-calibration is carried out, in which the pollutant concentration field and the flow field parameters (velocity and TKE) are set as the test parameters. The training case study is taken from a comprehensive full-scale measurement campaign ([55]), which integrates realistic environmental effects. A preliminary investigation of this dispersion data set shows the wide-ranging variation in the concentrations throughout the domain, ranging from 100 ppm near the source to 0.001 ppm downstream and away from the centerline (five orders of magnitude). Thus, specific considerations are required to define and evaluate the validation metrics for scalar concentrations by including logarithmic criteria, as using the typical linear measures alone would bias the fitting toward high-concentration zones.

We have chosen three linear and two logarithmic measures to examine the agreement of our numerical predictions with full-scale dispersion measurements. These measures were defined by Chang and Hanna [168], and their reliability and effectivity were exhaustively tested using several full-scale dispersion data sets [54]:

$$\text{FB} = \frac{(\overline{C_o} - \overline{C_p})}{0.5(\overline{C_o} + \overline{C_p})} \quad (4.17)$$

$$\text{NMSE} = \frac{(\overline{C_o - C_p})^2}{\overline{C_o} \overline{C_p}} \quad (4.18)$$

$$\text{MG} = \exp(\overline{\ln C_o} - \overline{\ln C_p}) \quad (4.19)$$

$$\text{VG} = \exp[\overline{(\ln C_o - \ln C_p)^2}] \quad (4.20)$$

$$\text{FAC2} = \frac{1}{N} \sum_{i=1}^N n_i \quad (4.21)$$

$$n_i = \begin{cases} 1 & \text{if } 0.5 \leq \left| \frac{C_o}{C_p} \right| \leq 2 \\ 0 & \text{otherwise} \end{cases}$$

$C_o$  and  $C_p$  are observed and predicted concentrations, respectively, while an over-bar denotes the average over the data set with  $N$  sampling points. FB and MG are fractional and mean geometric biases, respectively, metrics that measure the overall under/over-prediction. NMSE is the normalized mean square error, and VG is the geometric variance, quantifying the linear and logarithmic scatter of the predictions, respectively. FAC2 is another linear metric that denotes the fraction of predictions within the factor of 2 of the measurements. The necessity of analyzing all these measures lies in the nature of the atmospheric pollutant distribution. Linear metrics could be inordinately affected by the random extreme values, while logarithmic treatments might reflect a more balanced interpretation of them [54]. The ideal value of these performance measures and their acceptable ranges for field experiments are presented in Table 4.1. The application of these metrics is not limited to evaluating the predicted concentration field, as they also can be effectively considered to assess all the other flow parameters. Nevertheless, FAC2 might not be an adequately robust criterion for measuring the deviations between the observed and modeled velocity and TKE fields. Preliminary investigations indicated that even models with relatively deficient accuracy exhibit FAC2 larger than 85% for velocity and TKE. Hit-Rate (HR), on the other hand, sets more strict criteria and, therefore, could be an appropriate substitution for FAC2. As it can be deduced from Equation (4.22), HR gives the fraction of data points in which the relative deviation of predictions is within 25% of the measured values.  $P_i$  and  $M_i$  are the predicted and measured values of a parameter at data point  $i$ , respectively. An HR of at least 66% is required for the CFD model to be considered valid [190].

$$\text{HR} = \frac{1}{N} \sum_{i=1}^N m_i \quad (4.22)$$

$$m_i = \begin{cases} 1 & \text{if } \left| \frac{P_i - M_i}{M_i} \right| \leq 0.25 \\ 0 & \text{otherwise} \end{cases}$$

Table 4.1: The ideal value and the recommended ranges for validation metrics [54].

Validation metrics	FB	NMSE	MG	VG	FAC2	HR
Ideal value	0	0	1	1	1	1
Acceptable ranges	-0.3-0.3	0-4	0.7-1.3	1-1.6	0.5-1	0.66-1

Having the focus parameters defined as discussed, employing a systematic and so-called “economic” optimization scheme is utterly crucial to modify the input variables (i.e., closure coefficients). In our work, a recommended optimization framework ([185]) is adopted and modified to carry out a rigorous calibration of the standard  $k-\varepsilon$  model (adjusting all five coefficients) in the context of a large model (i.e., full-scale urban dispersion flow).

The inherent uncertainties of the empirical coefficients, combined with their highly nonlinear and synergistic effects on the output variables, make any linear sensitivity approach ineffective in obtaining an optimized set. Despite that, simple screening techniques can still be adopted to determine the input variables with the most influence on the validation metrics [118]. Here, the relative contribution of each closure coefficient to the predicted concentration field will be assessed by quantifying its elementary effect [191]. For a selected validation metric denoted by  $G$ , which is assumed to be a function of the vector of coefficients  $F = (f_1, \dots, f_m)$ , the first derivative term of the Taylor series can be used to give a measure of the elementary effect for each coefficient:

$$E_i(F) = \frac{[G(f_1, \dots, f_i + \Delta_i, \dots, f_m) - G(F)]}{\Delta_i} \quad (4.23)$$

where  $m$  is the number of coefficients to be assessed, and  $\Delta_i$  are step lengths determined to account for the variation of the  $i$ th coefficient within a given range.

Furthermore, the mean  $\overline{E}_i$  and the standard deviation  $\sigma_{E_i}$  of the elementary effects related to each input variable must be calculated. The interpretation of these quantities provides valuable insight into the possibility of prioritizing some coefficients over others, potentially simplifying the optimization exercise [192]. Therefore, any coefficient that demonstrates negligible and quasi-linear impacts on output variables can be ignored at the optimization stage by keeping it at its standard value. The modified value of this coefficient can be obtained later by performing a sensitivity analysis while the optimized values for other closure constants are considered.

The amended list of the coefficients, together with their revised ranges from the previous step, should be put through the calibration process. The eddy-viscosity closure coefficients are pragmatic in definition; hence, their optimum value for producing reliable and accurate outputs (i.e., pollutant concentration distribution and flow parameters in this study) cannot be attained through a deterministic approach. An appropriate optimization scheme can be implemented in such cases to effectively navigate the performance variation caused by the random but targeted variation of the coefficients in the considered parameter space. To mitigate the effects of the available uncertainties on output variables, two intrinsically analogous and robust objective functions are defined to be used at two levels of the optimization [193]:

$$O_{f1} = \sum_{i=1}^l (G_i - \Gamma_i)^2 \quad (4.24)$$

$$O_{f2} = \sum_{i=1}^l [(\overline{G}_i - \Gamma_i)^2 + \sigma_{G_i}^2] \quad (4.25)$$

Equation (4.24) is employed for assessing the performance of each analyzed set, aiding in the deliberate choice among them in every optimization trial, while Equation (4.25) contributes to refining the ranges following each iteration of optimization. For the validation metric  $i$ ,  $G_i$  is its calculated value for each considered coefficient set with  $\overline{G}_i$  and  $\sigma_{G_i}$  as its mean and standard deviation over each optimization iteration, respectively.  $\Gamma_i$  is the ideal value for the  $i$ th validation metric, and  $l$  is the number of

metrics included in this calibration study. The ranges for all input variables should be adjusted to minimize the objective function  $O_{f2}$ . The first term in Equation (4.25) ensures the accuracy of the model, while the second term ensures its reliability by reducing the variation in output responses within the proposed ranges.

Considering the complex and multidimensional parameter space in this work, the genetic algorithm (GA) was adopted and carefully adjusted to carry out the calibration exercise. GA is an optimization technique inspired by the natural selection analogy that facilitates reaching an optimal solution through evolution [194]. It offers balanced exploitation (cross-over) and exploration (mutation) of the search space, which effectively produces populations of new coefficient sets with a higher potential for success. Different adjustments of GA were tested to form a framework that best serves the re-calibration study in this work. Random selection of the coefficient sets from investigated ranges is carried out by employing the Monte-Carlo sampling method [195]. Using this selected population, the probability density function (PDF) of the validation metrics is calculated by repeatedly running CFD simulations. A rank-based selection based on the calculated  $O_{f1}$  values (Equation (4.24)), along with a uniform cross-over approach, is found to be more efficient in exploring the parameter space. A cross-over probability of 75% is considered, which falls within the recommended limits [196]. To explore new regions in the space that are not properly examined during the cross-over step, the generated off-springs (new sets) should be also mutated. In this regard, a Gaussian operator for the mutation step is adopted to introduce controlled perturbations to each coefficient of the sets with a probability of 10%. The new sets of coefficients generated in each iteration of the optimization process replace the sets from the previous step, and the optimal ranges for each individual coefficient are refined accordingly until the defined objective function  $O_{f2}$  reaches its converged minimum values.

Further investigations are required to evaluate the performance of the modified  $k - \varepsilon$  closure. To this aim, both the standard and optimized  $k - \varepsilon$  model will be

considered next for a comparative study (Table 4.2). In the end, the generality of the proposed set will be further tested by modeling three supplementary test cases.

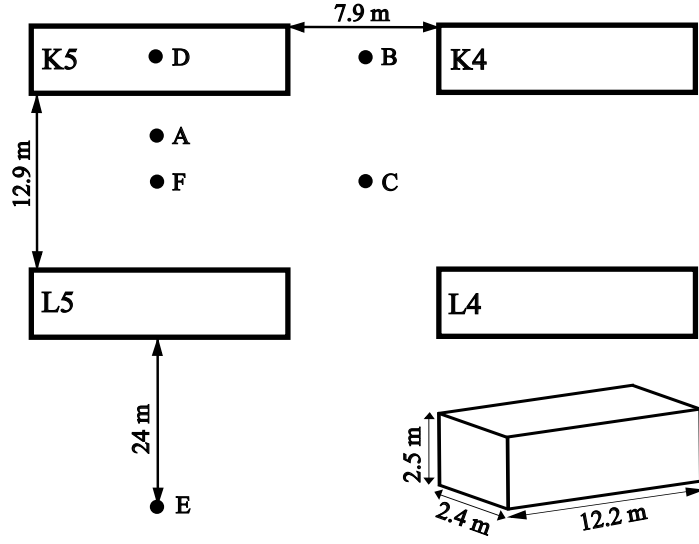
Table 4.2: Standard and revised values of  $k - \varepsilon$  empirical constants with their pre-determined variation ranges.

<b>Coefficient set</b>	$C_\mu$	$C_{\varepsilon 1}$	$C_{\varepsilon 2}$	$\sigma_k$	$\sigma_\varepsilon$
Original value [97]	0.09	1.44	1.92	1.00	1.30
Ranges	0.03–0.16	Equation 4.32	1.20–3.20	0.50–1.40	0.30–1.30

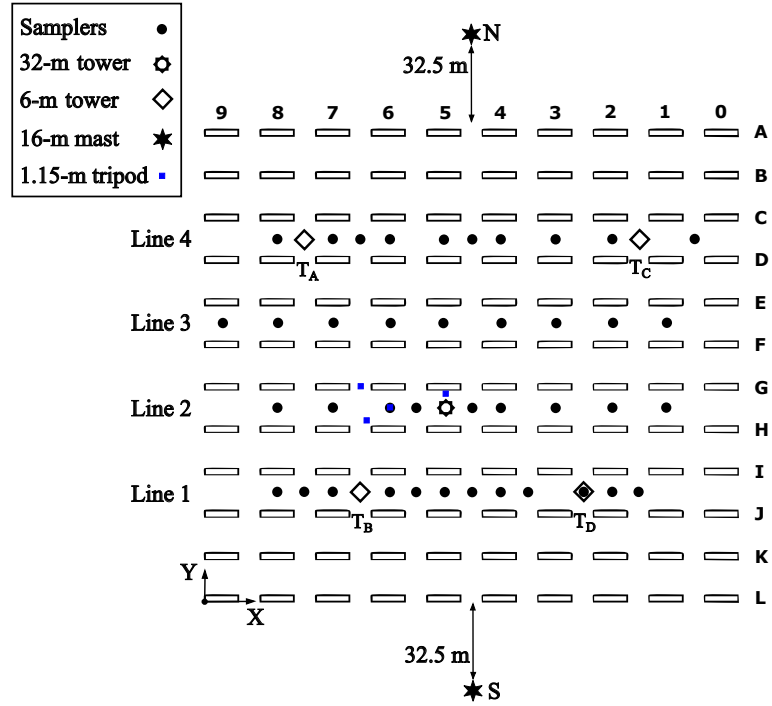
## 4.4 Description of case studies

The unique dispersion data set of the mock urban setting test (MUST) [55] was invaluable to calculate the objective function for calibrating the  $k - \varepsilon$  turbulence closure. MUST was sponsored by the U.S. Defense Threat Reduction Agency (DTRA) to provide a reliable resource that includes the meteorological and dispersion data to validate and verify the accuracy of the dispersion models and CFD simulations. An idealized urban-like geometry was designed in this experiment that consisted of a 10 by 12 array of shipping containers placed in the center of the test domain over relatively flat ground with a ground roughness of  $z_0 = 0.045$  m. Figure 4.1 illustrates the schematic of the MUST geometry, along with the dimensions of the obstacles (i.e., containers), spacing between obstacles, and site configurations. In total, 68 trials were performed in which propylene gas ( $C_3H_6$ ) was released from 37 different locations that can be classified into six main types with assigned letters A to F (Figure 4.1a). It is noteworthy that the elevation at which the aforementioned sources are located varies among all trials and should be identified prior to finalizing the CFD models.

Exhaustive measurements of the concentration field were carried out at 74 sampling points distributed throughout the array. Forty sensors were spread in four horizontal sampling lines of 1–4 (shown by black circles), and the remaining 32 sensors were installed on the central 32 m tower and four 6 m towers of  $T_A$ ,  $T_B$ ,  $T_C$ , and  $T_D$ ,



(a)



(b)

Figure 4.1: MUST experiment schematic; (a) Dimensions and source locations, (b) Top planar view with samplers locations.

positioned in each quadrant (Figure 4.1b). The mean velocity and turbulence measurements were obtained using several sensors installed on all towers and masts (22 measurement points). That includes the 32 m central tower, four 6 m towers, two 16

m pneumatic masts upstream and downstream of the array, and four 1.15 m tripods. The specifications of all sampling points considered in this calibration study are given in Table 4.3. The MUST data were further processed for time-averaged studies by conditionally sampling all measurements to extract 200 s in each trial with the lowest recorded temporal variation in the mean upstream wind speed and direction [49].

Table 4.3: Specifications of all MUST sampling points considered in the calibration study.

Location	Sensors					
	Quantity		Type		Elevation	
	Tracer	Flow	Tracer	Flow	Tracer	Flow
Lines 1, 2, 3, and 4	12, 9, 9, and 10	0	dPID <sup>a</sup>	–	1.6 m	–
Central tower	8	4	dPID	3D-SA <sup>b</sup>	1, 2, 4, 6, 8, 10, 12, and 16 m	4, 8, 16, and 32 m
T <sub>A</sub> , T <sub>B</sub> , T <sub>C</sub> , and T <sub>D</sub>	6 each	2 each	UVIC <sup>c</sup>	3A-UA <sup>d</sup>	1, 2, 3, 4, 5, and 5.9 m	2.4, and 6 m
S and N	0	3 each	–	2D-SA <sup>e</sup>	–	4, 8, and 16 m
Tripods	0	1 each	–	3D-SA	–	1.15 m

<sup>a</sup> Digital photo-ionization detector

<sup>d</sup> 3-axis Ultrasonic anemometer

<sup>b</sup> 3-dimensional sonic anemometer

<sup>e</sup> 2-dimensional sonic anemometer

<sup>c</sup> Ultra-violet ion collector

This paper considers four different trials: one as the training case to be used in the calibration study and three as test cases (TC-1 to TC-3), to evaluate the generality of the proposed coefficient set for various inflow boundary conditions and pollutant source locations. Table 4.4 summarizes all four cases with their main characteristics. This includes the averaged inflow velocity ( $S_{04}$ ) and direction ( $\alpha_{04}$ ) at 4 m height, source type and its elevation ( $Z_s$ ) with respect to ground, the tracer release rate ( $q_s$ ), and the Monin–Obukhov length ( $L_{MO}$ ). The positive value of  $\alpha_{04}$  is measured counter-clockwise from the  $y$ -axis.

Table 4.4: Summary of selected trials of MUST experiment for RANS calibration study.

Case study	Trial I.D.	Source type	$q_s$ ( $\frac{1}{\text{min}}$ )	$Z_s$ (m)	$S_{04}$ ( $\frac{\text{m}}{\text{s}}$ )	$\alpha_{04}$ (deg)	$L_{MO}$ (m)
Training case	2682320	D	225	2.6	4.55	-39	170
TC-1	2681829	F	225	1.8	7.93	-41	28000
TC-2	2692250	E	225	1.3	3.38	36	130
TC-3	2672150	A	200	0.15	2.30	36	150

## 4.5 CFD simulation

Performing a reliable and accurate CFD simulation strongly depends on modeling decisions at the setup stage. To this end, the following subsections deal with the general CFD settings and considerations, mesh independence study, and the importance of remediating the artificial horizontal inhomogeneity (i.e., the undesirable streamwise gradients in the vertical profiles of flow variables).

### 4.5.1 General settings

The pollutant dispersion within a compact urban setting is modeled on a high-resolution grid using the ANSYS CFX commercial code. The 3D steady-state RANS equations coupled with the Eulerian transport equation are discretized and solved by employing the hybrid finite element/volume method. High-resolution schemes are considered to evaluate advection terms and turbulence numerics, and the Rhie–Chow algorithm was adopted to implement pressure-velocity coupling. To ensure convergence of the solution, target values of root mean square (RMS) normalized residuals were set to  $10^{-6}$  and  $10^{-9}$  for flow variables and tracer concentrations, respectively. The minimum size of the computational domain was determined based on the recommendations of Tominaga et al. [197] and Franke et al. [18]. The additional domain sizes were examined to specify the proper dimensions for the MUST geometry to eliminate the possibility of any artificial flow accelerations around the buildings and

destructive backflow at the boundaries. Taking the height of the obstacles as  $H$ , distances from the MUST array are revised to  $14H$  from the inlet,  $10H$  from lateral boundaries,  $20H$  from the outlet, and  $12H$  from the top boundary. This ensures that the results are domain independent. Figure 4.2 illustrates a schematic of the computational domain. As can be seen, the rectangular domain is oriented so that the inflow wind stream is perpendicular to the inlet and outlet faces.

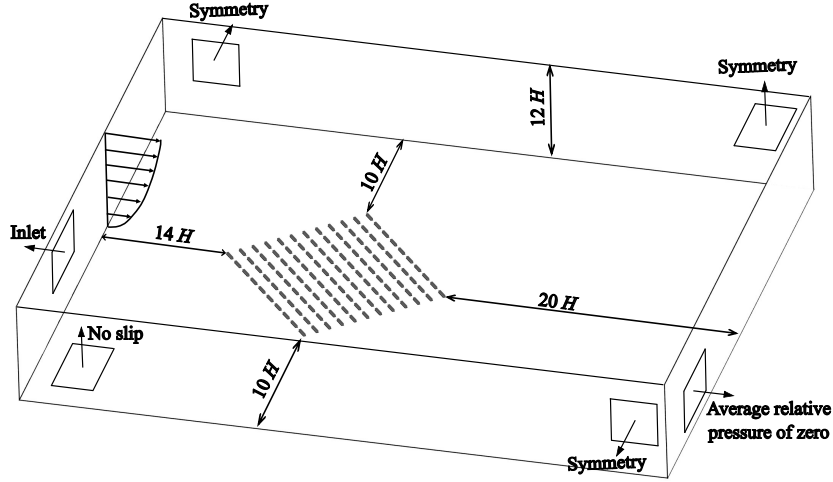


Figure 4.2: Computational domain

The next crucial step in setting up a CFD model is to define the proper constraints at the limits of the computational domain (i.e., boundary conditions). Assuming an equilibrium atmospheric surface layer, the inflow velocity and turbulence profiles can be approximated by [165]:

$$U(z) = \frac{u_\tau}{\kappa} \ln \left( \frac{z + z_0}{z_0} \right) \quad (4.26)$$

$$k(z) = \frac{u_\tau^2}{\sqrt{c_\mu}} \quad (4.27)$$

$$\varepsilon(z) = \frac{u_\tau^3}{\kappa(z + z_0)} \quad (4.28)$$

where  $u_\tau$  is the friction velocity,  $\kappa$  is the Von Kármán constant with the value of 0.4 [165], and  $z_0$  is the aerodynamic roughness. Having a reference velocity at a

reference height (Table 4.4), Equation (4.26) can be used to calculate  $u_\tau$  for each case study.

An average relative pressure of zero is specified at the outlet boundary. The top and lateral limits are set as symmetry. The faces of each container are treated as smooth walls with no-slip boundary conditions, while the ground is considered to be a rough wall with a physical roughness of  $z_0$ . The scalable wall function is employed to resolve the velocity and turbulence quantities near the walls. The given uniform ground roughness also represents the roughness of the upstream terrain that is not considered in the domain. This implies having a fully-developed atmospheric flow at the inlet, which, ideally, should not reflect any streamwise gradient as it progresses through the domain [88]. However, horizontal heterogeneity is a known issue in ABL flow simulations that needs to be carefully evaluated before claiming the reliability of the results [18].

### 4.5.2 Grid convergence study

Generating a high-quality grid has a pivotal impact on reducing the discretization error and enhancing the convergence of the solution. In the current study, a nested domain was defined in which the inner domain encloses the MUST array. As a consequence of taking this approach, the large empty portion of the domain was meshed using structured hexahedral elements, which improves the overall rate of convergence [94]. Unstructured tetrahedral cells are used to mesh the regions near the blocks within the inner domain, while several prismatic layers are considered near the solid surfaces (i.e., ground and faces of the blocks) to properly capture boundary layer gradients.

Following the “best-practice” guidelines in computational wind engineering, the sensitivity of the CFD model results to the grid resolution should be carefully assessed [197]. In this regard, three successive grid resolutions of coarse, medium, and fine were examined with 6.39, 9.68, and 14.62 million computational nodes, respec-

tively. The vertical profile of normalized velocity at the central 32 m tower and the horizontal profile of normalized pollutant concentration at the second sampling line are compared to assess the uncertainty of results due to the grid size. As Figure 4.3a illustrates, there are trivial deviations between the resultant velocity profiles using all three grid refinements, which necessitates evaluating a more sensitive variable (i.e., concentrations). Figure 4.3b, however, implies that employing the grid with medium refinement would be the appropriate choice with respect to the computational cost and dependency of the predictions to mesh sizes.

Additionally, another grid sensitivity study proposed by Celik et al. [166] was conducted to calculate the grid convergence index (GCI). The predicted pollutant concentration at 74 sampling points was selected as the variable of interest. For detailed mathematical steps and calculations of this investigation, please refer to our previous paper [183]. Considering the second-order discretizations used in this work and assuming a safety factor of 1.25 as suggested by Roache [167], the average relative error and GCI for the two finer grids are 2.09% and 5.94%, respectively. Comparing these quantities with ones of the coarse-medium case (average relative error of 4.93% and GCI of 14.05%) further justifies the decision to use the grid with medium refinement. For the selected grid, the building edges were divided into 20 elements and a 5-layer inflation region was considered for all the solid surfaces with a growth rate of 1.07 to ensure  $y^+$  values were well within the acceptable range of 30 to 300. It is worth noting that the simulations were run on a workstation with two 18-core Intel Xeon Gold 5220 CPUs (36 cores in total) and 256GB of RAM. On average, a fully converged solution for each CFD run was achieved in approximately 4–5 hours.

### 4.5.3 Horizontal homogeneity

To ensure that the numerical uncertainty is kept to a minimum, the horizontal homogeneity of the flow must be first verified. A lack of homogeneity in the incident

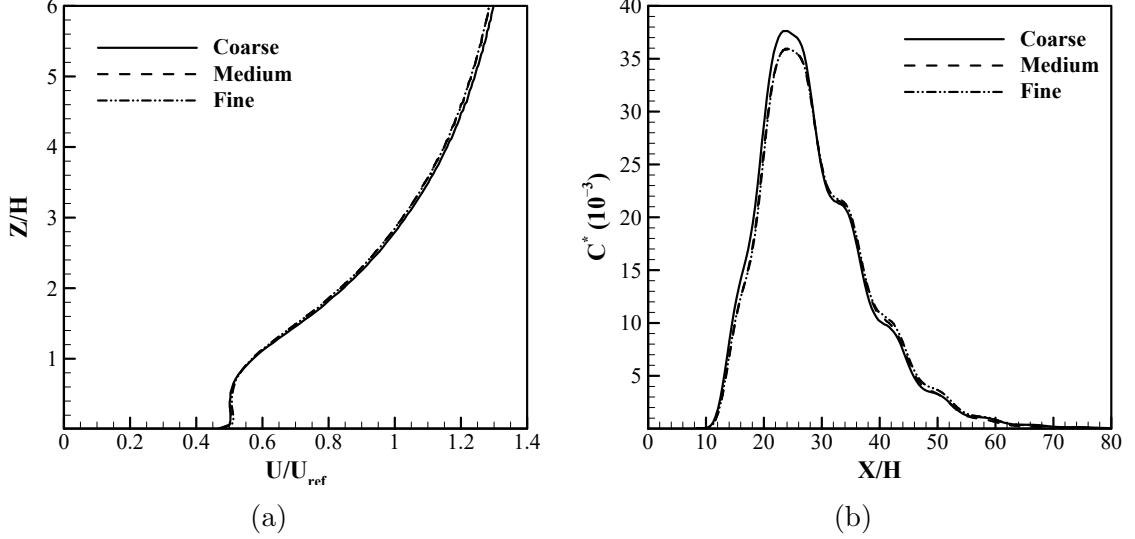


Figure 4.3: Mesh sensitivity of (a) normalized velocity at 32 m central tower and (b) normalized concentration at the second horizontal sampling line.

velocity profile can lead to erroneous results [94]. To account for the roughness of the wall, the majority of the commercial codes modify the wall function based on the equivalent sand grain roughness (i.e.,  $k_s$ ) approach [88]. As shown below, this method seems to capture the homogeneity of the flow better compared to other methods, such as replacing the no-slip with a constant shear boundary condition [91]. In order to incorporate the wall roughness into the CFX simulation, Equation (4.30) along with the modified wall function, Equation (4.31), are used [88]:

$$k_s = 29.6z_0 \quad (4.29)$$

$$k_s^+ = \frac{u_\tau k_s}{\nu} \quad (4.30)$$

$$\frac{U_P}{u_\tau} = \frac{1}{\kappa} \ln \left[ \frac{u_\tau y_P}{\nu(1 + 0.3\nu k_s^+)} \right] + 5.2 \quad (4.31)$$

where  $U_P$  is the velocity at the center of the first cell next to the wall, and  $k_s^+$  is the dimensionless sand grain roughness. These equations and the proper value of aerodynamic roughness were used to study the homogeneity of the incident profile in

an empty domain.

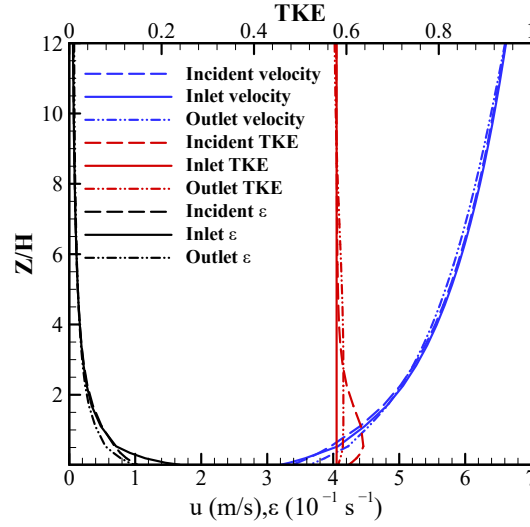


Figure 4.4: The velocity, TKE and turbulence dissipation rate profiles in an empty domain.

Figure 4.4 shows the velocity, TKE, and dissipation rate at three cross-sections in an empty domain. As can be seen, the horizontal homogeneity for the velocity and dissipation rate was near completely achieved with a mean average error of 1.3% and 1.7%, respectively. However, the TKE profile seems to display a small degree of streamwise inhomogeneity in regions close to the ground, reaching a mean average error of 2.4%. The analytical solution to the horizontally homogeneous atmospheric boundary layer requires the production of turbulence to be balanced by the dissipation at a constant rate leading to a uniform value for the TKE normal to the ground. However, as indicated in the work of the previous researchers [40] and from Figure 4.4, TKE varies with distance to the ground. The reason for this over-generation of turbulence in the vicinity of the wall in the  $k - \varepsilon$  model was previously discussed by Richards [198], and the inconsistent discretization of the turbulence production term at the wall is described as the source of this excessive generation.

## 4.6 Results and discussions

The suggested numerical scheme and the described methodology for closure model optimization in previous sections are employed to improve the accuracy and reliability of the RANS method in modeling the ABL dispersion flow within compact urban regions. First, the results of the optimization study are presented and discussed. Later, the modified closure is evaluated by comparing its resulting performance measures with ones of the standard model. Finally, the generality of the proposed model is examined by simulating three different case studies.

### 4.6.1 Closure re-calibration

Comprehensive optimization of the  $k - \varepsilon$  model demands the re-calibration of all five empirical coefficients. Given the large size of the computational domain in this work (i.e., full-scale compact urban setting), this process becomes prohibitively expensive in terms of computing time and power. In this regard, taking specific considerations is crucial to make this study more feasible and practical. A reasonable approach to achieve this goal is to reduce the number of variables that require simultaneous tuning. The necessity of maintaining a horizontally homogeneous flow in the atmospheric surface layer encouraged Richards to devise a relationship between the constants of the  $k - \varepsilon$  closure [165]. With this condition, the turbulence model, inflow profiles, and the resulting ground shear due to the aerodynamic roughness would be in equilibrium. Therefore, four out of the five constants ( $C_\mu$ ,  $C_{\varepsilon 1}$ ,  $C_{\varepsilon 2}$ , and  $\sigma_\varepsilon$ ) must take appropriate values to satisfy Equation (4.32). Accordingly, one of these four coefficients can be arbitrarily excluded from the re-calibration process, as it can be determined as a function of the remaining three. Following the recommendation of the previous studies,  $C_{\varepsilon 1}$  was omitted from the optimization process in this work [114, 199].

$$C_{\varepsilon 1} = C_{\varepsilon 2} - \frac{\kappa^2}{\sqrt{C_\mu \sigma_\varepsilon}} \quad (4.32)$$

A further simplification of closure optimization may be possible by investigating

the elementary effects of each coefficient on the objective parameters. To this aim, each constant is varied independently in a predetermined range, while other constants, except for  $C_{\varepsilon 1}$ , are kept at their original values. The preliminary ranges for closure coefficients in this work are specified conservatively based on the previous studies reviewed in Section 4.1 (Table 4.2). Considering 25 equally spaced values within each range, a total of 100 CFD runs was carried out and processed for this part of the study.

Prioritizing the accurate prediction of the concentration field, the elementary effects of input variables (coefficients) on this parameter are presented in Figure 4.5. As it can be deduced, increasing  $C_{\mu}$  leads to more accurate predictions of the concentration field (higher FAC2), while similar arguments cannot be made for the other constants. For instance, higher levels of FAC2 are generally associated with smaller values of  $C_{\varepsilon 2}$ . Ranging  $\sigma_{\varepsilon}$  from 0.3 up to values of approximately 1.15 enhances the model accuracy, whereas its further increase reduces the resulting FAC2. The variation in  $\sigma_k$  within its range exhibits considerably milder but analogous impacts on FAC2 to the ones in  $\sigma_{\varepsilon}$ . As discussed in Section 4.3, despite the undeniable importance of FAC2 as a measure of accuracy, the quality of the predicted concentration field should not be judged solely based on this metric.

For this reason, two linear measures of FB and NMSE for the predicted concentration field, and their logarithmic counterparts, MG and VG, are also included in the objective function. Figure 4.5 displays a drop for both FB and MG as  $C_{\varepsilon 2}$  and  $\sigma_{\varepsilon}$  increase, while opposite trends are shown for  $C_{\mu}$  and  $\sigma_k$ . Given the definition of the validation metrics, smaller amounts of FB and MG indicate stronger scalar dispersion and lower predicted concentrations at sampling points. It is worth noting that a VG greater than 1 and positive values of FB reflect under-predictions of the concentration field. However, due to the unavoidable presence of compensation errors in the calculations of FB and MG, there may be instances of significantly inaccurate predictions in which these metrics take their ideal values. To avoid such a misinterpretation of the

systematic errors, it is necessary to simultaneously calculate and explain NMSE and VG metrics, which also quantify the available random errors (scatter of predictions from measurements) [54]. Lower values of NMSE and VG that correspond to smaller scatters are shown in Figure 4.5 to be gained by larger values of  $C_\mu$  and  $\sigma_k$  within ranges of 0.1 to 0.16 and 0.9 to 1.4, respectively. Conversely, adopting smaller values of  $C_{\varepsilon 2}$  between 1.2 and 2 considerably mitigates the scatters. For  $\sigma_\varepsilon$  ranging from 0.3 to 0.6, the drastic fall of VG compared to the relatively moderate reduction of NMSE suggests that data points with exceedingly low concentrations may have overly influenced this logarithmic measure. Therefore, it is expected that the optimal value of  $\sigma_\varepsilon$  falls within the range of 0.8 to 1.2, which is in agreement with the recommended ranges acquired by analyzing the other validation metrics.

A further examination of Figure 4.5 implies minimal sensitivity of all validation metrics in response to the variation in  $\sigma_k$  compared to the rest of the coefficients. Such observation advocates the exclusion of  $\sigma_k$  from the optimization study to reduce computational expenses. However, the reliability of this decision must be assessed beforehand by quantifying the elementary effects of closure coefficients on output parameters using Equation (4.25). Heat maps are used as shown in Figure 4.6 to qualitatively compare the mean ( $\bar{E}$ ) and standard deviation ( $\sigma_E$ ) of the quantified contribution of each coefficient to the output parameters. By employing this color-coded scheme, we can promptly visualize the relative influence each parameter has on the validation metrics. This approach provides a concise assessment without the need for overwhelming numerical data and could serve as a complementary visualization to the other presented figures in this work. A larger value of  $\bar{E}$  for an input variable suggests its relatively greater net impact on the validation metrics, while a larger quantity of  $\sigma_E$  reflects its highly non-linear response or stronger interaction effects by other input variables on output parameters [191].

As Figure 4.6 implies, the variation in  $C_\mu$  shows the highest order of influence on all validation metrics with the most significant level of interaction effects with other

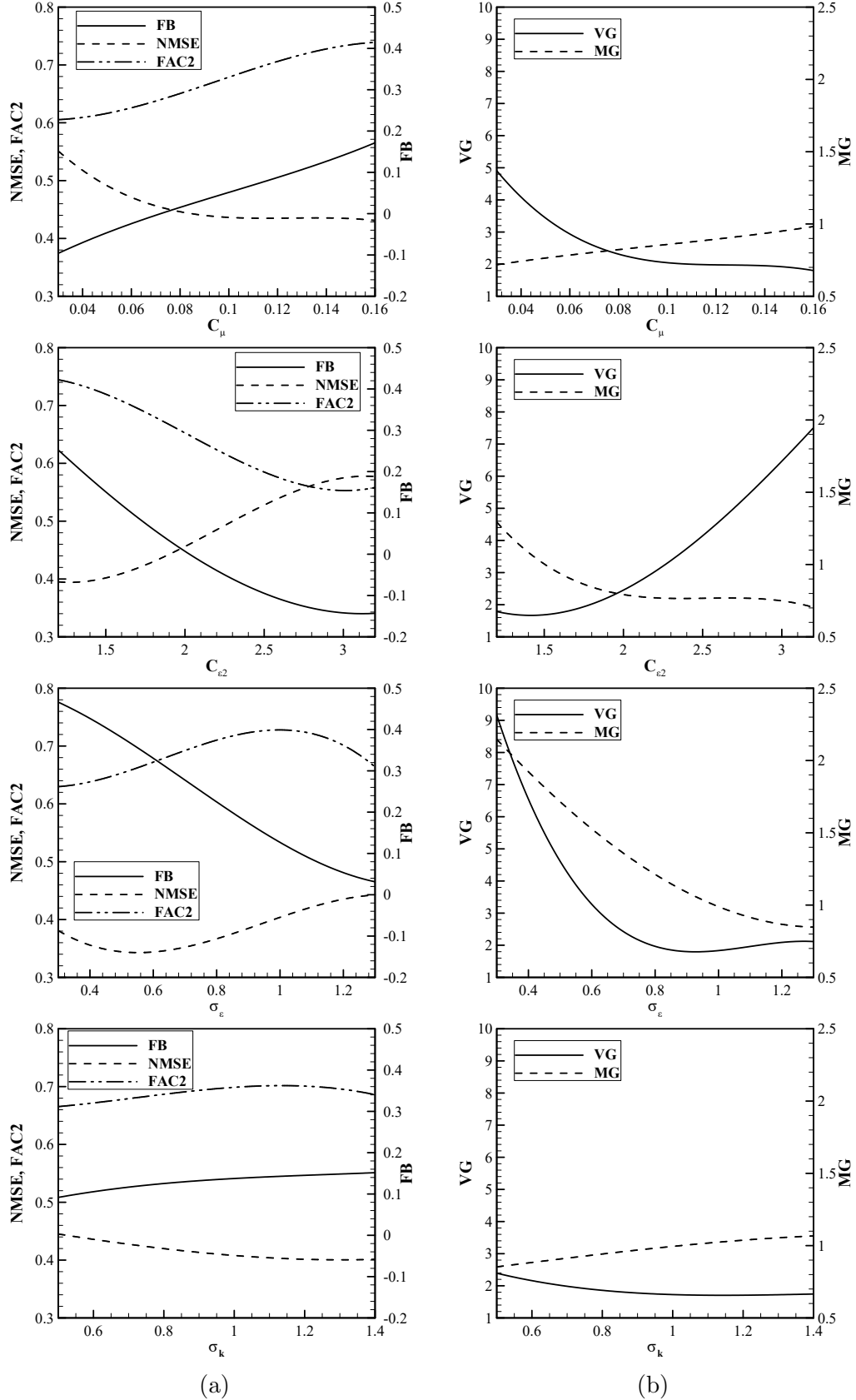


Figure 4.5: Elementary effects of closure coefficients on (a) linear and (b) logarithmic validation metrics.

factors. This remark was expected as  $C_\mu$  not only contributes to the modeled eddy viscosity (Equation (4.9)) and, consequently, scalar diffusion (Equation (4.11)), it also plays a part in the estimation of the inflow TKE profile (Equation (4.27)). The sensitivity of the validation metrics to variation in  $\sigma_\varepsilon$  and  $C_{\varepsilon 2}$  show roughly the same order of significance, which can be categorized as the second and third most influential factors, respectively. Finally, the calculated  $\bar{E}$  and  $\sigma_E$  of the output responses to  $\sigma_k$  variation hold the lowest orders relative to ones of other coefficients. Accordingly, it is reasonable to claim that the validation metrics are considerably less sensitive to  $\sigma_k$ , and this coefficient can be ignored at the optimization step. This statement is moreover supported by some of the previous studies [114, 189]. Given the fact that  $\sigma_k$  does not also correlate with other coefficients through Equation (4.32), its modified value can be obtained later by conducting a direct sensitivity study.

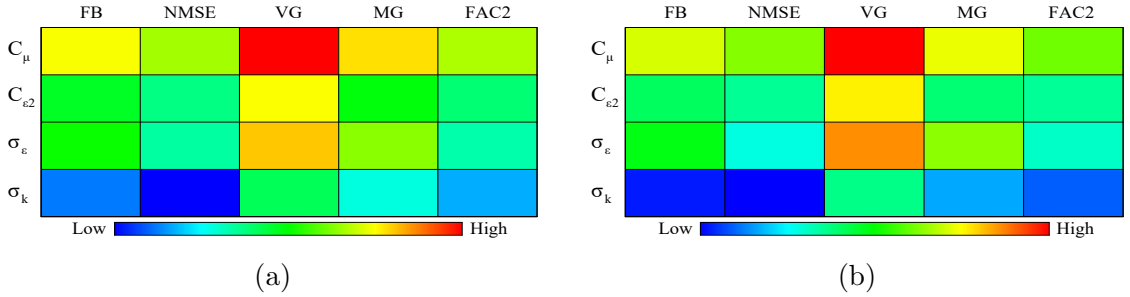


Figure 4.6: Comparing (a)  $\bar{E}$  and (b)  $\sigma_E$  of the elementary effects of closure coefficients on the validation metrics

The distinct responses of the model's accuracy to the variation in each closure constant demonstrate the necessity of implementing a more rigorous approach to navigate towards an optimized set. To this aim, the Monte-Carlo sampling method is used to generate random selections of  $C_\mu$ ,  $C_{\varepsilon 2}$ , and  $\sigma_\varepsilon$  within their associated ranges, while  $C_{\varepsilon 1}$  is estimated by Equation (4.32), and  $\sigma_k$  is kept at its standard value of 1. Given the definition of the proposed objective functions (Equations (4.24) and (4.25)), the GA optimization scheme aims at revising these ranges after each main iteration to detect ones in which the model coefficients collectively correspond to a minimum

value of  $O_{f2}$ . Uniform distributions of probability are assumed for all coefficients in their variation ranges, and 40 sample sets are generated randomly to produce the initial population for the optimization process.

Figure 4.7 reveals scatter plots presenting the PDFs of FAC2 and HR for the predicted concentration and TKE fields, respectively. These plots offer valuable insights into the variation and distribution of these metrics across the last 100 investigated coefficient sets during the re-calibration process. As can be seen, both the concentration and TKE fields exhibit noteworthy sensitivity to the variations among coefficient sets, which are evidenced by the widespread and diverse clustering of data points in the provided PDFs. The observed similarity and consistency between both the output responses (i.e., FAC2 and HR), further attest to the strong dependency of the predicted concentration field on the accuracy of the predicted TKE field, which justifies the definition of the objective function as described in Section 4.3.

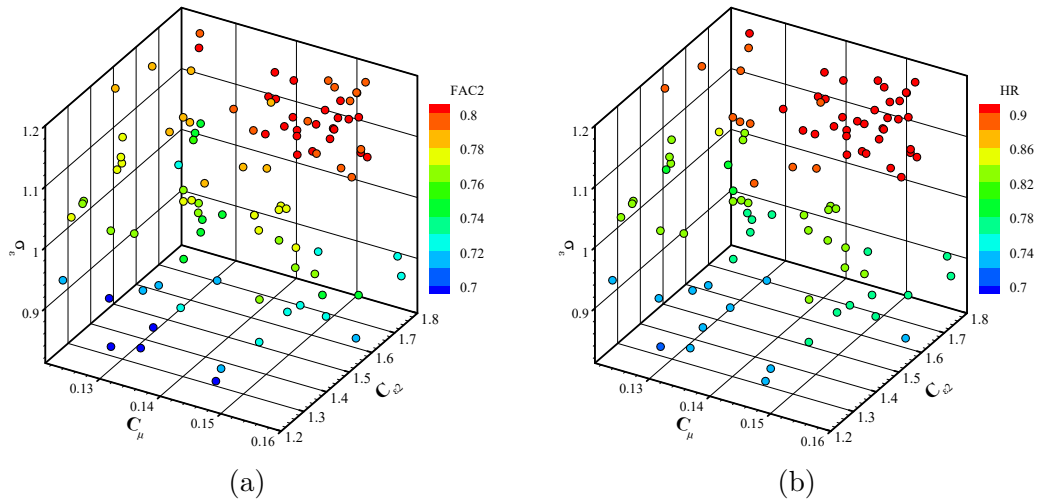


Figure 4.7: Variation of validation metrics during the re-calibration (a) FAC2 for pollutant concentration and (b) HR for TKE.

To better investigate the dependency of the model’s output responses on closure sets, Figure 4.8 illustrates surface plots of FAC2 resulting from variations in the considered closure constants during the re-calibration process. As can be concluded, higher fractions of predictions within FAC2 of measurements are generally achieved

for quantities of  $C_\mu$  ranging from 0.13 to 0.16. Increasing  $C_\mu$  from its standard value of 0.09 could result in relatively lower eddy viscosity and inflow TKE to be estimated, which could remediate the known flaw of the standard  $k - \varepsilon$  model: excessive over-prediction of the TKE [11]. The shown results in Figure 4.8 further suggest that decreasing  $\sigma_\varepsilon$  from its original value of 1.3 increases the probability of acquiring predictions with overall higher associated FAC2. Lower quantities of this constant basically result in promoting the diffusive transport of the rate of viscous dissipation; however, a general conclusion cannot be drawn due to the complex linked relationship of the TKE and  $\varepsilon$  and the heavy modeling applied to Equation (4.8) [72]. The optimal values of  $\sigma_\varepsilon$  vary between 1 and 1.2.  $C_{\varepsilon 2}$  appears as a factor for the sink term available in the  $\varepsilon$  transport equation and is expected to substantially affect the predicted turbulence field and, consequently, the resulting pollutant concentration field. The most accurate representation of the pollutant concentration field for the generic case of a compact urban setting is shown to be obtained by smaller values of  $C_{\varepsilon 2}$  than its standard value, differing between 1.6 and 1.8.

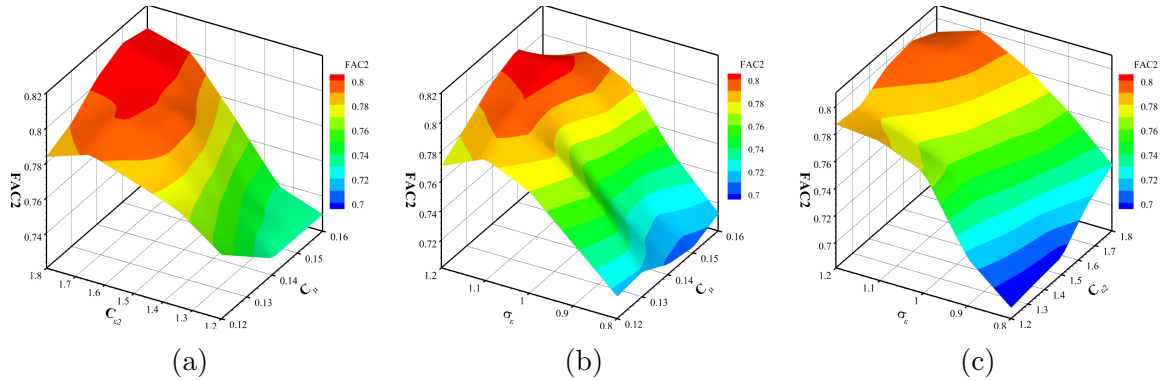


Figure 4.8: Surface plots of FAC2 variation for pollutant concentration field during the calibration process.

The quality of the predictions within the detected ranges for closure constants that contribute to the highest calculated FAC2 should be further examined. In this regard, the concentration-related output responses of the remaining validation metrics to different sets of closure coefficients are presented in Figure 4.9. Noting that the

calculated NMSE remains well inside the acceptable limits and near its ideal value ( $0.35 \leq \text{NMSE} \leq 0.55$ ), it was decided to mainly focus on the FB, VG, and MG metrics and omit the NMSE variation contours in this paper. As can be seen, both the linear and logarithmic measures of the model's systematic errors (i.e., FB and MG, respectively) exhibit roughly similar trends in response to the closure modification.

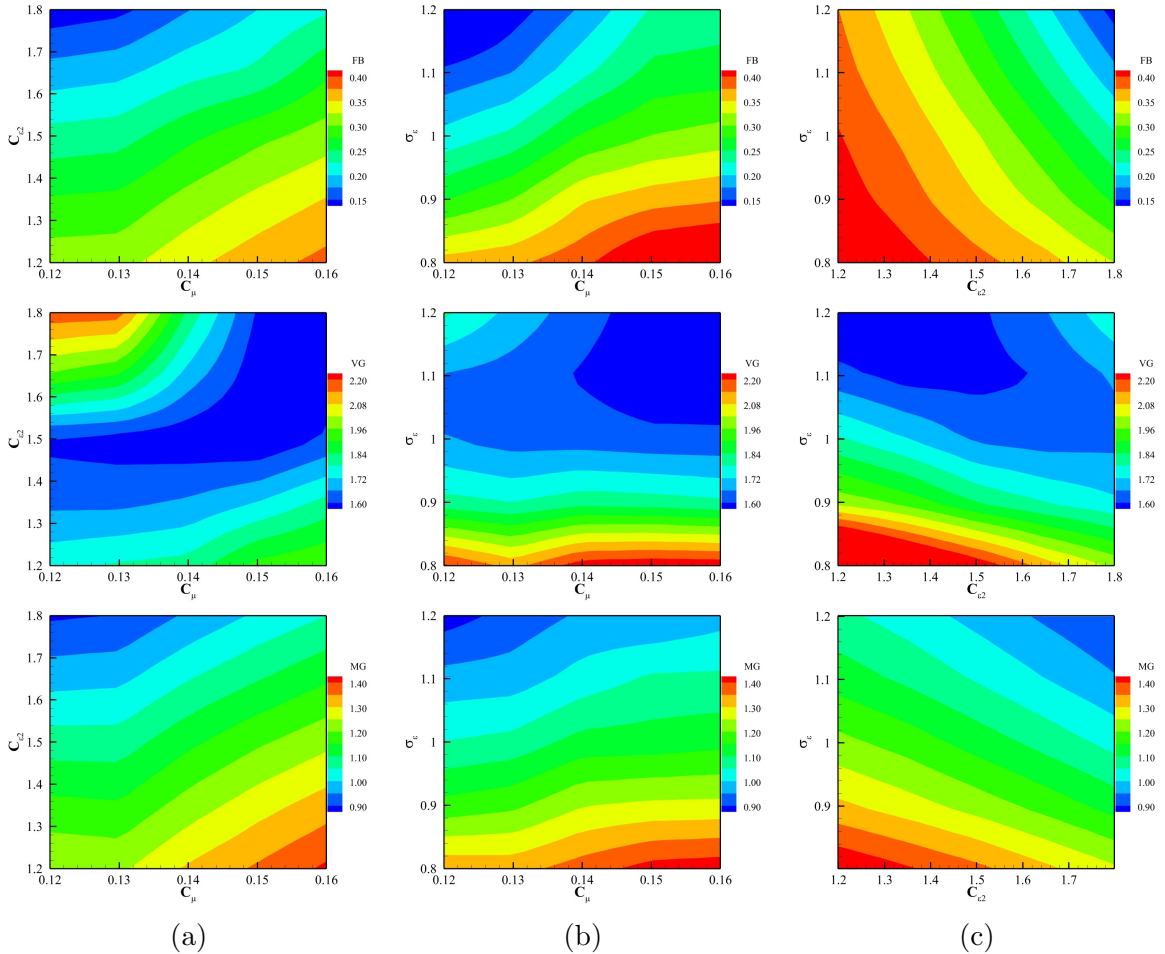


Figure 4.9: Variation of FB, VG, and MG for pollutant concentration field during the calibration process.

The analysis of Figure 4.9 suggests that the most desirable measures of FB and MG are attained as  $C_\mu$  takes values between 0.12 and 0.15, while  $1.68 \leq C_{\epsilon 2} \leq 1.80$  and  $1.12 \leq \sigma_\epsilon \leq 1.20$ . The variation in FB and MG within the given ranges reflects an overall under-prediction of the concentration field compared to the observations. On the other hand, evaluation of the resulting scatter from measurements (i.e., VG)

identifies the optimal ranges of coefficients as  $0.14 \leq C_\mu \leq 0.16$ ,  $1.50 \leq C_{\varepsilon 2} \leq 1.80$ , and  $1.05 \leq \sigma_\varepsilon \leq 1.20$ . These findings further emphasize the importance of collectively assessing the validation metrics, as well as the synergistic effects of closure coefficients on model outputs. The optimal ranges can be extracted from the intersections of the identified spans to ensure the greatest reliability of predictions (FAC2). The proposed ranges in this work are  $0.14 \leq C_\mu \leq 0.15$ ,  $1.68 \leq C_{\varepsilon 2} \leq 1.80$ , and  $1.12 \leq \sigma_\varepsilon \leq 1.20$ , in which a closure set of  $C_\mu = 0.147$ ,  $C_\varepsilon = 1.344$ ,  $C_{\varepsilon 2} = 1.693$ , and  $\sigma_\varepsilon = 1.196$  produces the most accurate and reliable predictions.

The optimal value of  $\sigma_k$  is successively derived by conducting a sensitivity study using the standard  $k - \varepsilon$  model in which the modified coefficients are implemented. As expected, all the output parameters demonstrate relatively weak sensitivity to the variation of this coefficient, with FAC2 being the least responsive (Figure 4.10). Increasing  $\sigma_k$  weakens the diffusive transport of TKE, consequently leading to larger turbulence mass diffusivity (i.e.,  $D_t$ ). This behavior of  $D_t$  enhances the under-prediction of the pollutant concentrations at the plume centerline, which justifies the consistent increase in FB shown in Figure 4.10a. Considering all the validation metrics together while prioritizing FAC2 (i.e., the model's accuracy), the range of  $0.87 \leq \sigma_k \leq 1.00$  is suggested, with  $\sigma_k = 0.927$  being the optimal value.

#### 4.6.2 Performance and generality evaluation

The performance of the improved closure model with the proposed coefficient set ( $C_\mu = 0.147$ ,  $C_{\varepsilon 1} = 1.344$ ,  $C_{\varepsilon 2} = 1.693$ ,  $\sigma_\varepsilon = 1.196$ , and  $\sigma_k = 0.927$ ) is evaluated in this section. Figure 4.11 depicts the iso-surfaces of pollutant concentration ( $C^* = 10^{-2}$ ) flooded by TKE contours that were predicted by all the considered revisions of the  $k - \varepsilon$  turbulence model. Even though the overall form of the predicted plume by both the optimized and standard turbulence closures display roughly similar shapes due to the interactions between flow and structures, the predicted volumes of the selected iso-surface exhibit clear differences. As for the TKE, the proposed model in

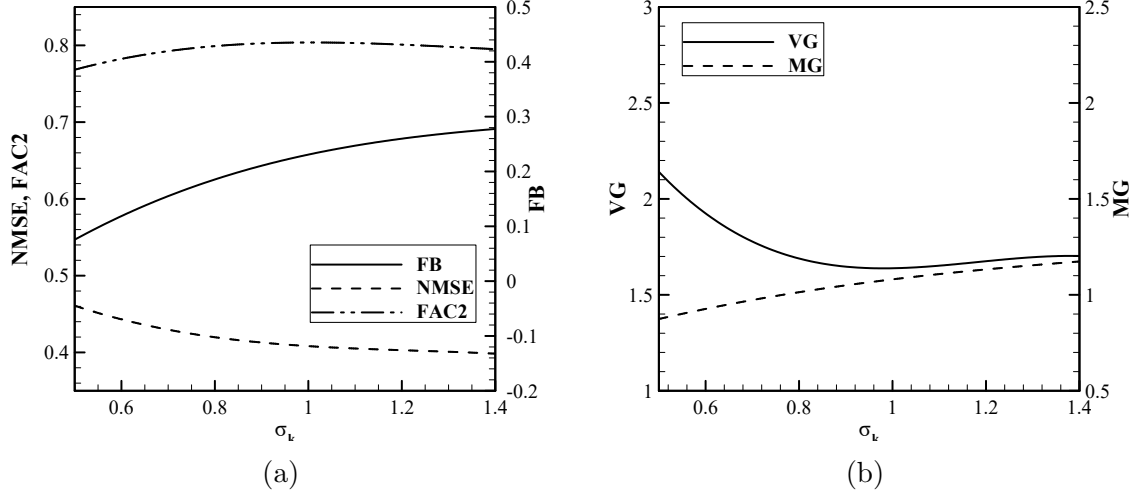


Figure 4.10: Sensitivity of the (a) linear and (b) logarithmic validation metrics to the variations of  $\sigma_k$

this work resulted in considerably lower values compared to the other revision (i.e., the standard version). The distinct differences observed among these models highlight the necessity of such re-calibration practices and lays the foundation for a more meticulous investigation of their performances. In this regard, rigorous statistical comparisons are subsequently required to further elucidate the strengths and weaknesses of the studied models.

The validation metrics of the predicted concentration field by all revisions of the standard  $k - \varepsilon$  are calculated and presented in Table 4.5. The most accurate reproduction of the concentration field was obtained using the optimized closure in this work, with 80% of the predictions within FAC2 of measurements. Evaluating all validation metrics together, the decisive superiority of the optimized closure for the generic case of a compact urban setting is apparent. The positive quantities of FB show the general under-prediction of the concentration field using all these revisions. The presented MG values further support this observation. Considering FB values of 0.13 and 0.21 by the original and optimized versions, respectively, these models demonstrate slight under-predictions of the concentration field. In terms of the recorded scatters, the optimized model in the current study strongly outperforms

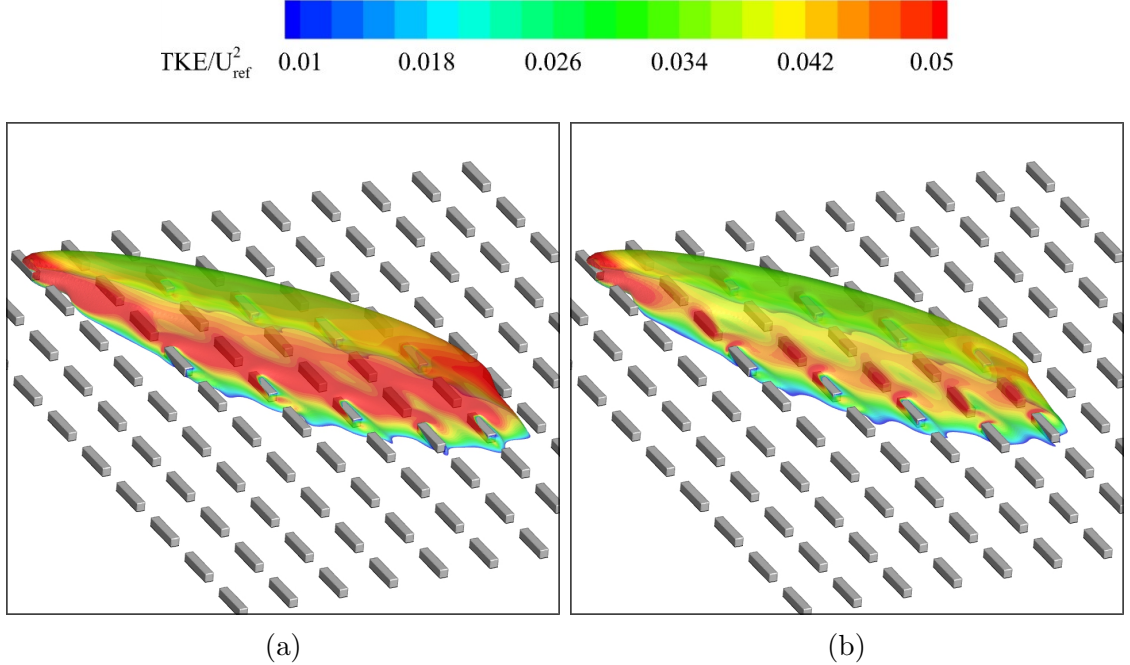


Figure 4.11: Normalized concentration iso-surfaces ( $C^* = 10^{-2}$ ) flooded with TKE, predicted by (a) standard, and (b) optimized revision of  $k - \varepsilon$  turbulence model.

the other revision with  $VG = 1.63$ .

Table 4.5: Performance evaluation of the modified closure model in predicting the pollutant concentration field.

Closure revision	FB	NMSE	MG	VG	FAC2
Standard [97]	0.13	0.41	0.98	1.82	0.72
Current study	0.21	0.40	1.05	1.63	0.80

A more rigorous interpretation of statistical measures in Table 4.5 is possible by analyzing the predicted concentration profiles throughout the domain. Figure 4.12 maps the concentration field at four horizontally distributed sampling lines. The original and optimized models over-predict the concentrations at the first two sampling lines. As the plume progresses downstream, the intensity of over-prediction decreases gradually until concentrations are entirely under-predicted at sampling line 4. It is also worth mentioning that the variation in the field measurements along the horizontal line closely resembles the profiles generated by the present optimized model.

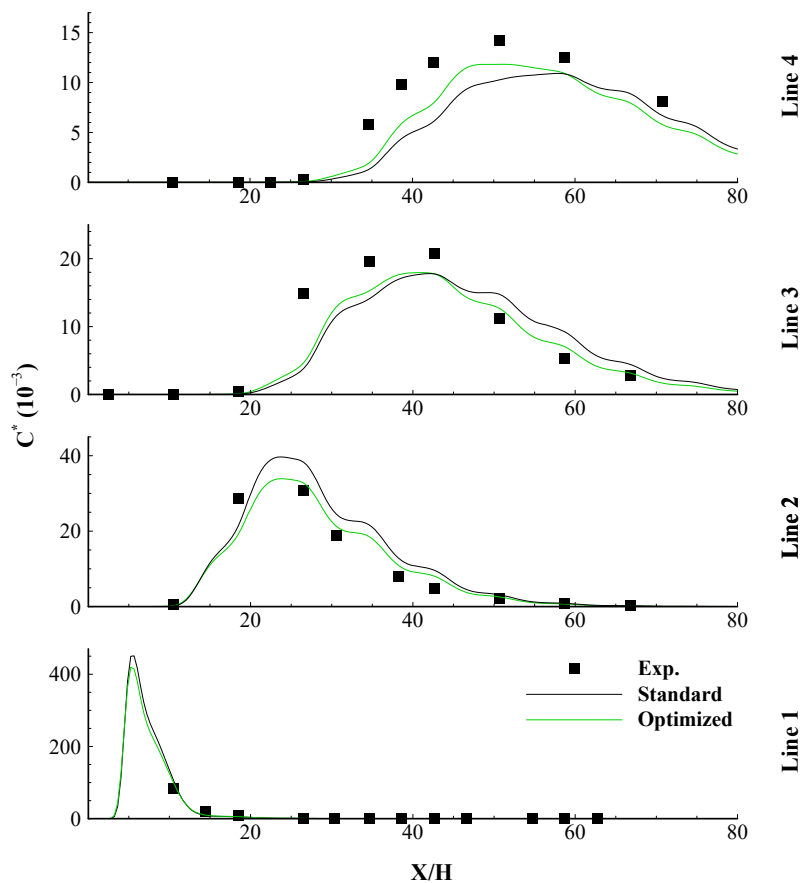


Figure 4.12: Comparison of the predicted concentration fields at horizontal sampling lines.

The predicted vertical profiles of pollutant concentrations are shown and compared in Figure 4.13. Given the direction of the upstream wind flow, two towers,  $T_A$  and  $T_D$ , did not detect any tracer quantities and were, thus, excluded from this study. As illustrated, the optimized model predicts relatively lower concentration levels along the vertical sampling lines, resulting in improved agreements with the field measurements. It should also be noted that the reproduced plume by the optimized models successfully exhibits the expected Gaussian shape as it passes through the selected vertical lines. To further evaluate the overall capability of the proposed model, a scatter diagram for all 74 sampling points is presented in Figure 4.14. The improved accuracy of the predictions by the optimized model is apparent by showing smaller scatters, which further supports the lowest calculated VG of 1.63 (Table 4.5). In

addition to sampling points with higher concentrations (near the source and plume centerline), the profound improvement in predictions for points with lower concentrations (near the plume’s edges and far from the source) is also evident, which implies a more accurate reproduction of the pollutant spread throughout the domain. As a result, a greater fraction of predictions is shown between the FAC2 lines using the optimized model, with almost no data point outside the FAC5 lines.

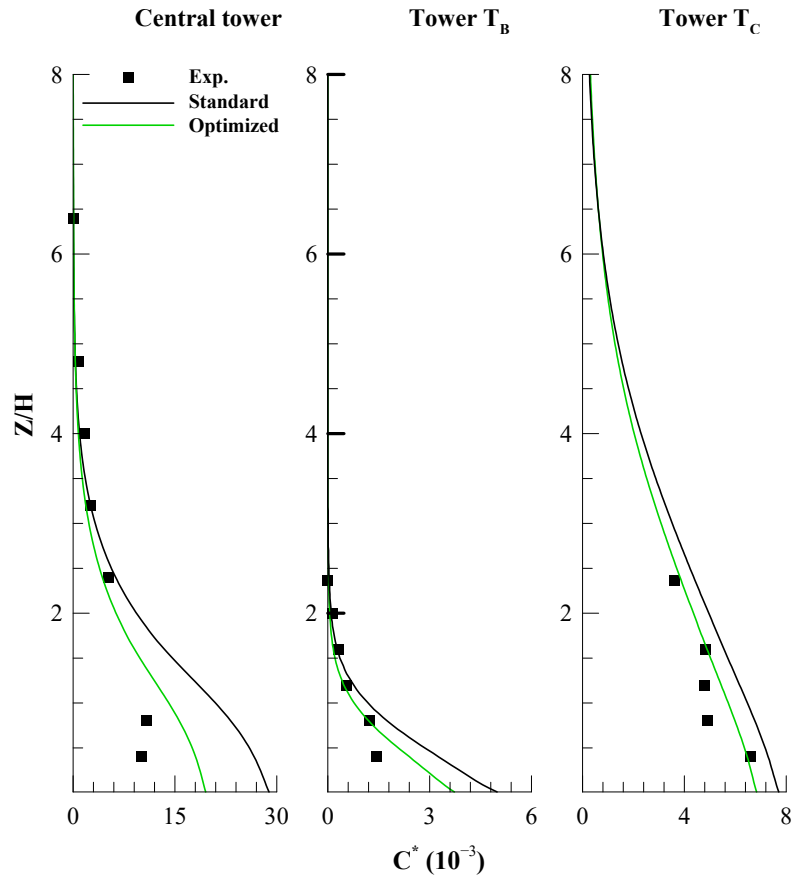


Figure 4.13: Comparison of the predicted concentration fields at vertical sampling lines.

The capability of the proposed coefficient set in capturing the wind and turbulence fields must also be examined to ensure the reliability of predictions exhaustively. Table 4.6 compares the calculated validation measures for both the predicted velocity and TKE fields obtained by optimized and standard versions of the  $k - \varepsilon$  model. As previously discussed in Section 4.3, FAC2 is not an adequately strict metric for this

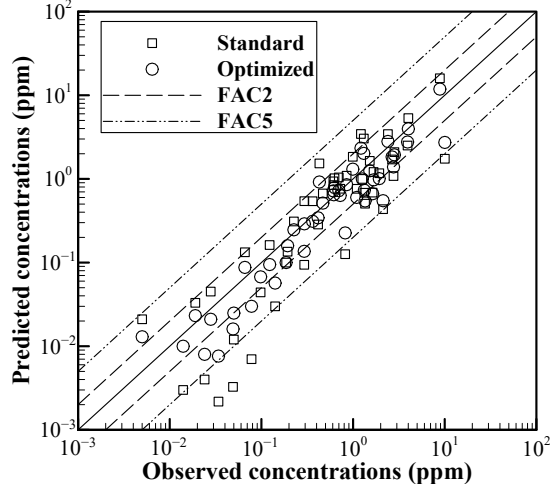


Figure 4.14: Scatter plot between the observed and predicted concentrations at all sampling points for standard and optimized closure sets.

part of the evaluation study and is replaced by HR. It should also be noted that the measurements of one of the sensors of tower T<sub>A</sub>, both sensors of tower T<sub>D</sub>, and one sensor of the upstream mast S are missing from the MUST data set and therefore are excluded from calculations. In terms of the flow field, approximately similar performances by both models are observed, with validation metrics well within the acceptable ranges. The predicted velocity fields are slightly overestimated (negative values of FB and MG below 1), and quantities of NMSE and VG suggest low scatter. A minimum HR of 66% is required to consider predictions as valid, which is obtained by all models.

As is expected, implementing different versions of coefficient sets leads to contrasting representations of the turbulence field. As suggested by the validation metrics, the standard revision of the  $k - \varepsilon$  coefficient sets substantially overestimates TKE compared to the optimized model. The cross-comparison of the considered coefficient sets and their associated impacts on the model's outputs argue that large values of  $C_{\varepsilon 1}$  might be the most influencing factor in TKE over-prediction. The appearance of a greater quantity of  $C_{\varepsilon 1}$  in the form of a factor to the source term in Equation (4.8), promotes the production of  $\varepsilon$ . Considering the coupled relationship of Equations (4.6)

and (4.8), it is expected that the production rate of TKE is large where its dissipation rate is large [68], which justifies considerably lower values of TKE predicted by the optimized set in this work compared to ones obtained by the standard version.

Table 4.6: Performance evaluation of the modified closure model in predicting the velocity and TKE fields for the training case study.

<b>Closure revision</b>	<b>Velocity</b>				
	<b>FB</b>	<b>NMSE</b>	<b>MG</b>	<b>VG</b>	<b>HR</b>
Standard [97]	-0.03	0.03	0.93	1.05	0.72
Current study	0	0.03	0.96	1.04	0.78
	<b>TKE</b>				
	<b>FB</b>	<b>NMSE</b>	<b>MG</b>	<b>VG</b>	<b>HR</b>
Standard [97]	-0.15	0.05	0.87	1.04	0.67
Current study	-0.03	0.02	0.98	1.02	0.94

The qualitative examination of the predicted turbulence field can be carried out by investigating the resulting TKE profiles at several locations within the building array. Figure 4.15 depicted the vertical variations of TKE at two different sample locations: at the center of the array (central tower) and on tower  $T_C$ , positioned nine rows into the array. It is worth noting that the predicted TKE fields show major dissimilarities at lower elevations, where the flow is primarily affected by the presence of objects, but they asymptotically converge as the array’s influence disappears aloft. Figure 4.16 is provided to facilitate a point-to-point comparison and evaluation of the predicted flow field parameters using the standard and optimized  $k - \varepsilon$  models at the 18 measuring points (which has measurements) spread across the MUST test domain. The statistical data for the predicted velocity field presented in Table 4.5 are further supported by Figure 4.16a, showcasing insignificant differences between the performances of these two models. Furthermore, a clear trend is observed for both the velocity and TKE, implying that the standard version of the turbulence model generally returns higher values of these parameters. The considerable difference in the predicted TKE values, despite what is noted for the velocity field, highlights

the ample improvement achieved by the optimized model in the predictions. As was already mentioned, TKE plays a pivotal role in the accurate representation of the concentration field through the definitions of the eddy viscosity,  $Sc_t$ , and consequently, the eddy diffusivity. This improved agreement can be attributed to the optimized model's ability to represent turbulent mixing and dispersion more accurately, resulting in a more realistic depiction of the concentration distribution in the flow field.

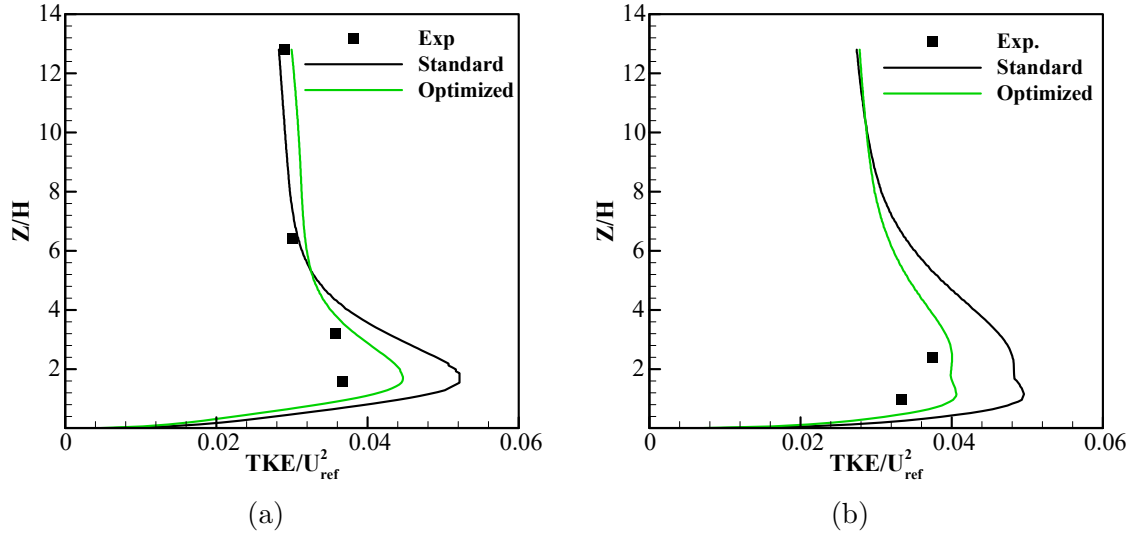
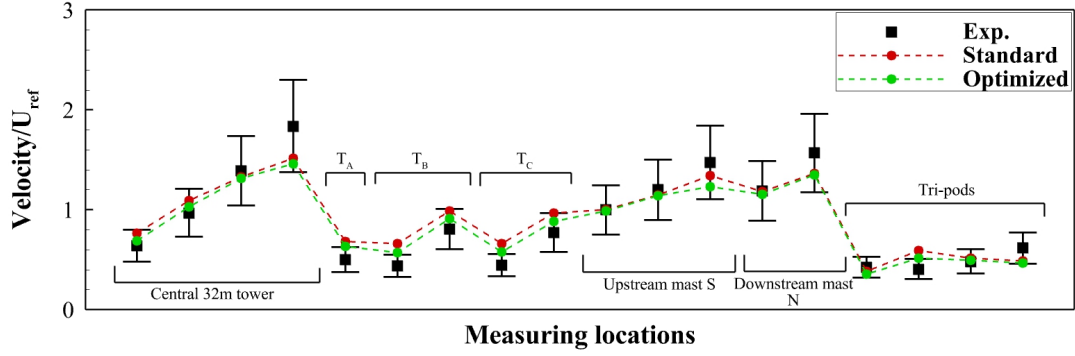
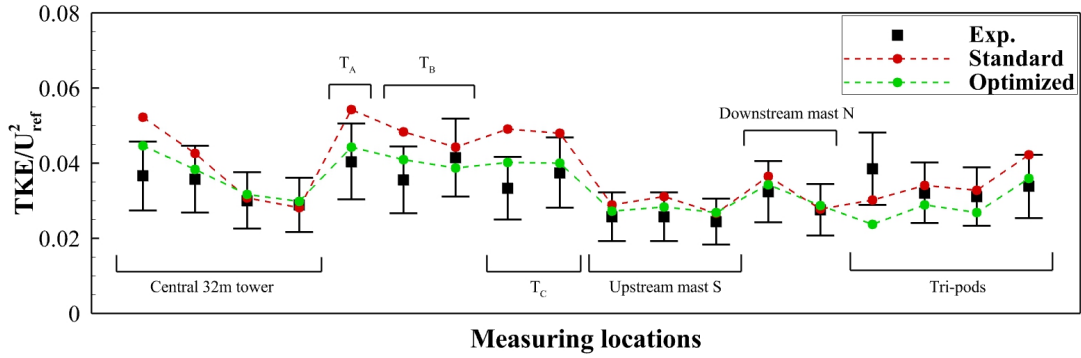


Figure 4.15: Vertical profiles of the predicted TKE (a) at 32 m central tower and (b) at the tower  $T_C$ .

As for the final step of this optimization study, the generality of the proposed set must be tested prior to claiming its utility. To this aim, three test cases are considered (Table 4.4), in which the performance of the optimized model is comparatively evaluated. As can be seen, all the test cases are selected to cover a diverse range of situations in terms of the tracer source type and location, array orientation, mean wind speed, and atmospheric condition. Referring to Figure 4.1b, the source in the training case is roof-based (i.e., type D) and positioned on container J9. For the test cases of TC-1, TC-2, and TC-3, the sources are, respectively, located between containers K8 and L8 (type F), 24 m upstream of container L1 (type E) and immediately upstream of container J3 (type A). In order to consider the distinct array orientations, cases with different incident directions of wind flow that generate unique flow structures



(a)



(b)

Figure 4.16: Point-to-point evaluation and comparison of the predicted flow field across the test domain: (a) Velocity, (b) TKE. The error bars represent a 25% deviation from the experimental measurements.

are chosen. The precise prediction of the scalar concentration field strongly depends on the accurate reproduction of flow and turbulence fields [10]. Therefore, by defining these test cases, opportunities to assess the extent of the applicability of the developed coefficient set were created. To further explore the limitations and uncertainties associated with the proposed framework, two atmospheric stability classes of fully neutral (TC-1), and stable near neutral (TC-2 and TC-3) are considered. Detailed evaluation studies are carried out for all three test cases, for which the corresponding statistical measures are given in Table 4.7.

The analysis of the presented data demonstrates the validity of the predicted flow fields in all test cases. However, consistent with our earlier statements, the reproduced velocity fields demonstrate minimal sensitivity to the modification of the closure co-

Table 4.7: Validation metrics for three selected test cases during the generalizability study.

Case	Revision	Velocity				
		FB	NMSE	MG	VG	HR
TC-1	Standard	-0.09	0.02	0.91	1.03	0.78
	Optimized	-0.07	0.01	0.94	1.03	0.89
TC-2	Standard	0.13	0.08	1.03	1.07	0.67
	Optimized	0.15	0.06	1.05	1.07	0.72
TC-3	Standard	0.25	0.30	1.07	1.16	0.78
	Optimized	0.26	0.28	1.09	1.15	0.78
		TKE				
		FB	NMSE	MG	VG	HR
TC-1	Standard	0.05	0.03	1.07	1.05	0.83
	Optimized	0.09	0.01	1.09	1.01	0.94
TC-2	Standard	0.13	0.04	1.07	1.08	0.72
	Optimized	0.18	0.01	1.11	1.02	0.89
TC-3	Standard	0.08	0.03	0.97	1.06	0.83
	Optimized	0.11	0.01	1.02	1.02	1.00
		Concentration				
		FB	NMSE	MG	VG	FAC2
TC-1	Standard	0.11	0.68	1.08	2.11	0.64
	Optimized	0.18	0.58	1.10	1.93	0.69
TC-2	Standard	0.12	0.47	1.10	1.52	0.70
	Optimized	0.19	0.45	1.17	1.41	0.76
TC-3	Standard	0.10	0.59	1.12	2.03	0.67
	Optimized	0.16	0.50	1.14	1.84	0.71

efficients. The same argument does not hold for pollutant concentration and TKE fields. Concerning TKE, the modified closure achieves noticeable enhancements in the accuracy and quality of predictions. In line with the output responses of the training case, a relatively more intense under-prediction of TKE by the optimized closure is observed, which has resulted in relatively higher quantities of FB and MG. The slightly higher levels of FB and MG, however, have modified the predictions in a manner that has led to smaller overall scatters (lower VG and NMSE) and raised

HR in all three test cases. Having a more accurate and reliable representation of the flow and turbulence parameters, an improvement in the predicted concentration field is consequently expected.

Any changes to solutions for Equations (4.6) and (4.8) (i.e., using a revised coefficient set) modify the estimated eddy viscosity ( $\nu_t$ ) and, accordingly, the turbulence mass diffusion ( $D_t$ ) in Equation (4.10). Additionally,  $D_t$  is also affected by the definition of  $Sc_t$  in this work (i.e., Equation (4.13)), which shows an explicit dependency on the local characteristics of turbulence. These contributions result in strong sensitivity of the predicted concentration field to different editions of closure constants, which is established by the presented data in Table 4.7. The evaluation of the validation metrics together exhibits an overall boost in the quality and reliability of predictions for the three test cases. Therefore, the potential applicability of the trained closure set for time-averaged modeling of atmospheric dispersion flow in compact urban settings is attested.

## 4.7 Conclusion

In an effort to improve the accuracy of the steady atmospheric dispersion modeling in the context of a compact urban setting, a re-calibration study is carried out on the empirical constants of the standard  $k - \varepsilon$  model. To this aim, in addition to the flow parameters (velocity and TKE), the pollutant concentration field is also selected as the parameter of focus, implemented through the definition of five different validation metrics (three linear and two logarithmic). An optimization scheme based on the GA algorithm is adopted here with some modifications to systematically select sets of coefficients from predetermined ranges to evaluate and eventually identify variation spans with the highest associated model's accuracy. The comprehensive and high-quality dispersion data set of full-scale field measurements in an urban-like geometry (i.e., the MUST experiment) was used to re-calibrate the model constants. In order to evaluate the performance of the optimized closure, the quality of predictions for

concentration, velocity, and TKE fields are further compared with the ones of the standard model. Finally, the general applicability of the modified set to other cases is examined by modeling three distinctive test cases with different inflow velocities, source locations, building orientations, and atmospheric states. The main steps and key findings of this study can be summarized as follow:

- Considering the large size of the model, making specific arrangements is essential to alleviate the associated computational costs. In this regard, the established relationship among  $C_\mu$ ,  $C_{\varepsilon 1}$ ,  $C_{\varepsilon 2}$ , and  $\sigma_\varepsilon$  within the atmospheric surface layer is utilized to omit  $C_{\varepsilon 1}$  from the optimization study, as it can be calculated using the other three constants.
- A screening method was used to quantify each constant's direct and interactional effects on the validation metrics. As suggested by the results, the model's outputs reflect a relatively minimal sensitivity to  $\sigma_k$ , which justifies the decision to exclude this coefficient from the optimization step and find its optimal value later through a simple sensitivity study.
- The rigorous analysis of all validation metrics together, while prioritizing achieving the highest quantities of FAC2, has led to recommending the optimal ranges for the generic case of a compact urban setting as follows:  $0.14 \leq C_\mu \leq 0.15$ ,  $1.68 \leq C_{\varepsilon 2} \leq 1.80$ ,  $1.12 \leq \sigma_\varepsilon \leq 1.20$ , and  $0.87 \leq \sigma_k \leq 1.00$ .
- Given the proposed ranges in this work, a closure set is found to generate predictions that agree best with the selected field measurements of this study, which consists of  $C_\mu = 0.147$ ,  $C_\varepsilon = 1.344$ ,  $C_{\varepsilon 2} = 1.693$ ,  $\sigma_\varepsilon = 1.196$ , and  $\sigma_k = 0.927$ .
- An exhausting assessment of the statistical measures resulting from the comparative study indicates that the optimized closure significantly outperforms the

other revision in reproducing the concentration and TKE fields, while both editions yield roughly similar results for the velocity field. Relative to predictions by the standard model, the FAC2 for the concentrations (among 74 sampling points) and HR for the TKE field (among 18 sampling points) are increased by 8% and 27%, respectively.

- The investigation of the general applicability of the proposed modifications suggests that except for the predicted velocity field, in which only minor improvements are observed, the closure model successfully enhances the quality and reliability of predictions for concentrations and the TKE field in all three test cases.

# Chapter 5

## Unravelling the synergistic effects of urban morphological characteristics on dilution of air pollution emitting from roof-based sources in proximity of the fresh air intakes

### 5.1 Introduction

The burgeoning world population and subsequent surge in urbanization have given rise to a pressing concern regarding the outdoor air quality in urban areas and its detrimental effects on public health. The gravity of this problem has initiated numerous works of research to direct our efforts toward effective approaches for promoting outdoor ventilation. Responding to this developing concern, specialists are actively investigating novel approaches to address air pollution and enhance the urban living environment. Given the complexity of urbanization and its effects on air quality, there is a growing necessity to delve into inventive methods for pollution control. Recent studies generally classify these fast-developing strategies into two main categories, namely the active and passive methods [24].

The active strategies refer to any attempt to exploit mechanical factors to reduce the pollutant concentration levels within areas of interest (e.g., street canyons,

vicinity of fresh air intakes, etc.). Broadly speaking, the active countermeasures comparatively encompass a wider variety of methods and often require energy provision and frequent human interference to operate efficiently. Examples are properly designing and operating the ventilation stacks to adequately disperse exhaust gases to the upper part of the atmosphere and to reduce the probability of their introduction into the built regions at unsafe concentrations [67]; using catalytic converters that break down air-contaminant chemical structures and transfer them into less harmful particles [200]; employing pollutant sinks such as electrostatic precipitators (ESP) at sensitive locations to electrically charge the available particles in the air and remove them by leveraging the electrostatic attraction principle [148]; planting green barriers to filter out pollutants from the air and to absorb carbon dioxide [109] and even imposing targeted regulations and demanding structural modifications to alleviate traffic and industrially generated air pollution [201].

While the effectiveness of such active methods is undeniable, they are associated with some drawbacks. For example, air pollution devices generally consume additional energy and can be quite sensitive to the environment's meteorological conditions (humidity, airflow speed, etc.), enforcing regulations may encounter public resistance and investment challenges, or exploiting the vegetation capability in this context does not offer immediate improvement and even may degrade urban air quality in some cases by reducing the local wind speed and ventilation rates [148].

As for passive strategies, effective manipulation of the urban morphological indices could immensely enhance the capability of the geometry in dispersing outdoor air pollution [15]. The recognition of the undeniable impact that urban structures and arrangements exert on the complex dynamics of atmospheric turbulence and dispersion flow has accentuated the need for strategic interventions in urban planning. A detailed survey of the relevant literature suggests that there are several geometric factors associated with urban layouts that have the most noticeable impacts on their dilution potential, such as planar density, planar non-uniformities (i.e., het-

erogeneities), urban setting orientation, and even the pollutant source location [3, 202, 203]. Therefore, carrying out a series of parametric investigations to assess the resulting dispersion patterns within generic forms of building arrangements holds substantial benefits for urban planning practices.

Many studies have explored how urban morphologies impact wind flow and pollutant dispersion within idealized and regularly aligned building arrays, yielding valuable and fundamental insights. An et al. numerically modeled idealized urban areas with different configurations to study the influence of the building separations on the accumulation of traffic-originated pollutants within street canyons [110]. As a general outcome, they observed a positive correlation between the array permeability and air quality within the pedestrian level (height below 2m), a conclusion supported by findings from several other studies [128, 129, 153]. However, regardless of the permeability levels, the ultimate state of air quality has been repeatedly shown to be heavily influenced by the specific formation of the array and its other geometric characteristics [44, 130, 204]. Furthermore, the idealized and aligned building arrays represent the most simplified forms of urban forms which are quite scarce, as the actual urban forms are completely heterogeneous. The presence of non-uniformities leads to much more complex flow and turbulence structures compared to regularly aligned arrays, entailing the extension of urban studies to include such cases [131].

In recent years, there have been limited studies focused on exploring the characteristics of atmospheric airflow within non-uniform idealized building arrays ([117, 132]) or realistic urban regions with unique terrain features ([110, 142]), with even fewer addressing the pollutant transport. Considering a staggered array effectively introduces deliberate and systematic non-uniformities in the generic urban forms under study, which facilitates investigating the influence of planar heterogeneities [124]. Bady et al. [205], compared the resulting flow fields of two cases with aligned and staggered arrays. They claimed that the former arrangement generally promotes breathability within the pedestrian level when the wind direction is perpendicular to the disposi-

tion line, while the latter performed relatively better in cases with a 45-degree wind direction of incidence. However, further investigation of the fundamentally distinct flow structures due to the array arrangements by Shen et al. [206] indicated stronger dilution of the pollutant stream within the staggered arrangement. This finding was in agreement with the conclusion of Goulart et al. which attested to the stronger outflow pollutant flux from urban canopies in staggered layouts [134]. One possible explanation for such conflicting statements on the impact of the staggered arrays might be the different planar densities considered in the aforementioned efforts. The synergistic effects of building spacing and disposition levels have the potential to drastically alter the mean and turbulent flows and subsequently lead to either pollutant accumulation or mitigation around the buildings. This further emphasizes the imperative for carrying out an in-depth and rigorous examination of the collective influence of geometric factors on pollutant dispersion flow. Such comprehensive analyses are conspicuously lacking in the existing literature, highlighting a timely need for their inclusion.

The direction of the incident wind (i.e., the urban setting orientation) has also been shown to significantly influence the mean flow and its state of turbulence within and around a group of buildings [133]. Hence, one expects the different wind directions to substantially affect the spatial distribution of the scalar pollutant. Prior attempts have predominantly focused on a single generic form of urban settings (for instance, arrays with a constant planar density or an extreme disposition level), missing the comprehensive examination of the wind direction effects in conjunction with arrays exhibiting a wide range of geometric parameters [207, 208]. Furthermore, most of the available systematic surveys into pollutant dispersion patterns are centered around the standard scenario of wind incidence perpendicular to the frontal face of the arrays [135, 209, 210]. These endeavors, while invaluable, overlook the complexity and significance of the possible flow patterns that emerge due to varying wind directions and their simultaneous interaction with diverse morphological indices.

Moreover, the majority of former investigations have either considered near-field or far-field dispersion of pollutants emitting from ground-based sources that respectively encompass traffic-related or industrial-originated pollution. These studies provide only a partial perspective on the broader spectrum of urban air quality dynamics, as roof-based ventilation exhaust is another principal source of air pollution within urban regions. The relatively higher elevation of these types of sources, coupled with the specific characteristics of the mean flow and induced turbulence over the roofs, results in unique patterns of pollutant dispersion that differ significantly from those originating from ground-level sources [111, 183]. Moreover, the undesirable poor dispersion of the exhaust gases from roof-based sources could potentially give rise to a supplementary issue: the infiltration of outdoor air contaminants into the indoor spaces via fresh air intakes that are typically positioned on the building's faces. Although this dearth in the literature underscores the need for incorporating roof-based sources into relevant studies concerning urban air quality, only a limited number of papers have ventured into this realm. Examples are the investigation of roof-based pollutant dispersion adjacent to an isolated building [120, 169, 211], a cross-shape tall building [111, 212], wake region between two buildings [67], and an elongated rectangular building [213]. Therefore, expanding the scope of consideration to include situations with clusters of buildings would inherently yield beneficial and valuable insights.

### **5.1.1 Objectives**

In order to complement the fast-developing urban planning trends, this study defines generic case studies consisting of a cluster of buildings that systematically incorporate typical urban irregularities. To this aim, several degrees of array disposition are considered to account for the urban planar heterogeneities. Consulting the recent body of the literature suggests that if employed strategically, typical geometric non-uniformities could immensely improve outdoor air quality. However, the effective-

ness of these irregularities is intrinsically linked with other influencing morphological indices. Therefore, to effectively contribute to formulating the urban planning guidelines, a parametric investigation is designed to analyze the synergistic effects of urban heterogeneities alongside two other well-established influencing parameters of planar density and wind direction. To accommodate this investigation, a series of case studies has been established, encompassing seven levels of block disposition, which include cases without any disposition to serve as references with aligned blocks, in addition to six planar density variations. Several quantitative ventilation indices, including the velocity ratio, retention time, non-dimensionalized pollutant concentration, and pollutant flow rates due to mean and turbulent flows are calculated to rigorously evaluate the performance of each design. To further bridge the recognized gaps in the literature, two wind directions of  $0^\circ$  and  $45^\circ$  are considered to cover the range of incidences, and the pollutant sources in this work are positioned atop a block upstream of the array (in accordance with the inflow wind direction). Considering roof-based sources enables the exploration of how urban morphology affects gas dispersion above the urban canopy and in proximity to potential locations for fresh air intakes. The quantitative and qualitative conclusions of this work contribute to forming the theoretical framework that can steer urban planning practices toward sustainable designs that result in higher outdoor air quality and efficient land use.

## **5.2 Fundamental and mathematical model**

As discussed earlier, the wind flow and consequently the pollutant distribution within the urban region are highly correlated with the morphological characteristics. The in-depth assessment of the resulting concentration field due to the specific urban texture, necessitates high-resolution modeling of the selected configuration at the neighborhood scale (i.e., horizontal length scales up to 2km) [214]. Evaluating outdoor air quality at larger scales, such as city-scale, can be misleading. This is because, while average ventilation indicators at this scale might fall well within health stan-

dard limits, local extremes caused by specific urban forms can pose serious health hazards [215]. These extremes impact not only pedestrians but also have the potential to degrade indoor air quality. Considering the inherently turbulent nature of the atmospheric urban flow, the Reynolds-averaged representation of the continuity and momentum equations can be employed to govern the steady-state, isothermal, and incompressible wind flow across the building arrays under study. A detailed description of the governing equations and the disintegration of the flow properties into their time-averaged and fluctuating components using the Reynolds decomposition approach are given in Section 4.2.

Appropriate turbulence closure models are further required to model the introduced Reynolds stress terms into the momentum equations and close the system of equations. Following the suggested modeling framework in Chapter 3, the standard  $k - \epsilon$  model has been shown to provide the most reliable and accurate prediction of the flow parameters in case of a cluster of obstacles. The standard  $k - \epsilon$  model demonstrates a greater overestimation of turbulence kinetic energy (TKE) in comparison to alternative closures, as explored in Chapter 3. This overestimation, along with the dominant turbulence generated by the structures within urban arrays, collectively compensates for the typical underestimation of turbulence diffusion associated with Reynolds-Averaged Navier-Stokes (RANS) due to its omission of large-scale eddies [11, 183]. The standard  $k - \epsilon$  model defines the eddy viscosity in Equation 4.3 as  $\mu_t = C_\mu(k^2/\epsilon)$  and introduces two additional transport equations to estimate turbulence kinetic energy (TKE) and the turbulence dissipation rate ( $\epsilon$ ), as shown in Equations 4.6 and 4.8. To enhance the accuracy of the standard  $k - \epsilon$  model in predicting mean and turbulent flow parameters within a generic urban array, an extensive re-calibration of its empirical coefficient set has been undertaken. A comprehensive account of this re-calibration process, along with a thorough evaluation, is detailed in Chapter 4. Consequently, this chapter will employ the modified set of model constants, which is as follows:

- $C_\mu = 0.147$ ,  $C_\varepsilon = 1.344$ ,  $C_{\varepsilon 2} = 1.693$ ,  $\sigma_\varepsilon = 1.196$ , and  $\sigma_k = 0.927$

To estimate the changes in pollutant concentration due to the near-field atmospheric dispersion, the Eulerian advection-diffusion transport equation should be solved (Equation 3.5). In this study, the pollutant is treated as an inert and passive gas, implying that Equation 3.5 is linked with the flow-related equations in one way and can be directly solved subsequent to the computation of the flow field parameters. Moreover, the substantial influence of the turbulence Schmidt number ( $Sc_t$ ) on pollutant diffusion has been a topic of extensive research [152–154, 170, 171]. The comprehensive examination detailed in Section 3.6.2 indicates that  $Sc_t$  is an intrinsic flow property tightly linked to turbulence characteristics. In light of this, a variable definition of  $Sc_t$  was incorporated into Equation 3.5, and its effectiveness was thoroughly assessed. Consistent with the modeling framework proposed in Chapter 3, Equation 3.18 will be applied in this segment of the study as well [172].

## 5.3 Methodology

This section offers a description of the chosen case studies, presents the structured parametric study, and introduces the selected outdoor ventilation and dispersion indices employed for assessing urban air quality.

### 5.3.1 Description of case studies

The primary objective in defining the case studies for this research is to adapt generic block arrays to asymptotically simulate actual urban settings commonly found in cities. More accurately, the idea is to closely mimic the airflow patterns and air pollutant dispersion within real street canyons. The main goal is to uncover the interplay between urban morphological parameters and the dispersion of rooftop-generated air contaminants near and on building facades, which are potential locations for fresh air intakes of the ventilation systems. To achieve this, the target building is situated

within an array consisting of four rows of buildings upstream within the direction of the inflow wind. This type of geometry ensures a more reliable generality of the numerical modeling outcomes and conclusions, as having an adequate number of buildings upstream of the target building generates the expected internal turbulence representative of an urban environment [216]. Moreover, previous investigations generally suggested that an approximate stream-wise equilibrium is often achieved for most flow parameters beyond three rows of blocks [124, 205, 217]. The number of rows in the transverse direction should be carefully determined to ensure that the pollutant plume remains sufficiently distant from the array's edge. This arrangement helps keep the plume away from the accelerating flow beyond the last lateral row of the buildings, especially when the internal flow within the array interacts with the free stream flow. The defined array consists of cubical obstacles with a block aspect ratio (height-to-width ratio) of  $AR = 2$ , which typically corresponds to mid-rise buildings commonly found in densely populated urban areas [218, 219]. Figure 5.1 illustrates a schematic of the building array used in this work to define the case studies.

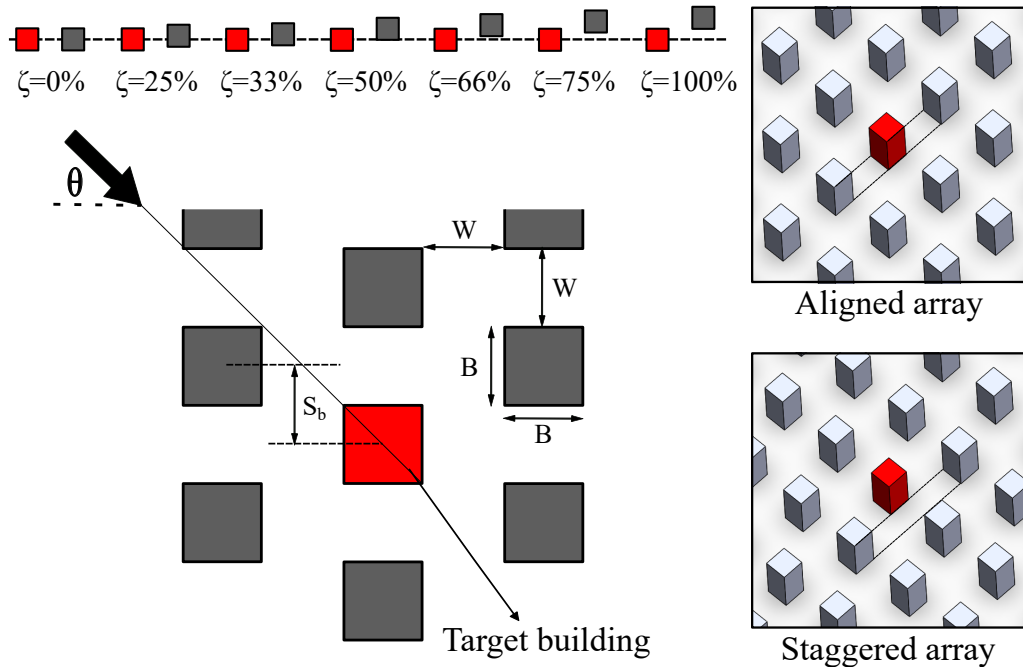


Figure 5.1: Schematic and model descriptions of the defined case studies.

The planar density ( $\lambda_p$ ), also known as the floor coverage ratio, is a crucial morphological index that significantly impacts urban planning decisions. It plays a pivotal role in balancing the efficient utilization of land with the ventilation capacity of the proposed urban design.  $\lambda_p$  is defined as the ratio of the planar area occupied by buildings to the total underlying area, and can be calculated as follows:

$$\lambda_p \% = \frac{B^2}{(B + W)^2} \times 100 \quad (5.1)$$

as shown in Figure 5.1,  $B$  and  $W$  denote building and street widths, respectively.  $B$  in this work is set to 10 m and remains constant among all case studies and will be used as the reference length scale to normalize other parameters where applicable. To facilitate a comprehensive parametric study covering diverse canopy flow scenarios, including isolated roughness flow, wake interference flow, and skimming flow, six levels of planar density are considered. Street width ( $W$ ) is systematically varied across the case studies, using values of  $B$ ,  $1.25B$ ,  $1.5B$ ,  $2B$ ,  $2.5B$ , and  $3B$  to represent a range of urban configurations from densely packed to sparsely arranged. To align with contemporary urban planning trends, this study primarily emphasizes denser configurations, as wide building separations exceeding  $3B$  are deemed impractical and inconsistent with efficient modern urban development [218].

Urban forms with higher planar densities inflict relatively greater resistance to the wind flow around the buildings, potentially weakening the pollutant removal rates below the roof levels and within the pedestrian regions. However, a more compact configuration of the heterogeneously arranged buildings intensifies the geometry-induced turbulence, which is expected to amplify the turbulent mixing and consequently affect pollutant dispersion greatly. Therefore, correlating the opposing influences of mean flow and turbulence with dispersion patterns in irregular but generic urban environments could significantly contribute to the current field of urban planning. To incorporate systematic planar heterogeneity into the case studies, six different building arrangements were considered. As depicted in Figure 5.1, each row of buildings

was shifted relative to its neighboring rows using incremental values of  $S_b$  ranging from  $0.25B$  to  $1B$ . The percentage of disposition, denoted as  $\zeta$ , with respect to the aligned array can be simply calculated as follows:

$$\zeta\% = \frac{S_b}{B} \times 100 \quad (5.2)$$

Moreover, in addition to the perpendicular wind direction ( $\theta = 0^\circ$ ), the extreme case of oblique wind incidence ( $\theta = 45^\circ$ ) is also considered. This addresses a notable gap in the existing literature by exploring the combined effects of oblique wind direction and urban non-uniformities. It is important to note that, as shown in Figure 5.1, only one direction of building disposition is taken into account to create staggered arrays, and thus parallel wind flow to the disposition line is not examined. Finally, for each scenario with a specific planar density, a corresponding baseline configuration was established (reference cases), where no building disposition was applied, and all rows of buildings remained aligned. The results that are acquired from defined case studies will be normalized by the results obtained from the corresponding reference cases. This approach facilitates a focused analysis of the interplay between these specific factors while keeping other parameters constant. The Table 5.1 summarizes all 84 case studies to be investigated in this research.

Table 5.1: Summary of geometric specifications for the investigated and reference case studies.

Case studies	Naming scheme	$\lambda_p(\%)$	$\zeta(\%)$	$\theta$	Pattern
Investigated cases	S- $\lambda_p$ - $\zeta$ - $\theta$	6, 8, 11, 16, 20, 25	25, 33, 50, 66, 75, 100	$0^\circ, 45^\circ$	Staggered
Reference cases	A- $\lambda_p$ - $\zeta$ - $\theta$	6, 8, 11, 16, 20, 25	0	$0^\circ, 45^\circ$	Aligned

### 5.3.2 Outdoor ventilation and dispersion indices

The capability of any urban configuration to dilute and disperse the gaseous pollutant contents within the underlying atmospheric regions can be assessed using well-

established ventilation indices. These indicators offer an opportunity to cross-compare all the possible urban redevelopment and modification strategies in terms of their potential to enhance outdoor ventilation and breathability. It is interesting to note that the expression of breathability is based on the inhale-and-exhale analogy, in which the assumed clean surrounding air will be delivered by atmospheric wind flow to the urban configuration, referring to the inhalation, and purges the undesirable pollution out of the area through the exhalation [220]. In the following, the indicators employed for quantitative investigation will be introduced. The regions considered for evaluating these ventilation indicators are presented in Figure 5.2. The faces of the evaluation volume and the target building are denoted by the letters T (top), F (front), R (right), B (back), and L (left), distinguished by the subscript letters v and b, respectively.

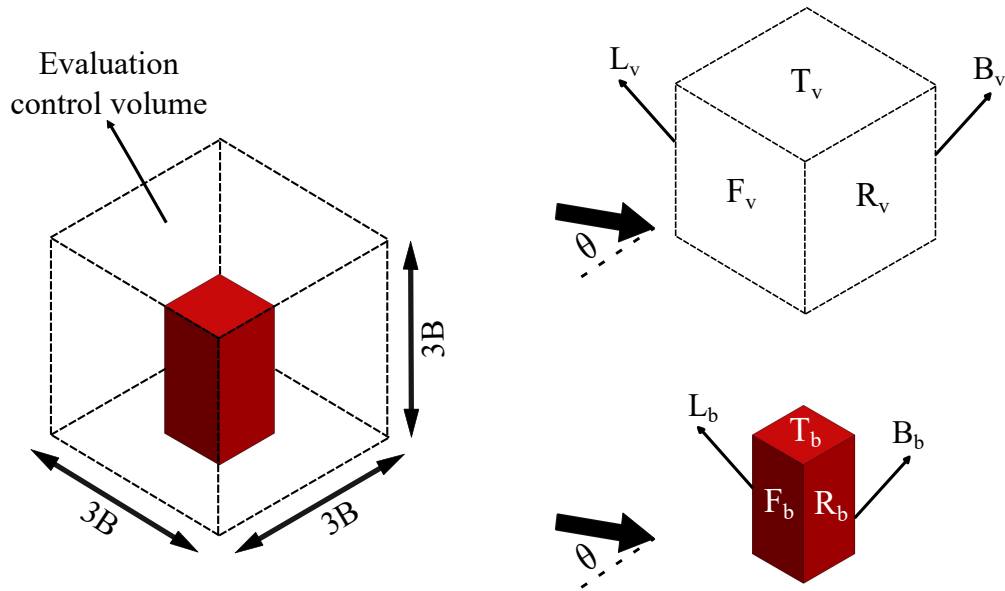


Figure 5.2: Evaluation regions to assess outdoor ventilation capacity in the proximity of the target building.

## Velocity ratio

The velocity ratio serves as the most simple, yet widely accepted indicator to effectively quantify the extent of the available wind in a region, which directly reveals the impact that a specific urban form can exert on the local flow field. It is simply defined as the ratio of the local time-averaged velocity at the desired location,  $\bar{U}$ , to the upwind undisturbed velocity magnitude measured at the corresponding height,  $U_\infty$ . To thoroughly evaluate the influence of the surrounding building configuration on the ventilation capacity near the target building, it is essential to calculate the area and volume-averaged velocity ratios ( $V^*$ ) across the designated regions and volumes (Figure 5.2). This can be accomplished using Equations 5.3 and 5.4.

$$V_A^* = \frac{1}{U_\infty A} \int_A \bar{U} dA \quad (5.3)$$

$$V_{vol}^* = \frac{1}{U_\infty V} \int_V \bar{U} dV \quad (5.4)$$

## Non-dimensionalized concentration

The non-dimensionalized concentration ( $C^*$ ) employed in this study serves as an atmospheric dispersion factor, representing the concentration of the pollutant at a given location relative to its concentration at the source. The term "normalized" indicates that the concentration is adjusted or scaled to enable comparisons. This normalization allows for the assessment of pollutant concentration relative to a reference point, aiding in the evaluation of air quality trends, the identification of areas with varying pollution levels, and the assessment of pollution control measures. Equation 5.5 provides a definition for  $C^*$ , where  $C$  is the predicted concentration at a given location,  $U_{ref}$  represents the reference velocity at a specified reference height,  $H$  is an arbitrary length scale chosen as the uniform height of the buildings in the defined case studies,  $C_s$  is the concentration of scalar at source, and  $q_s$  is the volumetric flowrate of pollutant emissions. Similar to  $V^*$ , the area and volume-averaged values of  $C^*$  can also

be calculated within the designated regions.

$$C^* = \frac{CU_{ref}H^2}{C_s q_s} \quad (5.5)$$

### Retention time

The retention time ( $\tau$ ) is an important outdoor ventilation index frequently utilized to quantitatively assess the dispersion properties of pollutants within a given environment.  $\tau$  is considered an air-exchange estimation index and provides an estimation of the pollutant residence time within the region of interest [221]. Several factors, such as local airflow patterns and the presence of physical barriers or obstructions, can affect the retention time. Longer retention times indicate higher pollutant concentrations in a particular area, thereby exerting a substantial impact on local air quality [23]. To calculate  $\tau$ , Equation 5.6 can be employed as follows:

$$\tau = \frac{1}{q_s} \int_V C^* dV \quad (5.6)$$

### Pollutant transport rate

Calculating the pollutant transport rates into the defined control volume in Figure 5.2 is essential for understanding the dynamics of the dispersion patterns under the influence of the surrounding urban configuration. As suggested by Equation 4.10, the total pollutant flow rate through each surface of the control volume can be decomposed into contributions arising from the mean and fluctuating velocity components. Equation 5.7 quantifies the convective pollutant flow rate carried by the mean flow, whereas Equation 5.8 estimates the diffusive transport due to turbulent flow [222]:

$$F_m = \int_A \vec{U} \cdot \vec{n} C dA \quad (5.7)$$

$$F_t = \int_A -D_t \frac{\partial C}{\partial n} dA \quad (5.8)$$

The velocity vector is represented by  $\vec{U}$ , while the normal unit vector to the control volume surfaces is denoted as  $\vec{n}$ .  $D_t$  is the eddy diffusivity, a property of the turbulent flow, and can be calculated as the ratio of the eddy viscosity,  $\nu_t$ , to the turbulence Schmidt number,  $Sc_t$ . It is important to note that negative values of  $F_m$  and  $F_t$  indicate pollutant contaminants exiting the control volume through the specific surface, whereas positive show pollutants entering.

### 5.3.3 Numerical scheme

The comprehensive explanation and examination of the general settings utilized to numerically solve the governing equations pertaining to atmospheric flow and pollutant dispersion in the context of urban geometries can be found in Section 3.4 and 4.5. Following the modeling framework presented in the aforementioned sections, a similar approach has been taken in this chapter to ensure the accurate and reliable simulation of all case studies. A brief summary of all the modeling decisions, grid convergence study, and numerical model validation are provided in the following.

The hybrid finite element/volume method is employed in ANSYS CFX commercial code to numerically solve the three-dimensional governing equations. In all cases, rectangular computational domains are defined, with inlet faces oriented perpendicular to the inflow wind direction. This arrangement allows for the application of symmetry boundary conditions not only on the top face of the domain but also on the side faces, simplifying the procedure. The minimum dimensions of the computational domain are specified based on the guidelines proposed by the previous works [18, 197], and are further customized to eliminate any possible non-physical influence by boundaries on the solution. In this regard, a distance equal to  $14H_{max}$  ( $H_{max}$  is the height of the tallest structure) between the array's windward edge and the inlet boundary is considered, while the distance between the outer edge of the last row of the array and outflow boundary is set to  $20H_{max}$ . The upper and side boundaries are also positioned  $10H_{max}$  away from the corresponding edges of the investigated array.

Considering the fact that a logarithmic approximation of the inflow wind profile offers a more physically accurate representation of the wind flow in the ABL, Equations 4.26, 4.27, and 4.28 proposed by Richards and Hoaxy [165] are employed at the inlet. The friction velocity required to evaluate the inflow atmospheric wind profile can be estimated using Equation 5.9, assuming a constant vertical shear stress in the atmospheric surface layer.  $U_{ref}$  is the reference velocity of 2m/s at the reference height of  $H_{ref}$  (which is the same as the uniform building heights), with an aerodynamic roughness height of  $z_0 = 0.4\text{m}$ , and  $\kappa = 0.4$  as the Von Karman constant [165]. As for the remaining boundaries, all the solid surfaces are considered walls with no-slip conditions, top and side boundaries are set as symmetry planes, and an average relative pressure of zero is defined at the outlet.

$$u_\tau = \frac{\kappa U_{ref}}{\ln\left(\frac{H_{ref}+z_0}{z_0}\right)} \quad (5.9)$$

The discretizations of the advection terms of momentum equations and turbulence numerics are carried out with the implementation of high-resolution schemes, and the velocity-pressure coupling is dealt with using the fourth-order Rhie-chow algorithm. The solutions to the flow equations (i.e., continuity, momentum, TKE, and  $\varepsilon$ ) are considered converged when the calculated normalized residuals reach values equal or less than  $10^{-6}$ , whereas the criterion is  $10^{-9}$  for the scalar transport equation.

### **Grid convergence study**

In the generation of the computational mesh for all case studies, a similar approach to that detailed and tested in Section 4.5.2 is applied. This approach involves the formation of a nested domain to distinguish between regions significantly affected by the presence of structures (i.e., inner region), where higher grid refinements are needed, and regions situated far from the built area (i.e., outer region), resembling open-field atmospheric flow. Structured and unstructured hexahedral cells are employed to mesh the outer and inner regions, respectively. Additionally, five layers of

inflation with a growth rate of 1.07 are applied to provide extra refinements near the solid surfaces. This ensures the proper resolution of boundary layer gradients while maintaining the  $y^+$  within the recommended range of 30 to 300 [88].

The dependency of the numerical solutions on the grid resolution is examined by comparing the results obtained from three progressively refined meshes. Figure 5.3 displays an example of the prediction made for the most sensitive parameters,  $C^*$ , by all three grids in case [S-25-25-45°]. The coarse grid comprises 8 million computational nodes, while the medium and fine grids consist of 11.4 and 17.9 million nodes, respectively. The minor deviation between predictions obtained from the medium and fine grids justifies the use of the medium grid due to its reasonable balance between accuracy and computational cost.

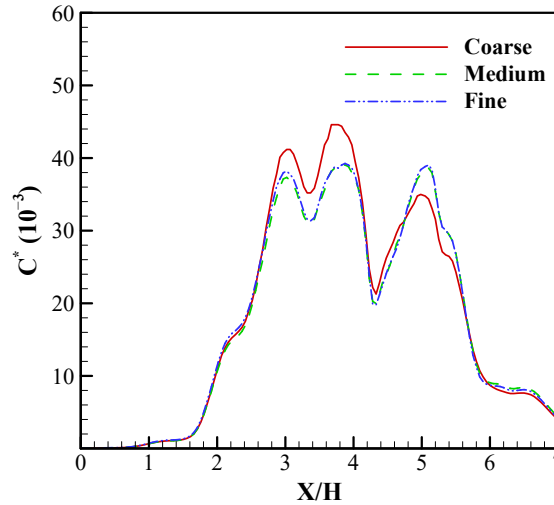


Figure 5.3: Pollutant concentration profile in case [S-25-25-45] along a horizontal line midway between the target building and its immediate upwind row at  $Z/H = 0.75$

### Validation study

The validity of the mathematical model, the modified turbulence closure, modeling settings, and the grid generation scheme employed in this work, were comprehensively validated in Section 4.6.2. For this validation study, the high-quality full-scale dispersion data set of Mock Urban Setting Tests (MUST) was used to rigorously evaluate

the accuracy and reliability of the numerical simulations in predicting both the flow and dispersion parameters. However, given that the blocks considered in the case studies of this chapter have different AR compared to the MUST geometry, it is considered prudent to conduct further validation studies using a case study that includes blocks with similar geometries to ensure the robustness of the model in different scenarios. In this regard, the data set from the well-known wind tunnel experiment “Case C” conducted by the Architectural Institute of Japan (AIJ) is used [59]. The geometry of this particular case study consists of a 3 by 3 cubical array, simulating a simplified and idealized urban configuration. The central block within this array shares a similar geometry with the blocks featured in the present parametric study with an AR=2, while it is surrounded by neighboring cubical blocks with an AR=1. Figure 5.4 illustrates schematics of the AIJ Case C geometry with the locations of all the measurement points.

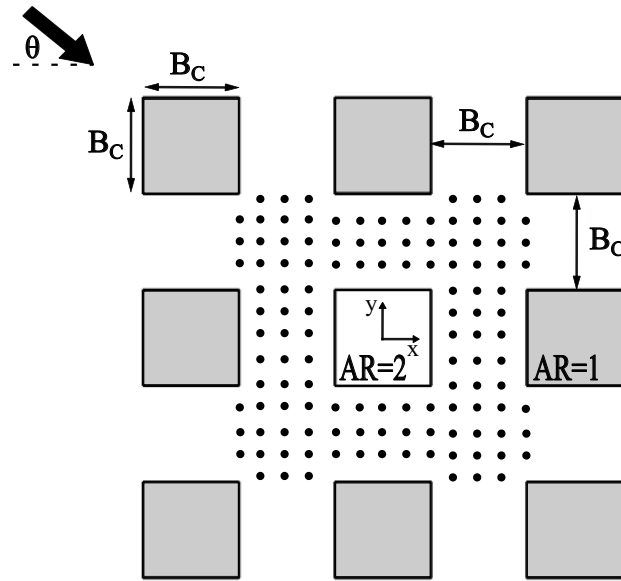


Figure 5.4: Schematic of the wind tunnel experiment “Case C” by Architectural Institute of Japan (AIJ). The model’s reference length scale is  $B_C=0.2$  m. Small black circles depict 120 measurement points.

This data set, however, only includes the velocity measurements at the given sampling points ( $Z/B_C = 0.1$ ), and does not include any dispersion data. Nonetheless, as

the tracer gas in this study is treated as a passive scalar due to its non-reactive nature and low mass fraction, its influence on the fluid dynamics in the domain is considered negligible. Therefore, it is justifiable to solve the transport equation after the flow field has been resolved within the geometry. As a result, simultaneous consideration of both validation studies, one with the MUST dispersion data and one with AIJ Case C flow data, can provide sufficient evidence to assess the validity of the numerical scheme presented in this chapter. Figure 5.5 maps  $V^*$  profiles at two horizontal sampling lines within the array for two different inflow wind directions of  $0^\circ$  and  $45^\circ$ . As it is evident, the predictions made using the employed modeling settings closely match the wind tunnel measurements, indicating the validity of the numerical model. Further statistical analysis over all 120 sampling points (Figure 5.4) demonstrates the superiority of the modified  $k - \varepsilon$  turbulence model over its standard version. The former achieved a Hit-Rate (HR, Equation 4.22) of 79.2% and 74.1% for  $0^\circ$  and  $45^\circ$  inflow winds, respectively, while the latter achieved 69.2% and 65.8%.

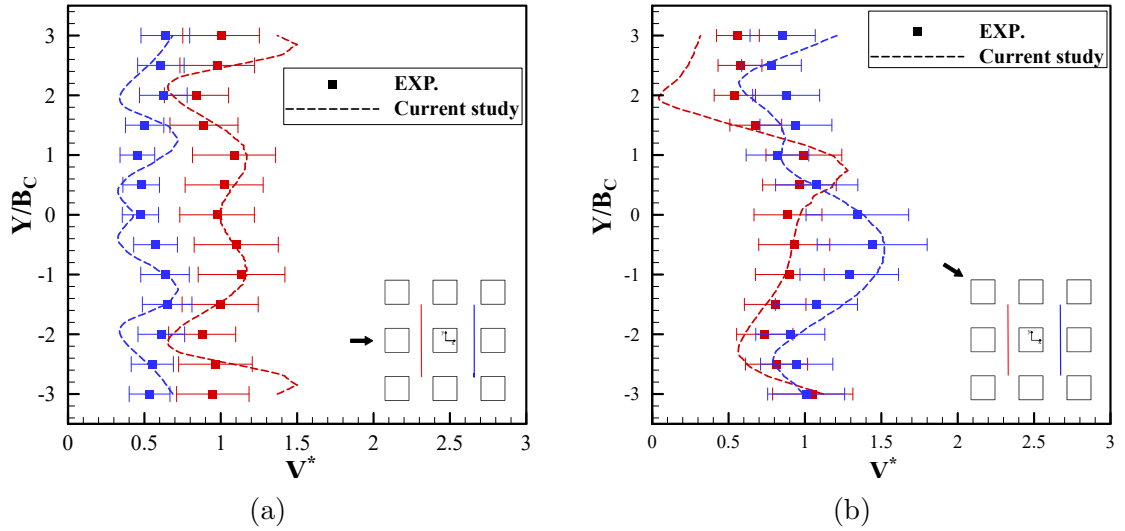


Figure 5.5: Predicted  $V^*$  profiles at shown sampling lines for inflow wind direction of (a)  $\theta = 0^\circ$ , and (b)  $\theta = 45^\circ$  at  $Z/B_C = 0.1$ . The error bars represent a 25% deviation from the experimental measurements.

## 5.4 Results and discussions

This parametric study is designed to investigate the collective influence of various morphological indices on urban air ventilation performance and pollutant dispersion. It will systematically examine factors such as the velocity ratio, pollutant retention, flow patterns, and convective and diffusive pollutant flow rates in proximity to building facets (referred to as the external faces of the buildings in this work) under different urban layouts. Finally, the study will include a regression analysis to formulate a correlation that accurately quantifies the combined impact of these morphological indices on volume-averaged pollutant concentration near building surfaces.

### 5.4.1 Outdoor ventilation and pollutant dispersion

To thoroughly analyze the sensitivity of urban ventilation capacity and its effectiveness in dispersing pollutants, two established indices, namely  $V^*$  and  $\tau$ , can serve as valuable tools for both quantitative and qualitative assessments. Given that the pollutant retention time,  $\tau$ , is a volume-based quantity, the defined control volume shown in Figure 5.2 (enclosing the target building) is considered for calculations in this section. Consequently, the availability of clean air flow in this region is also assessed by calculating the volume-averaged velocity ratio,  $V_{vol}^*$ . To effectively isolate and explore the combined impact of urban planar density and heterogeneities while controlling for other possible confounding effects, the resulting indices obtained from investigated cases with non-zero  $\zeta$  values are normalized against ones obtained from reference cases with no disposition (Table 5.1). Moving forward, all normalized values will be denoted with a subscript letter “n”. Considering the primary focus of this work, only the results for cases exhibiting planar heterogeneity within the range of  $25\% \leq \zeta \leq 100\%$  are presented, as the outcomes associated with reference cases ( $\zeta = 0$ ) are inherently expected to be unity.

Figure 5.6 showcases  $V_{vol,n}^*$  and  $\tau_n$  as a function of the  $\zeta$  for building clusters with

varying  $\lambda_p$ , under a perpendicular wind direction (i.e.,  $0^\circ$ ) to the disposition axis. In examining the velocity ratio as depicted in Figure 5.6a, a consistent pattern emerges across all cases, indicating that  $V_{vol,n}^*$  declines when transitioning from an aligned arrangement to a staggered one. This trend underscores the intricate relationship between urban planar heterogeneity and prevailing flow patterns. Specifically, the expected channeling flow characteristic of aligned arrays is disrupted in the staggered configuration. The diversion of airflow in staggered configurations significantly reduces the flow's overall momentum. This phenomenon can be interpreted as increased resistance to the mean flow, caused by the expansion of wake regions and intensified eddies due to enhanced heterogeneity. These conditions lead to pressure differences that act as barriers, resulting in a local velocity deceleration [223].

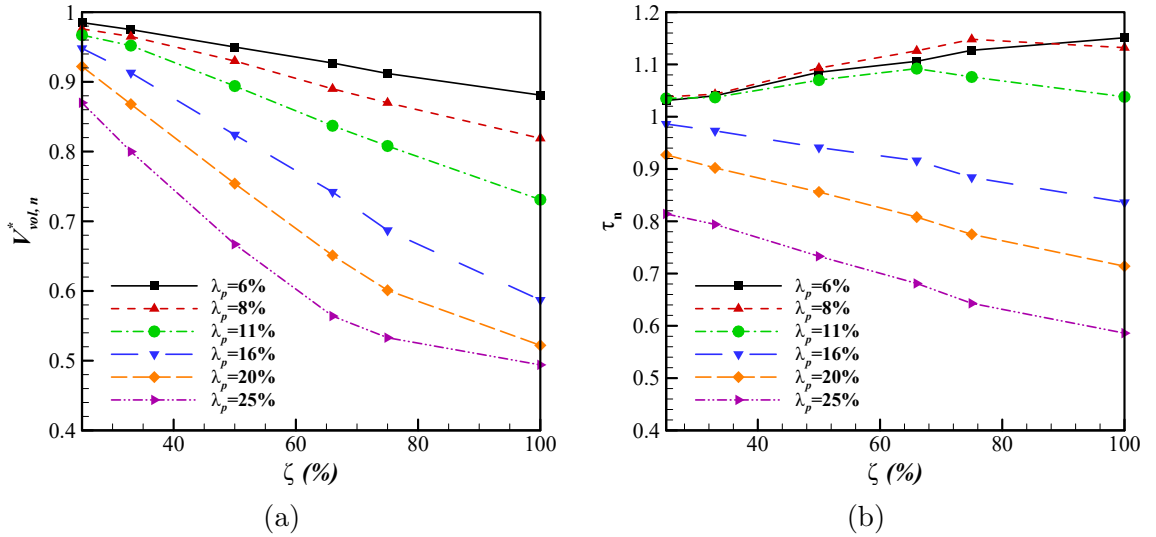


Figure 5.6: Variations in (a)  $V_{vol}^*$  and (b)  $\tau$ , normalized to their respective reference values with identical  $\lambda_p$  (but no disposition), within the control volume enclosing the target building under a  $\theta = 0^\circ$  wind incidence.

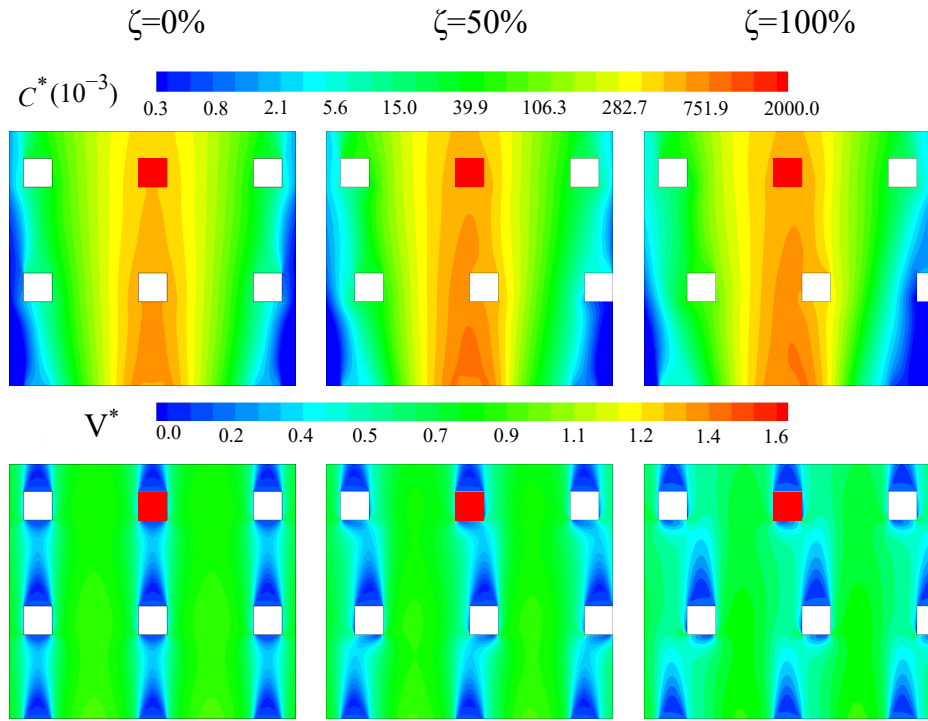
Furthermore, the evident distinction among all planar densities suggests that at any given disposition level, the ratio of velocity reduction compared to its corresponding aligned configuration increases moving towards denser arrangements (i.e., higher  $\lambda_p$ ). The gradient of the plotted curves in Figure 5.6a, which characterize the rate of change in  $V_{vol,n}^*$ , also varies with  $\lambda_p$ . The curve associated with  $\lambda_p = 6\%$  has a lower gradient,

indicating a less sensitivity of the velocity ratio to changes in building disposition. As the configurations become denser, steeper slopes are observed, suggesting a more responsive behavior of velocity ratios to the building orientation. In the least dense scenario ( $\lambda_p = 6\%$ ), the  $V_{vol,n}^*$  value decreases to approximately 0.88 at  $\zeta = 100\%$ , while for the most densely packed configuration, it drops to just below 0.50.

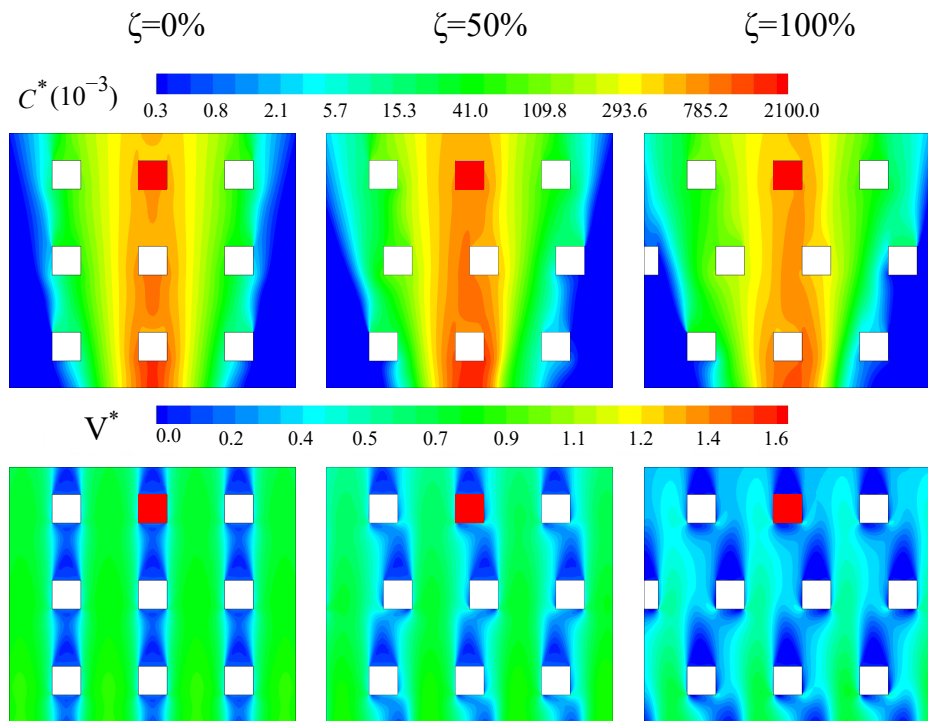
Such observation is consistent with the canopy regime classification introduced by Oke [123]. As buildings become more clustered, the wakes behind buildings interfere more extensively with the disturbed flow field in front of their downstream buildings. This leads to a transition in flow patterns near buildings, shifting from a semi-isolated roughness regime (as seen in case S-6-100-0) to full wake interference, or skimming flows. Consequently, the airflow patterns induced by one structure are incident upon the neighboring structures. This coupling of aerodynamic interference leads to stochastic wind patterns with venturi flow channels, vortices, multiple rates of strain, and multiple stagnation sites. Additionally, the higher  $\lambda_p$  results in a decrease in the available open channels for wind flow, unlike sparser arrangements where the wind can move more freely (Figure 5.7). Consequently, in denser urban configurations, building dispositions play a key role in dictating the macroscopic flow patterns.

Figure 5.6b demonstrates the complex relationship between the variation of  $\tau_n$ , representing the normalized pollutant retention time near the target building, and changes in  $V_{vol,n}^*$ . While expectations might imply an inverse correlation, where lower clean air availability (i.e., smaller velocity ratio) leads to pollutant contents lingering longer in the environment [130], this relationship does not hold for all cases studied in this work. Given that  $\tau$  also incorporates the effects of flow diffusion paths [23], analyzing this index in relation to the velocity ratio, which primarily reflects mean flow characteristics, can yield valuable insights.

There is a nearly constant, albeit slightly increasing, trend in  $\tau_n$  for  $\lambda_p = 6\%$  as disposition levels increase. This suggests a relatively low sensitivity to changes in



(a)  $\lambda_p = 6\%$



(b)  $\lambda_p = 11\%$

Figure 5.7: Contours of non-dimensionalized concentration ( $C^*$ ) and velocity ratio ( $V^*$ ) distribution at the midplane of the upper half of the cluster height ( $Z/H = 0.75$ ) for three different disposition levels in three cases: (a)  $\lambda_p = 6\%$ , (b)  $\lambda_p = 11\%$ , and (c)  $\lambda_p = 20\%$  for  $\theta = 0^\circ$  wind direction.

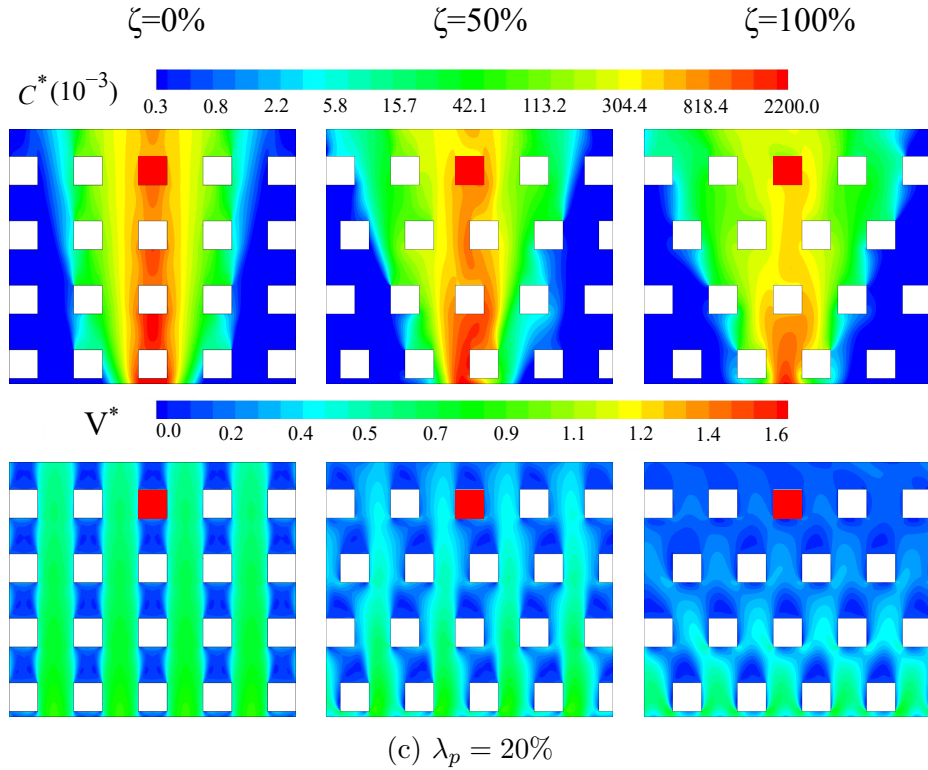


Figure 5.7: (Continued).

building arrangements (i.e., varying  $\zeta$ ) at this planar density, where the maximum value of  $\tau_n$  reaches 1.15. In sparse configurations like this one, where the flow is minimally affected by the presence of surrounding buildings, a gradual decrease in  $V_{vol,n}^*$  near the target building leads to a corresponding gradual increase in  $\tau_n$ , in line with expectations (Figure 5.7). This consistent behavior highlights the significance of open spaces, which enable wind to flow with minimal disruption and turbulence interactions. A similar trend is observed for cases with  $\lambda_p = 8\%$ , implying the diminished ventilation and prolonged pollutant presence up to disposition levels of 75%, where  $\tau_n$  starts to drop. One possible explanation is that at higher dispositions, the disturbances introduced by adjacent buildings within this relatively denser configuration reach the target area. The resulting enhanced turbulence appears to counteract the decreasing velocity ratio, thereby promoting pollutant dispersion and turbulent mixing in this region.

As for  $\lambda_p = 11\%$ , the packed building arrangement further amplifies the effects of turbulence interference induced by neighboring structures. As  $\zeta$  increases, the influence of neighboring buildings becomes even more pronounced, causing the trend to reverse earlier, around the  $\zeta = 66\%$ . Following the same justification, the dispersion pattern in the denser arrangements (i.e.,  $\lambda_p = 16\%$ ,  $20\%$ , and  $25\%$ ) is shown to be more influenced by the turbulent mixing from the outset, leading to considerably lower values of  $\tau_n$  at  $\zeta = 100\%$  (0.84, 0.71, and 0.59, respectively). As can be deduced from Figure 5.7, the contours of  $C^*$  and  $V^*$  variations across different level dispositions for three instances of planar densities, from sparse to densely packed arrangements, visually confirm these observations. The heightened turbulence structures within denser arrangements, driven by increased planar heterogeneity, clearly led to a signified lateral spread of the pollutant plume. This implies a reduced average concentration around the plume's centerline and a more uniformly distributed pollutant in the horizontal plane.

To explore the potential influence of array orientation on  $V_{vol,n}^*$  and  $\tau_n$  responses to urban configurations, an oblique inflow wind direction is also considered. The results for this scenario are depicted in Figure 5.8. The figures show for both the perpendicular and oblique wind directions, distinct classifications based on planar densities. The sparse configurations ( $\lambda_p = 6\%$ ,  $8\%$ , and  $11\%$ ) result in similar trajectories, each at its own magnitude. While the densely packed arrays ( $\lambda_p = 16\%$ ,  $20\%$ , and  $25\%$ ) also exhibit a consistent behavior.

Figure 5.8a,  $V_{vol,n}^*$  demonstrates a fundamentally different behavior in response to variation of the geometry compared to what was observed with perpendicular wind incidence. In the case of the  $45^\circ$  incidence, the skewed airflow less directly feeds vortex lines which are necessarily aligned with geometric edges [45, 69]. Instead, it tends to glide or skim alongside the buildings and experiences a redirection rather than facing a direct blockade. Consequently,  $V_{vol,n}^*$  does not exhibit the near linear decrease that was previously observed for  $0^\circ$  wind direction as disposition levels increase. For all

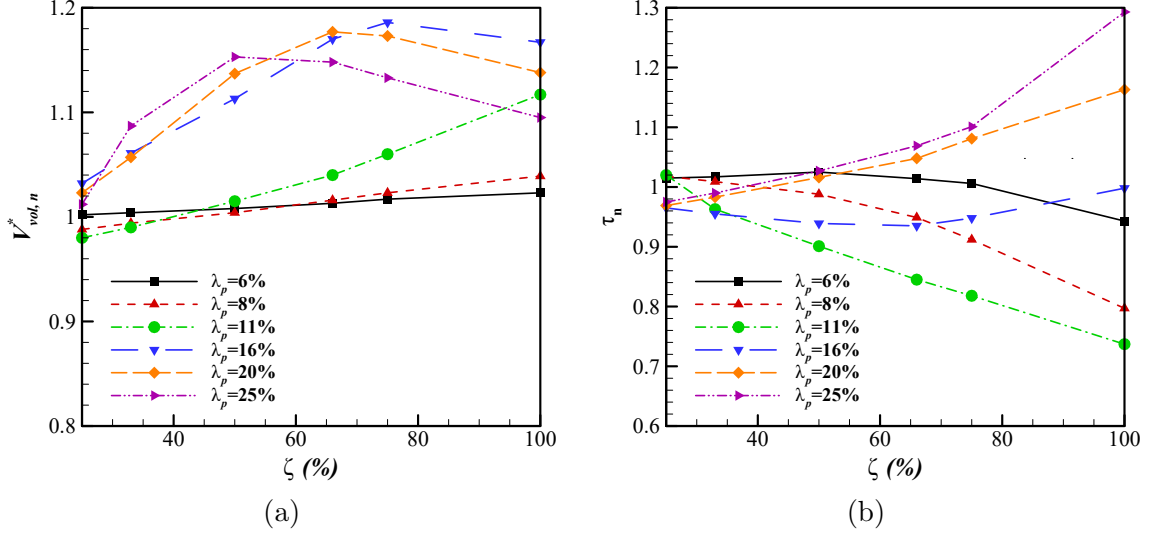
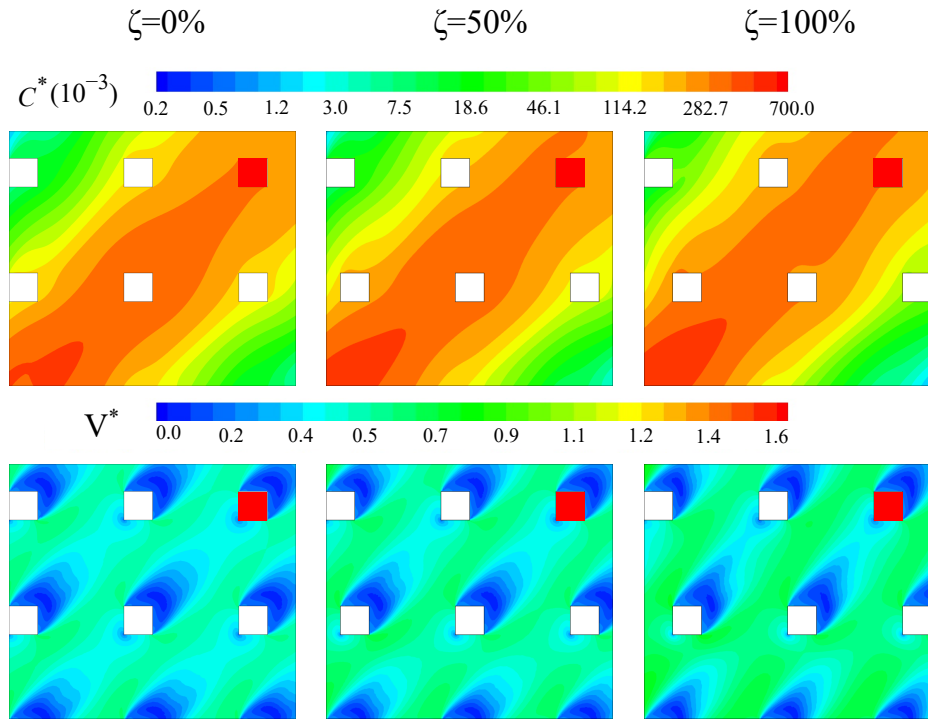


Figure 5.8: Variations in (a)  $V_{vol,n}^*$  and (b)  $\tau_n$ , normalized to their respective reference values with identical  $\lambda_p$  (but no disposition), within the control volume enclosing the target building under a  $\theta = 45^\circ$  wind incidence.

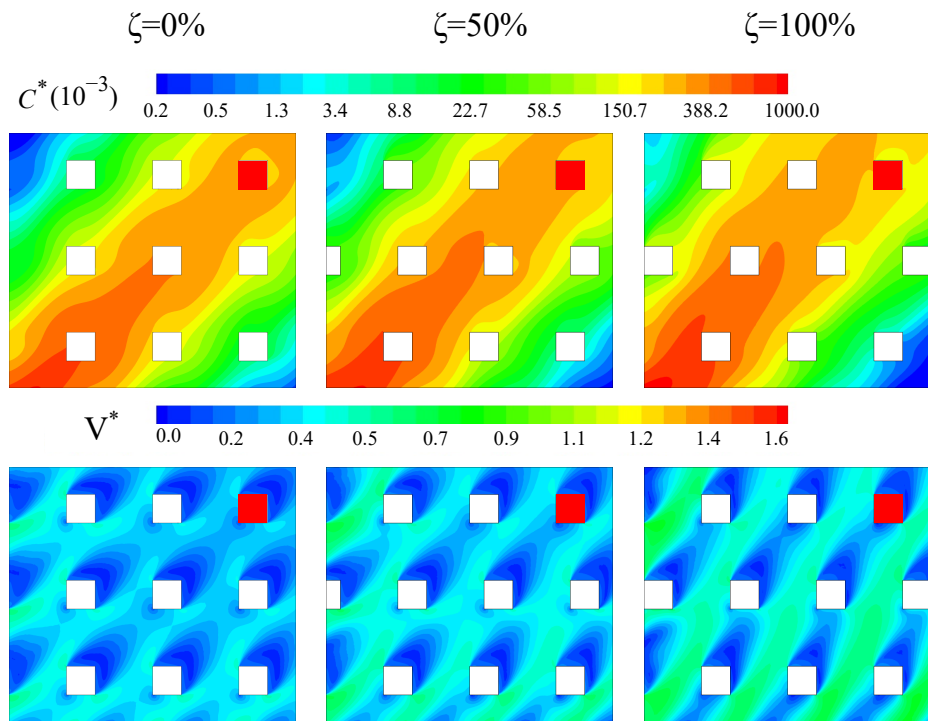
planar densities under the oblique wind incidence,  $V_{vol,n}^*$  mostly exceeds the baseline value of 1, suggesting an overall trend of enhanced ventilation relative to the aligned cases.

For the sparse configurations, the velocity ratio generally exhibits a lesser increase compared to the reference cases. Such behavior supports the claim that oblique wind encounters relatively modest resistance and diffuses more freely through alternative pathways in less densely built environments. Moving towards denser configurations, a notable surge in the positive gradient of  $V_{vol,n}^*$  can be observed, potentially associated with wind acceleration through tighter urban channels (Figure 5.9). However, as shown in Figure 5.9, the systematic increase in  $\zeta$  further obstructs these gaps and channels, leading to increased flow acceleration.

With further intensification of planar heterogeneity (increasing  $\zeta$ ), each of the arrangements within the densely built classification experiences a turning point where the gradient of  $V_{vol,n}^*$  reaches zero. Beyond these thresholds, the blockage effects of the available obstructions seem to start to take effect, showing a negative  $V_{vol,n}^*$  gradient, and suppress the previously amplified velocity ratios. For  $\lambda_p = 16\%$ , this



(a)



(b)

Figure 5.9: Contours of non-dimensionalized concentration ( $C^*$ ) and velocity ratio ( $V^*$ ) distribution at the midplane of the upper half of the cluster height ( $Z/H = 0.75$ ) for three different disposition levels in three cases: (a)  $\lambda_p = 6\%$ , (b)  $\lambda_p = 11\%$ , and (c)  $\lambda_p = 20\%$  for  $\theta = 45^\circ$  wind direction.

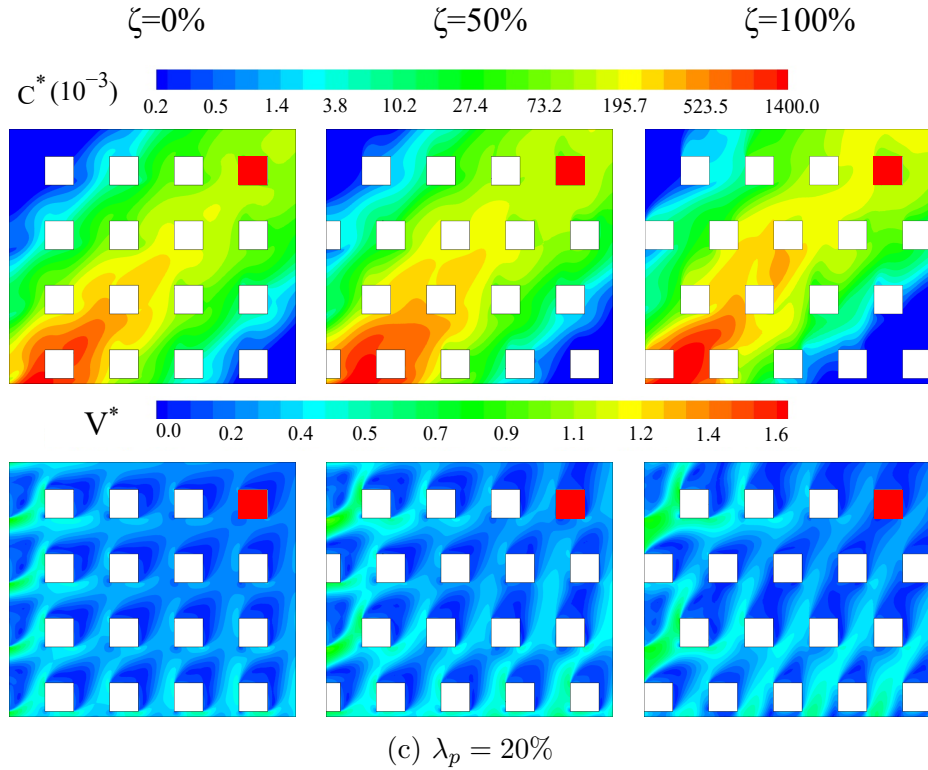


Figure 5.9: (Continued).

occurs around  $\zeta = 75\%$ , while this point arrives sooner for denser configurations ( $\zeta = 66\%$  and  $50\%$  for  $\lambda_p = 20\%$  and  $25\%$ , respectively). This observation can be explained by considering the cumulative blockage effect. In denser arrangements, the flow encounters more obstructions in cases with smaller  $\zeta$  values, meaning there are fewer channels for the wind to accelerate through (Figure 5.9c). As the  $\zeta$  further increases, any additional buildings or obstructions only serve to disrupt the previously established flow patterns, leading to a decrease in  $V_{vol,n}^*$ . It should be noted that even after these turning points, the normalized velocity ratios are greater than unity, implying an improvement in ventilation compared to the aligned case, regardless of  $\zeta$ .

The distribution of  $\tau_n$  depicted in Figure 5.8b for  $\theta = 45^\circ$  illustrates more than one competing effect. In the case of the two most sparse arrangements ( $\lambda_p = 6\%$  and  $8\%$ ), the anticipated inverse correlation between  $V_{vol,n}^*$  and  $\tau_n$  is evident. In particular,

with an increasing normalized velocity ratio relative to the aligned configuration, there is a corresponding decrease in retention time. This intuitively suggests that higher velocities, driven by the enhanced acceleration due to oblique wind direction and reduced blockage, cause more thorough ventilation, and consequently reduce the pollutant residence time within the studied area. The reduction in pollutant lingering times becomes more pronounced with incremental variations of  $\lambda_p$  up to 11%. It is worth noting that the curve corresponding to  $\lambda_p = 11\%$  exhibits a trend similar to its sparser counterparts, displaying a negative gradient across all  $\zeta$  values. In contrast to the sparse cases where their curves exhibit negative second derivatives, the curve associated with  $\lambda_p = 11\%$  shows a semi-linear reduction, with even a slight concavity observed. This observation can potentially point to a transitional phase in airflow behavior as planar density increases.

In the two most densely packed configurations,  $\lambda_p = 6$  and 8%, the ascending trajectory for  $\tau_n$  begins from the outset, starting at a relatively modest gradient that is progressively amplified with increasing planar heterogeneity. One possible explanation for this behavior is that at lower  $\zeta$  values, the enhanced ventilation (i.e., increasing  $V_{vol,n}^*$ ) counteracts the diffusion paths that seem to trap the pollutants around the target building. However, at higher  $\zeta$  where  $V_{vol,n}^*$  begins to decrease (as indicated by the local maximums shown in Figure 5.8a), the removal of the pollutant from the investigated region is hindered to a greater extent. This is evidenced by the steeper slope of the curve at higher  $\zeta$  values.

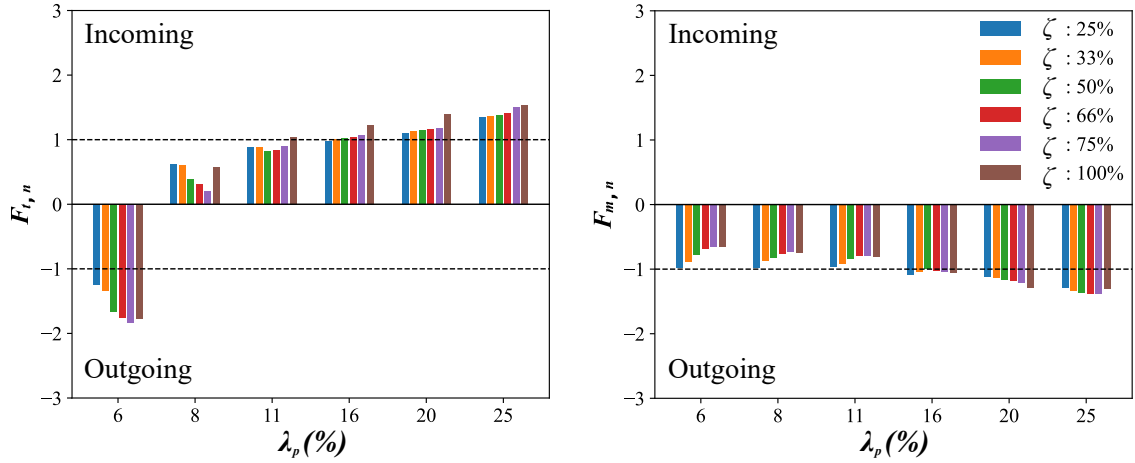
### 5.4.2 Dynamics of dispersion patterns

This section gives the analysis of the pollutant transport mechanism arising from convection and turbulent diffusion through the faces of the defined control volume (as illustrated in Figure 5.2) that encloses the target building. It provides a greater understanding of the dynamics of dispersion flow, which is influenced by urban geometry. Figure 5.10 displays bar charts showing the normalized pollutant transport

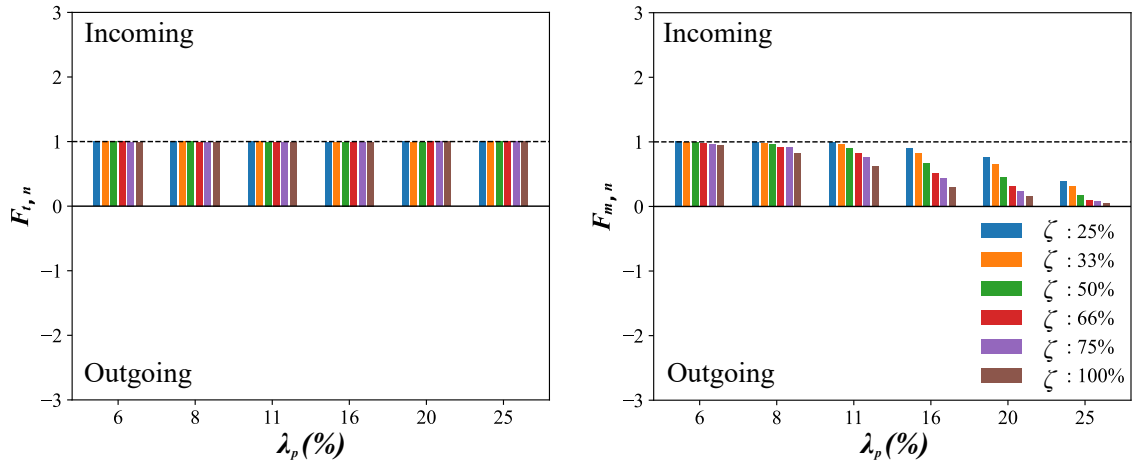
rates due to mean and turbulent flow, denoted as  $F_{t,n}$  and  $F_{m,n}$ , under the  $0^\circ$  inflow wind direction.

Given the physically elevated location of the scalar source in this work, the vertical pollutant transport should be comparable in magnitude to the stream-wise transport. This is despite the fact that the uniform building heights throughout the urban configuration suggest a relatively undisturbed flow at the height where the  $T_v$  plane is located [224]. As can be seen from Figure 5.10a, a net convective outflow is detected through the  $T_v$  (i.e., negative values) resulting from the slightly upwards wind flow deflected by buildings' leading edges. Notably, the observation of values greater than  $-1$  for the sparse category raises interesting insights. This suggests that as planar heterogeneity increases, there is a tendency for the outflow to decrease. One plausible explanation for this phenomenon lies in the relatively wide spacing between buildings in the sparse category. This increased heterogeneity appears to enhance the upstream building downwash effects, effectively pulling down the emitting plume. Consequently, the pollutant content adjacent to the  $T_v$  plane decreases, leading to a noticeable decrease in convective pollutant removal.

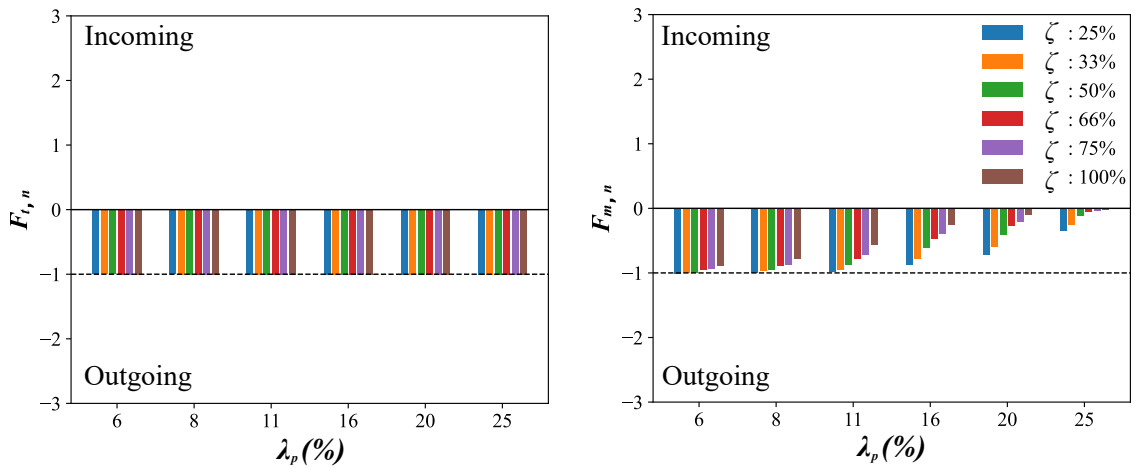
As the building array becomes denser, the impact on the flow regime caused by adjacent buildings collectively influences the flow patterns near the target building. Therefore, the flow regime transitions toward a mode in which downwash effects weaken as disposition levels increase, while the pollutant concentration just below the  $T_v$  height increases. This leads to a general increase in pollutant outflow through the top face. The existence of this phenomenon is further supported by assessing the diffusive transport rates. The fundamental principle underlying the Standard Gradient Diffusion Hypothesis advises that diffusion occurs in the opposite direction of the scalar gradient [225]. In the case of a planar density of 6%, there is an observation of outflow diffusion through the  $T_v$  plane, indicating that the concentration below the  $T_v$  height exceeds that above it. As the urban configuration becomes denser, a notable transition in turbulence diffusion becomes evident, with the shift from out-



(a) Location:  $T_v$

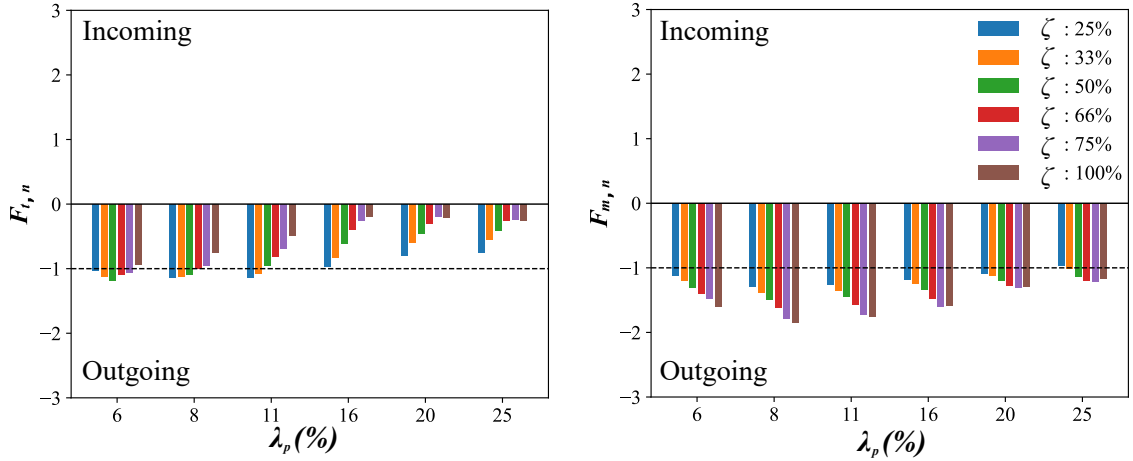


(b) Location:  $F_v$

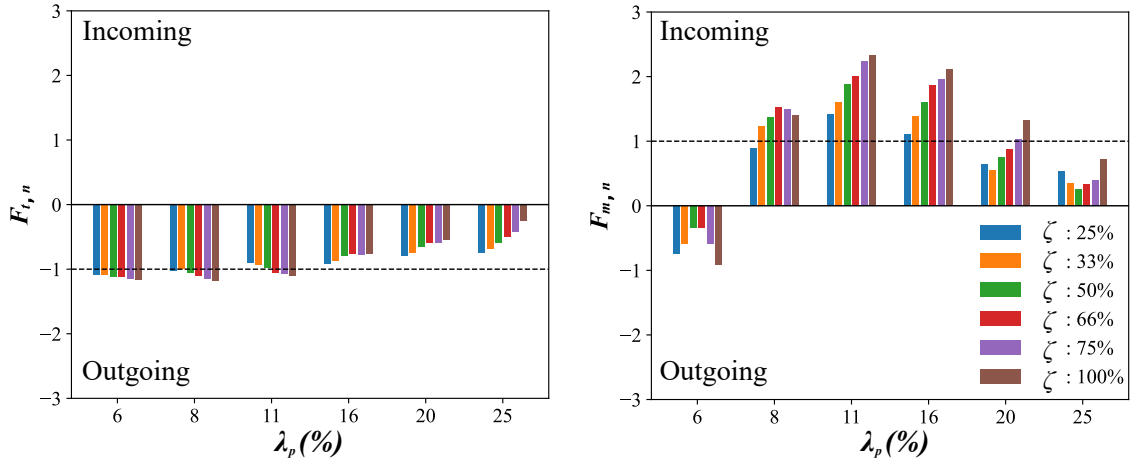


(c) Location:  $B_v$

Figure 5.10: Normalized pollutant transport rate due to turbulence diffusion,  $F_{t,n}$ , and due to mean flow,  $F_{m,n}$ , under  $\theta = 0^\circ$  inflow wind through faces of the defined control volume around the target building.



(d) Location:  $L_v$



(e) Location:  $R_v$

Figure 5.10: (Continued).

flow to inflow patterns. This transition highlights the intricate interplay of factors within the urban design, underscoring its profound impact on pollutant dispersion dynamics.

From Figures 5.10b and 5.10c, it is evident that the pollutant transport rates through the front and back faces of the control volume follow a relatively straightforward trend. As expected, an inflow of the pollutant is observed at  $F_v$ , while conversely, the mean flow carries the pollutant out of the control volume through  $B_v$ . In cases with low  $\lambda_p$  values, minimal variation compared to the baseline quantities is

recorded, which can be justified by the relatively minor disturbance that the stream-wise flow experiences. However, as a consequence of mean flow lateral diversion due to enhanced heterogeneity in more densely packed scenarios, pollutant mixing is significantly promoted while the stream-wise velocity is reduced. Furthermore, as discussed earlier, a relatively smaller portion of the elevated pollutant plume is drawn down into the “canyons”, further contributing to these dynamics. This reduction in pollutant concentration is reflected in the gradual decrease of  $F_{m,n}$  evident with an increase in  $\zeta$ . It is also noteworthy that considerably small stream-wise gradients of pollutant concentration are predicted, which resulted in negligible variation of diffusive transport rates through the  $F_v$  and  $B_v$  faces of the defined control volumes.

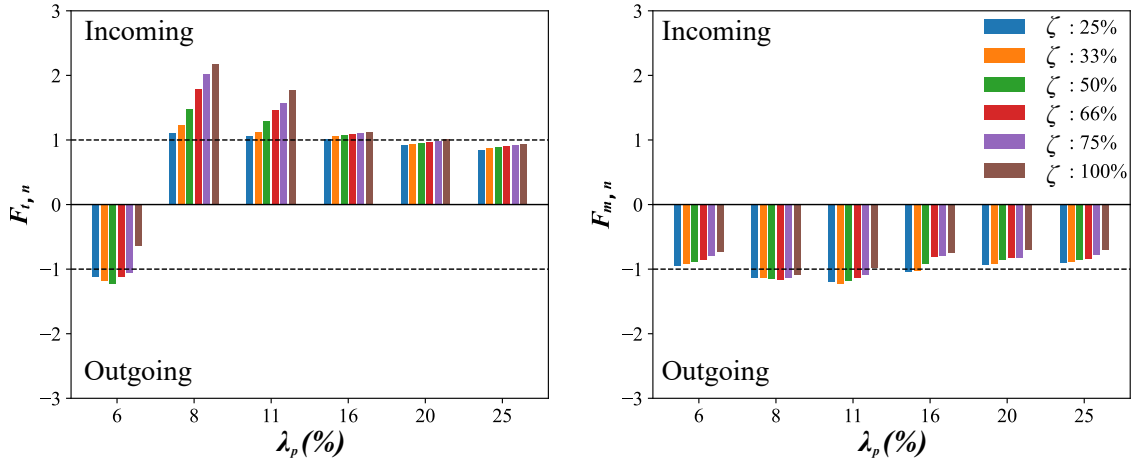
The presence of symmetry in both the geometry and inflow characteristics in the lateral direction for reference cases (i.e., aligned array), led to a similar convective outflow of the pollutant from side faces of  $L_v$  and  $R_v$ . However, as asymmetry is introduced by increasing  $\zeta$ , the removal of pollutants by mean flow through the left face of the control volume becomes more pronounced compared to the baseline values. This behavior aligns with expectations, as shifts in building rows redirect the plume to the left, consequently weakening the outflow through  $R_v$ . As shown in Figure 5.10e, in the most sparse arrangement ( $\lambda_p = 6\%$ ), where the level of flow disturbance is least, a net outflow was still observed through the right face. This indicates that, despite a reduction in outflow compared to the reference case, the dispersion pattern follows a trajectory similar to the reference case rather than resulting in an inflow. With a further increase in  $\lambda_p$  within the sparse category, the outflow through  $R_v$  transitions into an inflow, while the outflow through  $L_v$  is further intensified. In both cases, higher disposition levels typically enhance the pollutant transport rates in their respective directions. The gradual decrease in normalized transport rates observed in densely packed cases ( $\lambda_p = 16\%$ ,  $20\%$ , and  $25\%$ ) further supports the mentioned reduced entrained pollutant content from upper levels within these densely packed configurations. Concerning  $F_{t,n}$ , as concentrations within the control volume

exceed those outside, the diffusive outflow is recorded through both  $L_v$  and  $R_v$  faces. However, as pollutant mixing increases with  $\zeta$ , concentration distribution becomes more uniform, resulting in reduced turbulence diffusion.

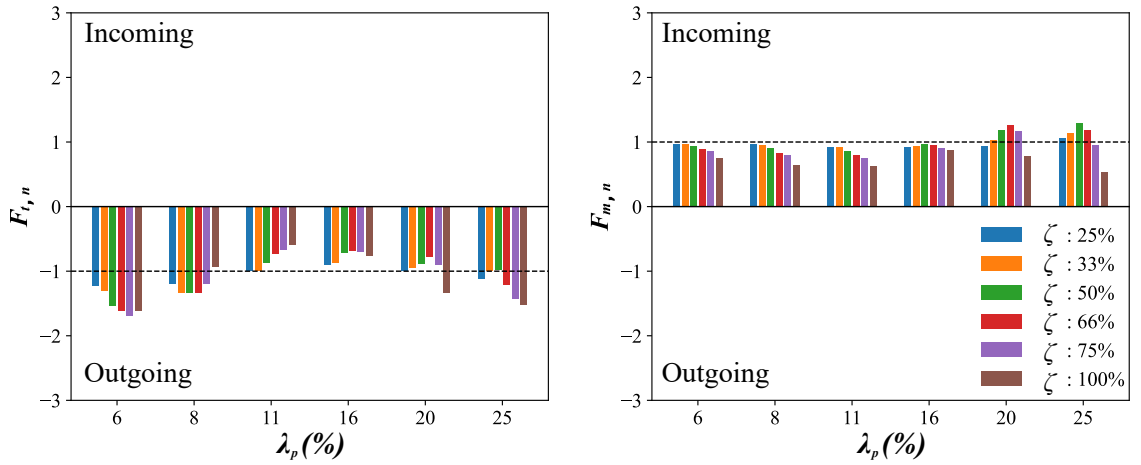
Following the conclusions derived in Section 5.4.1, it is evident that the orientation of the building cluster relative to the incident wind substantially influences dispersion patterns and flow dynamics. To emphasize these contrasts with the perpendicular wind, bar charts in Figure 5.11 are employed to quantify normalized pollutant transport rates under an oblique wind condition.

As can be seen in Figure 5.11a, the top boundary of the control volume for this orientation is also a primary egress route for pollutants. Similarly, the accumulation of pollutants well below the  $T_v$  is comparatively more pronounced in sparse configurations than in densely packed ones. However, it is clear that introducing planar heterogeneity does not exert as strong an influence on vertical convective transport rates as it does under  $0^\circ$  wind, as the quantities tend to hover closer to unity. This could be attributed to the fact that the urban flow already encounters an irregular arrangement in this orientation, and further disposition may either enhance or weaken the pre-existing flow structures. Nonetheless, there is an overall decrease in  $F_{m,n}$  quantities with increasing  $\zeta$ , which results from a complex interplay of various factors that affect the streamlines (e.g., downwash effects, circulatory vortices, flow separation, and wake regions) [205, 226]. This underscores the importance of data-driven analysis to effectively formulate flow responses to geometric variations in irregular cases. With regards to  $F_{t,n}$ , outflow due to turbulent diffusion is observed for cases with  $\lambda_p = 6\%$ , whereas for the remaining planar densities, the vertical gradient of pollutant concentration across the  $T_v$  plane implies an inflow.

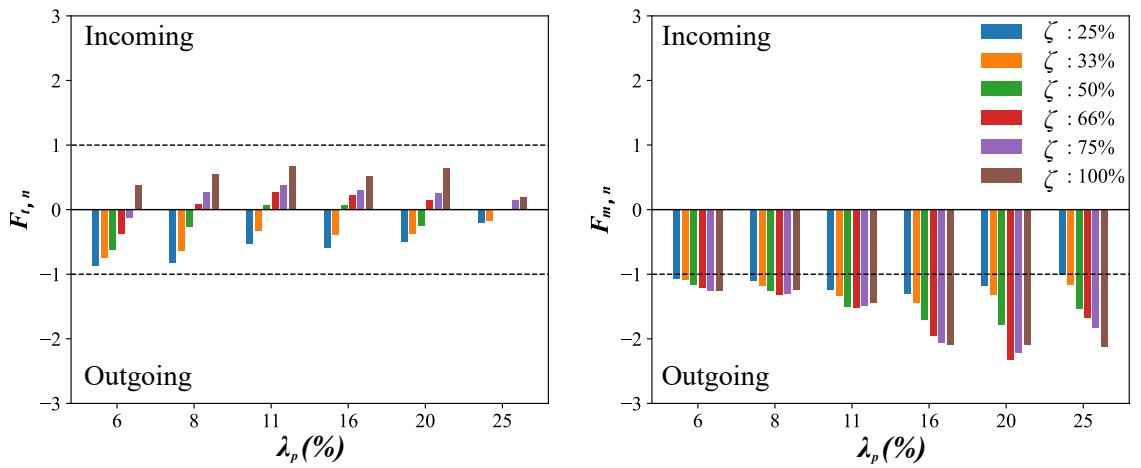
Unlike the  $0^\circ$  wind direction, it is not possible to distinctly classify the side faces of the control volume into stream-wise and lateral groups for the oblique wind. As illustrated in Figure 5.11, there is a convective net inflow of the pollutant into the control volume through the  $F_v$  and  $L_v$  borders (i.e., windward faces), while the oppo-



(a) Location:  $T_v$

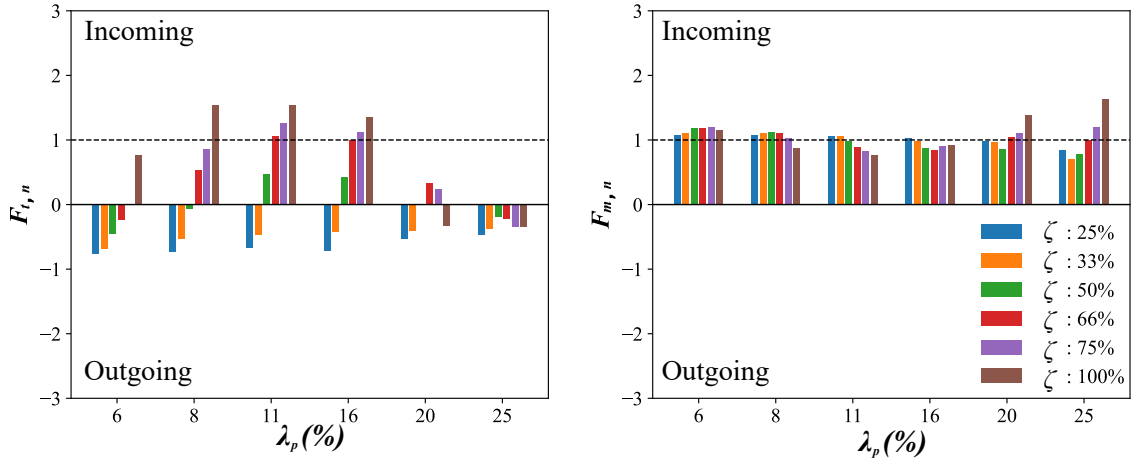


(b) Location:  $F_v$

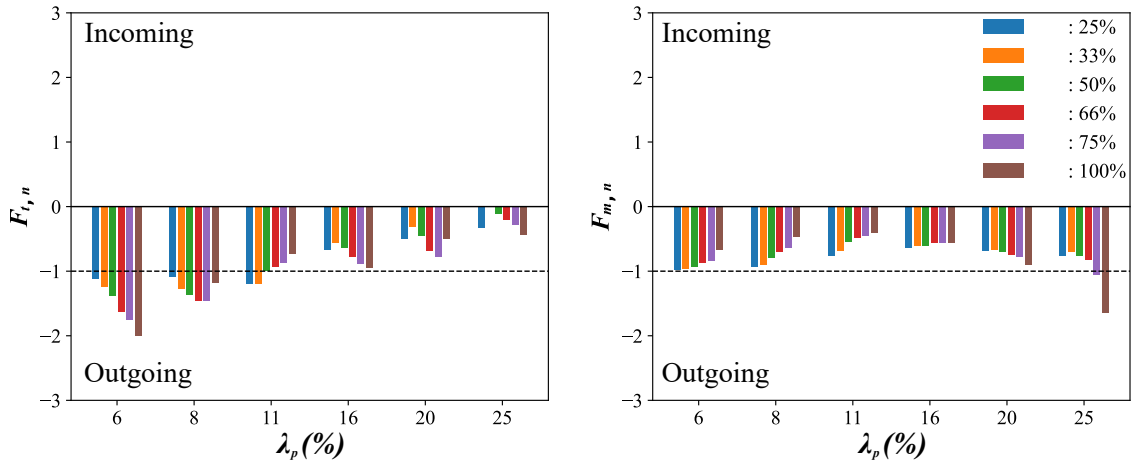


(c) Location:  $B_v$

Figure 5.11: Normalized pollutant transport rate due to turbulence diffusion,  $F_{t,n}$ , and due to mean flow,  $F_{m,n}$ , under  $\theta = 45^\circ$  inflow wind through faces of the defined control volume around the target building.



(d) Location:  $L_v$



(e) Location:  $R_v$

Figure 5.11: (Continued).

site situation holds true for the  $B_v$  and  $R_v$  (i.e., leeward faces). Among all faces, it is observed that the pollutant inflow rate by mean flow through  $F_v$  shows relatively low sensitivity to changes in  $\lambda_p$  within sparser arrangements. This observation suggests a weaker interaction with varying building spacing at this entry compared to its adjacent windward face  $L_v$ . The behavior of  $F_{m,n}$  at  $L_v$  becomes increasingly intricate as  $\lambda_p$  varies. In sparse configurations, there is a slight rise in convective pollutant inflow through  $L_v$  with  $\zeta$ , but this trend reaches a turning point where further disposition leads to a decrease in  $F_{m,n}$ . Similarly, densely packed arrangements display a

comparable trend at the  $F_v$  face, with an initial increase in inflow  $F_{m,n}$  followed by a subsequent decline. This turning point occurs earlier with higher  $\lambda_p$ . For dense cases at  $L_v$ ,  $F_{m,n}$  decreases initially with  $\zeta$ , but it starts to increase again after reaching a certain point, which arrives sooner with higher  $\lambda_p$ .

Regarding diffusive transport rates, an outflow through  $F_v$  is observed throughout all the cases, indicating higher pollutant concentrations than just outside the control volume, with variations in intensity in response to changing concentration gradients. In contrast, the  $L_v$  face experiences significant variability between the diffusive inflow and outflow pollutants, further complicating the response to  $\lambda_p$  and  $\zeta$ . For all levels of  $\lambda_p$ , the least disposition levels result in an outflow of pollutants, reflecting minimal geometric deviation from the reference cases. This trend diminishes as the spacing between buildings decreases. Interestingly, in denser arrays, an initial increase in  $\zeta$  appears to transition the diffusive pollutant transport rates from outflow to inflow. However, this trend reverses as  $\lambda_p$  increases and greater heterogeneity promotes pollutant outflow. This relationship, evident among the windward faces, also applies to the leeward faces  $R_v$  and  $B_v$ , albeit with more complexity. These trends highlight the significant impact of building orientation on pollutant transport, underscoring the need to consider directional disposition in urban planning to enhance air quality control.

Following the examination of the dynamics of dispersion patterns in response to varying geometrical parameters, the presentation of heat maps can provide a detailed visualization of the normalized area-averaged  $C^*$  across building facets. This approach helps clarify the impact of urban form on spatial pollutant distribution, as it provides an intuitive understanding of concentration gradients and hot spots. By highlighting areas of lower pollutant concentration, the heat maps provide valuable guidance about where to locate air intakes in the specific case of understudy to minimize the ingress of pollutants into buildings. This is particularly relevant in dense urban environments where strategic placement of these intakes can significantly

impact indoor air quality [5].

Figure 5.12 displays heat maps of  $C_{A,n}^*$  on five faces of the target building, showcasing the effects of varying  $\lambda_p$  and  $\zeta$  under a wind perpendicular to the disposition axis. Notably, an increase in the  $\lambda_p$  consistently results in the lowest recorded  $C_{A,n}^*$  across all facets. This is consistent with earlier discussions, indicating that in densely packed configurations, a relatively smaller amount of pollutants are drawn toward the vicinity of the target building from the elevated plume as planar heterogeneities are introduced to the geometry. Consequently, higher concentrations are detected at the top face compared to the side faces in densely packed arrangements, indicating the accumulation of pollutants at higher levels. In contrast, sparse cases exhibit the inverse pattern, in which side facets are generally prone to higher concentrations than roof areas. Nonetheless, it should be pointed out that the roof level exposure among sparse arrangements exhibits relatively modest variations compared to reference cases with  $C_{A,n}^*$  quantities hovering around unity. This trend is generally observed for other faces with low  $\lambda_p$  and  $\zeta$  as well, as they closely resemble the reference cases compared to others.

As  $\zeta$  increases, an overall consistent response is noticed among densely packed cases, where  $C_{A,n}^*$  gradually decreases on all faces. This indicates that pronounced flow interference, as evident from Figure 5.7, resulting from building proximity effects, could effectively contribute to the dispersion of pollutant contents [147]. In sparse configurations, the relatively modest flow interactions by neighboring buildings, coupled with the resulting diversion of the stream-wise flow in response to the increasing  $\zeta$ , facilitate the transport of a higher portion of pollutants to the windward facet ( $F_b$ ). Increased downwash and sheltering effects behind the target building for low  $\lambda_p$  and high  $\zeta$  values also lead to pollutant accumulation at the leeward face. At the side faces, the synergistic effect of geometric indices results in the most extreme responses, with the lateral disposition of building rows redirecting the pollutant plume either towards or away from these facets. For the cases investigated in this work,

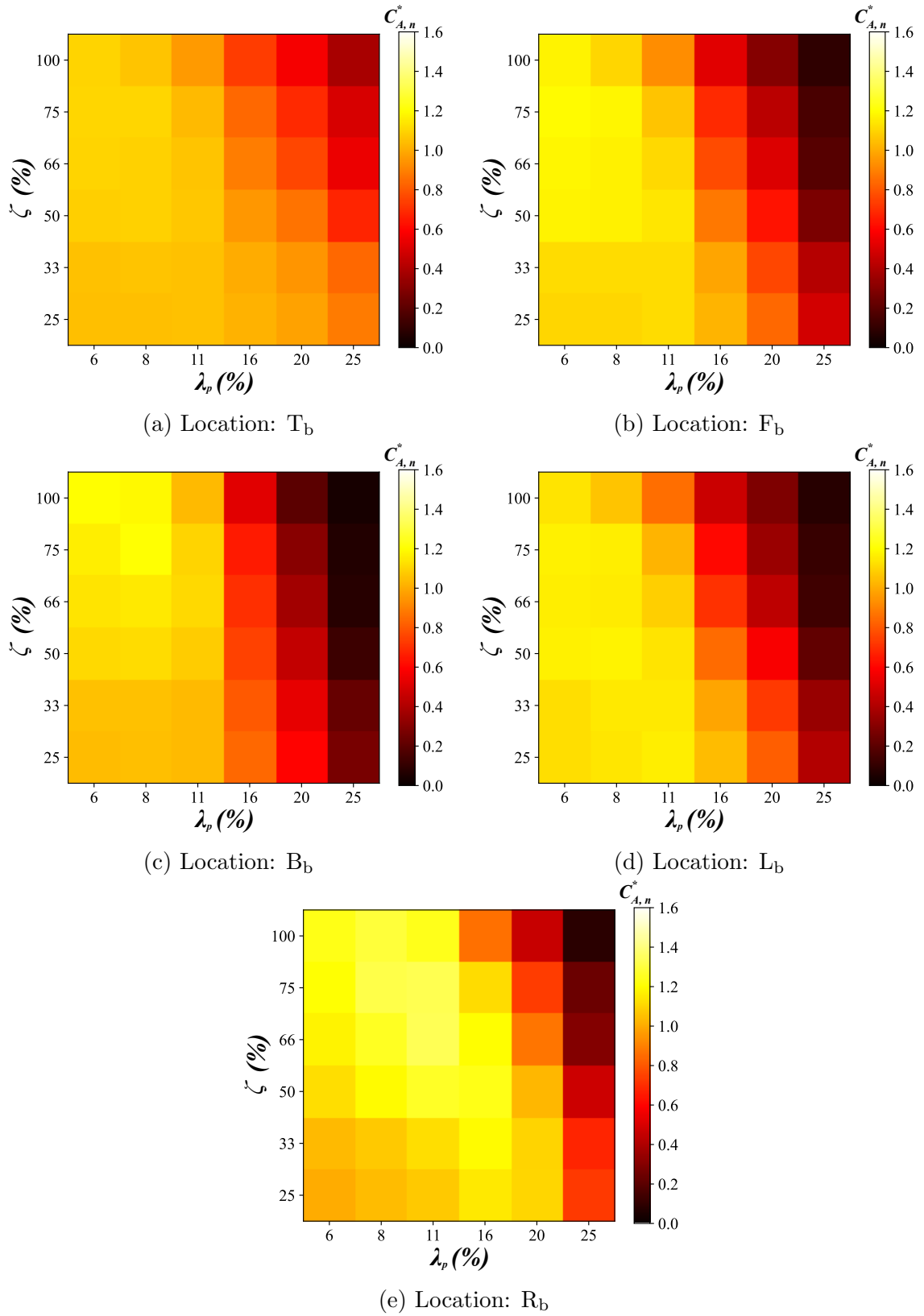


Figure 5.12: Heat maps of the area averaged  $C_n^*$  on the faces of the target building under  $\theta = 0^\circ$  wind direction: (a)  $T_b$ , (b)  $F_b$ , (c)  $B_b$ , (d)  $L_b$ , (e)  $R_b$ .

the highest quantities of  $C_{A,n}^*$  were obtained at  $R_b$  for  $\lambda_p = 11\%$  and  $\zeta$  between 50% to 75%. This implies that in such building arrangements, especially when there is a prevailing perpendicular wind, it is advisable to refrain from locating fresh air intakes on the side exterior faces.

The heat maps of  $C_{A,n}^*$  under oblique inflow wind conditions are presented in Figure 5.13, enabling a more comprehensive examination of the potential impacts that array orientation can exert on pollutant distribution. As can be seen, the responses to an oblique wind appear to introduce a higher degree of variability in recorded concentration levels at all exterior faces than the perpendicular wind. Roof-top exposure to pollutant content in sparse arrangements exhibits minimal sensitivity to planar heterogeneity. This argument holds to some extent for other facets as well, particularly for low quantities of  $\zeta$ . However, as  $\lambda_p$  and  $\zeta$  increase, the effects of building proximity become more pronounced, leading to a more noticeable response to geometric variations, in which  $C_{A,n}^*$  gradually decrease with  $\zeta$ .

Moving towards denser configurations, increased sensitivity to variations of  $\zeta$  is observed for windward facets, namely  $F_b$  and  $L_b$ . Opposite to the cases with low  $\lambda_p$ , the pollutant exposure levels do not exhibit a consistent trend with  $\zeta$ , and rather they show oscillating trends. This variability can be attributed to the intricate airflow dynamics within dense urban layouts, which can lead to the formation of various flow structures, including vortices or eddies. These flow structures can locally influence the velocity and direction of the wind, resulting in the observed variability in pollutant exposure levels. Nonetheless, increased heterogeneity in dense cases, in general, led to higher levels of pollutant exposure, albeit with variations among different cases. The analysis of the provided heat maps, when integrated with practical urban development considerations (e.g., land use efficiency, regulatory compliance, and infrastructure planning), aids urban planners with a more informed data-driven basis for positioning fresh air intakes. It is essential, however, to first acknowledge the specific direction of building disposition considered in this work, and only then adjust the estimations

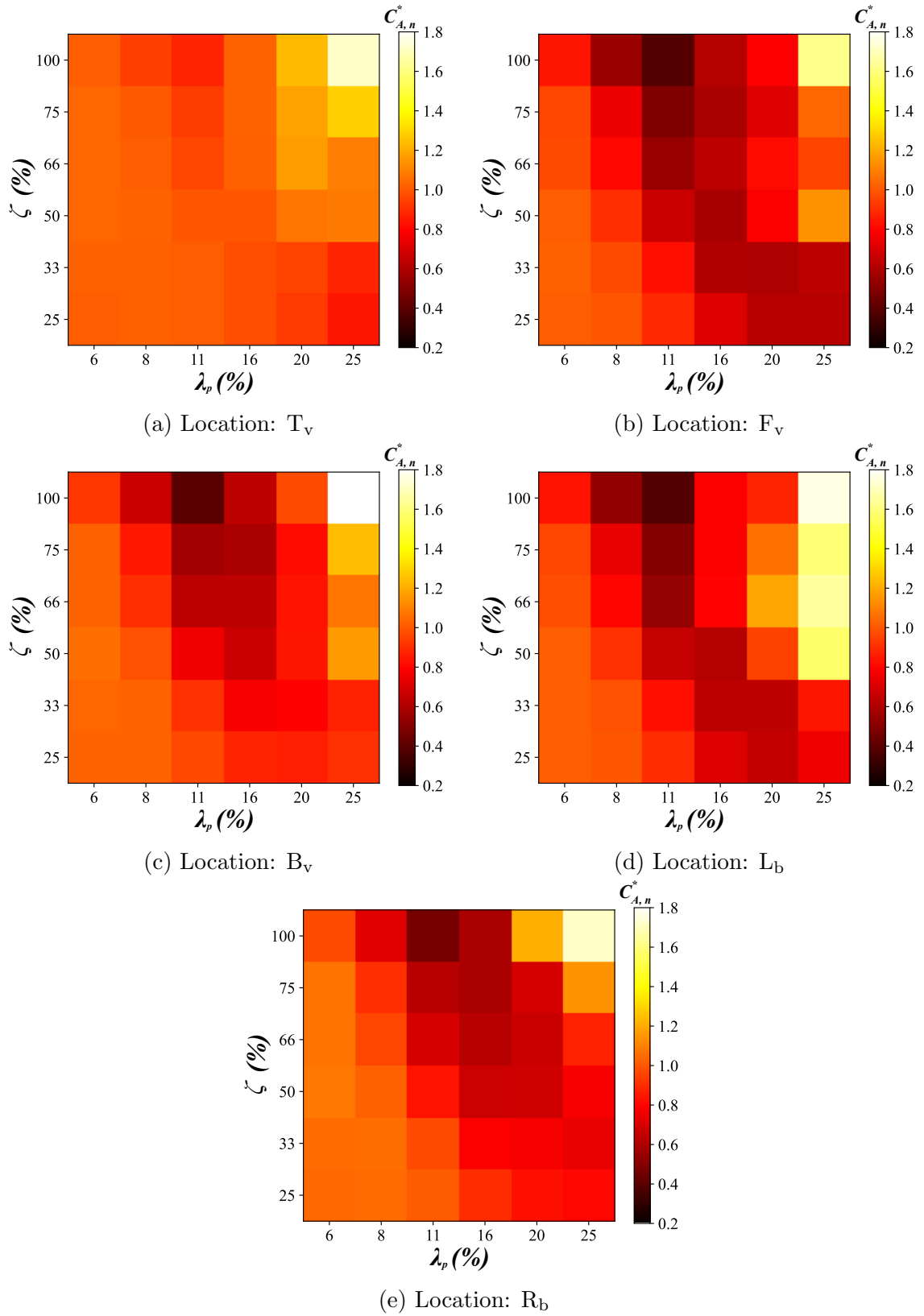


Figure 5.13: Heat maps of the area averaged  $C_n^*$  on the faces of the target building under  $\theta = 45^\circ$  wind direction: (a)  $T_b$ , (b)  $F_b$ , (c)  $B_b$ , (d)  $L_b$ , (e)  $R_b$ .

of the potential hot spots accordingly based on the prevailing wind patterns. This ensures that conclusions are aligned with the unique aerodynamic characteristics of each urban model.

### 5.4.3 Regression analysis

In this subsection, a regression analysis is presented, aimed at modeling the relationship between the normalized bulk concentrations in close proximity to a building, the dependent variable, and the urban form characterized by planar density and planar heterogeneity, serving as independent variables. Through the application of bi-variate polynomial regressions with variable order (linear, quadratic, and cubic), this analysis endeavors to capture the complex interactions between urban form and pollutant exposures. This multifaceted approach provides a richer understanding of urban flow dynamics, uncovering both linear trends and more complex patterns of non-linearity. The outcomes of this regression analysis contribute to the formulation of urban planning guidelines, providing a statistical foundation for informed decision-making. To achieve this goal, a curve-fitting is carried out, resulting in polynomials described by the general form presented in Equation 5.10. Table 5.2 presents the specific values of these polynomial coefficients, along with the coefficient of determination,  $R^2$ , for each of the regression models.

$$C_{vol,n}^* = a_1 + a_2\zeta + a_3\lambda_p + a_4\lambda_p\zeta + a_5\zeta^2 + a_6\lambda_p^2 + a_7\lambda_p\zeta^2 + a_8\lambda_p^2\zeta + a_9\lambda^3 + a_{10}\zeta^3 \quad (5.10)$$

The visual representation of the fitted regression models is presented in Figures 5.14 and 5.15 for  $0^\circ$  and  $45^\circ$  inflow winds, respectively. Regarding the  $0^\circ$  wind, the linear model provides a foundational understanding, achieving an  $R^2$  value of 0.864, which suggests that a linear relationship accounts for a substantial portion of the variability in  $C_{vol,n}^*$ . However, the quadratic model, with a higher  $R^2$  of 0.978, demonstrates that incorporating squared terms captures higher order aspects of the relationship more

Table 5.2: Coefficients of the bi-variate polynomials (Equation 5.10) fitted over the  $C_{vol,n}^*$  data.

$\theta$	Order	Coefficients									
		$a_1$	$a_2$ ( $10^{-3}$ )	$a_3$ ( $10^{-1}$ )	$a_4$ ( $10^{-4}$ )	$a_5$ ( $10^{-4}$ )	$a_6$ ( $10^{-3}$ )	$a_7$ ( $10^{-4}$ )	$a_8$ ( $10^{-4}$ )	$a_9$ ( $10^{-4}$ )	$a_{10}$ ( $10^{-4}$ )
	One	1.302	-0.768	-0.214							
0°	Two	0.937	4.732	0.100	-2.886	-0.111	-0.477				
	Three	0.532	8.891	0.898	-8.541	-0.170	-4.982	0.018	0.112	0.821	-0.001
	One	0.901	-0.111	0.062							
45°	Two	1.403	-6.066	-0.445	3.445	0.083	1.002				
	Three	1.504	5.423	-1.222	-7.805	-0.580	8.818	0.042	0.201	-1.915	

Table 5.3: Performance evaluation of fitted regressions given in Table 5.2, using coefficient of determination ( $R^2$ ), average relative error ( $e_{avg}$ ), and maximum relative error ( $e_{max}$ ).

$\theta$	Order	$R^2$	$e_{avg}(\%)$	$e_{max}(\%)$
	One	0.864	5.301	17.912
0°	Two	0.978	1.998	9.526
	Three	0.993	1.111	2.928
	One	0.190	7.056	30.056
45°	Two	0.703	4.334	20.766
	Three	0.888	2.810	10.034

effectively. The contours generated by the quadratic model reveal that the influence of planar density and heterogeneity on pollutant distribution is not strictly proportional but exhibits curvature, indicating interactions between these independent variables that a simple linear model cannot capture. The cubic model, although offering the highest  $R^2$  of 0.993, suggests further non-linear complexity, yet the modest increase in explanatory power over the quadratic model might not justify its use in practical urban planning scenarios. The mean relative error obtained by the cubic model,  $e_{avg} = 1.111\%$ , shows minimal improvement compared to the quadratic model, with  $e_{avg} = 1.998\%$  (Table 5.3). It should be also noted that even  $\zeta$  is a key factor in

determining  $C_{vol,n}^*$ , regression analysis reveals a semi-linear sensitivity of the bulk concentration to this variable, compared to its strongly non-linear relationship with  $\lambda_p$ .

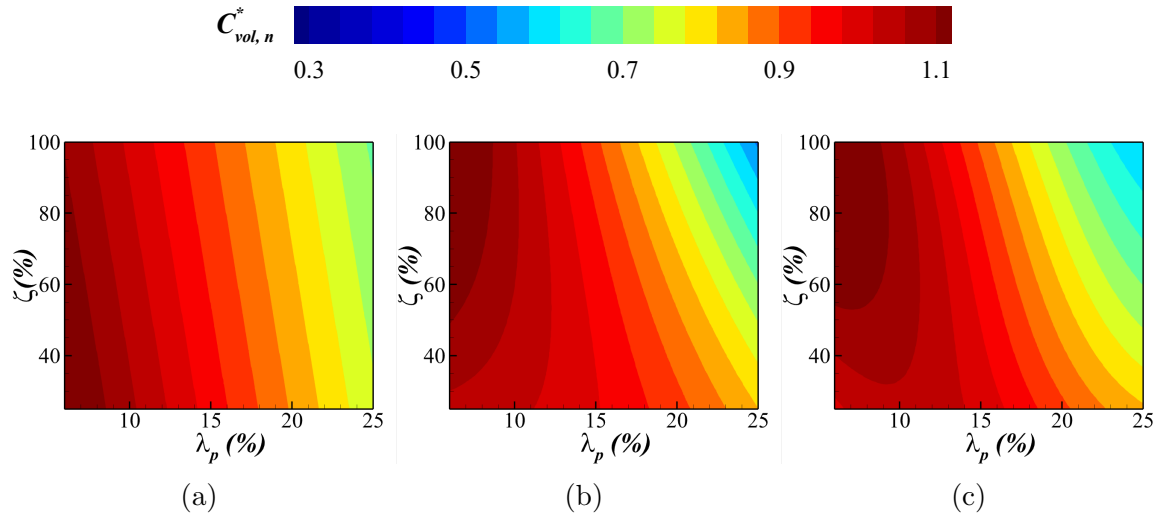


Figure 5.14:  $C_{vol,n}^*$  distribution in terms of the  $\lambda_p$  and  $\zeta$  under  $\theta = 0^\circ$  wind direction using (a) linear, (b) quadratic, and (c) cubic polynomials.

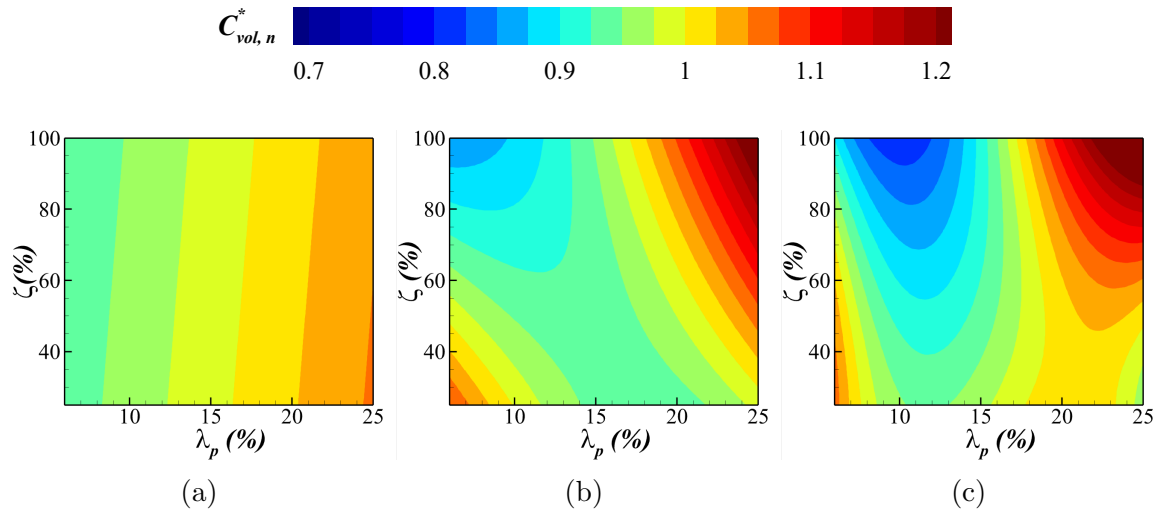


Figure 5.15:  $C_{vol,n}^*$  distribution in terms of the  $\lambda_p$  and  $\zeta$  under  $\theta = 45^\circ$  wind direction using (a) linear, (b) quadratic, and (c) cubic polynomials.

For the 45-degree wind direction, the regression analysis presents a compelling contrast to the 0-degree case. The  $R^2$  values and corresponding contours underscore a distinct departure from linearity, with the linear model's  $R^2$  of 0.190 indicating

a poor fit and thus indicating its unsuitability for capturing the dynamics of pollutant concentration. In contrast, the quadratic model, with an  $R^2$  of 0.703, provides a considerably better fitting representation, although it does not capture the non-linear interactions of the independent variables as robustly as in the  $0^\circ$  case. The cubic model for the  $45^\circ$  wind direction yields an  $R^2$  of 0.888, which, although significant, suggests that the higher order effects in this orientation are more pronounced than those of the  $0^\circ$  wind direction. Nevertheless, the cubic model outperforms the quadratic model by more thoroughly capturing the non-linear relationships among variables, with mean relative errors of 2.810% and 4.334%, respectively. However, it is recommended to refrain from using high-order fits when possible. This is because applying a high-order fit can lead to significant discrepancies for input data that fall outside the range of the data used in the regression analysis.

## 5.5 Conclusion

A rigorous investigation of the outdoor air quality and ventilation was carried out in simulated urban environments, with a particular focus on the dispersion of pollutants originating from roof-based sources. The objectives of this study were motivated by the need to advance the understanding of how varying urban forms impact air pollution distribution, especially in relation to the strategic placement of fresh air intakes. The synergistic effects of several of the most influential urban morphological characteristics were numerically explored through the definition of six levels of planar density, seven levels of building dispositions, and two array orientations with respect to inflow wind direction. Normalized velocity ratio ( $V_n^*$ ), retention time ( $\tau_n$ ), non-dimensionalized concentration ( $C_n^*$ ), and convective and diffusive transport rates ( $F_{m,n}$  and  $F_{t,n}$ ) were analyzed in close proximity to a target building to assess urban form effectiveness and dispersion flow dynamics. This study yielded the following key findings:

- For  $0^\circ$  inflow wind, the volume-averaged  $V_n^*$  consistently decreased when transitioning from aligned to staggered building configurations. This reduction was more pronounced in denser urban arrays, highlighting the significant impact of disrupting the channeling flow characteristic of aligned arrays on the resistance to purging flow. Notably, a maximum reduction of 12% was observed for  $\lambda_p = 6\%$  at the highest  $\zeta$ , while it reached approximately 50% for  $\lambda_p = 25\%$ .
- For the  $\tau_n$  under  $0^\circ$  wind, the response varied notably with urban density. In sparse configurations, where the urban flow was minimally affected, the decrease in  $V_n^*$  led to a modest increase in  $\tau_n$ , confirming the conventional inverse relationship between these two parameters. In contrast, densely packed layouts exhibited an unexpected decrease as planar heterogeneity increased, with reductions of up to 41% for  $\lambda_p = 25\%$  and  $\zeta = 100\%$ . This suggests that in dense urban landscapes, the heightened turbulence structures caused by neighboring buildings more effectively disperse the pollutants around buildings. However, it needs to be acknowledged that the results of this study pertain to the dispersion of an elevated plume. The considerable decline in  $V_n^*$  as  $\zeta$  increases in compact settings, could adversely impact the ventilation at pedestrian height, and in turn hinder the dispersion of pollutants at ground level (e.g., traffic-related pollutants).
- Under an oblique wind direction, the increase in  $V_n^*$  in sparsely packed arrangements indicated an enhanced ventilation which corresponded with a decrease in  $\tau_n$ , suggesting more efficient pollutant dispersion. In cases with  $\lambda_p = 16\%$ ,  $20\%$ , and  $25\%$ ,  $V_n^*$  initially increased due to wind acceleration through urban channels but later decreased at higher disposition levels due to blockage effects, impeding airflow. Simultaneously,  $\tau_n$  exhibited a complex pattern, initially improving ventilation at lower planar heterogeneities but later hindering pollutant purge as blockage effects intensified.

- Dynamics of dispersion patterns were explored through the examination of pollutant transport rates to a control volume enclosing the target building. For the perpendicular wind, convective outflow through the top plane was generally observed, while for denser configurations modifications to flow patterns caused by adjacent buildings led to increased pollutant outflow through the top face and a shift in diffusive transport rates from outflow to inflow. Additionally, the planar heterogeneity promoted asymmetrical pollutant dispersion in lateral directions, enhancing removal on one side of the control volume while reducing it on the other.
- In the oblique wind orientation, sparse setups had higher vertical convective transport rates than dense ones, with planar heterogeneity showing relatively modest impacts. Interestingly, both convective and diffusive pollutant transport rates across different faces of the control volume showed varying sensitivities to  $\lambda_p$  and  $\zeta$ , emphasizing the importance of considering building orientation and disposition in urban planning for effective air quality control.
- Under  $0^\circ$  wind conditions, transitioning to denser layouts progressively reduced the area-averaged  $C_n^*$  across all faces of the target building due to the diminished downward pull of the elevated pollutant plume. In sparser layouts, the side facets showed relatively higher exposures compared to the roof, with the  $R_b$  facet in a case with  $\lambda_p = 11\%$  and  $\zeta = 66\%$  experiencing a notable 33% increase. Under oblique winds, sparse configurations showed relatively modest changes, particularly at lower levels of  $\zeta$ . However, with increasing  $\lambda_p$  and  $\zeta$ , the proximity of surrounding buildings led to more pronounced but variable exposure levels across different facets. This variability was particularly evident in denser settings, emphasizing the importance of considering the specific orientation of building clusters and prevailing wind directions in urban planning practices.

- For the 0-degree wind direction, the quadratic regression model, with an  $R^2$  of 0.978, adequately captured the non-linear relationship between bulk morphological parameters and normalized concentrations, indicating a more complex interaction than suggested by the linear model. Under a 45-degree wind, the linear regression model exhibited significant inadequacies, while the cubic model proved to be a suitable choice for accurately representing the data, achieving an  $R^2$  value of 0.888. Nonetheless, the quadratic model is generally preferred,  $R^2 = 0.703$ , as higher order models might not perform well when used to make estimations for input variables that fall outside the range of the data used in the curve fitting process.

In the end, it is necessary to acknowledge that in numerical simulations of flow over an array of blocks representing urban buildings, there is an inherent limitation due to the use of symmetry boundary conditions, in particular over the lateral faces of the computational domain. These conditions, while simplifying the computational process, may not accurately represent the complex and varied nature of real-world urban environments. However, the adoption of symmetry boundary conditions is justified in this context, as it significantly reduces computational resources and time, allowing for a more focused analysis of dispersion dynamics in the presence of generic urban non-uniformities. This approach is particularly useful in conceptual studies where the objective is to understand flow patterns and interactions, rather than to replicate specific urban scenarios in full detail. It is crucial to recognize these limitations when interpreting the results, ensuring that the conclusions drawn are contextualized within the scope of the study's assumptions.

# Chapter 6

## Conclusions and Future Work

### 6.1 Conclusions

This research addresses the complexities of modeling and controlling urban pollutant dispersion, effectively linking theoretical advancements to practical applications in urban environmental engineering. Computational Fluid Dynamics (CFD) was employed to facilitate advancing the accuracy of numerical predictions concerning the dispersion patterns of pollutants emitted from roof-based sources. In the following, the specific outcomes of each research objective are outlined. These findings not only advance current knowledge of urban dispersion flow dynamics but also hold promise for influencing future urban development, where growth and sustainability align.

The first objective set the stage for the study by establishing a well-tested framework for the numerical modeling of atmospheric pollutant dispersion. To this aim, the high-quality and full-scale dispersion data set of the Mock Urban Setting Tests (MUST) experiment was used to benchmark various modeling settings in the context of complex urban geometries. Given the primary interest in the bulk quantities of the flow and dispersion parameters, the steady-state framework was selected to treat the governing equations. To align with the guidelines recommended in the existing literature regarding the minimum dimensions of the computational domain, it became necessary to expand these limits further, especially for geometries similar to that of the MUST experiment with relatively wide spanwise dimensions. This extension was

crucial not only to attain more reliable results but also to prevent nonphysical back-flows at the outlet or any artificial acceleration of the flow, thereby improving the rate of convergence. The logarithmic inflow velocity profile was selected over the power-law, as it provided a more physically meaningful representation of the atmospheric boundary layer. Several turbulence closure models were also tested to identify the most appropriate representation of Reynolds stresses, leading to the least deviation between the predicted and measured pollutant concentrations in urban configurations with a particular focus on the source location.

The overall superiority of the standard  $k - \varepsilon$  model was evident among all cases by successfully predicting an average of 66% of concentrations within a factor of two (FAC2) of the measurements. In comparison, the RNG  $k - \varepsilon$  and SST  $k - \omega$  models achieved this accuracy for 61% and 59% of concentrations, respectively. An over-prediction of the pollutant concentration field was recorded by all turbulence closures in cases with pollutant sources located within the array. This stemmed from the known shortcoming of RANS in under-predicting the turbulence kinetic energy. However, this deficiency was more effectively mitigated by the combined influence of geometry-induced turbulence and the relatively higher turbulence kinetic energy predictions provided by the standard  $k - \varepsilon$  model compared to other closure models. The statistical analysis further revealed that standard  $k - \varepsilon$  more accurately represented the vertical concentration patterns (average FAC2 of 68%) than horizontal distributions (average FAC2 of 62%). While generally over-predicting near the source, the model under-predicted at greater horizontal distances, particularly in the farthest sampling line. Despite some accuracy degradation, the standard  $k - \varepsilon$  model remained the preferred choice compared to alternative models. In the end, due to the practical challenges of acquiring reliable dispersion data for urban geometries, conventional methods for determining the optimal turbulence Schmidt number ( $Sc_t$ ) become impractical. In response, this study adopted a locally variable definition of  $Sc_t$  and examined it in the context of urban dispersion flows. Using the MUST data

set, implementing this method resulted in  $Sc_t$  values ranging from 0.70 to 0.75, which led to 8% improvement in matching experimental findings.

The second objective built upon the established framework in the first step, aiming to fine-tune the selected turbulence closure model (i.e., standard  $k - \varepsilon$ ) to enhance its applicability and accuracy in predicting atmospheric dispersion in urban environments. In this regard, an adapted optimization framework employing a carefully adjusted genetic algorithm was used to re-calibrate the turbulence model. A training scenario featuring a roof-based source was selected from the MUST full-scale dispersion data set, which inherently accounts for realistic atmospheric conditions. Through exploiting the empirical correlation among coefficients in the atmospheric surface layer,  $C_{\varepsilon 1}$  was excluded from the re-calibration process, as it could be calculated using  $C_\mu$ ,  $C_{\varepsilon 2}$ , and  $\sigma_\varepsilon$ . Additionally, an exhaustive sensitivity study was also carried out to investigate the possibility of further reducing the computational load of the optimization exercise. It was shown that  $\sigma_k$  had minimal impact on all validation metrics, allowing it to be disregarded during optimization. Instead, its adjusted value was determined through a direct sensitivity analysis after the optimized values for the remaining coefficients were found.

The parameter spaces of empirical constants within the recommended intervals were systematically explored to extract a refined range for each. A robust objective function was formulated, incorporating both linear and logarithmic validation metrics. This objective function navigated the re-calibration process, gradually converging toward coefficient sets that produced more accurate and reliable representations of flow (velocity and turbulence kinetic energy) and dispersion (pollutant concentration) fields. The proposed ranges identified as most effective for atmospheric dispersion modeling in generic urban clusters are  $0.14 \leq C_\mu \leq 0.15$ ,  $1.30 \leq C_{\varepsilon 1} \leq 1.46$ ,  $1.68 \leq C_{\varepsilon 2} \leq 1.80$ ,  $1.12 \leq \sigma_\varepsilon \leq 1.20$ , and  $0.87 \leq \sigma_k \leq 1.00$ . Respectively, 8% and 27% increase in accuracy of the predicted concentrations (among 74 sampling points) and turbulence kinetic energy (among 18 sampling points) was recorded. The gen-

eral applicability of the modified model was further tested and verified by modeling additional cases with varied inlet boundary conditions, source locations, and building orientations. Across all test cases, there was an average increase in prediction accuracy of 15% for turbulence kinetic energy, and an improvement of 5% for both velocity and concentrations.

Implementing the assembled infrastructure specifically tailored for CFD simulations of atmospheric pollutant distributions facilitated the next objective, which was to unravel the synergistic effects of urban geometric bulk characteristics on dispersion dynamics. This aspect of the study was pivotal in translating the enhanced modeling capabilities into practical insights regarding the impact of urban forms on outdoor and indoor air quality concerning pollutants emitted from roof-based sources. To ensure that the results could be translated and applied to urban planning practices, a series of case studies were defined, systematically varying some of the most influencing bulk and specific characteristics, namely planar density, planar heterogeneity levels, and array orientation. The high-resolution modeling within a block array was carried out at the neighborhood scale to investigate the localized dispersion patterns within varied urban configurations.

The study yielded valuable insights. Under perpendicular wind conditions relative to the disposition axis, there was a consistent decrease in ventilation capacity when moving from aligned to staggered building configurations. This reduction was more pronounced in denser urban arrays, with a maximum decrease of 50% in the most densely packed case, compared to 12% in the most sparsely arranged layout. The pollutant retention time showed an overall modest increase in sparser layouts as expected, while, interestingly, denser layouts exhibited significant decreases as planar heterogeneity increased (up to 41% reduction in the most extreme scenario), indicating that pronounced turbulent mixing induced by surrounding buildings plays a dominant role in diluting the pollutant stream. Under oblique wind conditions, varying land use and planar heterogeneity showed diverse impacts on pollutant dispersion.

In sparsely populated urban layouts, there was improved ventilation and more efficient pollutant dispersion as heterogeneity increased, resulting in a maximum reduction of 26% in pollutant content. However, in denser urban areas, ventilation capacity initially increased due to wind channeling but later decreased due to blockage effects. This led to complex patterns in pollutant retention time, with some cases showing an increase in pollution levels as high as 29%.

The examination of pollutant transport rates revealed that denser configurations, especially under perpendicular wind conditions, led to significant changes in flow patterns. A consistent convective outflow through the top plane was observed, which was intensified as the urban layouts became denser. This trend caused a shift in diffusive pollutant transport, transitioning from outflow to inflow due to significant changes in concentration gradients. Planar heterogeneity led to uneven pollutant dispersion, promoting removal on one side while reducing it on the other. In oblique wind conditions, sparser setups had higher vertical convective transport rates than denser ones, while planar heterogeneity exhibited a modest impact. Pollutant transport rates varied across control volume side faces, highlighting the need to acknowledge the prevailing wind and disposition directions in the planning stage for better air quality management.

Analyzing area-averaged concentrations on building facets revealed reduced exposures with increased planar density and heterogeneity, attributed to decreased downwash of the elevated plume. In sparser configurations, side facets of buildings exhibited higher pollutant exposure, notably with moderate planar density and heterogeneity levels (33% increase compared to the associated generic reference case). Under oblique wind conditions, this pattern became more variable, with denser configurations displaying pronounced fluctuations in exposure levels across different building facets. Lastly, the relationship between urban morphology and variation of pollutant levels (normalized by quantities obtained from well-studied generic geometries of aligned arrays) was analyzed via regression analysis, contributing to the formulation

of the urban planning guidelines. Under perpendicular wind, a quadratic regression model effectively captured the inherently non-linear relationship between these variables, with a coefficient of determination ( $R^2$ ) of 0.978 and a mean relative error of about 2%. However, under an oblique wind, the linear model displayed significant inadequacies ( $R^2 = 0.190$ ), while both the quadratic and cubic models offered a more precise representation with  $R^2$  values of 0.703 and 0.888, respectively. These fitted regressions could aid urban planners in estimating the extent to which changes in bulk geometric parameters might affect the bulk pollutant concentration levels around buildings.

This study stands as a testament to the intricate relationship between urban design and environmental health. Each objective, while distinct in focus, collectively underlines the importance of accurate and reliable modeling in urban air quality management. The advancements in CFD modeling and turbulence model optimization contribute notably to our ability to predict and mitigate urban air pollution. Meanwhile, the exploration of urban morphology's effects offers practical insights for urban planners, highlighting how design choices can influence air quality. Going forward, the methodologies and insights derived from this research have the potential to improve urban planning policies and practices. The refined modeling techniques can aid in developing more effective pollution control strategies, particularly in dense urban areas where air quality is a pressing concern. Furthermore, the study's emphasis on sustainable urban design aligns with global efforts to create healthier urban environments, resonating with contemporary themes in urban development.

## 6.2 Future Work

While providing valuable insights into urban pollutant dispersion, this research encounters several limitations inherent in its methodologies and model assumptions. The utilization of steady-state Reynolds-Averaged Navier-Stokes (RANS) models, despite their computational efficiency, presents a limitation due to their inability to

capture the full complexity of turbulence structures compared to Large Eddy Simulations (LES). Nevertheless, it's important to recognize that conducting high-fidelity simulations like LES in the context of building clusters remains challenging and computationally demanding, even with current computing capabilities. Additionally, the assumption that pollutants are passive and inert gases, coupled with the focus on neutral atmospheric stability conditions, may not fully capture the dynamics and chemically reactive nature of realistic urban atmospheric dispersions. Given these limitations, several areas are ripe for future research to build upon and enhance the findings of this study:

- Regarding methodological advancements, efforts should be expanded beyond the assumption of pollutants as neutrally buoyant and inert gases. Additionally, accounting for diverse atmospheric stability conditions should be considered to improve the realism and applicability of the models.
- Additional wind directions beyond the extreme cases of perpendicular and oblique orientations need to be explored. That provides a more comprehensive understanding of pollutant dispersion under diverse urban wind scenarios.
- The exploration of how urban morphology affects pollutant dispersion could be enhanced by examining a larger number of cases featuring more complex heterogeneities, such as simplified geometries that closely resemble realistic urban blocks (e.g., varying building heights and aspect ratios). This approach would enable further refinement of the correlations and guidelines, improving their applicability and accuracy across a wider range of diverse urban configurations.
- The investigation into how the momentum ratio of pollutant sources interacts with urban forms in determining dispersion patterns could present new avenues for promoting sustainable urban designs. This approach, which merges active and passive strategies, could significantly enhance operational practices

for rooftop emissions. Such improvements have the potential to lead to substantial reductions in unnecessary energy waste, thereby contributing to more energy-efficient and environmentally friendly urban environments.

- The potential of LES in urban dispersion modeling within compact geometries should be investigated to exploit its capability to capture finer details of turbulence and more accurate representations of Reynold's stressed components. That can further contribute to understanding airflow and pollutant dispersion in complex urban environments.
- The impact of urban non-uniformities on indoor air quality can be further systematically studied in the context of natural cross ventilation. The results could inform decisions on the location and types (e.g., symmetrical or asymmetrical) of the openings.

# Bibliography

- [1] W. H. O. (WHO), *Ambient (outdoor) air pollution*, 2022. [Online]. Available: [https://www.who.int/news-room/fact-sheets/detail/ambient-\(outdoor\)-air-quality-and-health#](https://www.who.int/news-room/fact-sheets/detail/ambient-(outdoor)-air-quality-and-health#) (visited on 12/01/2023).
- [2] R. Fuller and et al., “Pollution and health: a progress update,” *The Lancet Planetary Health*, vol. 6, no. 6, e535–e547, 2022. DOI: 10.1016/S2542-5196(22)00090-0.
- [3] Z. Li *et al.*, “Review on pollutant dispersion in urban areas-part A: Effects of mechanical factors and urban morphology,” *Building and Environment*, vol. 190, p. 107534, 2021. DOI: 10.1016/J.BUILDENV.2020.107534.
- [4] F. S. Lien, E. Yee, H. Ji, A. Keats, and K. J. Hsieh, “Progress and challenges in the development of physically-based numerical models for prediction of flow and contaminant dispersion in the urban environment,” *International Journal of Computational Fluid Dynamics*, vol. 20, no. 5, pp. 323–337, 2006. DOI: 10.1080/10618560600898528.
- [5] M. Lateb, C. Masson, T. Stathopoulos, and C. Bédard, “Numerical simulation of pollutant dispersion around a building complex,” *Building and Environment*, vol. 45, no. 8, pp. 1788–1798, 2010. DOI: 10.1016/J.BUILDENV.2010.02.006.
- [6] F. Toja-Silva, C. Pregel-Hoderlein, and J. Chen, “On the urban geometry generalization for CFD simulation of gas dispersion from chimneys: Comparison with Gaussian plume model,” *Journal of Wind Engineering and Industrial Aerodynamics*, vol. 177, pp. 1–18, 2018. DOI: 10.1016/j.jweia.2018.04.003.
- [7] S. Park, H. Park, and J. Seo, “Analysis on the Exhaust Air Recirculation of the Ventilation System in Multi-Story Building,” *Applied Sciences*, vol. 11, no. 10, p. 4441, 2021. DOI: 10.3390/app11104441.
- [8] K. Lam, S. Kot, K. Fung, and R. Ma, “A field validation of a roof-top dispersion formula in an urban centre,” *Journal of Wind Engineering and Industrial Aerodynamics*, vol. 21, no. 3, pp. 295–305, 1985. DOI: 10.1016/0167-6105(85)90041-8.
- [9] B. Hajra, T. Stathopoulos, and A. Bahloul, “Assessment of pollutant dispersion from rooftop stacks: ASHRAE, ADMS and wind tunnel simulation,” *Building and Environment*, vol. 45, no. 12, pp. 2768–2777, 2010. DOI: 10.1016/J.BUILDENV.2010.06.006.

- [10] M. Lateb, R. N. Meroney, M. Yataghene, H. Fellouah, F. Saleh, and M. C. Boufadel, “On the use of numerical modelling for near-field pollutant dispersion in urban environments: A review,” *Environmental Pollution*, vol. 208, pp. 271–283, 2016. DOI: 10.1016/J.ENVPOL.2015.07.039.
- [11] Y. Tominaga and T. Stathopoulos, “CFD simulation of near-field pollutant dispersion in the urban environment: A review of current modeling techniques,” *Atmospheric Environment*, vol. 79, pp. 716–730, 2013. DOI: 10.1016/J.ATMOENV.2013.07.028.
- [12] B. Blocken, “50 years of Computational Wind Engineering: Past, present and future,” *Journal of Wind Engineering and Industrial Aerodynamics*, vol. 129, pp. 69–102, 2014. DOI: 10.1016/J.JWEIA.2014.03.008.
- [13] Y. Tominaga and T. Stathopoulos, “Ten questions concerning modeling of near-field pollutant dispersion in the built environment,” *Building and Environment*, vol. 105, pp. 390–402, 2016. DOI: 10.1016/j.buildenv.2016.06.027.
- [14] B. Hajra, T. Stathopoulos, and A. Bahloul, “A wind tunnel study of the effects of adjacent buildings on near-field pollutant dispersion from rooftop emissions in an urban environment,” *Journal of Wind Engineering and Industrial Aerodynamics*, vol. 119, pp. 133–145, 2013. DOI: 10.1016/J.JWEIA.2013.05.003.
- [15] Y. Yang, S. Guangrong, Z. Chen, S. Hao, Z. Zhouyiling, and Y. Shan, “Quantitative analysis and prediction of urban heat island intensity on urban-rural gradient: A case study of Shanghai,” *Science of the Total Environment*, vol. 829, p. 154264, 2022. DOI: 10.1016/j.scitotenv.2022.154264.
- [16] Y. Dai, C. M. Mak, J. Hang, F. Zhang, and H. Ling, “Scaled outdoor experimental analysis of ventilation and interunit dispersion with wind and buoyancy effects in street canyons,” *Energy and Buildings*, vol. 255, p. 111688, 2022. DOI: 10.1016/J.ENBUILD.2021.111688.
- [17] Y. Toparlar, B. Blocken, B. Maiheu, and G. van Heijst, “A review on the CFD analysis of urban microclimate,” *Renewable and Sustainable Energy Reviews*, vol. 80, pp. 1613–1640, 2017. DOI: 10.1016/j.rser.2017.05.248.
- [18] J. Franke, A. Hellsten, K. Schlünzen, and B. Carissimo, “Best practice guideline for the cfd simulation of flows in the urban environment-a summary,” in *11th Conference on Harmonisation within Atmospheric Dispersion Modelling for Regulatory Purposes, Cambridge, UK, July 2007*, Cambridge Environmental Research Consultants, 2007.
- [19] R. Yoshie *et al.*, “Cooperative project for CFD prediction of pedestrian wind environment in the Architectural Institute of Japan,” *Journal of Wind Engineering and Industrial Aerodynamics*, vol. 95, no. 9-11, pp. 1551–1578, 2007. DOI: 10.1016/j.jweia.2007.02.023.
- [20] R. Zhao, S. Liu, J. Liu, N. Jiang, and Q. Chen, “Generalizability evaluation of k- $\epsilon$  models calibrated by using ensemble Kalman filtering for urban airflow and airborne contaminant dispersion,” *Building and Environment*, vol. 212, no. January, p. 108823, 2022. DOI: 10.1016/j.buildenv.2022.108823.

- [21] M. Pantusheva, R. Mitkov, P. O. Hristov, and D. Petrova-Antonova, “Air Pollution Dispersion Modelling in Urban Environment Using CFD: A Systematic Review,” *Atmosphere*, vol. 13, no. 10, pp. 1–35, 2022. DOI: 10.3390/atmos13101640.
- [22] *Paper-Based Theses — Modern Languages and Cultural Studies*. [Online]. Available: <https://www.ualberta.ca/modern-languages-and-cultural-studies/graduate-program-information/graduate-guide/program-guidelines/paper-based-theses.html> (visited on 12/09/2023).
- [23] Z. R. Huang, Y. J. Zhang, Y. B. Wen, Y. F. Tang, C. W. Liu, and F. Y. Zhao, “Synoptic wind driven ventilation and far field radionuclides dispersion across urban block regions: Effects of street aspect ratios and building array skylines,” *Sustainable Cities and Society*, vol. 78, no. November 2021, p. 103606, 2022. DOI: 10.1016/j.scs.2021.103606.
- [24] Z. Li *et al.*, “Review on pollutant dispersion in urban areas-part B: Local mitigation strategies, optimization framework, and evaluation theory,” *Building and Environment*, vol. 198, p. 107890, 2021. DOI: 10.1016/J.BUILDENV.2021.107890.
- [25] C. S. Bonner *et al.*, “Thickness of the Atmospheric Boundary Layer Above Dome A, Antarctica, during 2009,” *Publications of the Astronomical Society of the Pacific*, vol. 122, no. 895, pp. 1122–1131, 2010. DOI: 10.1086/656250.
- [26] R. B. Stull, *An introduction to boundary layer meteorology*. Kluwer Academic Publishers, 1988.
- [27] B. Hennemuth and A. Lammert, “Determination of the Atmospheric Boundary Layer Height from Radiosonde and Lidar Backscatter,” *Boundary-Layer Meteorology*, vol. 120, no. 1, pp. 181–200, 2006. DOI: 10.1007/s10546-005-9035-3.
- [28] S. Emeis, *Wind Energy Meteorology - Second Edition* (Green Energy and Technology). Zug, Switzerland: Springer, 2018, pp. 31–56. DOI: 10.1007/978-3-319-72859-9.
- [29] J. C. Kaimal and J. J. Finnigan, *Atmospheric Boundary Layer Flows*. Oxford University Press, 1994. DOI: 10.1093/oso/9780195062397.001.0001.
- [30] S. R. Hanna, *Handbook on atmospheric diffusion models*. US Department of Energy, 1981.
- [31] T. R. Oke, *Boundary Layer Climates*. Routledge, 2002. DOI: 10.4324/9780203407219.
- [32] E. Boeker and R. Van Grondelle, *Environmental Physics*, Third. Wiley, 2011.
- [33] R. E. Britter and S. R. Hanna, “Flow and dispersion in urban areas,” *Annual Review of Fluid Mechanics*, vol. 35, no. 1, pp. 469–496, 2003. DOI: 10.1146/annurev.fluid.35.101101.161147.

- [34] B. Blocken and T. Stathopoulos, “CFD simulation of pedestrian-level wind conditions around buildings: Past achievements and prospects,” *Journal of Wind Engineering and Industrial Aerodynamics*, vol. 121, pp. 138–145, 2013. DOI: 10.1016/J.JWEIA.2013.08.008.
- [35] “Effect of atmospheric stability on concentration fluctuations and wake retention times for dispersion in the vicinity of an isolated building,” *Environmetrics*, vol. 6, no. 6, pp. 571–581, 1995. DOI: 10.1002/env.3170060604.
- [36] Y. Tominaga and T. Stathopoulos, “Numerical simulation of dispersion around an isolated cubic building: Model evaluation of RANS and LES,” *Building and Environment*, vol. 45, no. 10, pp. 2231–2239, 2010. DOI: 10.1016/J.BUILDENV.2010.04.004.
- [37] C. Lin, R. Ooka, H. Kikumoto, T. Sato, and M. Arai, “CFD simulations on high-buoyancy gas dispersion in the wake of an isolated cubic building using steady RANS model and LES,” *Building and Environment*, vol. 188, no. August 2020, p. 107478, 2021. DOI: 10.1016/j.buildenv.2020.107478.
- [38] M. Lateb, C. Masson, T. Stathopoulos, and C. Bédard, “Comparison of various types of  $k-\epsilon$  models for pollutant emissions around a two-building configuration,” *Journal of Wind Engineering and Industrial Aerodynamics*, vol. 115, pp. 9–21, 2013. DOI: 10.1016/J.JWEIA.2013.01.001.
- [39] X. Jin, L. Yang, X. Du, and Y. Yang, “Sensitivity analyses of ultrafine particle dispersion inside an isolated street canyon,” *Powder Technology*, vol. 304, pp. 143–156, 2016. DOI: 10.1016/J.POWTEC.2016.07.060.
- [40] E. Keshavarzian, R. Jin, K. Dong, and K. C. Kwok, “Effect of building cross-section shape on air pollutant dispersion around buildings,” *Building and Environment*, vol. 197, p. 107861, 2021. DOI: 10.1016/J.BUILDENV.2021.107861.
- [41] M. Pirhalla, D. Heist, S. Perry, W. Tang, and L. Brouwer, “Simulations of dispersion through an irregular urban building array,” *Atmospheric Environment*, vol. 258, p. 118500, 2021. DOI: 10.1016/J.ATMOENV.2021.118500.
- [42] Q. Li *et al.*, “Numerical Investigations of Urban Pollutant Dispersion and Building Intake Fraction with Various 3D Building Configurations and Tree Plantings,” *Atmosphere*, 2022. DOI: <https://doi.org/10.3390/ijerph19063524>.
- [43] Y. Hu, F. Xu, and Z. Gao, “A Comparative Study of the Simulation Accuracy and Efficiency for the Urban Wind Environment Based on CFD Plug-Ins Integrated into Architectural Design Platforms,” *Buildings 2022, Vol. 12, Page 1487*, vol. 12, no. 9, p. 1487, 2022. DOI: 10.3390/BUILDINGS12091487.
- [44] F. T. da Silva, N. C. Reis, J. M. Santos, E. V. Goulart, and C. E. de Alvarez, “Influence of urban form on air quality: The combined effect of block typology and urban planning indices on city breathability,” *Science of the Total Environment*, vol. 814, p. 152670, 2022. DOI: 10.1016/j.scitotenv.2021.152670.

- [45] J Hall, D, M Spanton, A, R MacDonald, and S Walker, “A review of requirements for simple urban dispersion models,” Building Research Establishment, Tech. Rep., 1996.
- [46] P. Huq and P. Franzese, “Measurements of Turbulence and Dispersion in Three Idealized Urban Canopies with Different Aspect Ratios and Comparisons with a Gaussian Plume Model,” *Boundary-Layer Meteorology*, vol. 147, no. 1, pp. 103–121, 2013. DOI: 10.1007/s10546-012-9780-z.
- [47] A. C. Vaz, C. B. Paris, A. L. Dissanayake, S. A. Socolofsky, J. Gros, and M. C. Boufadel, “Dynamic coupling of near-field and far-field models,” *Deep Oil Spills: Facts, Fate, and Effects*, pp. 139–154, 2020.
- [48] J. C. Kaimal, “Turbulenece spectra, length scales and structure parameters in the stable surface layer,” *Boundary-Layer Meteorology*, vol. 4, no. 1-4, pp. 289–309, 1973. DOI: 10.1007/BF02265239.
- [49] E. Yee and C. A. Biltoft, “Concentration Fluctuation Measurements in a Plume Dispersing Through a Regular Array of Obstacles,” *Boundary-Layer Meteorology*, vol. 111, no. 3, pp. 363–415, 2004. DOI: 10.1023/B:BOUN.0000016496.83909.ee.
- [50] T. Foken, “50 Years of the Monin–Obukhov Similarity Theory,” *Boundary-Layer Meteorology*, vol. 119, no. 3, pp. 431–447, 2006. DOI: 10.1007/s10546-006-9048-6.
- [51] H. Montazeri and B. Blocken, “CFD simulation of wind-induced pressure coefficients on buildings with and without balconies: Validation and sensitivity analysis,” *Building and Environment*, vol. 60, pp. 137–149, 2013. DOI: 10.1016/j.buildenv.2012.11.012.
- [52] D. J. Wilson and B. K. Lamb, “Dispersion of exhaust gases from roof-level stacks and vents on a laboratory building,” *Atmospheric Environment*, vol. 28, no. 19, pp. 3099–3111, 1994. DOI: 10.1016/1352-2310(94)E0067-T.
- [53] T. Stathopoulos, L. Lazure, P. Saathoff, and A. Gupta, “The effect of stack height, stack location and rooftop structures on air intake contamination- A laboratory and full-scale study,” Institut de recherche Robert-Sauvé en santé et en sécurité du travail (IRSST), Montreal, Canada, Tech. Rep., 2004.
- [54] S. R. Hanna, O. R. Hansen, and S. Dharmavaram, “FLACS CFD air quality model performance evaluation with Kit Fox, MUST, Prairie Grass, and EMU observations,” *Atmospheric Environment*, vol. 38, no. 28, pp. 4675–4687, 2004. DOI: 10.1016/J.ATMOENV.2004.05.041.
- [55] C. Biltoft, “Customer report for mock urban setting test,” 2001.
- [56] B. Hajra and T. Stathopoulos, “A wind tunnel study of the effect of downstream buildings on near-field pollutant dispersion,” *Building and Environment*, vol. 52, pp. 19–31, 2012. DOI: 10.1016/J.BUILDENV.2011.12.021.

- [57] D. Mu, N. Gao, and T. Zhu, “Wind tunnel tests of inter-flat pollutant transmission characteristics in a rectangular multi-storey residential building, part A: Effect of wind direction,” *Building and Environment*, vol. 108, pp. 159–170, 2016. DOI: 10.1016/j.buildenv.2016.08.032.
- [58] M. F. Yassin, “A wind tunnel study on the effect of thermal stability on flow and dispersion of rooftop stack emissions in the near wake of a building,” *Atmospheric Environment*, vol. 65, pp. 89–100, 2013. DOI: 10.1016/j.atmosenv.2012.10.013.
- [59] *Guidebook for CFD Predictions of Urban Wind Environment*. [Online]. Available: [https://www.aij.or.jp/jpn/publish/cfdguide/index\\_e.htm](https://www.aij.or.jp/jpn/publish/cfdguide/index_e.htm) (visited on 10/26/2023).
- [60] X. T. Huang, Y. D. Huang, N. Xu, Y. Luo, and P. Y. Cui, “Thermal effects on the dispersion of rooftop stack emission in the wake of a tall building within suburban areas by wind-tunnel experiments,” *Journal of Wind Engineering and Industrial Aerodynamics*, vol. 205, p. 104295, 2020. DOI: 10.1016/j.jweia.2020.104295.
- [61] R. Meroney, “Turbulent diffusion near buildings,” *Engineering Meteorology*, 1982.
- [62] “Airflow around the buildings,” in *ASHRAE Fundamental Handbook*, Atlanta, GA, USA: American Society of Heating, Refrigerating and Air-conditioning Engineers, 2009.
- [63] D. J. Wilson and R. E. Britter, “Estimates of building surface concentrations from nearby point sources,” *Atmospheric Environment (1967)*, vol. 16, no. 11, pp. 2631–2646, 1982. DOI: 10.1016/0004-6981(82)90345-6.
- [64] “Airflow around the buildings,” in *ASHRAE Fundamental Handbook*, Atlanta, GA, USA: American Society of Heating, Refrigerating and Air-conditioning Engineers, 2011.
- [65] C. McHugh, D. Carruthers, and H. Edmunds, “ADMS and ADMS-Urban,” *Environment and Pollution*, vol. 8, no. 3-6, pp. 438–440, 2014.
- [66] A. Riddle, D. Carruthers, A. Sharpe, C. McHugh, and J. Stocker, “Comparisons between FLUENT and ADMS for atmospheric dispersion modelling,” *Atmospheric Environment*, vol. 38, no. 7, pp. 1029–1038, 2004. DOI: 10.1016/J.ATMOENV.2003.10.052.
- [67] M. Lateb, C. Masson, T. Stathopoulos, and C. Bédard, “Effect of stack height and exhaust velocity on pollutant dispersion in the wake of a building,” *Atmospheric Environment*, vol. 45, no. 29, pp. 5150–5163, 2011. DOI: 10.1016/J.ATMOENV.2011.06.040.
- [68] H. K. Versteeg and W. Malalasekera, *An Introduction to Computational Fluid Dynamics*, Second. Harlow, UK: Pearson Education, 2007, ISBN: 9780131274983.

- [69] A. Scaperdas, *Modelling the Small Scale Variation of CO Concentration at an Urban Canyon Junction*. Centre for Environmental Technology, Imperial College, 1996.
- [70] P. Moonen, T. Defraeye, V. Dorer, B. Blocken, and J. Carmeliet, “Urban Physics: Effect of the micro-climate on comfort, health and energy demand,” *Frontiers of Architectural Research*, vol. 1, no. 3, pp. 197–228, 2012. DOI: 10.1016/j.foar.2012.05.002.
- [71] A. N. Kolmogorov, “The local structure of turbulence in incompressible viscous fluid for very large reynolds numbers,” *Proceedings: Mathematical and Physical Sciences*, vol. 434, no. 1890, pp. 9–13, 1991.
- [72] J. H. Ferziger, M. Perić, and R. L. Street, *Computational methods for fluid flow*. Fourth. Zug, Switzerland: Springer, 2020. DOI: 10.1007/978-3-319-99693-6.
- [73] J. Smagorinsky, “General circulation experiments with the primitive equations,” *Monthly Weather Review*, vol. 91, no. 3, pp. 99–164, 1963. DOI: 10.1175/1520-0493(1963)091<0099:GCEWTP>2.3.CO;2.
- [74] O. Reynolds, “On the dynamical theory of incompressible viscous fluids and the determination of the criterion,” *Proceedings of the Royal Society of London*, vol. 56, no. 336-339, pp. 40–45, 1894. DOI: 10.1098/rspl.1894.0075.
- [75] W. Rodi, “Comparison of LES and RANS calculations of the flow around bluff bodies,” *Journal of Wind Engineering and Industrial Aerodynamics*, vol. 69-71, pp. 55–75, 1997. DOI: 10.1016/S0167-6105(97)00147-5.
- [76] S. M. Salim, R. Buccolieri, A. Chan, and S. Di Sabatino, “Numerical simulation of atmospheric pollutant dispersion in an urban street canyon: Comparison between RANS and LES,” *Journal of Wind Engineering and Industrial Aerodynamics*, vol. 99, no. 2-3, pp. 103–113, 2011. DOI: 10.1016/J.JWEIA.2010.12.002.
- [77] G. Vita, S. Salvadori, D. A. Misul, and H. Hemida, “Effects of Inflow Condition on RANS and LES Predictions of the Flow around a High-Rise Building,” *Fluids*, vol. 5, no. 4, p. 233, 2020. DOI: 10.3390/fluids5040233.
- [78] X. Zheng and J. Yang, “CFD simulations of wind flow and pollutant dispersion in a street canyon with traffic flow: Comparison between RANS and LES,” *Sustainable Cities and Society*, vol. 75, p. 103307, 2021. DOI: 10.1016/J.SCS.2021.103307.
- [79] B. Blocken, “LES over RANS in building simulation for outdoor and indoor applications: A foregone conclusion?” *Building Simulation 2018 11:5*, vol. 11, no. 5, pp. 821–870, 2018. DOI: 10.1007/S12273-018-0459-3.
- [80] J. H. Ferziger, “Approaches to turbulent flow computation: Applications to flow over obstacles,” *Journal of Wind Engineering and Industrial Aerodynamics*, vol. 35, pp. 1–19, 1990. DOI: 10.1016/0167-6105(90)90208-T.

- [81] X. Zheng, H. Montazeri, and B. Blocken, “CFD simulations of wind flow and mean surface pressure for buildings with balconies: Comparison of RANS and LES,” *Building and Environment*, vol. 173, no. November 2019, p. 106747, 2020. DOI: 10.1016/j.buildenv.2020.106747.
- [82] B. Blocken, W. Janssen, and T. van Hooff, “CFD simulation for pedestrian wind comfort and wind safety in urban areas: General decision framework and case study for the Eindhoven University campus,” *Environmental Modelling Software*, vol. 30, pp. 15–34, 2012. DOI: 10.1016/j.envsoft.2011.11.009.
- [83] Y. Abu-Zidan, P. Mendis, and T. Gunawardena, “Optimising the computational domain size in CFD simulations of tall buildings,” *Heliyon*, vol. 7, no. 4, e06723, 2021. DOI: 10.1016/j.heliyon.2021.e06723.
- [84] M. M. Hefny and R. Ooka, “CFD analysis of pollutant dispersion around buildings: Effect of cell geometry,” *Building and Environment*, vol. 44, no. 8, pp. 1699–1706, 2009. DOI: 10.1016/j.buildenv.2008.11.010.
- [85] T. van Hooff, B. Blocken, and M. van Harten, “3D CFD simulations of wind flow and wind-driven rain shelter in sports stadia: Influence of stadium geometry,” *Building and Environment*, vol. 46, no. 1, pp. 22–37, 2011. DOI: 10.1016/j.buildenv.2010.06.013.
- [86] S. Jena and A. Gairola, “Novel boundary conditions for investigation of environmental wind profile induced due to raised terrains and their influence on pedestrian winds,” vol. 27, no. 1, 77 – 85, 2022. DOI: 10.37934/araset.27.1.7785.
- [87] N. Amahjour, A. Sofi, J. R. R. Galván, A. E. Kharrim, and A. Khamlichi, “An evaluation of inflow profiles for cfd modeling of neutral abl and turbulent airflow over a hill model,” *Journal of Applied Fluid Mechanics*, vol. 16, no. 8, 1515 – 1530, 2023. DOI: 10.47176/jafm.16.08.1702.
- [88] B. Blocken, T. Stathopoulos, and J. Carmeliet, “CFD simulation of the atmospheric boundary layer: wall function problems,” *Atmospheric Environment*, vol. 41, pp. 238–252, 2007. DOI: 10.1016/j.atmosenv.2006.08.019.
- [89] S. Schalaus, A. Habib, and S. Michel, “Atmospheric Wind Field Modelling with OpenFOAM for Near-Ground Gas Dispersion,” *Atmosphere*, vol. 12, no. 8, p. 933, 2021. DOI: 10.3390/atmos12080933.
- [90] M. Cindori, F. Juretić, H. Kozmar, and I. Džijan, “Steady RANS model of the homogeneous atmospheric boundary layer,” *Journal of Wind Engineering and Industrial Aerodynamics*, vol. 173, pp. 289–301, 2018. DOI: 10.1016/j.jweia.2017.12.006.
- [91] K. RahnamayBahambary and B. A. Fleck, “Effects of inflow parameters and disk thickness on an actuator disk inside the neutral atmospheric boundary layer,” *Wind*, vol. 2, no. 4, pp. 733–746, 2022. DOI: 10.3390/wind2040038.
- [92] W. H. Snyder, “Guideline for fluid modeling of atmospheric diffusion. fluid modeling report no. 10,” Apr. 1981.

- [93] M. Schatzmann, S. Rafailidis, and M. Pavageau, “Some remarks on the validation of small-scale dispersion models with field and laboratory data,” *Journal of Wind Engineering and Industrial Aerodynamics*, vol. 67-68, pp. 885–893, 1997. DOI: 10.1016/S0167-6105(97)00126-8.
- [94] B. Blocken, “Computational Fluid Dynamics for urban physics: Importance, scales, possibilities, limitations and ten tips and tricks towards accurate and reliable simulations,” *Building and Environment*, vol. 91, pp. 219–245, 2015. DOI: 10.1016/j.buildenv.2015.02.015.
- [95] A. Zhang, C. Gao, and L. Zhang, “Numerical simulation of the wind field around different building arrangements,” *Journal of Wind Engineering and Industrial Aerodynamics*, vol. 93, no. 12, pp. 891–904, 2005. DOI: <https://doi.org/10.1016/j.jweia.2005.09.001>.
- [96] Y. Tominaga, L. L. Wang, Z. J. Zhai, and T. Stathopoulos, “Accuracy of CFD simulations in urban aerodynamics and microclimate: Progress and challenges,” *Building and Environment*, vol. 243, p. 110 723, 2023. DOI: 10.1016/j.buildenv.2023.110723.
- [97] B. E. Launder and D. B. Spalding, “The numerical computation of turbulent flows,” *Computer Methods in Applied Mechanics and Engineering*, vol. 3, no. 2, pp. 269–289, 1974. DOI: 10.1016/0045-7825(74)90029-2.
- [98] V. Yakhot and S. A. Orszag, “Renormalization-group analysis of turbulence,” *Physical Review Letters*, vol. 57, no. 14, pp. 1722–1724, 1986. DOI: 10.1103/PHYSREVLETT.57.1722.
- [99] T. H. Shih, W. W. Liou, A. Shabbir, Z. Yang, and J. Zhu, “A new  $k-\epsilon$  eddy viscosity model for high reynolds number turbulent flows,” *Computers & Fluids*, vol. 24, no. 3, pp. 227–238, 1995. DOI: 10.1016/0045-7930(94)00032-T.
- [100] D. C. Wilcox, *Turbulence modeling for CFD*, Third. DCW Industries La Canada, CA, 2006.
- [101] F. R. Menter, “Two-equation eddy-viscosity turbulence models for engineering applications,” *AIAA Journal*, vol. 32, no. 8, pp. 1598–1605, 1994. DOI: 10.2514/3.12149.
- [102] P. SPALART and S. ALLMARAS, “A one-equation turbulence model for aerodynamic flows,” in *30th Aerospace Sciences Meeting and Exhibit*, Reston, Virginia: American Institute of Aeronautics and Astronautics, 1992. DOI: 10.2514/6.1992-439.
- [103] N. Glover, S. Guillas, and L. Malki-Epshtein, “Statistical calibration of CFD modelling for street canyon flows,” *Proceedings of Building Simulation 2011: 12th Conference of International Building Performance Simulation Association*, pp. 1513–1520, 2011.
- [104] Y. Han and M. K. Stoellinger, “RANS simulations of neutral atmospheric boundary layer flow over complex terrain with comparisons to field measurements,” *Wind Energy*, vol. 23, no. 2, pp. 91–119, 2020. DOI: 10.1002/we.2412.

- [105] A. Narjisse and K. Abdellatif, “Assessment of RANS turbulence closure models for predicting airflow in neutral ABL over hilly terrain,” *International Review of Applied Sciences and Engineering*, vol. 12, no. 3, pp. 238–256, 2021. DOI: 10.1556/1848.2021.00264.
- [106] M. Balogh, A. Parente, and C. Benocci, “Rans simulation of abl flow over complex terrains applying an enhanced k- model and wall function formulation: Implementation and comparison for fluent and openfoam,” *Journal of Wind Engineering and Industrial Aerodynamics*, vol. 104-106, pp. 360–368, 2012, ISSN: 0167-6105. DOI: <https://doi.org/10.1016/j.jweia.2012.02.023>.
- [107] R. Ramponi and B. Blocken, “CFD simulation of cross-ventilation for a generic isolated building: Impact of computational parameters,” *Building and Environment*, vol. 53, pp. 34–48, 2012. DOI: 10.1016/j.buildenv.2012.01.004.
- [108] Y. Tominaga, “Flow around a high-rise building using steady and unsteady RANS CFD: Effect of large-scale fluctuations on the velocity statistics,” *Journal of Wind Engineering and Industrial Aerodynamics*, vol. 142, pp. 93–103, 2015. DOI: 10.1016/J.JWEIA.2015.03.013.
- [109] A. Hosseinzadeh and A. Keshmiri, “Computational Simulation of Wind Microclimate in Complex Urban Models and Mitigation Using Trees,” *Buildings 2021, Vol. 11, Page 112*, vol. 11, no. 3, p. 112, 2021. DOI: 10.3390/BUILDINGS11030112.
- [110] K. An, S. M. Wong, and J. C. H. Fung, “Exploration of sustainable building morphologies for effective passive pollutant dispersion within compact urban environments,” *Building and Environment*, vol. 148, pp. 508–523, 2019. DOI: 10.1016/J.BUILDENV.2018.11.030.
- [111] E. Keshavarzian, R. Jin, K. Dong, K. C. Kwok, Y. Zhang, and M. Zhao, “Effect of pollutant source location on air pollutant dispersion around a high-rise building,” *Applied Mathematical Modelling*, vol. 81, pp. 582–602, 2020. DOI: 10.1016/j.apm.2020.01.019.
- [112] T. Stathopoulos, “Computational wind engineering: Past achievements and future challenges,” *Journal of Wind Engineering and Industrial Aerodynamics*, vol. 67-68, pp. 509–532, 1997. DOI: 10.1016/S0167-6105(97)00097-4.
- [113] H. W. Detering and D Etling, “Application of the E-e turbulence model to the atmospheric boundary layer,” *Boundary Layer Meteorology*, vol. 33, no. 1983, pp. 113–133, 1985.
- [114] A Bechmann, N. N. Sørensen, C. A. Bechmann, and R. Dtu, “Hybrid RANS/LES method for wind flow over complex terrain,” *Wind Energy*, vol. 13, no. 1, pp. 36–50, 2010. DOI: 10.1002/WE.346.
- [115] Q. M. Zahid Iqbal and A. Chan, “Pedestrian level wind environment assessment around group of high-rise cross-shaped buildings: Effect of building shape, separation and orientation,” *Building and Environment*, vol. 101, pp. 45–63, 2016. DOI: 10.1016/j.buildenv.2016.02.015.

- [116] S. Guillas, N. Glover, and L. Malki-Epshtein, “Bayesian calibration of the constants of the k- $\epsilon$  turbulence model for a CFD model of street canyon flow,” *Computer Methods in Applied Mechanics and Engineering*, vol. 279, pp. 536–553, 2014. DOI: 10.1016/j.cma.2014.06.008.
- [117] M. Shirzadi, M. Naghashzadegan, and P. A. Mirzaei, “Improving the CFD modelling of cross-ventilation in highly-packed urban areas,” *Sustainable Cities and Society*, vol. 37, pp. 451–465, 2018. DOI: 10.1016/J.SCS.2017.11.020.
- [118] M. Shirzadi, P. A. Mirzaei, and M. Naghashzadegan, “Improvement of k-epsilon turbulence model for CFD simulation of atmospheric boundary layer around a high-rise building using stochastic optimization and Monte Carlo Sampling technique,” *Journal of Wind Engineering and Industrial Aerodynamics*, vol. 171, pp. 366–379, 2017. DOI: 10.1016/J.JWEIA.2017.10.005.
- [119] S. Murakami, “Comparison of various turbulence models applied to a bluff body,” *Journal of Wind Engineering and Industrial Aerodynamics*, vol. 46-47, no. C, pp. 21–36, 1993. DOI: 10.1016/0167-6105(93)90112-2.
- [120] S. J. Jeong and A. Ra Kim, “CFD study on the influence of atmospheric stability on near-field pollutant dispersion from rooftop emissions,” *Asian Journal of Atmospheric Environment*, vol. 12, no. 1, pp. 47–58, 2018. DOI: 10.5572/ajae.2018.12.1.047.
- [121] G. Jiang and R. Yoshie, “Side ratio effects on flow and pollutant dispersion around an isolated high-rise building in a turbulent boundary layer,” *Building and Environment*, vol. 180, p. 107078, 2020. DOI: 10.1016/J.BUILDENV.2020.107078.
- [122] X. Huang, L. Gao, D. Guo, and R. Yao, “Impacts of high-rise building on urban airflows and pollutant dispersion under different temperature stratifications: Numerical investigations,” *Atmospheric Pollution Research*, vol. 12, no. 3, pp. 100–112, 2021. DOI: 10.1016/J.APR.2021.02.001.
- [123] T. Oke, “Street design and urban canopy layer climate,” *Energy and Buildings*, vol. 11, no. 1-3, pp. 103–113, 1988. DOI: 10.1016/0378-7788(88)90026-6.
- [124] M. Davidson, W. Snyder, R. Lawson, and J. Hunt, “Wind tunnel simulations of plume dispersion through groups of obstacles,” *Atmospheric Environment*, vol. 30, no. 22, pp. 3715–3731, 1996. DOI: 10.1016/1352-2310(96)00103-3.
- [125] R. MacDonald, R. Griffiths, and S. Cheah, “Field experiments of dispersion through regular arrays of cubic structures,” *Atmospheric Environment*, vol. 31, no. 6, pp. 783–795, 1997. DOI: 10.1016/S1352-2310(96)00263-4.
- [126] P. Edussuriya, A. Chan, and A. Ye, “Urban morphology and air quality in dense residential environments in Hong Kong. Part I: District-level analysis,” *Atmospheric Environment*, vol. 45, no. 27, pp. 4789–4803, 2011. DOI: 10.1016/j.atmosenv.2009.07.061.

- [127] W. Theurer, “Typical building arrangements for urban air pollution modelling,” *Atmospheric Environment*, vol. 33, no. 24-25, pp. 4057–4066, 1999. DOI: 10.1016/S1352-2310(99)00147-8.
- [128] T. Kubota, M. Miura, Y. Tominaga, and A. Mochida, “Wind tunnel tests on the relationship between building density and pedestrian-level wind velocity: Development of guidelines for realizing acceptable wind environment in residential neighborhoods,” *Building and Environment*, vol. 43, no. 10, pp. 1699–1708, 2008. DOI: 10.1016/J.BUILDENV.2007.10.015.
- [129] K. Hu, S. Cheng, and Y. Qian, “CFD simulation analysis of building density on residential wind environment,” *Journal of Engineering Science and Technology Review*, vol. 11, no. 1, pp. 35–43, 2018. DOI: 10.25103/jestr.111.05.
- [130] M. N. A. W. M. Yazid, A. S. B. Sharif, N. A. C. Sidik, M. H. Hanipah, F. M. Zawawi, and U. Abidin, “Effects of staggered array of cubical obstacles on near-ground wind environment and air quality,” *Journal of Advanced Research in Fluid Mechanics and Thermal Sciences*, vol. 58, no. 2, pp. 261 – 274, 2019.
- [131] C. Yuan, E. Ng, and L. K. Norford, “Improving air quality in high-density cities by understanding the relationship between air pollutant dispersion and urban morphologies,” *Building and Environment*, vol. 71, no. 2, pp. 245–258, 2014. DOI: 10.1016/j.buildenv.2013.10.008.
- [132] Y.-H. Juan, C.-Y. Wen, Z. Li, and A.-S. Yang, “Impacts of urban morphology on improving urban wind energy potential for generic high-rise building arrays,” *Applied Energy*, vol. 299, p. 117304, 2021. DOI: <https://doi.org/10.1016/j.apenergy.2021.117304>.
- [133] D. J. Wise, V. B. Boppana, K. W. Li, and H. J. Poh, “Effects of minor changes in the mean inlet wind direction on urban flow simulations,” *Sustainable Cities and Society*, vol. 37, no. August 2017, pp. 492–500, 2018. DOI: 10.1016/j.scs.2017.11.041.
- [134] E. V. Goulart, N. C. Reis, V. F. Lavor, I. P. Castro, J. M. Santos, and Z. T. Xie, “Local and non-local effects of building arrangements on pollutant fluxes within the urban canopy,” *Building and Environment*, vol. 147, pp. 23–34, 2019. DOI: 10.1016/J.BUILDENV.2018.09.023.
- [135] Y. B. Wen, Z. R. Huang, Y. F. Tang, D. R. Li, Y. J. Zhang, and F. Y. Zhao, “Air exchange rate and pollutant dispersion inside compact urban street canyons with combined wind and thermal driven natural ventilations: Effects of non-uniform building heights and unstable thermal stratifications,” *Science of the Total Environment*, vol. 851, no. August, p. 158053, 2022. DOI: 10.1016/j.scitotenv.2022.158053.
- [136] “2018 Revision of World Urbanization Prospects,” United Nations Department of Economics and Social Affairs (UNDESA), New York, Tech. Rep., 2018.

- [137] N. S. Holmes and L. Morawska, “A review of dispersion modelling and its application to the dispersion of particles: An overview of different dispersion models available,” *Atmospheric Environment*, vol. 40, no. 30, pp. 5902–5928, 2006. DOI: 10.1016/J.ATMOSENV.2006.06.003.
- [138] Y. Du, B. Blocken, S. Abbasi, and S. Pirker, “Efficient and high-resolution simulation of pollutant dispersion in complex urban environments by island-based recurrence CFD,” *Environmental Modelling Software*, vol. 145, p. 105172, 2021. DOI: 10.1016/J.ENVSOFT.2021.105172.
- [139] A. Ricci, I. Kalkman, B. Blocken, M. Burlando, A. Freda, and M. P. Repetto, “Local-scale forcing effects on wind flows in an urban environment: Impact of geometrical simplifications,” *Journal of Wind Engineering and Industrial Aerodynamics*, vol. 170, pp. 238–255, 2017. DOI: 10.1016/J.JWEIA.2017.08.001.
- [140] L. Daniel Sang-Hoon and M. Dasaraden, “Rans based cfd simulations for urban wind prediction field verification against motus.,” *Wind and Structures, An International Journal*, vol. 33, no. 1, pp. 29–40, 2021.
- [141] F. Trindade da Silva, N. C. Reis, J. M. Santos, E. V. Goulart, and C. Engel de Alvarez, “The impact of urban block typology on pollutant dispersion,” *Journal of Wind Engineering and Industrial Aerodynamics*, vol. 210, p. 104524, 2021. DOI: 10.1016/J.JWEIA.2021.104524.
- [142] S. J. Mattar, M. R. K. Nezhad, M. Versteeg, C. F. Lange, and B. A. Fleck, “Validation Process for Rooftop Wind Regime CFD Model in Complex Urban Environment Using an Experimental Measurement Campaign,” *Energies 2021, Vol. 14, Page 2497*, vol. 14, no. 9, p. 2497, 2021. DOI: 10.3390/EN14092497.
- [143] C. Yang, Z. Hong, J. Chen, L. Xu, M. Zhuang, and Z. Huang, “Characteristics of secondary organic aerosols tracers in PM<sub>2.5</sub> in three central cities of the Yangtze river delta, China,” *Chemosphere*, vol. 293, p. 133637, 2022. DOI: 10.1016/J.CHEMOSPHERE.2022.133637.
- [144] J. Zou, Y. Yu, J. Liu, J. Niu, K. Chauhan, and C. Lei, “Field measurement of the urban pedestrian level wind turbulence,” *Building and Environment*, vol. 194, p. 107713, 2021. DOI: 10.1016/J.BUILDENV.2021.107713.
- [145] P. A. Mirzaei, “CFD modeling of micro and urban climates: Problems to be solved in the new decade,” *Sustainable Cities and Society*, vol. 69, p. 102839, 2021. DOI: 10.1016/J.SCS.2021.102839.
- [146] Y. Du, B. Blocken, and S. Pirker, “A novel approach to simulate pollutant dispersion in the built environment: Transport-based recurrence CFD,” *Building and Environment*, vol. 170, p. 106604, 2020. DOI: 10.1016/J.BUILDENV.2019.106604.
- [147] M. Chavez, B. Hajra, T. Stathopoulos, and A. Bahloul, “Assessment of near-field pollutant dispersion: Effect of upstream buildings,” *Journal of Wind Engineering and Industrial Aerodynamics*, vol. 104–106, pp. 509–515, 2012. DOI: 10.1016/J.JWEIA.2012.02.019.

- [148] T. Lauriks *et al.*, “Application of Improved CFD Modeling for Prediction and Mitigation of Traffic-Related Air Pollution Hotspots in a Realistic Urban Street,” *Atmospheric Environment*, vol. 246, p. 118127, 2021. DOI: 10.1016/J.ATMOSENV.2020.118127.
- [149] A. M. Hassan, A. A. ELMokadem, N. A. Megahed, and O. M. Abo Eleinen, “Urban morphology as a passive strategy in promoting outdoor air quality,” *Journal of Building Engineering*, vol. 29, p. 101204, 2020. DOI: 10.1016/J.JOBE.2020.101204.
- [150] T. Ming *et al.*, “Assessment of pollutant dispersion in urban street canyons based on field synergy theory,” *Atmospheric Pollution Research*, vol. 12, no. 2, pp. 341–356, 2021. DOI: 10.1016/J.APR.2020.11.015.
- [151] D. Elfverson and C. Lejon, “Use and scalability of openfoam for wind fields and pollution dispersion with building-and ground-resolving topography,” vol. 12, no. 9, 2021. DOI: 10.3390/atmos12091124.
- [152] Y. Tominaga and T. Stathopoulos, “Turbulent Schmidt numbers for CFD analysis with various types of flowfield,” *Atmospheric Environment*, vol. 41, no. 37, pp. 8091–8099, 2007. DOI: 10.1016/J.ATMOSENV.2007.06.054.
- [153] S. Di Sabatino, R. Buccolieri, B. Pulvirenti, and R. Britter, “Simulations of pollutant dispersion within idealised urban-type geometries with CFD and integral models,” *Atmospheric Environment*, vol. 41, no. 37, pp. 8316–8329, 2007. DOI: 10.1016/J.ATMOSENV.2007.06.052.
- [154] B. Blocken, T. Stathopoulos, P. Saathoff, and X. Wang, “Numerical evaluation of pollutant dispersion in the built environment: Comparisons between models and experiments,” *Journal of Wind Engineering and Industrial Aerodynamics*, vol. 96, no. 10-11, pp. 1817–1831, 2008. DOI: 10.1016/J.JWEIA.2008.02.049.
- [155] A. Speranza and V. Lucarini, “Environmental science, physical principles and applications,” in *Encyclopedia of Condensed Matter Physics*, F. Bassani, G. L. Liedl, and P. Wyder, Eds., Oxford: Elsevier, 2005, pp. 146–156, ISBN: 978-0-12-369401-0. DOI: 10.1016/B0-12-369401-9/00735-X.
- [156] M. Mohamed and D. Wood, “Computational modeling of wind flow over the university of calgary campus,” *Wind Engineering*, vol. 40, no. 3, pp. 228–249, 2016. DOI: 10.1177/0309524X16642082.
- [157] A. Inc., *ANSYS CFX-Solver Theory Guide Release 2020-r1*. Canonsburg, PA, USA, 2020, pp. 79–90.
- [158] M. Milliez, B. Carissimo, M. Milliez, and B. Carissimo CERE, “Numerical simulations of pollutant dispersion in an idealized urban area, for different meteorological conditions,” vol. 122, pp. 321–342, 2007. DOI: 10.1007/s10546-006-9110-4.

- [159] R. P. Donnelly, T. J. Lyons, and T. Flassak, “Evaluation of results of a numerical simulation of dispersion in an idealised urban area for emergency response modelling,” *Atmospheric Environment*, vol. 43, no. 29, pp. 4416–4423, 2009. DOI: 10.1016/j.atmosenv.2009.05.038.
- [160] P. Kumar, S. K. Singh, A. A. Feiz, and P. Ngae, “An urban scale inverse modelling for retrieving unknown elevated emissions with building-resolving simulations,” *Atmospheric Environment*, vol. 140, pp. 135–146, 2016. DOI: 10.1016/j.atmosenv.2016.05.050.
- [161] M. L. Bahlali, E. Dupont, and B. Carissimo, “Atmospheric dispersion using a Lagrangian stochastic approach: Application to an idealized urban area under neutral and stable meteorological conditions,” *Journal of Wind Engineering and Industrial Aerodynamics*, vol. 193, no. August, p. 103976, 2019. DOI: 10.1016/j.jweia.2019.103976.
- [162] C. Tee, E. Ng, and G. Xu, “Analysis of transport methodologies for pollutant dispersion modelling in urban environments,” *Journal of Environmental Chemical Engineering*, vol. 8, no. 4, p. 103937, 2020. DOI: 10.1016/j.jece.2020.103937.
- [163] Z. Zhang and K. Wang, “Quantifying and adjusting the impact of urbanization on the observed surface wind speed over China from 1985 to 2017,” *Fundamental Research*, vol. 1, no. 6, pp. 785–791, 2021. DOI: 10.1016/J.FMRE.2021.09.006.
- [164] L. Tian, N. Zhao, T. Wang, W. Zhu, and W. Shen, “Assessment of inflow boundary conditions for RANS simulations of neutral ABL and wind turbine wake flow,” *Journal of Wind Engineering and Industrial Aerodynamics*, vol. 179, pp. 215–228, 2018. DOI: 10.1016/J.JWEIA.2018.06.003.
- [165] P. J. Richards and R. P. Hoxey, “Appropriate boundary conditions for computational wind engineering models using the k- $\epsilon$  turbulence model,” *Journal of Wind Engineering and Industrial Aerodynamics*, vol. 46-47, pp. 145–153, 1993. DOI: 10.1016/0167-6105(93)90124-7.
- [166] I. B. Celik, U. Ghia, P. J. Roache, C. J. Freitas, H. Coleman, and P. E. Raad, “Procedure for estimation and reporting of uncertainty due to discretization in CFD applications,” *Journal of Fluids Engineering, Transactions of the ASME*, vol. 130, no. 7, pp. 0780011–0780014, 2008. DOI: 10.1115/1.2960953/444689.
- [167] P. J. Roache, “Quantification of uncertainty in computational fluid dynamics,” *Annual Review of Fluid Mechanics*, vol. 29, no. 1, pp. 123–160, 1997. DOI: 10.1146/annurev.fluid.29.1.123.
- [168] J. C. Chang and S. R. Hanna, “Air quality model performance evaluation,” *Meteorology and Atmospheric Physics 2004 87:1*, vol. 87, no. 1, pp. 167–196, 2004. DOI: 10.1007/S00703-003-0070-7.

- [169] Y. Tominaga and T. Stathopoulos, “Numerical simulation of dispersion around an isolated cubic building: Comparison of various types of k- models,” *Atmospheric Environment*, vol. 43, no. 20, pp. 3200–3210, 2009. DOI: 10.1016/J.ATMOENV.2009.03.038.
- [170] K. Koeltzsch, “The height dependence of the turbulent Schmidt number within the boundary layer,” *Atmospheric Environment*, vol. 34, no. 7, pp. 1147–1151, 2000. DOI: 10.1016/S1352-2310(99)00369-6.
- [171] R. Longo, M. Fürst, A. Bellemans, M. Ferrarotti, M. Derudi, and A. Parente, “CFD dispersion study based on a variable Schmidt formulation for flows around different configurations of ground-mounted buildings,” *Building and Environment*, vol. 154, pp. 336–347, 2019. DOI: 10.1016/J.BUILDENV.2019.02.041.
- [172] R. Longo, A. Bellemans, M. Derudi, and A. Parente, “A multi-fidelity framework for the estimation of the turbulent Schmidt number in the simulation of atmospheric dispersion,” *Building and Environment*, vol. 185, p. 107066, 2020. DOI: 10.1016/J.BUILDENV.2020.107066.
- [173] Z. Li *et al.*, “Review on pollutant dispersion in urban areas-part A: Effects of mechanical factors and urban morphology,” *Building and Environment*, vol. 190, p. 107534, 2021. DOI: 10.1016/J.BUILDENV.2020.107534.
- [174] C. Lu, L. Cao, D. Norbäck, Y. Li, J. Chen, and Q. Deng, “Combined effects of traffic air pollution and home environmental factors on preterm birth in China,” *Ecotoxicology and Environmental Safety*, vol. 184, p. 109639, 2019. DOI: 10.1016/J.ECOENV.2019.109639.
- [175] Y. Xia, D. Guan, X. Jiang, L. Peng, H. Schroeder, and Q. Zhang, “Assessment of socioeconomic costs to China’s air pollution,” *Atmospheric Environment*, vol. 139, pp. 147–156, 2016. DOI: 10.1016/J.ATMOENV.2016.05.036.
- [176] H. L. Gough *et al.*, “Field measurement of natural ventilation rate in an idealised full-scale building located in a staggered urban array: Comparison between tracer gas and pressure-based methods,” *Building and Environment*, vol. 137, pp. 246–256, 2018. DOI: 10.1016/J.BUILDENV.2018.03.055.
- [177] B. Li, C. Li, Q. Yang, Y. Tian, and X. Zhang, “Full-scale wind speed spectra of 5Year time series in urban boundary layer observed on a 325m meteorological tower,” *Journal of Wind Engineering and Industrial Aerodynamics*, vol. 218, p. 104791, 2021. DOI: 10.1016/J.JWEIA.2021.104791.
- [178] Y. He, Z. Liu, and E. Ng, “Parametrization of irregularity of urban morphologies for designing better pedestrian wind environment in high-density cities – A wind tunnel study,” *Building and Environment*, vol. 226, p. 109692, 2022. DOI: 10.1016/J.BUILDENV.2022.109692.
- [179] J. Hang and G. Chen, “Experimental study of urban microclimate on scaled street canyons with various aspect ratios,” *Urban Climate*, vol. 46, p. 101299, 2022. DOI: 10.1016/J.UCLIM.2022.101299.

- [180] D. Guo, P. Zhao, R. Wang, R. Yao, and J. Hu, “Numerical simulations of the flow field and pollutant dispersion in an idealized urban area under different atmospheric stability conditions,” *Process Safety and Environmental Protection*, vol. 136, pp. 310–323, 2020. DOI: 10.1016/j.psep.2020.01.031.
- [181] N. Reiminger, J. Vazquez, N. Blond, M. Dufresne, and J. Wertel, “CFD evaluation of mean pollutant concentration variations in step-down street canyons,” *Journal of Wind Engineering and Industrial Aerodynamics*, vol. 196, 2020. DOI: 10.1016/j.jweia.2019.104032.
- [182] M. R. K. Nezhad, C. F. Lange, and B. A. Fleck, “Evaluating the validity of computational fluid dynamics model of dispersion in a complex urban geometry using two sets of experimental measurements,” *International Journal of Mechanical and Mechatronics Engineering*, vol. 17, no. 3, pp. 78–86, 2023.
- [183] M. R. Kaviani Nezhad, C. F. Lange, and B. A. Fleck, “Performance Evaluation of the RANS Models in Predicting the Pollutant Concentration Field within a Compact Urban Setting: Effects of the Source Location and Turbulent Schmidt Number,” *Atmosphere*, vol. 13, no. 7, p. 1013, 2022. DOI: 10.3390/atmos13071013.
- [184] W. N. Edeling, P. Cinnella, R. P. Dwight, and H. Bijl, “Bayesian estimates of parameter variability in the  $k-\epsilon$  turbulence model,” *Journal of Computational Physics*, vol. 258, pp. 73–94, 2014. DOI: 10.1016/J.JCP.2013.10.027.
- [185] M. Shirzadi, P. A. Mirzaei, and Y. Tominaga, “RANS model calibration using stochastic optimization for accuracy improvement of urban airflow CFD modeling,” *Journal of Building Engineering*, vol. 32, p. 101756, 2020. DOI: 10.1016/J.JOBE.2020.101756.
- [186] B. Blocken, Y. Tominaga, and T. Stathopoulos, “CFD simulation of micro-scale pollutant dispersion in the built environment,” *Building and Environment*, vol. 64, pp. 225–230, 2013. DOI: 10.1016/J.BUILDENV.2013.01.001.
- [187] Z. Warhaft, “Passive Scalars in Turbulent Flows,” *Annual Reviews*, vol. 32, pp. 203–240, 2003. DOI: 10.1146/ANNUREV.FLUID.32.1.203.
- [188] R. Rossi and G. Iaccarino, “Numerical simulation of scalar dispersion downstream of a square obstacle using gradient-transport type models,” *Atmospheric Environment*, vol. 43, no. 16, pp. 2518–2531, 2009. DOI: 10.1016/j.atmosenv.2009.02.044.
- [189] M. Shirzadi, P. A. Mirzaei, M. Naghashzadegan, and Y. Tominaga, “Modelling enhancement of cross-ventilation in sheltered buildings using stochastic optimization,” *International Journal of Heat and Mass Transfer*, vol. 118, pp. 758–772, 2018. DOI: 10.1016/J.IJHEATMASSTRANSFER.2017.10.107.
- [190] Q. Wang, J. Wang, Y. Hou, R. Yuan, K. Luo, and J. Fan, “Micrositing of roof mounting wind turbine in urban environment: CFD simulations and lidar measurements,” *Renewable Energy*, vol. 115, pp. 1118–1133, 2018. DOI: 10.1016/J.RENENE.2017.09.045.

- [191] F. Campolongo and R. Braddock, “Sensitivity analysis of the IMAGE greenhouse model,” *Environmental Modelling and Software*, vol. 14, no. 4, pp. 275–282, 1999. DOI: 10.1016/S1364-8152(98)00079-6.
- [192] F. Campolongo and R. Braddock, “The use of graph theory in the sensitivity analysis of the model output: a second order screening method,” *Reliability Engineering & System Safety*, vol. 64, no. 1, pp. 1–12, 1999. DOI: 10.1016/S0951-8320(98)00008-8.
- [193] P. N. Koch, R. J. Yang, and L. Gu, “Design for six sigma through robust optimization,” *Structural and Multidisciplinary Optimization 2004 26:3*, vol. 26, no. 3, pp. 235–248, 2004. DOI: 10.1007/S00158-003-0337-0.
- [194] D. E. Goldberg, “Genetic algorithms in search optimization and machine learning,” 1988. [Online]. Available: <https://api.semanticscholar.org/CorpusID:38613589>.
- [195] J. Hammersley and D. Handscomb, *Monte Carlo Methods*. Chapman and Hall, 1964.
- [196] J. M. Gimenez and F. Bre, “Optimization of RANS turbulence models using genetic algorithms to improve the prediction of wind pressure coefficients on low-rise buildings,” *Journal of Wind Engineering and Industrial Aerodynamics*, vol. 193, p. 103978, 2019. DOI: 10.1016/J.JWEIA.2019.103978.
- [197] Y. Tominaga *et al.*, “AIJ guidelines for practical applications of CFD to pedestrian wind environment around buildings,” *Journal of Wind Engineering and Industrial Aerodynamics*, vol. 96, no. 10-11, pp. 1749–1761, 2008. DOI: 10.1016/J.JWEIA.2008.02.058.
- [198] P. J. Richards and S. E. Norris, “Appropriate boundary conditions for computational wind engineering models revisited,” *Journal of Wind Engineering and Industrial Aerodynamics*, vol. 99, no. 4, pp. 257–266, 2011. DOI: 10.1016/j.jweia.2010.12.008.
- [199] F. Toja-Silva, C. Peralta, O. Lopez-Garcia, J. Navarro, and I. Cruz, “Roof region dependent wind potential assessment with different RANS turbulence models,” *Journal of Wind Engineering and Industrial Aerodynamics*, vol. 142, pp. 258–271, 2015. DOI: 10.1016/J.JWEIA.2015.04.012.
- [200] K. Misawa, Y. Sekine, Y. Kusukubo, and K. Sohara, “Photocatalytic degradation of atmospheric fine particulate matter (PM 2.5 ) collected on TiO 2 supporting quartz fibre filter,” *Environmental Technology*, vol. 41, no. 10, pp. 1266–1274, 2020. DOI: 10.1080/09593330.2018.1530696.
- [201] S. Quarmby, G. Santos, and M. Mathias, “Air Quality Strategies and Technologies: A Rapid Review of the International Evidence,” *Sustainability*, vol. 11, no. 10, p. 2757, 2019. DOI: 10.3390/su11102757.

- [202] D. Voordeckers, T. Lauriks, S. Denys, P. Billen, T. Tytgat, and M. Van Acker, “Guidelines for passive control of traffic-related air pollution in street canyons: An overview for urban planning,” *Landscape and Urban Planning*, vol. 207, 2021. DOI: 10.1016/j.landurbplan.2020.103980.
- [203] J. Lu, N. Nazarian, M. A. Hart, E. S. Krayenhoff, and A. Martilli, “Novel Geometric Parameters for Assessing Flow Over Realistic Versus Idealized Urban Arrays,” *Journal of Advances in Modeling Earth Systems*, vol. 15, no. 7, e2022MS003287, 2023. DOI: 10.1029/2022MS003287.
- [204] Y. Ishida, T. Okaze, and A. Mochida, “Influence of urban configuration on the structure of kinetic energy transport and the energy dissipation rate,” *Journal of Wind Engineering and Industrial Aerodynamics*, vol. 183, pp. 198–213, 2018. DOI: 10.1016/J.JWEIA.2018.10.016.
- [205] M. Bady, S. Kato, and H. Huang, “Towards the application of indoor ventilation efficiency indices to evaluate the air quality of urban areas,” *Building and Environment*, vol. 43, no. 12, pp. 1991–2004, 2008. DOI: 10.1016/J.BUILDENV.2007.11.013.
- [206] Z. Shen, B. Wang, G. Cui, and Z. Zhang, “Flow pattern and pollutant dispersion over three dimensional building arrays,” *Atmospheric Environment*, vol. 116, pp. 202–215, 2015. DOI: 10.1016/J.ATMOSENV.2015.06.022.
- [207] J. J. Kim and J. J. Baik, “A numerical study of the effects of ambient wind direction on flow and dispersion in urban street canyons using the RNG  $k-\epsilon$  turbulence model,” *Atmospheric Environment*, vol. 38, no. 19, pp. 3039–3048, 2004. DOI: 10.1016/J.ATMOSENV.2004.02.047.
- [208] J. Claus, O. Coceal, T. G. Thomas, S. Branford, S. E. Belcher, and I. P. Castro, “Wind-Direction Effects on Urban-Type Flows,” *Boundary-Layer Meteorology*, vol. 142, no. 2, pp. 265–287, 2012. DOI: 10.1007/S10546-011-9667-4/METRICAL.
- [209] C. Huang *et al.*, “Effect of urban morphology on air pollution distribution in high-density urban blocks based on mobile monitoring and machine learning,” *Building and Environment*, vol. 219, p. 109 173, 2022. DOI: 10.1016/j.buildenv.2022.109173.
- [210] R. Jia, J. Yang, X. Zhu, F. Xu, and L. Wang, “A study on the gaseous radionuclide dispersion in the highway across urban blocks: Effects of the urban morphology, roadside vegetation and leakage location,” *Sustainable Cities and Society*, vol. 95, p. 104 617, 2023. DOI: 10.1016/J.SCS.2023.104617.
- [211] A. U. Weerasuriya, X. Zhang, K. T. Tse, C. H. Liu, and K. C. Kwok, “RANS simulation of near-field dispersion of reactive air pollutants,” *Building and Environment*, vol. 207, p. 108 553, 2022. DOI: 10.1016/J.BUILDENV.2021.108553.
- [212] G. Z. Guo, Y. Yu, K. C. Kwok, and Y. Zhang, “Air pollutant dispersion around high-rise buildings due to roof emissions,” *Building and Environment*, vol. 219, p. 109 215, 2022. DOI: 10.1016/j.buildenv.2022.109215.

- [213] S. G. Perry, D. K. Heist, L. H. Brouwer, E. M. Monbureau, and L. A. Brixey, “Characterization of pollutant dispersion near elongated buildings based on wind tunnel simulations,” *Atmospheric Environment*, vol. 142, pp. 286–295, 2016. DOI: 10.1016/J.ATMOSENV.2016.07.052.
- [214] P. Y. Cui, Z. Li, and W. Q. Tao, “Wind-tunnel measurements for thermal effects on the air flow and pollutant dispersion through different scale urban areas,” *Building and Environment*, vol. 97, pp. 137–151, 2016. DOI: 10.1016/j.buildenv.2015.12.010.
- [215] Y. Gao, Z. Wang, C. Liu, and Z. R. Peng, “Assessing neighborhood air pollution exposure and its relationship with the urban form,” *Building and Environment*, vol. 155, no. December 2018, pp. 15–24, 2019. DOI: 10.1016/j.buildenv.2018.12.044.
- [216] K. An, J. Fung, and S. Yim, “Sensitivity of inflow boundary conditions on downstream wind and turbulence profiles through building obstacles using a CFD approach,” *Journal of Wind Engineering and Industrial Aerodynamics*, vol. 115, pp. 137–149, 2013. DOI: 10.1016/j.jweia.2013.01.004.
- [217] S. Hanna, S. Tehranian, B. Carissimo, R. Macdonald, and R. Lohner, “Comparisons of model simulations with observations of mean flow and turbulence within simple obstacle arrays,” *Atmospheric Environment*, vol. 36, no. 32, pp. 5067–5079, 2002. DOI: 10.1016/S1352-2310(02)00566-6.
- [218] C. Grimmond and T. Oke, “Aerodynamic properties of urban areas derived from analysis of surface form,” *Journal of Applied Meteorology*, vol. 38, no. 9, pp. 1262 – 1292, 1999. DOI: 10.1175/1520-0450(1999)038<1262:APOUAD>2.0.CO;2.
- [219] J. Hang and Y. Li, “Ventilation strategy and air change rates in idealized high-rise compact urban areas,” *Building and Environment*, vol. 45, no. 12, pp. 2754–2767, 2010. DOI: 10.1016/j.buildenv.2010.06.004.
- [220] Y. Peng, R. Buccolieri, Z. Gao, and W. Ding, “Indices employed for the assessment of “urban outdoor ventilation” - A review,” *Atmospheric Environment*, vol. 223, p. 117211, 2020. DOI: 10.1016/j.atmosenv.2019.117211.
- [221] S.-J. Mei, J.-T. Hu, D. Liu, F.-Y. Zhao, Y. Li, and H.-Q. Wang, “Airborne pollutant dilution inside the deep street canyons subjecting to thermal buoyancy driven flows: Effects of representative urban skylines,” *Building and Environment*, vol. 149, pp. 592–606, 2019. DOI: 10.1016/j.buildenv.2018.12.050.
- [222] J. Hang, M. Sandberg, Y. Li, and L. Claesson, “Pollutant dispersion in idealized city models with different urban morphologies,” *Atmospheric Environment*, vol. 43, no. 38, pp. 6011–6025, 2009. DOI: 10.1016/j.atmosenv.2009.08.029.
- [223] L. Chen, J. Hang, M. Sandberg, L. Claesson, S. Di, and H. Wigo, “The impacts of building height variations and building packing densities on flow adjustment and city breathability in idealized urban models,” *Building and Environment*, vol. 118, pp. 344–361, 2017. DOI: 10.1016/j.buildenv.2017.03.042.

- [224] J. Hang, Y. Li, M. Sandberg, R. Buccolieri, and S. Di, “The influence of building height variability on pollutant dispersion and pedestrian ventilation in idealized high-rise urban areas,” *Building and Environment*, vol. 56, pp. 346–360, 2012. DOI: 10.1016/j.buildenv.2012.03.023.
- [225] C. B. da Silva and J. C. F. Pereira, “Analysis of the gradient-diffusion hypothesis in large-eddy simulations based on transport equations,” *Physics of Fluids*, vol. 19, no. 3, 2007. DOI: 10.1063/1.2710284.
- [226] Y. H. Juan, Z. Li, Y. T. Lee, C. Y. Wen, and A. S. Yang, “Effect of wind-based climate-responsive design on city breathability of a compact high-rise city,” *Journal of Building Engineering*, vol. 78, p. 107773, 2023. DOI: 10.1016/j.job.2023.107773.